ABSTRACT

Title of dissertation: MODELING SUPERCONDUCTING CIRCUITS FOR QUANTUM COMPUTING AND QUANTUM SENSING APPLICATIONS

Brittany Rachel Richman
Doctor of Philosophy, 2025

Dissertation directed by: Professor Jacob M. Taylor
Department of Physics

Superconducting circuits are at the forefront of quantum computing and quantum sensing technologies, where accurate modeling and simulation are crucial for understanding and optimizing their performance. In this dissertation, we study modeling techniques and novel device designs to advance these technologies, focusing on efficient simulations, direct velocity measurement, and nonreciprocal devices for quantum information processing. First, we investigate the use of discrete variable representations (DVRs) to numerically represent superconducting circuits, exploring their use and effectiveness in several prototypical examples. We find that not only are these DVRs capable of achieving decoherence-accurate simulation, i.e., accuracy at the resolution of experiments subject to decay, decoherence, and dephasing, they also demonstrate improvements in efficiency with smaller basis sizes and better convergence over current standard approaches, showing that DVRs are an advantageous

alternative for representing superconducting circuits.

We then consider a specific quantum sensing application, direct velocity measurement in superconducting circuits. We propose and characterize theoretical models for backaction evading, direct velocity measurement that utilize traditional electric and magnetic transducers. We consider the readout of this signal via electric or magnetic field sensing by creating generic models analogous to the standard optomechanical position-sensing problem, thereby facilitating the assessment of measurement-added noise. Using simple models that characterize a wide range of transducers, we find that the choice of readout scheme — voltage or current — for each mechanical detector configuration implies access to either the position or velocity of the mechanical sub-system.

Finally, we explore the application of superconducting circuits in nonreciprocal devices, such as circulators. Commercial circulators in the microwave domain typically use ferromagnetic materials and wave interference, requiring large devices and large magnetic fields. However, quantum information devices for sensing and computation require small sizes, lower fields, and better on-chip integration. Equivalences to ferromagnetic order — such as the XY model — can be realized at much lower magnetic fields by using arrays of superconducting islands connected by Josephson junctions. Here we show that the quantum-coherent motion of a single vortex in such an array suffices to induce nonreciprocal behavior, enabling a small-scale, moderate-bandwidth, and low insertion loss circulator at very low magnetic fields and at microwave frequencies relevant for experiments with qubits.

MODELING SUPERCONDUCTING CIRCUITS FOR QUANTUM COMPUTING AND QUANTUM SENSING APPLICATIONS

by

Brittany Rachel Richman

Dissertation submitted to the Faculty of the Graduate School of the
University of Maryland, College Park in partial fulfillment
of the requirements for the degree of
Doctor of Philosophy
2025

Advisory Committee:
Professor Christopher J. Lobb, Chair/Co-Advisor
Professor Jacob M. Taylor, Advisor
Professor Victor M. Galitski
Professor Saikat Guha
Professor Alicia J. Kollár

© Copyright by
Brittany Rachel Richman
2025

Acknowledgments

The path I've taken through grad school certainly hasn't been easy, and definitely not brief! However, despite the incredible challenges it often presented, I know that this process has not only taught me a tremendous amount of physics, but also a tremendous amount about myself and my own resilience. While I'm incredibly proud of myself for reaching this point — it's truly not something I ever thought myself capable of — I don't think I could've made it this far without the help, guidance, and encouragement of many very wonderful people, and I'd like to take a moment to appreciate and recognize their contributions now.

I'm incredibly grateful to my advisor Jake Taylor and my co-advisor Chris Lobb. Despite next to no research experience and only a bunch of very neat homework assignments as a writing sample, Jake welcomed me into the group, and over the years has provided a wealth of scientific insight, guidance, and advice. My co-advisor Chris has provided a near weekly source of support and encouragement for the last several years, always happy to be a sounding board for the science I'm musing about and always insistent that I was making progress and shouldn't give up. I'm so appreciative of all you both have provided me over years.

I'd also like to thank my undergraduate advisor Gary DeLeo, without whom I would've never pursued physics or grad school. At a time when I was terrified of physics and felt I didn't and couldn't ever belong, Professor DeLeo — despite my fear and protest — never wavered in his belief that I was exactly where I was supposed

to be. I'm so grateful for all that he's done for me over the years: exposing me to science outreach, immersing me in the physics department at Lehigh, introducing me to professors and grad students, and continuing to remain an invaluable part of my support system.

Working in Jake's group for so long has afforded me the honor and privilege of knowing and working with some of the kindest and smartest people I've ever known. I'm so grateful to so many of our group members over the years: Steve Ragole, Chiao-Hsuan Wang, Andrew Glaudell, Minh Tran, Shangjie Guo, Sohitri Ghosh, Justyna Zwolak, Dan Carney, Jon Kunjummen, Gaya Premawardhana, and Huy Nguyen. I feel incredibly lucky that my path has crossed with all of theirs in small and large ways, and have valued all the stimulating discussions, guidance, and advice they have provided me. I'd also like to especially thank Minh and Sohitri, who over the course of our time in Jake's group have become wonderful and supportive friends who have helped me both in science and in life.

To my unbelievable friends Amanda, Jamie, and Kristi — thank you for always being there to listen and encourage, regardless of distance or time apart. And to Kristi especially, I'm so grateful that grad school brought us together nearly a decade ago. Thank you for always being at the ready to provide any and all manner of help — everything from providing a safe space to cry to scheming about how you'd avenge any and all who wronged me. I'm incredibly lucky to have had you to lean on and learn from throughout this process.

To my parents, Keith and Carol, my sisters, Hannah and Becca, along with the rest of my family — all I can say is thank you. Thank you for always listening to every trial and tribulation of grad school, for your wild enthusiasm for every small inch of progress I was able to make, and for always believing, no matter how stressed or concerned I was, that I would reach this goal. I'm in awe of the confidence you place in me, but it has provided so much motivation, comfort, and reassurance over the years. I love you all so much, thank you.

Finally, to Josey — you've had a front-row view of this entire journey, and I don't think I can fully capture the immense gratitude and appreciation I have for you and all you have done to help me over the years. Thank you for being my emotional support human, for putting up with my psychotic sleep schedule (especially as of late), and for continuing to encourage me through countless panic spirals. No matter how many 'Brittany-Josey science times' I've put you through, talking your ear off about nearly every aspect of my work, your unrelenting support and love over the years has been a constant source of comfort. I'm so thankful for you (along with Stella and Penny!) and the life we've built together, I love you.

Table of Contents

Acknowledgements **ii**

List of Figures **x**

List of Tables **xiii**

List of Acronyms and Abbreviations **xiv**

1 Introduction **1**

1.1 Superconductivity: A Brief Origin Story 1

1.2 The Josephson Effect 3

1.3 The First Wave of Superconducting Circuit Applications 5

1.4 Macroscopic Quantum Phenomena 9

1.5 The Current Landscape: Recent Past and Present 12

2 Utilizing Discrete Variable Representations for Decoherence-Accurate Numerical Simulation of Superconducting Circuits **16**

2.1 Introduction 16

2.2 Overview of Sinc DVRs 19

2.2.1 The Traditional Sinc DVR 20

2.2.2 The Truncated Sinc DVR 24

2.2.3 Representing Operators 26

2.3 Numerical Features and Applications of Sinc DVRs 32

2.3.1 LC Oscillator 33

2.3.2 Fluxonium 40
2.3.2.1 Level Convergence 41
2.3.2.2 Basis State Contributions 47
2.3.2.3 Phase Shifts 50
2.3.3 Transmon 56
2.3.3.1 Level Convergence 57
2.3.3.2 Basis State Contributions 59
2.4 Outlook 61

Appendix 2.A Discrete Variable Representations 64
2.A.1 Orthogonal Polynomial DVRs 68
2.A.2 The Traditional Sinc DVR 70
2.A.3 The Truncated Sinc DVR 73
Appendix 2.B Details for the LC Oscillator Example 76
Appendix 2.C Details for the Fluxonium Example 79
Appendix 2.D The Finite Difference Method 83
2.D.1 Lowest Order FD Method 83
2.D.2 General Derivation of the FD Approximation 88

3 Backaction-Evading Receivers with Magnetomechanical and Electromechanical Sensors 91
3.1 Introduction 91
3.2 Transducers 94
3.2.1 Magnetomechanical Detector Scheme 94
3.2.2 Electromechanical Detector Scheme 100
3.3 Idealized Receivers 103
3.3.1 Electric Field Sensing 105
3.3.2 Magnetic Field Sensing 108
3.3.3 Exploiting the Optomechanics Analogy 111

3.4 Combinations of Transducers and Receivers 112
3.4.1 The Equations of Motion 113
3.4.2 Assembling the Noise PSD 117
3.4.3 Comparison to Optomechanical Systems 124
3.4.4 Details of the Noise Curves 128
3.4.5 Analysis in the Context of Windchime 132
3.5 Outlook 137

Appendix 3.A Faraday's Law 139
Appendix 3.B Circuit Analysis of the Detector Schemes 141
3.B.1 Magnetomechanical Circuit Analysis 143
3.B.2 Electromechanical Circuit Analysis 147
Appendix 3.C Adding the Drive and Moving to the Linearized Regime . . 154
Appendix 3.D Defining the Input and Output Bath Modes 156
Appendix 3.E Explicit Solutions for the Output Phase Quadratures . . . 158
Appendix 3.F Explicit Noise PSD Solutions 160
Appendix 3.G Analysis of Optomechanical Systems for Comparison 162

4 Circulation by Microwave-Induced Vortex Transport for Signal Isolation 164
4.1 Introduction 164
4.2 Vortex-Based Nonreciprocity 168
4.2.1 Model Circuit 168
4.2.2 Entering the Vortex Regime 171
4.2.3 Quantum Behavior of Vortices in the Intermediate Tunneling Regime 173
4.2.4 Connecting Vortex Behavior with the Microwave Response . . 178
4.3 Central Circuit Coupled to External Circuits 181
4.3.1 The Full Circuit Model 181

4.3.2 Single-Excitation S-Matrix Analysis 183
4.3.3 Conditions for Ideal Circulation 185
4.4 Numerical Results 189
4.4.1 Bandwidth, Nonreciprocity, and Circulation 190
4.4.2 Resilience to Charge and Flux Noise 194
4.5 Outlook 197

Appendix 4.A Alternative Circuit — Floating Central Island 199
Appendix 4.B Classical and Semi-Classical Analysis of the Central Circuit 204
4.B.1 Classical Ground State Vortex Configuration 204
4.B.2 Semi-Classical Analysis of the Central Circuit 206
Appendix 4.C Derivation of the Full System Hamiltonian 211
4.C.1 Lagrangian of the Transmission-Line Resonators 212
4.C.2 Assembling the Remainder of the Full System Lagrangian . . 219
4.C.3 The Weak Coupling Limit 220
4.C.4 Assembling the Total Hamiltonian 224
Appendix 4.D Input-Output Theory in the Single Excitation Manifold . . 230
Appendix 4.E General Conditions for Ideal Circulation 233
Appendix 4.F Investigation of Additional External Flux Regions 236
Appendix 4.G Parameter Considerations 241
Appendix 4.H Details of the Noise Investigations 245
4.H.1 Statistical Analysis 247
4.H.2 Fabrication Disorder 249

5 Conclusions **252**

Bibliography **256**

List of Figures

1.1 Schematic representation of a Josephson junction. 3

2.1 Functional forms of the DVR basis states for the traditional sinc DVR and truncated sinc DVR. 22
2.2 Circuit schematics of the LC oscillator, the fluxonium, and the transmon. 32
2.3 Example behavior of the absolute value of the energy difference $|\Delta_0|$ as function of matrix size in the ground state of the LC oscillator. . . 35
2.4 The decoherence-accurate matrix size R as a function of grid size in the LC oscillator's ground state, for all four of the DVRs considered. 37
2.5 The decoherence-accurate matrix size R as a function of grid size for the fluxonium ground state, for all four of the DVRs considered. . . . 43
2.6 The decoherence-accurate matrix size R and the saturation precision P for the first five energy eigenstates of the fluxonium in the traditional phase DVR, the traditional charge number DVR, and the harmonic oscillator basis. 46
2.7 Eigenstate decompositions showing $|\langle\Psi_i|\psi_\alpha\rangle|^2$ for the first eight energy eigenstates of the fluxonium for the traditional phase DVR, the traditional charge number DVR, and the harmonic oscillator basis. . . 49
2.8 Effects of the phase shift operation in the ground state of the fluxonium. 55
2.9 The absolute value of the energy difference $|\Delta_0|$ as function of matrix size in the ground state of the transmon in both the transmon limit and the charge limit, using the traditional charge DVR and truncated phase DVR. 58
2.10 Eigenstate decompositions showing $|\langle\Psi_i|\psi_\alpha\rangle|^2$ for the first eleven energy eigenstates of the transmon in the transmon limit using the traditional charge DVR and the truncated phase DVR. 60

2.11 Eigenstate decompositions showing $|\langle\Psi_i|\psi_\alpha\rangle|^2$ for the first eleven energy eigenstates of the transmon in the charge limit using the traditional charge DVR and the truncated phase DVR. 61
2.12 The absolute value of the energy difference $|\Delta_0|$ as function of matrix size in the ground state of the LC oscillator, in all four DVRs. 77
2.13 The absolute value of the energy difference $|\Delta_0|$ as function of matrix size in the ground state of the fluxonium, in all four DVRs. 80
2.14 The absolute value of the energy difference $|\Delta_0|$ as function of matrix size in the ground state of the LC oscillator, using the FD method as well as higher-order approximations. 87

3.1 Schematic representation of the magnetomechanical and electromechanical transducers, as well as their circuit implementations. 96
3.2 Schematic representations of configurations for voltage and current measurement via electric and magnetic field sensing. 104
3.3 Total measurement-added noise for each detector configuration and readout choice. 125
3.4 The noise PSD representing total measurement-added noise in an optomechanical system for both position- and velocity-sensing. 126
3.5 Details of the total measurement-added noise to explicitly show the individual contributions from shot noise and backaction noise. 129
3.6 The $\mathrm{SNR}^2_{\mathrm{opt}}$ as a function of the radius of the sensor for a gravitational impulse from a dark matter interaction. 135
3.7 Schematic highlighting the two spanning trees associated with each gauge in the magnetomechanical detector configuration. 144

4.1 Schematic representation of the circulator model and its supported vortices. 169
4.2 Energy eigenvalues and persistent currents in the central circuit as a function of flux penetration. 176
4.3 Microwave response of the central circuit to an incoming voltage perturbation, including a visual of the generated rotating vortices. 179
4.4 The phase difference $\Delta\theta$ as a function of driving frequency ω, including a visual representation of the energy level structure at our chosen operating point. 191

4.5 Nonreciprocal transmission and bandwidth performance of the circulator model as well as its resilience to charge and flux noise. 193
4.6 Uniform charge disorder in the original model. 203
4.7 Loop currents corresponding to the classical ground state vortex configuration as a function of A. 205
4.8 Spin wave frequencies of the central circuit as a function of the flux penetration A. 208
4.9 The first four energy levels associated with the spin-wave excitations of the central circuit as a function of the flux penetration A. 210
4.10 Schematic of the k^{th} arm of the model that capacitively couples a transmission-line resonator to the k^{th} island of the central circuit as well as a semi-infinite transmission line. 211
4.11 Summary of circulator performance and understanding at the first alternative flux point. 237
4.12 Summary of circulator performance and understanding at the second alternative flux point. 239
4.13 The effect of offset charge number variations from the ideal on the minimum of the extinction ratio ER_0 (in dB) between ports one and two. 247
4.14 A pairwise plot of the minimum of the extinction ratio ER_0 and the maximum of the insertion loss IL_0 in the presence of charge noise and flux noise. 248
4.15 Effects of fabrication disorder in the junctions on circulator performance. 250

List of Tables

4.1 External Circuit Parameters for Nonreciprocal Points 192

List of Acronyms and Abbreviations

AC alternating current

BCS Bardeen, Cooper, and Schrieffer

BKT Berezinskii–Kosterlitz–Thouless

CPB Cooper-pair box

CW clockwise

CCW counterclockwise

DC direct current

DM dark matter

DVR discrete variable representation

FD finite difference

GL Ginzburg-Landau

JJA Josephson junction array

MQT macroscopic quantum tunneling

PSD power spectral density

QED quantum electrodynamics

QND quantum non-demolition

QPS quantum phase slip

RF radio frequency

RF-SET radio-frequency single-election transistor

RSFQ rapid single-flux-quantum

SFQ single flux quanta

SNR signal-to-noise ratio

SQL standard quantum limit

SQUID Superconducting Quantum Interference Device

Chapter 1: Introduction

Just as the development of the theory of superconductivity and the Josephson effect fueled a wave of novel superconducting circuit applications in the 1960s, '70s, and '80s, theoretical and experimental work on macroscopic quantum phenomena in superconducting circuits in the 1980s — coupled with the increasing interest in quantum computing — has spurred a new wave of innovations using superconducting circuits over the past three decades. Driven by the quest to realize a quantum computer on superconducting platforms, a remarkably rapid development in our understanding and relevant technologies has occurred. Despite this, today's most powerful quantum processors still face many technical hurdles, and are a long way from being realized in a commercial setting. However, these challenges only continue to drive research and development into superconducting circuits, yielding new insights and advancements that extend far beyond quantum computing.

1.1 Superconductivity: A Brief Origin Story

The existence of the low-temperature superconducting state was first discovered in 1911 by Heike Kamerlingh Onnes [1–3], with the identification of likely the most well-

known property of superconductivity: the presence of a critical temperature below which electrical resistance disappears. Despite this early revelation, another now-characteristic feature of superconductivity was not discovered until 1933 [4], when Meissner and Ochsenfeld found that magnetic fields were expelled from a material as it transitioned into its superconducting state. Shortly thereafter, the London brothers established the first theoretical description of superconductivity, the London equations [5], which captured both of these important properties.

Despite these developments, the underlying mechanisms of superconductivity remained a mystery, and its theoretical understanding continued to be primarily phenomenological until the 1950s, when experimental work [6–9] began to uncover key features of the superconducting state. These observations ultimately culminated in the groundbreaking work of Bardeen, Cooper, and Schrieffer (BCS) in 1957 that predicted the formation of Cooper pairs [10], the charge carriers of the superconducting state that were created by the pairing of two electrons, as well as a full microscopic theory of superconductivity [11]. The BCS theory captured and predicted, to a high degree of accuracy, numerous experimental phenomena, providing fundamental answers to the questions raised since the initial discovery of superconductivity nearly 50 years prior.

While this progress was momentous, a potentially more impactful development came only a couple years later, in 1959 [12], when Gor'kov was able to use the BCS theory to derive an older, lesser known, and mostly phenomenological theory, the

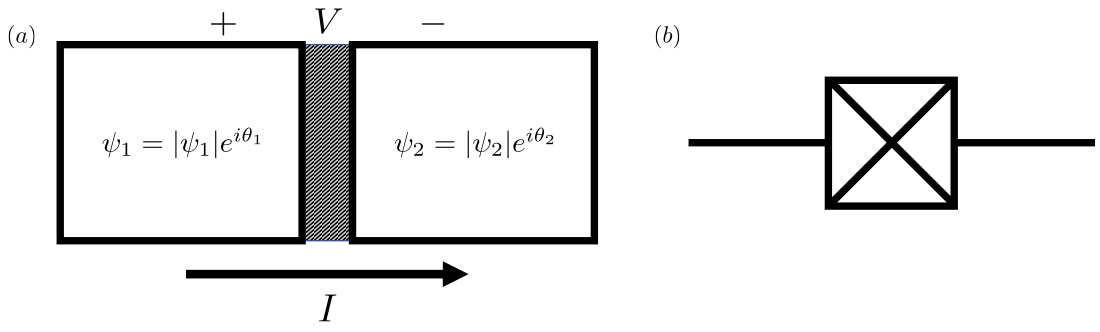


Figure 1.1: (a) Schematic representation of a Josephson junction, consisting of two superconductors characterized by the macroscopic wavefunctions ψ_1 and ψ_2, separated by a thin barrier. (b) Circuit symbol for a Josephson junction.

Ginzburg-Landau (GL) theory of superconductivity [13]. This was of particular relevance, because the GL theory of superconductivity was a macroscopic description of the superconducting state, centered around the charge carriers (Cooper pairs) as well as a complex order parameter $\psi = |\psi|e^{i\theta}$. Gor'kov was able to show that this order parameter could be understood as a macroscopic wavefunction of all the Cooper pairs in a superconducting material. This succinct description was ultimately of immense value, becoming a crucial element of the most important prediction for the development of superconducting circuits: the Josephson effect.

1.2 The Josephson Effect

In 1962, Brian Josephson theorized [14] that Cooper pairs were capable of tunneling through a thin barrier that separated two superconductors, thus generating a measurable supercurrent. For two superconductors characterized by macroscopic wavefunctions with complex phases θ_1 and θ_2 on either side of the barrier, Josephson

predicted that the current I through the barrier as well as the voltage V across the barrier, shown schematically in Fig. 1.1a, were dependent on the phase difference $\theta_1 - \theta_2$ between the superconductors. This was captured by the current and voltage relations,

$$\begin{aligned} I &= I_C \sin \gamma_{12} \\ V &= \frac{\hbar}{2e} \frac{d\gamma_{12}}{dt} \end{aligned} \quad , \tag{1.1}$$

where I_C represented the critical current — the maximum supercurrent that the barrier can support — with e the elementary electron charge and $\hbar$ the reduced Planck constant. Here we express Josephson's equations in terms of the gauge-invariant phase difference [15, 16],

$$\gamma_{12} = \theta_1 - \theta_2 - \frac{2e}{\hbar} \int_1^2 \mathbf{A} \cdot d\mathbf{l} \ , \tag{1.2}$$

to account for the possible presence of an external magnetic field that is characterized by the vector potential $\mathbf{A}$.

Josephson's equations predicted both direct current (DC) and alternating current (AC) effects. Even in the absence of a voltage across the barrier, Eq. 1.1 indicated that a DC supercurrent is generated so long as $\gamma_{12} \neq 0$ for the two superconductors, a feature quite distinct from normal conductors. Alternatively, with a DC or AC voltage bias applied across the barrier, AC effects relating voltage and frequency were predicted. Using Eq. 1.1, the application of a constant voltage bias V_{dc} results in an AC supercurrent that oscillates at a frequency of $2eV_{\mathrm{dc}}/\hbar$. Upon the addition of a

time-varying component $V_{\rm ac}\cos\omega t$, it can be shown that for specific, quantized values $V_{\rm dc}^n = n\hbar\omega/2e$, a DC supercurrent is generated with a magnitude that depends on both $V_{\rm ac}$ and ω of the time-varying component. Josephson's equations also implied another important feature, namely, the energy stored in this supercurrent. Since energy is given by integrating the product of current and voltage, by combining the current and voltage relations in Eq. (1.1), the energy stored in the supercurrent is found to be $-E_J\cos\gamma_{12}$, with E_J representing the characteristic energy scale associated with the tunneling of Cooper pairs, defined as $E_J = \hbar I_C/2e$ and typically referred to as the Josephson energy.

The impact of Brian Josephson's discovery cannot be overstated — he predicted macroscopic, measurable effects that were the consequence of microscopic quantum processes. While initially met with skepticism, these predictions were all quickly verified experimentally [17–19], providing the underpinning for superconducting circuits and the superconducting circuit applications to come, via the circuit element that has come to be known as the Josephson junction (Fig. 1.1b).

1.3 The First Wave of Superconducting Circuit Applications

The next several decades saw the utilization of Josephson junctions and superconducting circuits for a variety of applications, particularly with regard to sensing, metrology, condensed matter physics, and computing. These developments began by utilizing small-scale superconducting circuits of only one or two Josephson junctions,

and as fabrication technologies advanced, eventually expanded to larger and more complex circuits and array structures.

Shortly following the experimental verification of the Josephson effect, in 1964 the first SQUID (Superconducting Quantum Interference Device) was developed, the DC SQUID [20], consisting of two Josephson junctions in parallel, threaded by an external flux. This device demonstrated quantum interference between the supercurrents of each junction, resulting in a total supercurrent whose critical current oscillated with a frequency dependent on the external flux. By biasing the two parallel junctions with an external current larger than the maximum supercurrent, a measurable voltage was generated across them that similarly oscillated with external flux [15, 21, 22]. Only a few years later, the RF SQUID [23] appeared, instead using a single junction in a superconducting loop threaded by an external flux, inductively coupled to a RF-driven LC circuit whose properties were modified by the external flux [15, 21, 22]. Both of these devices were highly sensitive to magnetic fields, making them extremely valuable for a variety of uses across many fields, including physics, medicine, material science, and geophysics [24]. Over the course of the 1970s and 1980s, SQUIDs found use in the implementation of magnetometers [25–33], gradiometers [34–45], voltmeters [46], amplifiers [47, 48], and susceptometers [49–51], and remain the most sensitive magnetic field detectors available to date.

Another near immediate application of the Josephson junction was in metrology, with the evolution of the voltage standard. Starting in the mid-1960s, the AC Joseph-

son effect was used to establish extremely precise values of $2e/h$ in systems of one or two Josephson junctions [52–57], culminating in the updating of the voltage standard in 1972 [58]. However, these systems only generated very small voltages (about 1-10 millivolts), which limited their precision. Motivated to improve these standards further by increasing the generated voltage, work focused on increasing the number of Josephson junctions, specifically by utilizing numerous Josephson junctions to connect islands of superconducting material in series, forming a one-dimensional Josephson junction array (JJA) [59–67]. This ultimately led to yet another update to the voltage standard in 1985 [68, 69], with continued updates, expansions, and improvements over the course of the latter half of the decade and beyond [70–79].

As one-dimensional JJAs were being proposed to improve the voltage standard, experiments on two-dimensional JJAs began in the late 1970s and early 1980s, largely motivated by theoretical work on two-dimensional systems in the early 1970s by Berezinskii, Kosterlitz, and Thouless [80–84]. Their work identified a unique phase transition, now referred to as the Berezinskii–Kosterlitz–Thouless (BKT) transition, in systems such as the XY model, a two-dimensional lattice of spins confined to rotate in the XY-plane with a nearest-neighbor interaction. The BKT transition relied on the idea that above a characteristic, finite temperature, specific spin configurations known as vortices [85, 86] were freely created due to thermal fluctuations, and below this temperature, the low energy, ordered state could be understood as a state without a free vortex, only bound pairs of vortices and their counter-configurations, anti-

vortices.

Notably, two-dimensional JJAs can be understood as physical realizations of the XY model, where the phase associated with each superconducting island is identified with each spin's angle with the x-axis and the interaction energy with nearest-neighbors is simply the Josephson energy associated with the junctions coupling the islands. In this system, the spin configuration corresponding to a vortex translates to variations in the phases of the islands, inducing a circulating supercurrent about a unit of the array, whose creation and motion was measurable in experiments [16, 87]. By 1979, various theoretical works [88–90] indicated that the BKT transition was accessible to JJAs, ushering in a wave of experimental work on two-dimensional JJAs and their properties [91, 92], ultimately highlighted by the demonstration and theoretical understanding of the BKT transition in two-dimensional JJAs [93–95]. Further, as the presence of an external magnetic field was captured by the gauge-invariant phase difference [Eq. (1.2)], two-dimensional JJAs permitted investigations into the effects of frustration on the XY model and the BKT transition as well as the creation of vortices, which continued throughout the 1980s [96–102] and spurred further research into non-linear and chaotic phenomena in JJAs [103–106].

Another field of study to gain attention in the 1980s was related to utilizing superconductivity and Josephson junctions, specifically circulating supercurrent, to enable logical operations for digital computation. Technically, this area of research originated in 1966 [107], but focused instead on a binary system defined by the presence or ab-

sence of voltage across a Josephson junction. With the potential for computational applications with low power and high speeds, research in this area grew, exemplified by the IBM program started in 1967 with the goal of creating such a Josephson junction-based computer. While this program had numerous developments [108–118], it was ultimately ended in 1983, as semiconductor technologies for computation rapidly improved and unresolved technical issues remained [119]. In 1985, a logic system was proposed that encoded information in terms of the presence or absence of single flux quanta (SFQ), i.e., circulating supercurrents in the loops of a superconducting circuit corresponding to the magnetic flux quantum $\Phi_0 = h/2e$. This logic family, rapid single-flux-quantum (RSFQ) logic [120–122], utilized voltage pulses to transfer SFQ and defined several elementary logical operations in terms of superconducting circuits that incorporated numerous Josephson junctions. RSFQ logic was soon experimentally realized, demonstrating very fast processing times with numerous applications [123–144], albeit without commercialization. It remained an active area of research over the course of the 1990s up to the present day, with various extensions and improvements in that timeframe [145–159].

1.4 Macroscopic Quantum Phenomena

In the midst of these experimental developments and technological advances, theoretical and experimental work pivoted to a key question: could the macroscopic variable measured in superconducting circuit experiments — the phase — be

treated quantum-mechanically? This was first succinctly raised by Anthony Leggett in 1978 [160], and further detailed in 1980 [161], where he speculated on the possibility of observing macroscopic quantum tunneling (MQT) of the phase degree of freedom as well as macroscopic quantum superpositions of distinct phase states. Not only did he consider ideal conditions under which this tunneling may be observed, but he also cautioned that a full understanding would require the incorporation of dissipation, as this would necessarily play a role in the ability to observe such a phenomenon. This inspired a collection of efforts over the next several years to develop a quantum mechanical understanding of superconducting circuits including dissipation [162–168]. At the same time, these ideas were being experimentally verified, with observations of MQT in SQUIDs and current-biased Josephson junctions [169–173], including the demonstration of quantized energy levels in a current-biased Josephson junction in 1985 [174] by John Martinis, Michel Devoret, and John Clarke. With this macroscopic quantum mechanical description confirmed, attention turned to the potential demonstration of a quantum superposition of these macroscopic states. Unfortunately, this proved to be quite challenging [161, 175] due to limitations in noise isolation, and progress in this area waned.

However, around this time, a new facet of quantum behavior in Josephson junctions was proposed [176, 177], instead focused on the variable conjugate to the phase, charge number, and the conditions under which it was a good quantum variable. In essence, Josephson junctions up to this point in time were relatively large, i.e.,

they had large capacitances which resulted in small charging energies relative to the Josephson energy E_J. By treating phase and charge number as quantum operators, where they are a non-commuting, conjugate pair, such Josephson junctions yielded a well-defined phase degree of freedom but highly uncertain charge number, with minimal phase fluctuations leading to MQT. However, if junctions could be made small enough to ensure relatively larger charging energies, the opposite regime may be explored, where charge number is well-defined and possible effects related to the discrete tunneling of Cooper pairs may be observed.

This shift in focus was ultimately of great value. In the coming years, advances in the fabrication of Josephson junctions enabled smaller sizes and larger charging energies, confirming these discrete charge effects [178, 179]. Most importantly however, it resulted in the identification and manipulation of macroscopic charge states [180, 181]. These developments were of critical value when in 1994, Peter Shor's work [182] launched broad efforts, across various fields, to develop qubits for quantum computing. Research into charging effects and macroscopic charge states was ultimately the foundation for the prospects of superconducting qubits, where the eventual demonstration of the superposition of macroscopic charge states [183, 184] culminated in the demonstrated creation and control of the first superconducting qubit, the charge qubit [185].

1.5 The Current Landscape: Recent Past and Present

The developments over the course of the 1980s and 1990s launched a massive research effort that has continued to expand over the last 25 years, motivated largely by quantum computing but also by the potential for using superconducting circuits for a variety of other physics applications. Their macroscopic size, tunability, and compatibility with existing fabrication technologies have made superconducting circuits a leading quantum computing platform. The development of the charge qubit was quickly followed by several other superconducting qubits, including the flux qubit [186–189], the phase qubit [190, 191], the transmon [192], and the fluxonium [193]. Companies like Google and IBM have heavily invested in superconducting platforms for quantum computing, utilizing the transmon to build and operate relatively large-scale quantum computers [194–203]. This has contributed to continuing research over the years, with no shortage of proposed superconducting qubits [204–219], all aiming to improve performance by exploiting different features of their particular designs.

A key research area to emerge has focused on the numerical modeling of superconducting circuits for hardware design and the modeling of relevant dynamics. As applications for superconducting circuits have grown, and circuits grow in size, Hamiltonian construction and diagonalization is an increasingly difficult computational problem, leading to the development of various alternative analysis methods [220–

226]. As quantum computers have progressed, numerous software tools have been built to aid in device design, Hamiltonian construction, and system characterization [227–233], recognizing the eventual need for a software tool-chain akin to that available for semiconductor circuits. With this in mind, a fundamental aspect to consider is the basis representations utilized by these tools to construct Hamiltonians, and the accuracy and efficiency they may provide for a given system. This is the focus of Chapter 2 of this dissertation, where a generalized approach to basis construction is utilized and compared to current standard approaches.

Superconducting circuits have also found use in fundamental physics and metrological applications, beginning with the development of the RF-SET (radio-frequency single-election transistor) [234, 235]. As a highly charge-sensitive, Josephson junction-based electrometer, the RF-SET was utilized in early studies to probe for quantum mechanical behavior in macroscopic mechanical oscillators [236–238], specifically via an electromechanical coupling between the RF-SET and an oscillator formed from a mechanically-varying capacitor. Over time, this field continued to evolve, instead coupling mechanical degrees of freedom to superconducting resonators, phase qubits, charge qubits (now typically referred to as Cooper-pair boxes [CPBs]), transmons, and SQUIDs. Through both electromechanical coupling and magnetomechanical coupling (via a mechanically-variable flux penetration) to nanometer and micrometer-scale oscillators, these systems were able to demonstrate increasingly stronger couplings, highly sensitive position and force measurements, and the preparation and

control of quantum oscillator states [239–248]. More recently, SQUIDs have been used to make precise position measurements of magnetically levitated superconducting spheres [249–251]. However, focus has begun to shift towards accomplishing direct velocity measurements, as these measurements offer the ability to reduce quantum measurement-added noise via the backaction evasion provided by performing a quantum non-demolition (QND) measurement. This is discussed in more detail in Chapter 3 of this dissertation, where we provide a general theoretical framework for accomplishing direct velocity measurements using superconducting circuits.

In addition to these sensing applications, the development of large-scale quantum computers has been a driver for research into additional uses for superconducting circuits, beyond qubit design. This has included many developments in the supporting hardware for quantum computers, including Josephson junction-based amplifiers [252–258], tunable couplers for multi-qubit systems [259–267], Purcell filters to suppress qubit decay [268–271], as well as systems and infrastructure for qubit control [272–275]. Importantly, as quantum computing devices have scaled up in size, the need for small-scale, on-chip solutions is increasingly relevant, particularly for key components such as circulators and isolators. These elements are critical for signal routing between qubits and isolation from noise, however, their current implementation relies on commercial ferrite devices with large sizes and large magnetic fields. As a result, a large research area has developed with numerous approaches to achieving the nonreciprocity required for these components [276–290]. In Chapter 4 of this

dissertation, we consider a JJA-based circulator model, inspired by Refs. [276, 284], which operates via the quantum tunneling of persistent-current vortices created in the presence of a small external magnetic field.

Beyond quantum computing and sensing, applications for superconducting circuits have been far-reaching. In recent years, superconducting qubits have been utilized to study chaos [291–293], quantum thermodynamics [294–297], and quantum error correction [298–302]. Uniquely designed superconducting circuits have been used to realize systems such as superconducting diodes [303–305] and Weyl semi-metals [306], while JJAs and arrays of superconducting qubits have been used as quantum simulators, representing spin and lattice systems [307–315] from condensed matter physics. Due to their rich and varied capability to explore quantum phenomena, superconducting platforms will likely continue to find vast applicability in scientific and technological developments in the foreseeable future.

Chapter 2: Utilizing Discrete Variable Representations for Decoherence-Accurate Numerical Simulation of Superconducting Circuits[1]

2.1 Introduction

Quantum superconducting circuits have emerged as one of the most promising platforms for building quantum computers, thanks to their scalability, tunability, and compatibility with existing fabrication technologies. A key aspect of developing this technology is the development of computational tools to aid in the design, modeling, and fabrication of various components, akin to the software tool-chains utilized for semiconductor circuits. With this in mind, there have been various efforts [220–233] to develop accessible software tools and refine modeling methods to achieve efficient and accurate numerical simulation of these systems.

Of particular relevance is what we colloquially refer to as 'decoherence-accurate simulation,' i.e., simulation that surpasses a given level of accuracy achievable in experiment, below which resolution is limited by errors such as systemic parameter

[1] This chapter is a reproduction of Ref. [316], a pre-print currently on arXiv.

variability, decay, decoherence, and dephasing. This is conceptually analogous to the principle of 'chemical accuracy' [317, 318] from chemical physics, which defines the target accuracy for numerical models based on the anticipated experimental accuracy. In our case of interest — superconducting qubits — we generally assume some degree of decay, decoherence, and dephasing of the superconducting levels. If we characterize this rate as that associated with the decoherence time T_2 [319, 320] of the system, we can estimate that energetic effects relevant for high fidelity operations may no longer matter for energy scales much less than $1/T_2$. This provides a definition of 'decoherence-accurate simulation' — the accuracy required from our numerical simulations to be on par with experimental accuracy, determined by the decoherence in a system. In what follows, we consider a decoherence accuracy of 10^{-6} GHz ($T_2 \approx 1$ ms), consistent with the best superconducting qubits in use today [321–324].

With this definition in hand, we have a quantifiable threshold to assess not only when a numerical simulation is sufficiently accurate, but also at what point an analysis has become less efficient for computational purposes. Any simulation that achieves accuracy beyond this threshold is necessarily expending more computational resources for an accuracy level not verifiable in experiment. However, as sources of error are managed, minimized, or eliminated, we are motivated to continue to improve the numerical accuracy of simulations.

This accuracy level hinges on the basis that we choose to represent the Hamiltonian, as well as the truncation associated with this (usually infinite) basis set. Most

numerical tools [227, 229, 232, 233] utilize some combination of the harmonic oscillator basis and the charge basis [325, 326] with a sufficiently large enough truncation to ensure proper convergence of energy levels. Here, we consider the use of discrete variable representations (DVRs) [327–329], specifically various 'sinc DVRs' [327, 330–332], which generalize and expand upon the charge basis to offer a variety of choices in basis and truncation. DVRs are basis sets that discretize one of a system's degrees of freedom according to a particular grid, where the individual basis states are localized about the grid points on which they are defined. They employ the diagonal approximation to represent the potential and any other operator which is a function of the discretized variable, resulting in trivial diagonal forms for these Hamiltonian contributions.

As a consequence of the errors introduced by the diagonal approximation, DVRs are inherently non-variational in nature, sometimes resulting in level convergence below the reference or true energy. This property and its associated pitfalls are well-documented [327, 333–336], as DVRs in various forms have long been used in chemical and nuclear physics [330, 331, 337–343]. Additionally, Hamiltonian contributions from operators that are *not* functions of the discretized variable, while capable of being analytically evaluated, often result in nontrivial, full matrices. In spite of this, we show that we can achieve and surpass decoherence accuracy in three prototypical superconducting circuits: the LC oscillator, the fluxonium, and the transmon. We demonstrate in these examples that the DVRs we consider outperform the typical

sparse method, the finite difference method, and in many cases match or outperform traditional numerical approaches.

This chapter is organized as follows. Section 2.2 provides an overview of the DVRs employed in our numerical analysis, including specific functional forms, variable definitions, and operator representations. Numerical results are presented in Section 2.3, highlighting the features of these DVRs in the LC oscillator, the fluxonium, and the transmon, where we compare their performance to standard approaches. We conclude and discuss the implications of our results in Section 2.4. In the appendices that follow, we provide an overview and derivation of DVRs as well as additional numerical details for our analysis.

2.2 Overview of Sinc DVRs

Here we provide an overview of the various DVRs we consider in Section 2.3, including the explicit forms of the basis states and relevant operator representations for numerical analysis. In general, DVRs are formed by projecting a discrete grid of points onto some orthonormal and complete basis set, and demanding that the resulting states themselves be orthonormal and complete. Relevant details and derivations for the generic construction of a DVR can be found in Appendix 2.A. In particular, we focus on sinc DVRs, which are created using the Fourier basis.

Sinc DVRs leverage both the orthonormality and completeness of the Fourier basis on various intervals as well as the Fourier transform, which connects the conjugate

variables of a given system. With our focus being superconducting circuits, we follow the usual circuit quantization procedures [325], taking the Cooper pair number N and superconducting phase of a node θ as our conjugate variables. These dimensionless variables are related to the usual node charge Q and node flux Φ of a circuit via $N = Q/(-2e)$ and $\theta = 2\pi\Phi/\Phi_0$, where e is the elementary electron charge and Φ_0 is the magnetic flux quantum. As a consequence, the basis states for each of the following DVRs are all expressed in terms of N and θ.

2.2.1 The Traditional Sinc DVR

The traditional sinc DVR is constructed by projecting a set of discretized points onto the continuous Fourier basis, taking advantage of the Fourier series expansion to enable the creation of a DVR. This permits a discretization of either N or θ, while its respective conjugate variable, θ or N, is continuous and bounded. See Appendix 2.A.2 for the details of its construction.

Discretizing θ yields a phase DVR with the basis states

$$\left|\psi^A_{\alpha,\theta}\right\rangle = \frac{1}{\sqrt{2N_{\max}}} \int_{-N_{\max}}^{N_{\max}} dN \; e^{iN\theta_\alpha} \left|f_N\right\rangle \quad , \tag{2.1}$$

which in functional form are sinc functions,

$$\psi^A_{\alpha,\theta}(\theta) = \sqrt{\frac{N_{\max}}{\pi}} \frac{\sin\left[N_{\max}(\theta - \theta_\alpha)\right]}{N_{\max}(\theta - \theta_\alpha)} \quad , \tag{2.2}$$

hence the naming of this DVR as a 'sinc DVR.' We index the states with an integer α corresponding to their grid point, the discretized variable (here θ), as well as an additional superscript A to distinguish this DVR from the truncated sinc DVR discussed in the following subsection. This DVR is valid for an infinite, uniform grid of points $\theta_\alpha = \alpha\Delta\theta$, spaced according to $\Delta\theta = \pi/N_{\max}$, where $\pm N_{\max}$ bounds the continuous variable N. The states $|f_N\rangle$ represent the θ-space functions used in the projector to construct the DVR, i.e., the continuous Fourier basis, where $\langle\theta|f_N\rangle = f(\theta, N) = e^{-iN\theta}/\sqrt{2\pi}$ [analogous to Eq. (2.A18)]. Note that in this case, the DVR's basis functions are non-periodic with infinite extent in θ-space (as shown in Fig. 2.1a), but periodic in conjugate space (charge number) on the interval $[-N_{\max}, N_{\max}]$, since the Fourier transform of $\psi^A_{\alpha,\theta}(\theta)$ is simply the band-limited complex exponential $e^{-iN\theta_\alpha}/\sqrt{2N_{\max}}$.

Similarly, discretization of N yields a charge number DVR with the basis states

$$\left|\psi^A_{\alpha,N}\right\rangle = \frac{1}{\sqrt{2\theta_{\max}}} \int_{-\theta_{\max}}^{\theta_{\max}} d\theta \; e^{-iN_\alpha\theta} \left|f_\theta\right\rangle \quad , \tag{2.3}$$

which in functional form are again sinc functions, but now in N-space:

$$\psi^A_{\alpha,N}(N) = \sqrt{\frac{\theta_{\max}}{\pi}} \frac{\sin\left[\theta_{\max}(N - N_\alpha)\right]}{\theta_{\max}(N - N_\alpha)} \quad . \tag{2.4}$$

In this case, we require an infinite, uniform grid $N_\alpha = \alpha\Delta N$, spaced according to $\Delta N = \pi/\theta_{\max}$, where $\pm\theta_{\max}$ bounds the continuous variable θ. The states $|f_\theta\rangle$ rep-

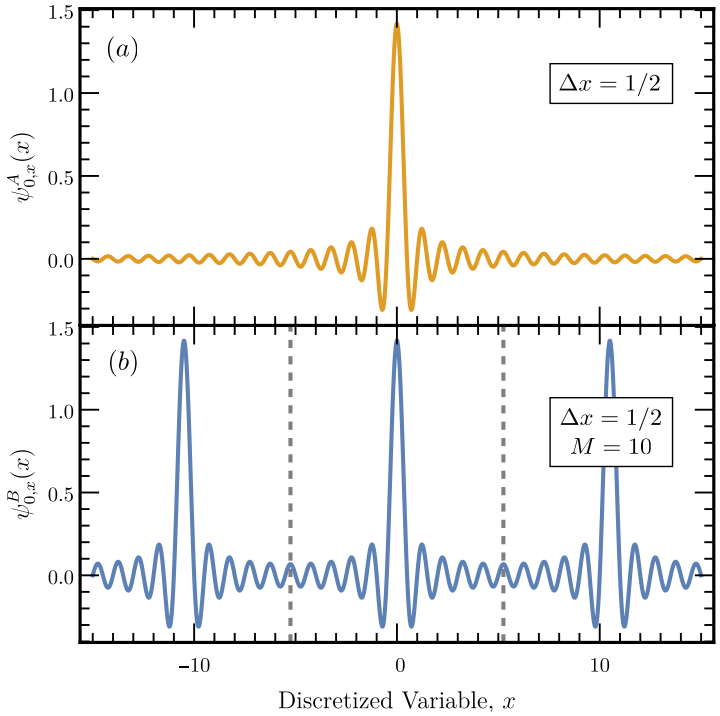


Figure 2.1: Functional forms of the DVR basis states for the (a) traditional sinc DVR and (b) truncated sinc DVR, both for an indexed $\alpha = 0$ state. Remaining basis states are generated by translating these functions in the positive and negative directions. The functional width of these basis functions is increased or decreased by increasing or decreasing the grid size. In (b), we have included dashed grey vertical lines to indicate the bounded region on which the DVR is valid, representing the interval on which its basis functions are periodic. Variations in both the number of states M and the grid size Δx affect this interval.

resent the N-space functions used in the projector to construct the DVR, $\langle N|f_\theta\rangle = f(\theta, N)^* = e^{iN\theta}/\sqrt{2\pi}$ [analogous to Eq. (2.A18)]. Here, we find that this DVR's basis functions are instead non-periodic with infinite extent in N-space, but periodic in phase space on the interval $[-\theta_{\max}, \theta_{\max}]$.

While these DVRs are quite general, with a variety of available discretization choices, we note that one of the standard basis sets used in superconducting circuit analysis, the charge basis [325, 326], is in fact a specific instance of the charge number

DVR in Eq. (2.3). The charge basis is typically represented with the charge number and phase states,

$$|N\rangle = \frac{1}{\sqrt{2\pi}} \int_{-\pi}^{\pi} e^{-i\theta N} |\theta\rangle \, d\theta \tag{2.5}$$

and

$$|\theta\rangle = \frac{1}{\sqrt{2\pi}} \sum_{N=-\infty}^{\infty} e^{i\theta N} |N\rangle \quad , \tag{2.6}$$

respectively, where charge number is integer-valued and phase is 2π-periodic and continuous. This is exactly the charge number DVR in Eq. (2.3), with the specific choice of $\theta_{\max} = \pi$ and $\Delta N = 1$. The widespread implementation of this discretization choice, i.e., the charge basis, originates from the simplest superconducting circuit, a Josephson junction connecting two islands of superconducting material. This system is described by the Hamiltonian

$$\hat{H} = 4E_C \hat{N}^2 - E_J \cos\hat{\theta} \quad , \tag{2.7}$$

with $E_C = e^2/2C_J$ the junction's charging energy, E_J its Josephson energy, and C_J the junction capacitance. Critically, this Hamiltonian's potential is 2π-periodic, thus demanding that charge be quantized and integer-valued. However, this periodicity is not ubiquitous, enabling the more general use of both charge number and phase DVRs, as we explore in Section 2.3.

2.2.2 The Truncated Sinc DVR

The traditional sinc DVR requires an infinite number of basis states, which must necessarily be truncated in any numerical representation. Numerical truncation introduces a source of error, particularly for state spaces not large enough to be considered 'approximately infinite.' However, we can similarly construct sinc DVRs that are instead finite-sized by definition using the partially discrete Fourier basis. As in the traditional case, we can discretize either the charge number or phase variable, yielding DVRs we interpret as truncations of the traditional sinc DVRs already discussed. This truncated DVR instead exploits the discrete Fourier transform for its creation — details of the construction of this DVR can be found in Appendix 2.A.3. We now highlight their form and relevant features, along with their connection to the DVRs already presented.

A truncated sinc DVR that discretizes phase is given by the basis states

$$\left|\psi^{B}_{\alpha,\theta}\right\rangle = \frac{1}{\sqrt{2M+1}} \sum_{n=-M}^{M} e^{iN_n\theta_\alpha} \left|f_n\right\rangle \quad , \tag{2.8}$$

and a finite-sized grid $\theta_\alpha = \alpha\Delta\theta$, with α an integer such that $\alpha = -M, ..., M$, and $\Delta\theta\Delta N = 2\pi/(2M+1)$. As before, we index the states according to their grid point α, the discretized variable (here θ), as well as an additional index B to distinguish this DVR from the traditional sinc DVR discussed in the previous subsection. The basis used to construct this DVR is the partially discrete Fourier basis in θ-space,

$\langle\theta|f_n\rangle = f_n(\theta) = e^{-iN_n\theta}/\sqrt{2\theta_{\max}}$ [analogous to Eq. (2.A22)], where charge number is already discretized according to $N_n = n\Delta N$ and phase is continuous and bounded by $\theta_{\max} = \pi/\Delta N$. These states are represented in θ-space with the functional form,

$$\begin{aligned}\psi^B_{\alpha,\theta}(\theta) &= \frac{1}{(2M+1)\sqrt{\Delta\theta}} \sum_{n=-M}^{M} e^{-iN_n(\theta-\theta_\alpha)} \\ &= \frac{1}{(2M+1)\sqrt{\Delta\theta}} \frac{\sin\left[\frac{\pi}{\Delta\theta}(\theta-\theta_\alpha)\right]}{\sin\left[\frac{\pi}{\Delta\theta}(\theta-\theta_\alpha)/(2M+1)\right]}\end{aligned} \quad , \tag{2.9}$$

where we see that now, not only is the basis for this DVR finite-sized, its states are periodic in the discretized variable on the interval $[-\theta_{\max}, \theta_{\max}]$, as shown in Fig. 2.1b.

Analogously, a truncated sinc DVR that discretizes charge number takes the form

$$\left|\psi^B_{\alpha,N}\right\rangle = \frac{1}{\sqrt{2M+1}} \sum_{n=-M}^{M} e^{-iN_\alpha\theta_n} \left|g_n\right\rangle \quad , \tag{2.10}$$

utilizing a finite-sized grid of points $N_\alpha = \alpha\Delta N$ with $\alpha = -M, ..., M$, which are again spaced according to $\Delta\theta\Delta N = 2\pi/(2M+1)$. In this case, the basis used to construct the DVR is the partially discrete Fourier basis in N-space, $\langle N|g_n\rangle = g_n(N) = e^{iN\theta_n}/\sqrt{2N_{\max}}$ [analogous to Eq. (2.A23)], where phase is already discretized, $\theta_n = n\Delta\theta$, and charge number is continuous and bounded by $N_{\max} = \pi/\Delta\theta$. These states are represented in N-space with the functional form,

$$\begin{aligned}\psi^B_{\alpha,N}(N) &= \frac{1}{(2M+1)\sqrt{\Delta N}} \sum_{n=-M}^{M} e^{i(N-N_\alpha)\theta_n} \\ &= \frac{1}{(2M+1)\sqrt{\Delta N}} \frac{\sin\left[\frac{\pi}{\Delta N}(N-N_\alpha)\right]}{\sin\left[\frac{\pi}{\Delta N}(N-N_\alpha)/(2M+1)\right]}\end{aligned} \quad . \tag{2.11}$$

Once again, this DVR's basis is finite-sized and periodic in the discretized variable (now charge number), on the interval $[-N_{\max}, N_{\max}]$.

These two DVRs can be interpreted as truncations of the traditional sinc DVRs in Section 2.2.1 upon comparing their respective basis states. Examining the DVRs which discretize phase [Eqs. (2.1) and (2.8)], we find that the traditional sinc DVR [Eq. (2.1)] is a continuum limit of the truncated sinc DVR [Eq. (2.8)], where we take $M \to \infty$ and keep $\Delta\theta$ fixed, resulting in a continuous and bounded conjugate variable N. It is then clear that the truncation of the traditional DVR's state space (and thus the discretized variable θ) leads to a discretization of the continuous variable N, resulting in the truncated DVR states in Eq. (2.8). This description connecting the traditional and truncated DVRs applies analogously to the DVRs which discretize charge number [Eqs. (2.3) and (2.10)]. We note that this is consistent with the connection between the discrete, rotor, and continuous phase spaces described in Ref. [344], as one might expect, with the only distinction being that we have generalized to consider arbitrarily-sized grid spacings.

2.2.3 Representing Operators

Having established in Sections 2.2.1 and 2.2.2 the various DVRs of interest, we now consider the implementation of these DVRs in numerics, specifically via the matrix representation of operators relevant for superconducting circuit analysis. Importantly, representing these operators using each DVR's basis states allows us to exploit a

characteristic feature of all DVRs, namely, the 'diagonal approximation.'

As outlined in Appendix 2.A, this approximation assumes a diagonal matrix representation for operators that are functions of the discretized variable of a DVR, essentially approximating a DVR's basis states as eigenstates of the 'discretized' operator. Thus, for operators that are a function of θ, a matrix representation using the traditional or traditional phase DVRs yields a diagonal form. For operators such as $\hat{\theta}$, $\hat{\theta}^2$, or $\cos\Big(\hat{\theta} \pm 2\pi\mathcal{A}\Big)$, found often in the Hamiltonians of superconducting circuits with Josephson junctions, we have,

$$\begin{aligned}
\left\langle \psi_{\alpha,\theta}^{(A,B)} \right| \hat{\theta} \left| \psi_{\beta,\theta}^{(A,B)} \right\rangle &= \theta_\alpha \delta_{\alpha\beta} \ , \\
\left\langle \psi_{\alpha,\theta}^{(A,B)} \right| \hat{\theta}^2 \left| \psi_{\beta,\theta}^{(A,B)} \right\rangle &= \theta_\alpha^2 \delta_{\alpha\beta} \ , \\
\left\langle \psi_{\alpha,\theta}^{(A,B)} \right| \cos\Big(\hat{\theta} \pm 2\pi\mathcal{A}\Big) \left| \psi_{\beta,\theta}^{(A,B)} \right\rangle &= \cos(\theta_\alpha \pm 2\pi\mathcal{A}) \delta_{\alpha\beta} \ ,
\end{aligned} \tag{2.12}$$

where $\left|\psi_{\alpha,\theta}^{(A,B)}\right\rangle$ represents the traditional or truncated sinc DVRs in Eqs. (2.1) or (2.8), respectively. Here we have included an often-present term, $\pm 2\pi\mathcal{A}$, which characterizes a system's external flux frustration via the ratio $\mathcal{A} = \Phi^{\text{ext}}/\Phi_0$. Analogously, the traditional and truncated charge DVRs yield diagonal matrix representations for operators that are a function of N, such as $\hat{N}$ or $\hat{N}^2$. Their matrix elements are simply

$$\begin{aligned}
\left\langle \psi_{\alpha,N}^{(A,B)} \right| \hat{N} \left| \psi_{\beta,N}^{(A,B)} \right\rangle &= N_\alpha \delta_{\alpha\beta} \ , \\
\left\langle \psi_{\alpha,N}^{(A,B)} \right| \hat{N}^2 \left| \psi_{\beta,N}^{(A,B)} \right\rangle &= N_\alpha^2 \delta_{\alpha\beta} \ ,
\end{aligned} \tag{2.13}$$

where $\left|\psi^{(A,B)}_{\alpha,N}\right\rangle$ represents the charge number DVRs in Eqs. (2.3) or (2.10). While this assumption greatly simplifies the numerical representation of the associated Hamiltonian terms of these operators, notably, the diagonal approximation introduces a quadrature error that is not guaranteed to be positive. Thus, DVRs are inherently non-variational basis representations, and care must be taken when examining their convergence properties.

The diagonal approximation assumes a DVR's basis states are eigenstates of the discretized variable, however, the basis set utilized in the construction of each sinc DVR we consider (the Fourier basis) holds particular relevance as well, namely, as eigenstates of the conjugate variable. For each of the phase DVRs in Eqs. (2.1) and (2.8), the basis states $|f_N\rangle$ and $|f_n\rangle$ are eigenstates of $\hat{N} = i\partial/\partial\theta$, while for each of the charge number DVRs in Eqs. (2.3) and (2.10), the basis states $|f_\theta\rangle$ and $|g_n\rangle$ are eigenstates of $\hat{\theta} = -i\partial/\partial N$. As a consequence, matrix elements of operators which are functions of the variable conjugate to the discretized variable can be evaluated analytically using the basis states of each DVR.

Considering first the traditional sinc DVRs in Section 2.2.1, the charge number operators $\hat{N}$ and $\hat{N}^2$ are represented in the discrete phase basis [Eq.(2.1)] with the matrix elements,

$$\left\langle \psi^A_{\alpha,\theta}\right| \hat{N} \left|\psi^A_{\beta,\theta}\right\rangle = \frac{1}{2N_{\max}} \int_{-N_{\max}}^{N_{\max}} dN N e^{-iN(\theta_\alpha - \theta_\beta)} = \begin{cases} 0 & \text{if } \alpha = \beta \\ \frac{i(-1)^{\alpha+\beta}}{\Delta\theta(\alpha-\beta)} & \text{if } \alpha \neq \beta \end{cases}, \quad (2.14)$$

and

$$\left\langle \psi^A_{\alpha,\theta} \right| \hat{N}^2 \left| \psi^A_{\beta,\theta} \right\rangle = \frac{1}{2N_{\max}} \int_{-N_{\max}}^{N_{\max}} dN N^2 e^{-iN(\theta_\alpha - \theta_\beta)} = \begin{cases} \frac{N_{\max}^2}{3} & \text{if } \alpha = \beta \\ \frac{2(-1)^{\alpha+\beta}}{\Delta\theta^2(\alpha-\beta)^2} & \text{if } \alpha \neq \beta \end{cases} . \tag{2.15}$$

Analogously, the phase operators $\hat{\theta}$ and $\hat{\theta}^2$ are represented in the discrete charge number basis [Eq.(2.3)] with the matrix elements,

$$\left\langle \psi^A_{\alpha,N} \right| \hat{\theta} \left| \psi^A_{\beta,N} \right\rangle = \frac{1}{2\theta_{\max}} \int_{-\theta_{\max}}^{\theta_{\max}} d\theta \ \theta e^{i(N_\alpha - N_\beta)\theta} = \begin{cases} 0 & \text{if } \alpha = \beta \\ \frac{-i(-1)^{\alpha+\beta}}{\Delta N(\alpha-\beta)} & \text{if } \alpha \neq \beta \end{cases} , \tag{2.16}$$

and

$$\left\langle \psi^A_{\alpha,N} \right| \hat{\theta}^2 \left| \psi^A_{\beta,N} \right\rangle = \frac{1}{2\theta_{\max}} \int_{-\theta_{\max}}^{\theta_{\max}} d\theta \ \theta^2 e^{i(N_\alpha - N_\beta)\theta} = \begin{cases} \frac{\theta_{\max}^2}{3} & \text{if } \alpha = \beta \\ \frac{2(-1)^{\alpha+\beta}}{\Delta N^2(\alpha-\beta)^2} & \text{if } \alpha \neq \beta \end{cases} . \tag{2.17}$$

To find the matrix elements analogous to Eqs. (2.14)-(2.17) assembled from the truncated sinc DVRs in Eqs. (2.8) and (2.10), we must evaluate finite sums rather than definite integrals, e.g.,

$$\left\langle \psi^B_{\alpha,\theta} \right| \hat{N} \left| \psi^B_{\beta,\theta} \right\rangle = \frac{\Delta N}{2M+1} \sum_{n=-M}^{M} n \ e^{-i2\pi n(\alpha-\beta)/(2M+1)} . \tag{2.18}$$

While this sum and those for the other relevant operators in Eqs. (2.15)-(2.17) can

be evaluated analytically to yield closed-form expressions distinct from those already presented, these expressions are non-trivial in nature and do not provide any additional insight. Hence, we omit their specific forms here. We note that all of these matrices, while evaluated analytically, are full, a feature that is certainly not ideal for numerical analysis. Thus, we are motivated to compare the performance of these DVRs to a standard sparse method, the finite difference (FD) method. This comparison is discussed and included in our results in Section 2.3.1.

Yet to be discussed is an operator of particular relevance to superconducting systems — the cosine operator represented in a discrete charge number basis. For simplicity, we restrict ourselves to the instances where $1/\Delta N$ is integer-valued, yielding the expression

$$\left\langle \psi_{\alpha,N}^{(A,B)} \right| \cos\left(\hat{\theta} \pm 2\pi\mathcal{A}\right) \left| \psi_{\beta,N}^{(A,B)} \right\rangle = \frac{1}{2}\left(e^{\pm i2\pi\mathcal{A}}\delta_{\alpha,\gamma^-} + e^{\mp i2\pi\mathcal{A}}\delta_{\alpha,\gamma^+}\right) \quad , \tag{2.19}$$

where $\gamma^{\pm} = \beta \pm 1/\Delta N$. This specific choice yields a sparse matrix with trivial values along only two bands, which is identical for both the traditional and truncated charge number DVRs. In addition, the operator's physical interpretation becomes more apparent — as a tunneling operator between the basis states of the DVR, connecting a state at the grid point α to those indexed $\pm 1/\Delta N$ away. While this matrix element can be evaluated in either the traditional or truncated case for arbitrary, non-integer $1/\Delta N$, the resulting matrices are full with non-trivial elements. Therefore, when this operator is to be evaluated, specifically in the fluxonium example in Section 2.3.2, we

proceed with a consideration of integer-valued $1/\Delta N$ only.

Before moving to concrete examples and implementing these matrix representations in numerical analysis, there are two important points of note. Firstly, the matrix representations utilizing the traditional sinc DVRs are technically of infinite size and must be truncated in any numerical representation. Typically, we use the expressions which assume an infinite-sized basis [Eqs. (2.14)-(2.17)], only in a matrix of some finite size. This discrepancy introduces a truncation error that decreases with increasing matrix size. In contrast, the truncated sinc DVRs we consider provide matrix representations that are already finite-sized — their expressions are exact at any matrix size. Naturally, with large enough matrix sizes, the truncation error associated with the traditional sinc DVR is negligible, and the discrepancy between the traditional and truncated DVRs is nonexistent. As discussed in Section 2.2.2, as the matrix size increases, we reach a continuum limit where the truncated sinc DVR becomes the traditional one.

We also note that the finite-sized, fully discrete nature of the truncated sinc DVR necessitates that the truncated DVR's basis states [Eqs. (2.8) or (2.10)] and the functions used to construct them ($|f_n\rangle$ or $|g_n\rangle$) are related by a discrete Fourier transform. As previously noted, these states are eigenstates of the operator conjugate to the discretized variable. Thus, this relationship enables a diagonalization of the conjugate variable (represented in the truncated sinc DVR's basis) via a discrete Fourier transform. In other words, the matrix representation of the conjugate variable in the

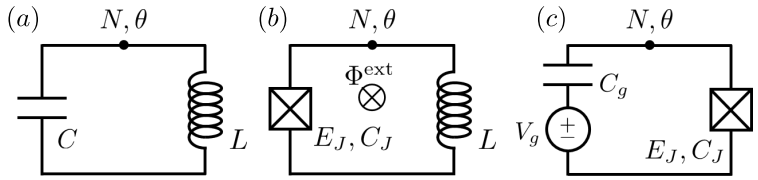


Figure 2.2: Circuit schematics of (a) the LC oscillator, (b) the fluxonium, and (c) the transmon, the three examples considered in the text, including relevant parameter and variable definitions.

truncated DVR's basis [e.g., Eq. (2.18)] can alternately be assembled via the discrete Fourier transform of the operator in its eigenbasis. This feature can enable more efficient construction and manipulation of these otherwise non-trivial and full matrices, as well as greatly simplify operations such as the trotterization of a Hamiltonian.

2.3 Numerical Features and Applications of Sinc DVRs

We now turn our attention to the focus of our investigation: the utilization of DVRs in the numerical analysis of superconducting circuits and the advantages they may provide. The DVRs outlined in Section 2.2 capture a variety of possibilities with regard to boundary conditions and discretization choice, allowing for broad application to a range of systems. Here, we consider straightforward, prototypical systems [shown in Fig. 2.2] to highlight each DVR's applicability, convenience, and in some cases, advantage over traditional numerical representations.

In what follows, we consider the use of these DVRs to examine three features of interest for numerical analysis: energy level convergence, basis state contributions, and phase shift implementations. We first leverage the LC oscillator and its analyt-

ical solutions as a proof-of-concept, examining the level convergence of each DVR, introducing the relevant metrics we consider to assess performance, and comparing performance to the FD method, which is known to be sparse. We then focus on the use of each DVR in the fluxonium as well as their more limited application in the transmon.

2.3.1 LC Oscillator

We now examine the use of DVRs for the evaluation of energy eigenvalues of the LC oscillator (Fig. 2.2a), to serve as a point of reference to assess and understand DVR performance. The LC oscillator has exact, well-known solutions to compare to, and given this system's bounded, non-periodic potential, we can consider all four of the DVRs presented in Section 2.2 for comparison. Expressed in terms of the dimensionless variables N and θ, the Hamiltonian is written as

$$\hat{H} = 4E_C\hat{N}^2 + \frac{E_L}{2}\hat{\theta}^2 \tag{2.20}$$

where the capacitive energy is given by $E_C = \frac{e^2}{2C}$ and the inductive energy is given by $E_L = \frac{1}{L}\left(\frac{\Phi_0}{2\pi}\right)^2$. Here the circuit's capacitance is defined as C, its inductance defined as L, with e the elementary electron charge and Φ_0 the magnetic flux quantum.

We assess the energy level convergence properties of each DVR by examining the absolute value of the energy difference Δ_n as a function of matrix size, i.e., the number

of a DVR's basis states included in a numerical representation. Here,

$$\Delta_n = E_n^{\mathrm{DVR}} - E_n^{\mathrm{ref}} \ , \tag{2.21}$$

where E_n^{DVR} is the energy of n^{th} level found using a DVR and E_n^{ref} is the reference energy of that same level. In the LC oscillator, we have exact solutions to serve as a reference point: $E_n^{\mathrm{ref}} = \sqrt{8E_C E_L}(n + 1/2)$. Naturally, as a DVR converges to the reference energy, here the exact energy of the system, $\Delta_n \to 0$.

In Fig. 2.3, we plot the LC oscillator's ground state level convergence as a function of matrix size for three different grid sizes in the traditional charge number DVR, corresponding to the three general categories of behavior we observe in such plots, across all DVRs and examples. For grid sizes that are too large, no amount of basis states yields an improvement in level convergence, which never approaches the reference energy or decoherence accuracy. This is indicated by the black, flat line in Fig. 2.3, where $\Delta N = 3/2$. We also find a manifestation of the non-variational nature of DVRs — this convergence is *below* the true energy, indicated by the open data points in Fig. 2.3.

For grid sizes that are too small, we observe very slow level convergence with increasing matrix sizes, which does not saturate within the working precision and/or largest matrix sizes considered, but does often reach decoherence accuracy at larger matrix sizes, indicated by the lightest descending curve in Fig. 2.3, where $\Delta N = 1/10$. The behavior of these two extremes can be understood as a consequence of the grid

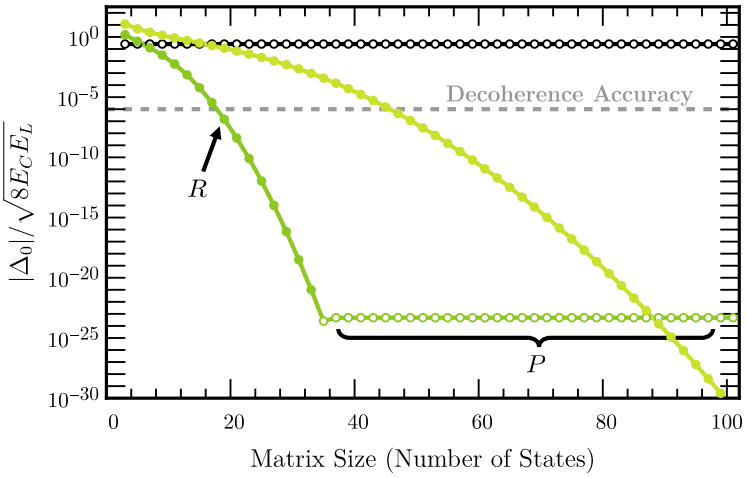


Figure 2.3: Example behavior of the absolute value of the energy difference $|\Delta_0|$ as function of matrix size in the ground state of the LC oscillator, using the traditional charge number DVR with grid sizes $\Delta N = 3/2$ (darkest green), $\Delta N = 1/4$ (green), and $\Delta N = 1/10$ (lightest green), all scaled according to the LC frequency. Decoherence accuracy (also scaled according to the LC frequency) is indicated with a horizontal gray dashed line. Additionally, the decoherence-accurate matrix size R and saturation precision P are identified. Open data points indicate where $\Delta_0 < 0$, in order to note and highlight the non-variational nature of DVRs.

size's effect on the basis functions of the DVRs introduced in Section 2.2, namely, that increasing the grid size increases the function's width while decreasing the size of the conjugate variable's subspace. Essentially, grid sizes that are too large yield basis functions that are too broad to be able to resolve the wavefunction of interest, and cut off relevant, contributing regions of its conjugate subspace. On the other hand, grid sizes that are too small capture all relevant regions of conjugate space, but result in basis functions that are so narrow as to require very large numbers of states to accurately represent the function of interest.

Finally, for intermediate grid sizes, we observe level convergence that improves with increases in matrix size, surpassing decoherence accuracy and saturating with

high precision to some level of accuracy relative to the reference energy, shown in Fig. 2.3 for the grid size $\Delta N = 1/4$. Once again, we observe non-variational behavior, where the asymptotic convergence of the DVR is in fact below the true energy. This curve is additionally labeled with the two metrics we use to assess and compare DVR performance across the various grid sizes, DVRs, and examples. The smallest matrix size that achieves decoherence accuracy, the decoherence-accurate matrix size, is labeled with R, while the asymptotic behavior, or saturation precision, is labeled with P. Together, these metrics capture the relevant behavior of a DVR, addressing whether or not decoherence accuracy is reached, and how quickly, as well as what degree of accuracy a given DVR can achieve for a function of interest. While the curves and grid sizes shown in Fig. 2.3 are specific to the LC oscillator ground state with the traditional charge number DVR, the general behavior described above extends to the other DVRs and examples we consider.

To utilize these metrics to assess each DVR's performance in the LC oscillator, we expand upon Fig. 2.3 to consider a range of grid sizes in all four DVRs. A sampling of curves akin to those in Fig. 2.3 for each DVR is shown in Appendix 2.B, along with additional numerical details. This analysis enables an examination of both the decoherence-accurate matrix size R and saturation precision P as a function of the grid size, shown in Figs. 2.4a and 2.4b, respectively.

With regard to decoherence accuracy, Fig. 2.4a demonstrates an overall increase in the decoherence-accurate matrix size R as the grid size decreases, for all four DVRs.

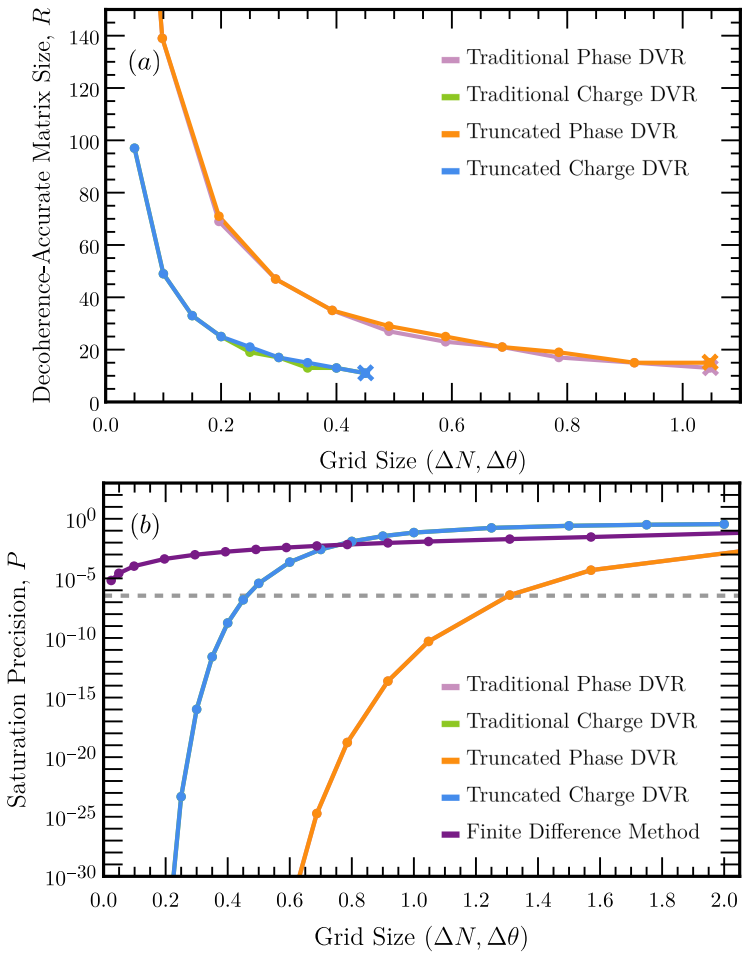


Figure 2.4: (a) The decoherence-accurate matrix size R as a function of grid size in the LC oscillator's ground state, for all four of the DVRs considered and colored according to the included legend. The grid size cutoff for R, i.e., the largest grid size that surpasses decoherence accuracy, is indicated with an 'X' data point. (b) The saturation precision P as a function of grid size in the LC oscillator's ground state, for all four of the DVRs considered as well as the lowest-order FD method, as indicated in the legend. Decoherence accuracy (scaled according to the LC frequency) is indicated with a horizontal gray dashed line.

As the grid size increases, R decreases, but ultimately reaches a cutoff (indicated by the final 'X' data point) beyond which decoherence accuracy is never achieved. This behavior is consistent with the general understanding of the impact of grid size on a DVR's basis functions described previously. This cutoff in R indicates where the grid

size of a particular DVR has become too large to approximate a function of interest — in the phase DVRs, this corresponds to grid sizes larger than $\Delta\theta = \pi/3$, while in the charge DVRs, this cutoff occurs at the grid size $\Delta N = 0.45$. As grid size decreases, we find a rapid increase in R, indicative of a worse performance, where the grid size is small enough to enable good approximation of the function, but requiring numerous states to do so. We also note minor variations in R between the traditional and truncated DVRs of each type, particularly at smaller matrix sizes. We understand these discrepancies to be a consequence of the relationship between the truncated and traditional sinc DVRs — as the matrix size increases, the required numerical truncation in the traditional case has less impact, and we approach the continuum limit in the truncated case. However, these variations are quite small, almost negligible. Clearly, this truncation does not introduce very large error in the traditional sinc DVR and the truncated sinc DVR performs similarly well, ultimately demonstrating the effectiveness of all four DVRs to represent the system.

In Fig. 2.4b, we plot the saturation precision P as a function of the grid size for all four DVRs. Most notably, the traditional and truncated sinc DVRs of both types are nearly identical. As this metric corresponds to the asymptotic behavior observed at large matrix sizes, this is exactly as expected given the relationship between these DVRs — the continuum limit is being reached. Larger grid sizes tend towards saturation at worse accuracy, while smaller grid sizes lead to rapid improvements, saturating below decoherence accuracy in numerous cases. We note that the strict condition to

identify the smallest matrix size *below* decoherence accuracy does not capture grid sizes such as $\Delta\theta = 5\pi/12$, which saturate barely above decoherence accuracy.

Also visible in Fig. 2.4b is an additional curve representing the performance of the FD method. As detailed in Appendix 2.D, this approach discretizes the continuous phase representation of the Hamiltonian in Eq. (2.20) over some finite region of phase space, which is determined by the chosen grid size and the number of grid points included. We consider here the usual lowest-order approximation, a three-point approximation that yields a sparse, tri-diagonal representation of the conjugate variable. Upon varying the matrix size (determined by the number of grid points) for various grid sizes, analogously to the DVRs, we examine R and P as a function of $\Delta\theta$. As we show in Appendix 2.D, only a single point surpasses decoherence accuracy, with a matrix of dimension 499×499, far beyond the range of Fig. 2.4a. In Fig. 2.4b, we see that even the smallest grid sizes do not reach decoherence accuracy, and saturate at accuracy levels far larger than any of the DVRs. As we highlight in Appendix 2.D, this saturation also occurs at far larger matrix sizes, and while some improvement in P can be found by utilizing higher-order approximations of the FD method, this does not yield dramatic improvement in matrix size and reduces the most attractive quality of this approach — its sparseness. This behavior is common to all the examples we consider, hence, it is excluded in our results going forward.

2.3.2 Fluxonium

Of particular interest is the fluxonium [193, 319, 322, 345], shown in Fig. 2.2b, which has no exact analytical solution and whose standard numerical approach is known to be less than ideal [345]. We can model the fluxonium by replacing the capacitance in the LC oscillator with a superconducting tunneling element, the Josephson junction, which has an associated Josephson energy E_J and junction capacitance C_J, and demanding that the inductance be large, such that $E_J \gg E_L$. This results in the Hamiltonian

$$\hat{H} = 4E_C\hat{N}^2 + \frac{E_L}{2}\hat{\theta}^2 - E_J\cos\Big(\hat{\theta} + 2\pi\mathcal{A}\Big) \ , \tag{2.22}$$

where analogous to the LC oscillator, we have the charging energy $E_C = \frac{e^2}{2C_J}$ and the inductive energy $E_L = \frac{1}{L}\left(\frac{\Phi_0}{2\pi}\right)^2$. The fluxonium is also threaded by an external flux Φ^{ext}, captured by the parameter $\mathcal{A} = \frac{\Phi^{\text{ext}}}{\Phi_0}$, with e the elementary electron charge and Φ_0 the magnetic flux quantum.

The standard numerical approach [229, 345] consists of representing the fluxonium's Hamiltonian using a harmonic oscillator basis that diagonalizes Eq. (2.22)'s first two terms. This is described in more detail in Appendix 2.C. However, this method is known to require larger state spaces for convergence, as the harmonic oscillator basis is not a good approximation for the fluxonium's eigenstates. Thus, we are motivated to consider alternative approaches for a numerical representation

of this system. Like the LC oscillator, the fluxonium has a bounded, non-periodic potential, and as a result, there are no requirements on a variable's periodicity to restrict the usage of DVRs. Therefore, we consider all four of the DVRs presented in Section 2.2 for comparison with each other and to the standard numerical method, exploring their features and performance in the context of level convergence, basis state contributions, and phase shifts.

2.3.2.1 Level Convergence

We assess the energy level convergence properties of each DVR by examining the absolute value of the energy difference, Δ_n [Eq. (2.21)], as a function of matrix size, i.e., the number of DVR basis states included in a numerical representation. However, for the fluxonium, no exact solution exists to serve as the reference energy E_n^{ref} in Eq. (2.21). Instead, in this example, we take E_n^{ref} to be that provided by the standard numerical approach using a sizable number of basis states. Thus, we represent the fluxonium using the standard harmonic oscillator basis [Eqs.(2.C1)-(2.C2)] with the length scale $\theta_0 = (8E_C/E_L)^{1/4}$ and 1001 basis states, assuring that the lowest levels of the system are well-converged to serve as a reference point for the DVRs as well as the harmonic oscillator basis with smaller matrix sizes and alternative length scales.

Analogously to the LC oscillator, we consider various grid sizes in all four DVRs, employing the use of the decoherence-accurate matrix size R and saturation precision P to assess each DVR's relative performance. A key distinction in this example is that

for the charge DVRs, we consider only those grid sizes for which $1/\Delta N$ is an integer, yielding a trivial form for the contribution from the cosine operator, as discussed in Section 2.2.3. Appendix 2.C includes visuals of $|\Delta_0|$ as a function of matrix size for a sampling of grid sizes, from which we extract R and P, as well as additional details of the numerical analysis. We note that while there exists some functional variation in $|\Delta_0|$ upon comparison with the LC oscillator case (which we attribute to the oscillatory contribution to the potential), the overall behavior of these curves with respect to grid size, as described in Section 2.3.1, is the same.

We plot the decoherence-accurate matrix size R and the saturation precision P as a function of a DVR's grid size in Figs. 2.5a and 2.5b, respectively, specifically for the ground state of the fluxonium. Overall, we find behavior that is analogous to that found in the LC oscillator. Fig. 2.5a demonstrates an overall increase in R as the grid size decreases, for all four DVRs. As the grid size increases, R decreases, ultimately reaching a cutoff beyond which decoherence accuracy is never reached. In Fig. 2.5b, we see again how larger grid sizes tend towards saturation at worse accuracy, while smaller grid sizes lead to rapid improvements, saturating below decoherence accuracy in numerous cases.

While P is nearly identical across the traditional and truncated DVRs, as anticipated, we see slightly more variation in R. We also find smaller grid size cutoffs for R in the fluxonium, where grid sizes larger than $\Delta N = 0.25$ and $\Delta\theta = \pi/4, 7\pi/32$ do not achieve decoherence accuracy. Notably, the phase DVRs have different grid size

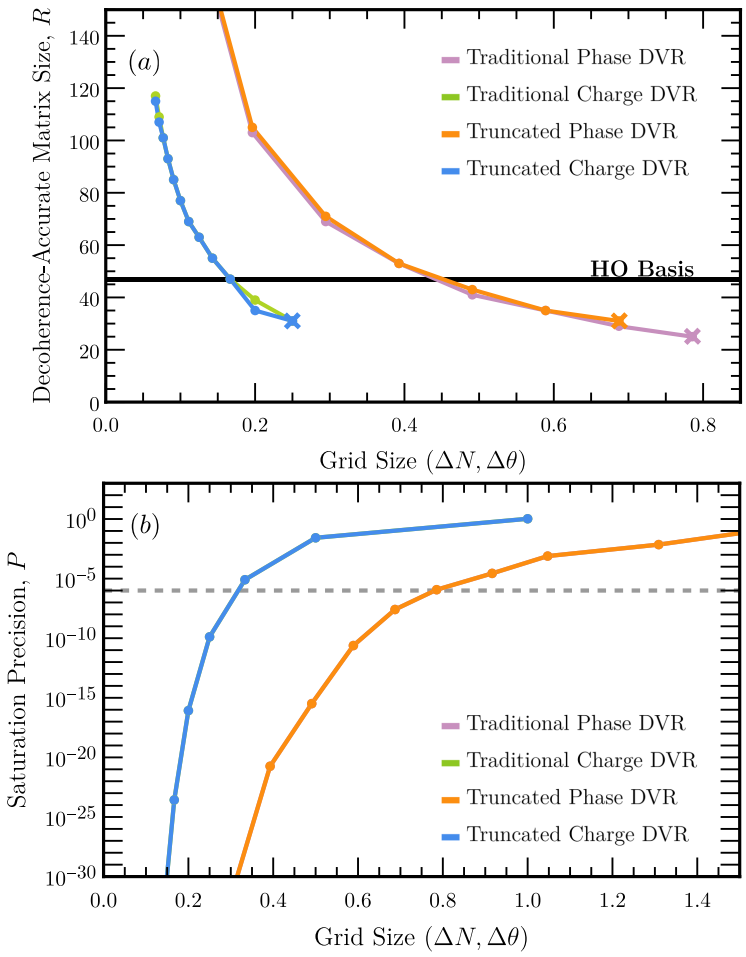


Figure 2.5: (a) The decoherence-accurate matrix size R as a function of grid size for the fluxonium ground state, for all four of the DVRs considered and colored according to the included legend. The matrix size at which the standard numerical approach, the harmonic oscillator basis, reaches decoherence accuracy is indicated by a horizontal solid black line. The grid size cutoff for R, i.e., the largest grid size that surpasses decoherence accuracy, is indicated with an 'X' data point. (b) The saturation precision P as a function of grid size for the fluxonium ground state, for all four of the DVRs considered. Decoherence accuracy is indicated with a horizontal gray dashed line. Parameters for these plots are $E_C/h = 2.5$ GHz, $E_L/h = 0.5$ GHz, $E_J/h = 10$ GHz, and $\mathcal{A} = 1/2$.

cutoffs in R. However, in the traditional phase DVR, the largest grid size to achieve decoherence accuracy is one that, according to Fig. 2.5b, saturates barely *above* decoherence accuracy. This discrepancy is a manifestation of the non-variational nature of DVRs, where in the process of converging below the reference energy, high ac-

curacy (below decoherence accuracy) is achieved before ultimately converging at a worse accuracy level, further from the reference energy. Thus, these differing cutoffs are a consequence of both the non-variational nature of DVRs in general as well as the close proximity of this particular grid size's saturation precision to decoherence accuracy. In total, these variations between the truncated and traditional DVRs are still quite small, indicating that the approximation made in the traditional case does not introduce very large error in this system.

Included in Fig. 2.5a is a horizontal black line indicating the matrix size at which the standard numerical approach, the harmonic oscillator basis, first surpasses decoherence accuracy. Importantly, there are numerous grid sizes, particularly in the phase DVRs, which achieve this level of accuracy at noticeably smaller matrix sizes. We also note that the harmonic oscillator basis does not saturate — hence no point of comparison in Fig. 2.5b — but continues to increase in accuracy with increased matrix size. As we highlight further in Appendix 2.C using Fig. 2.13, level convergence is achieved in all four DVRs, with various grid sizes, at consistently higher accuracy and smaller matrix sizes than the harmonic oscillator basis. This suggests that both the phase and charge number DVR's basis states are better approximations to the fluxonium's eigenstates than the harmonic oscillator basis, potentially providing an alternative numerical approach that is a more efficient and accurate representation for the fluxonium than current standard methods.

This improvement can be made more tangible by considering the impact of smaller

matrix sizes on the computational cost of matrix diagonalization and the maximum number of qubits capable of being simulated by a given machine. Consider a system with η degrees of freedom, i.e., qubits, where each qubit is described by a Hamiltonian matrix with dimension R, the smallest matrix size to achieve decoherence accuracy. The diagonalization of the entire system, neglecting sparseness from the tensor product structure, has a computational cost that scales as $\mathcal{O}(R^{3\eta})$, as matrix diagonalization is an operation that scales as $\mathcal{O}(\mathcal{N}^3)$ with $\mathcal{N} = R^\eta$, the matrix dimension of the entire system. With the decoherence-accurate matrix sizes indicated in Fig. 2.5a, $R_{\mathrm{HO}} = 47$ and $R_{\mathrm{DVR}} = 31$, we find the speed up provided by DVRs is given by the factor $(R_{\mathrm{DVR}}/R_{\mathrm{HO}})^{3\eta} \approx (2/3)^{3\eta}$, which only increases with more degrees of freedom. Alternatively, we can consider the largest number of qubits a given machine can represent in its memory, given by $\eta^{\max} = \log \mathcal{N}^{\max} / \log R$, where $\mathcal{N}^{\max}$ corresponds to the largest matrix dimension capable of being diagonalized. While the ratio $\eta^{\max}_{\mathrm{DVR}}/\eta^{\max}_{\mathrm{HO}}$ scales logarithmically and R_{HO} and R_{DVR} are of the same order, the improvements offered by DVRs in this instance still provide about 12% more qubits.

Thus far, we have only considered the ground state of the LC oscillator and the fluxonium in our assessment of a DVR's performance. However, in the fluxonium, energy levels beyond the ground state are particularly relevant. Thus, in Fig. 2.6, we examine the decoherence-accurate matrix size R and the saturation precision P for the first five energy eigenstates of the fluxonium. In Fig. 2.6a we compare R across the first five levels in the traditional phase and charge number DVRs as well as the

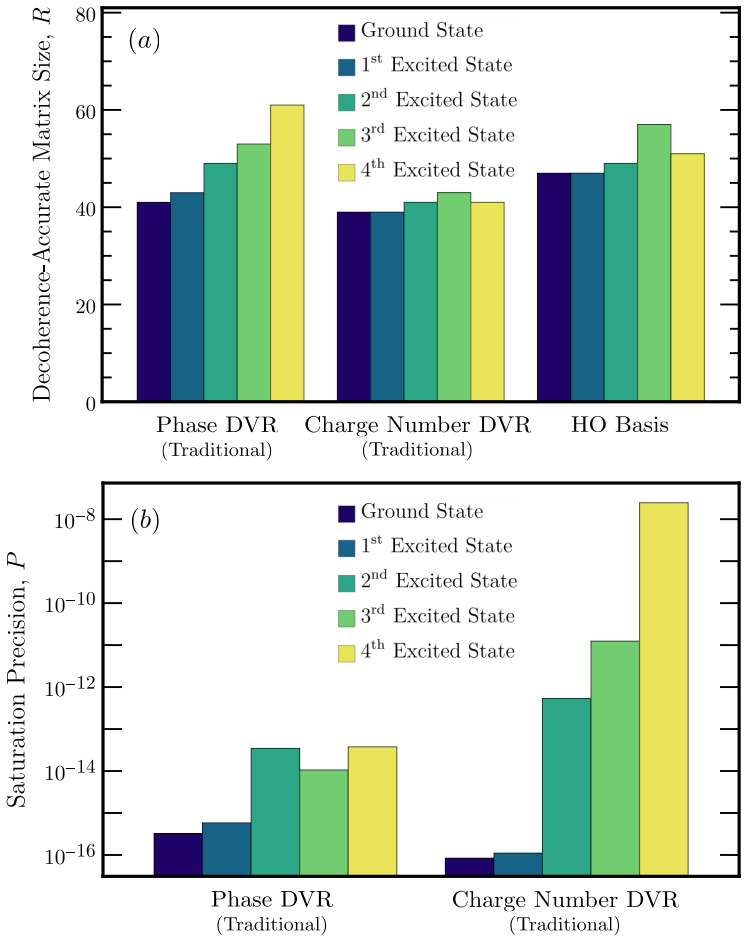


Figure 2.6: (a) The decoherence-accurate matrix size R for the first five energy eigenstates of the fluxonium in the traditional phase DVR ($\Delta\theta = 5\pi/32$), the traditional charge number DVR ($\Delta N = 1/5$), and the harmonic oscillator basis. (b) The saturation precision P for the first five energy eigenstates of the fluxonium in the traditional phase DVR ($\Delta\theta = 5\pi/32$) and the traditional charge number DVR ($\Delta N = 1/5$). Parameters for these plots are $E_C/h = 2.5$ GHz, $E_L/h = 0.5$ GHz, $E_J/h = 10$ GHz, and $\mathcal{A} = 1/2$.

harmonic oscillator basis. In particular, we choose the grid sizes $\Delta N = 1/5$ and $\Delta\theta = 5\pi/32$ for comparison, as they saturate to similar levels of accuracy, well below decoherence accuracy, and are the smallest grid sizes that outperform the harmonic oscillator basis in the ground state with regard to R. Given the similarity between the traditional and truncated DVRs of each type, we opt to show only the traditional

case in Fig. 2.6.

For both R and P, Fig. 2.6 indicates a degradation in performance whose severity varies depending on the basis used to represent the fluxonium. With respect to R, Fig. 2.6a shows that the phase DVR exhibits the largest drop in performance, while the charge number DVR is relatively stable with respect to increases in energy level. The harmonic oscillator basis similarly degrades in performance for higher energy levels, but not to the extent of the phase DVR. Notably, the charge number DVR outperforms the harmonic oscillator basis, with smaller values of R at all energy levels. Examining the saturation precision P in Fig. 2.6b, we instead find that while the phase DVR's saturation precision does worsen at higher energy levels, it is relatively stable when compared to the charge number DVR, which demonstrates a far more severe degradation in performance. Ultimately, if considering the use of either DVR to numerically represent the fluxonium, choices in grid size and matrix size must be made to mitigate the influence of this degradation in performance. However, even with this drop in performance at higher energy, the charge number and phase DVRs can outperform the harmonic oscillator basis.

2.3.2.2 Basis State Contributions

In addition to comparing the level convergence properties of each DVR against that of the harmonic oscillator basis, we also examine and compare the energy eigenstate decompositions associated with each approach, aiming to characterize the size

of each basis state's contribution to an energy eigenstate when represented in a given basis. We accomplish this by considering the magnitude of the overlap of the i^{th} energy eigenstate of the fluxonium $|\Psi_i\rangle$ and the α-indexed state of a particular basis $|\psi_\alpha\rangle$, i.e., $|\langle\Psi_i|\psi_\alpha\rangle|^2$. Here, we compare eigenstate decompositions in terms of the traditional phase and charge number DVRs, as well as the harmonic oscillator basis. Once again, given the similarity we have demonstrated between the traditional and truncated DVRs, we opt to focus on only the traditional case here.

To examine the eigenstate contributions from the traditional phase and charge number DVRs, we restrict ourselves to a single instance of each, i.e., one grid size and matrix size per DVR. For each grid size, we choose $\Delta\theta = 5\pi/32$ for the phase DVR and $\Delta N = 1/5$ for the charge number DVR. At these grid sizes, a state space of 81 basis states is sufficient for both DVRs to have converged to saturation precision in the ground state, which is of similar accuracy in both cases. This can be confirmed in Fig. 2.13 of Appendix 2.C. For appropriate comparison, we also consider the harmonic oscillator basis with a state space of equivalent size.

In Fig. 2.7, we show $|\langle\Psi_i|\psi_\alpha\rangle|^2$ for the first eight energy eigenstates of the fluxonium across a state space of 81 basis states of the traditional phase DVR, the traditional charge number DVR, and the harmonic oscillator basis. In all cases, these higher energy levels have reached decoherence accuracy and are considered sufficiently well-approximated. It is immediately clear from Fig. 2.7c that the contributions to an eigenstate represented in the harmonic oscillator basis are markedly different from

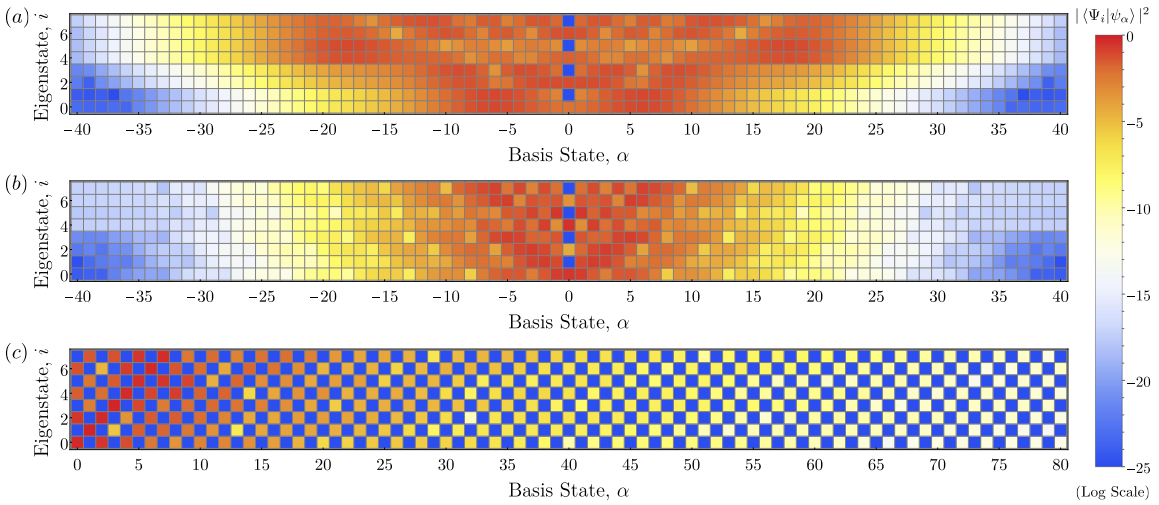


Figure 2.7: Eigenstate decompositions showing $|\langle\Psi_i|\psi_\alpha\rangle|^2$ for the first eight energy eigenstates of the fluxonium across a state space of 81 basis states for (a) the traditional phase DVR ($\Delta\theta = 5\pi/32$), (b) the traditional charge number DVR ($\Delta N = 1/5$), and (c) the harmonic oscillator basis. Values are shown on a log scale, colored according to their power, as indicated by the legend. We enforce a cutoff at 10^{-25}, hence grid spaces with values smaller than this cutoff are automatically colored blue. Parameters for these plots are $E_C/h = 2.5$ GHz, $E_L/h = 0.5$ GHz, $E_J/h = 10$ GHz, and $\mathcal{A} = 1/2$.

those represented with either the phase or charge number DVRs, shown in Fig. 2.7a or Fig. 2.7b, respectively. With the harmonic oscillator basis, only states of common parity contribute to a given eigenstate, permitting one to effectively neglect half of the defined state space. This is not present with either DVR, however, we do find an analogous effect specifically with regard to the contribution from the central basis state of each DVR — its contribution (or lack thereof) alternates with increasing energy.

Notably, Fig. 2.7b indicates that the traditional charge number DVR is a particularly compact representation. The main contributions to an eigenstate come from the central 10 to 20 states, which is consistently true even at higher energy. The

drop in magnitude beyond this range is dramatic, with minimal contributions coming from the edge states. The phase DVR exhibits a similar drop in magnitude away from the central contributing states, however, those states vary considerably more with increased energy. While low-lying levels are relatively compact, with comparable numbers of basis states contributing largely, as in the charge number DVR, higher energy levels demonstrate considerable broadening in this regard. The harmonic oscillator basis appears to fall somewhere in between — its main contributing states are certainly focused about the lowest harmonic oscillator states, which increase slightly with increased energy. However, the drop in magnitude away from these main contributing states is considerably slower than in either DVR. This may point to the harmonic oscillator's worse performance with regard to accuracy and matrix size, indicating far more states are required to reach equivalent levels of accuracy achieved with DVRs.

2.3.2.3 Phase Shifts

A specific application for which the traditional and truncated phase DVRs are particularly well suited is the implementation of phase shifts in a system's wavefunction. The construction of these DVRs results in the discretization of the phase variable, enabling a convenient mathematical definition for such a phase-shift operation. As we now show, with a straightforward choice for the size of the phase shift, we need only shift a state's expansion coefficients relative to the DVR's basis states to generate the

phase shift.

Consider a system's eigenstate $|\Psi_n\rangle$ expanded in terms of either phase DVR,

$$|\Psi_n\rangle = \sum_\alpha c_{\alpha n} \left|\psi_{\alpha,\theta}^{(A,B)}\right\rangle \ , \tag{2.23}$$

where $c_{\alpha n}$ is the expansion coefficient corresponding to the overlap between the eigenstate and each basis state, $\left\langle \psi_{\alpha,\theta}^{(A,B)} \middle| \Psi_n \right\rangle$. In a continuous phase representation, where $f(\theta) = \langle \theta | f \rangle$, this expansion becomes

$$\Psi_n(\theta) = \sum_\alpha c_{\alpha n} \psi_{\alpha,\theta}^{(A,B)}(\theta) \ . \tag{2.24}$$

Implementing a phase shift $\pm\phi$, like with any other basis, is then accomplished by taking $\theta \to \theta \pm \phi$, yielding

$$\Psi_n^{\pm}(\theta) \equiv \Psi_n(\theta \pm \phi) = \sum_\alpha c_{\alpha n} \psi_{\alpha,\theta}^{(A,B)}(\theta \pm \phi) \ . \tag{2.25}$$

This procedure is greatly simplified, however, by noting that the α-indexed basis states of a phase DVR are only a phase shift of the grid size $\Delta\theta$ away from each other. Therefore, if the phase shift $\pm\phi$ can be written as an integer multiple of the DVR's grid size, i.e., $\pm\phi = \pm\beta\Delta\theta$ with β a positive integer, we can express the

phase-shifted basis state in Eq. (2.25) as just another indexed basis state,

$$\psi_{\alpha,\theta}^{(A,B)}(\theta \pm \phi) = \psi_{\kappa,\theta}^{(A,B)}(\theta) \ , \tag{2.26}$$

where $\kappa = \alpha \mp \beta$. The particular direction of the shift relative to α is readily confirmed by examining the forms of $\psi_{\alpha,\theta}^{(A,B)}(\theta \pm \phi)$ [Eqs. (2.2) and (2.9)], where we can re-write the quantity $\pm\phi - \theta_\alpha = -(\alpha \mp \beta)\Delta\theta = -\kappa\Delta\theta = -\theta_\kappa$.

The phase-shifted eigenstate $\Psi_n^{\pm}(\theta)$ can then be written conveniently in Dirac notation as

$$\left|\Psi_n^{\pm}\right\rangle = \sum_\alpha c_{\alpha n} \left|\psi_{\kappa,\theta}^{(A,B)}\right\rangle \ , \tag{2.27}$$

where we see that these two phase DVRs accomplish a phase shift $\pm\phi = \pm\beta\Delta\theta$ via a corresponding shift in the DVR's basis states relative to their expansion coefficients. Further, this straightforward implementation of a phase shift in the traditional and truncated phase DVRs enables the identification of a phase-shift operator $\hat{\mathcal{O}}_{\pm}^{(A,B)}$,

$$\left|\Psi_n^{\pm}\right\rangle = \sum_\alpha c_{\alpha n} \left|\psi_{\kappa,\theta}^{(A,B)}\right\rangle = \sum_\alpha \left|\psi_{\alpha\mp\beta,\theta}^{(A,B)}\right\rangle \left\langle\psi_{\alpha,\theta}^{(A,B)}\middle|\Psi_n\right\rangle = \hat{\mathcal{O}}_{\pm}^{(A,B)} \left|\Psi_n\right\rangle \ , \tag{2.28}$$

which we can re-express as iterations of a single matrix,

$$\hat{\mathcal{O}}_{\pm}^{(A,B)} = \sum_\alpha \left|\psi_{\alpha\mp\beta,\theta}^{(A,B)}\right\rangle \left\langle\psi_{\alpha,\theta}^{(A,B)}\right| = \left(\sum_\alpha \left|\psi_{\alpha\mp1,\theta}^{(A,B)}\right\rangle \left\langle\psi_{\alpha,\theta}^{(A,B)}\right|\right)^{\beta} \ . \tag{2.29}$$

The matrix inside the parenthesis represents a raising or lowering operator that con-

nects the basis states of a phase DVR — essentially carrying out the $\Delta\theta$ phase shift that separates them. By multiplying this matrix β times, we generate the desired phase shift $\pm\phi = \pm\beta\Delta\theta$, as expected. However, we must be mindful of the specific characteristics of each phase DVR that influence the form of this matrix.

Recall that the traditional sinc DVR is a basis of infinite size, where $\alpha = -\infty, ..., \infty$. Thus, for an eigenstate expansion written in terms of the traditional phase DVR, the phase-shift operator $\hat{\mathcal{O}}_{\pm}^{A}$ is an infinite-dimensional matrix. In theory, β can be any value, with $\hat{\mathcal{O}}_{\pm}^{A}$ capable of implementing phase shifts of arbitrary size. In practice, however, this matrix is truncated at some finite size such that the function of interest and its phase shift are well-approximated, i.e., contributions from the basis states at the numerically-imposed boundary are near zero, and β is much smaller than the total size of the state space. We note that upon implementing the phase-shift operator in this truncated state space, the boundary terms appearing in the iterated matrix in Eq. (2.29) are set to zero, and a β-number of coefficients are shifted outside of the state space and replaced with zero. However, so long as the state space is large enough, this introduces no appreciable errors, which can be numerically confirmed by checking the state's norm.

For an energy eigenstate expansion written in terms of the truncated phase DVR, the phase-shift operator $\hat{\mathcal{O}}_{\pm}^{B}$ is instead a finite-sized matrix with dimension $2M + 1$, as this basis is finite-sized by definition with $\alpha = -M, ..., M$. Importantly, the basis states of the truncated phase DVR are $2\theta_{\max}$-periodic, corresponding to a phase shift

with $\beta = 2M + 1$. Therefore, the boundary terms appearing in the iterated matrix in Eq. (2.29) map back inside the interval $[-M, M]$. While β can take on any value, the resulting phase shift, characterized by κ, always maps back to a state indexed inside $[-M, M]$, resulting in a net phase shift no larger than $2\theta_{\max}$. As expected, $\beta = 2M + 1$ yields no net phase shift and the phase-shift operator is the identity, $\hat{\mathcal{O}}^B_{\pm} = \mathbb{1}$. As in the traditional case, in practice we choose the size of the state space, determined by M, to be large enough to well-approximate a function of interest as well as its phase shift, which is particularly relevant when choosing to represent and generate phase shifts with a non-periodic function using this basis.

The identification of the matrix in Eq. (2.29) as a phase shift operator yields a convenient method for manipulating state vectors numerically to generate a phase shift, without requiring an explicit functional form. This allows for a straightforward examination of the impact of such phase shifts on a system. As an example, we include Fig. 2.8, which shows the effects of phase shifts in the fluxonium, specifically for the ground state wavefunction, its energy, and its associated currents. We generate phase shifts in the fluxonium ground state using the traditional phase DVR, with a grid size $\Delta\theta = \pi/8$ and a matrix size corresponding to 101 states. This is sufficiently large enough to accurately represent the ground state (see Fig. 2.13a) as well as any associated phase shift we implement here, which can be confirmed numerically via the state norm.

Fig. 2.8a shows the ground state wavefunction $\Psi_0(\theta)$ of the fluxonium for an

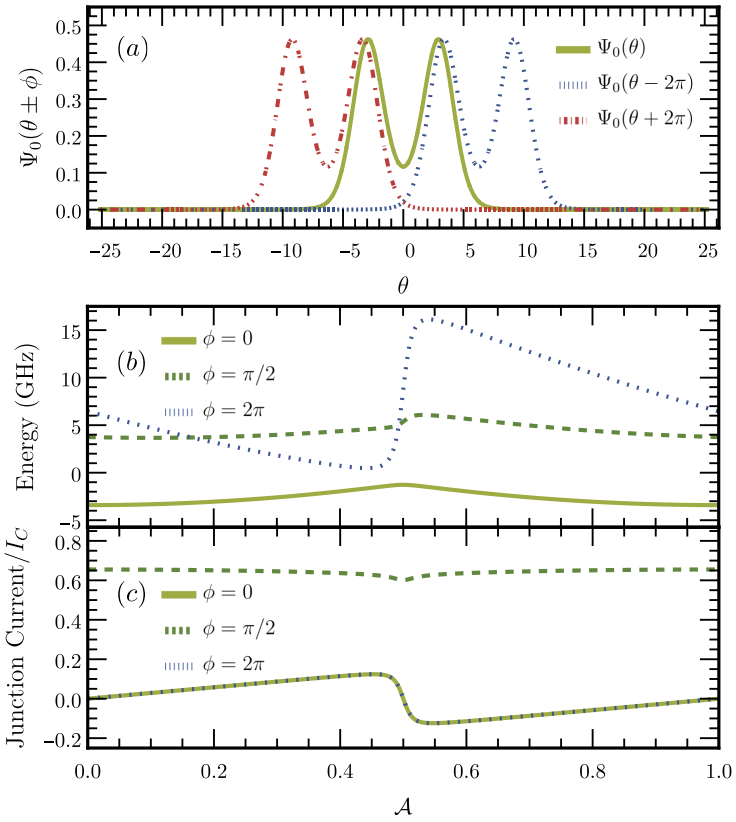


Figure 2.8: (a) Visualization of the phase shift operation in the ground state of the fluxonium with a flux penetration corresponding to $\mathcal{A} = 1/2$, specifically comparing the original wavefunction to the forward and backward phase-shifted wavefunctions with a phase shift of 2π. In (b) and (c), we specifically focus on the forward-shifted state $\Psi_0(\theta - \phi)$ with phase shifts of $\phi = 0, \pi/2, 2\pi$. In (b), we plot the average energy of the state $\langle \Psi_0^- | \hat{H} | \Psi_0^- \rangle$ as a function of the external flux while in (c), we plot the supercurrent through the Josephson junction $\langle \Psi_0^- | \hat{I}/I_C | \Psi_0^- \rangle$ as a function of the external flux, where $\hat{I} = I_C \sin\left(\hat{\theta} + 2\pi\mathcal{A}\right)$, with I_C the junction's critical current. Parameters for these plots are $E_C/h = 2.5$ GHz, $E_L/h = 0.5$ GHz, and $E_J/h = 10$ GHz. All phase-shifted functions are generated via the methods outlined in the main text.

external flux threading corresponding to $\mathcal{A} = 1/2$, as well as its phase-shifted counterparts $\Psi_0(\theta \pm \phi)$ for $\phi = 2\pi$, generated via the phase shift operator in Eq. (2.29). Phase-shifted states such as those shown in Fig. 2.8a can then be utilized to consider the effect of such a phase shift on the energy of the ground state. In Fig. 2.8b, we plot the average energy in each of these phase-shifted states as a function of the

flux penetration, evaluating the energy by taking the expectation value of the fluxonium Hamiltonian in Eq. (2.22) with the phase-shifted states, i.e., $\left\langle \Psi_0^- \right| \hat{H} \left| \Psi_0^- \right\rangle$, for $\phi = 0, \pi/2, 2\pi$. We can similarly examine the effect of the phase shift on the current through the Josephson junction, shown in Fig. 2.8c, by instead taking the expectation value of the operator corresponding to the supercurrent through the junction, $\hat{I} = I_C \sin\Big(\hat{\theta} + 2\pi\mathcal{A}\Big)$, where I_C represents the junction's critical current and the operator $\hat{I}$ is constructed analogously to those presented in Section 2.2.3. In both instances, we observe increases in energy and current due to these manufactured phase shifts, which vary in size as a function of the flux penetration as well as the size of the phase shift. Importantly, we demonstrate the applicability of phase DVRs for generating and modeling the impacts of phase shifts in systems like the fluxonium.

2.3.3 Transmon

One standard circuit that presents a unique, albeit more restrictive, use-case for DVRs is the transmon/CPB [185, 192, 319, 326, 346], shown in Fig. 2.2c. This system's Hamiltonian is written as

$$\hat{H} = 4E_C(\hat{N} - N_g)^2 - E_J \cos\hat{\theta} \ , \tag{2.30}$$

where the characteristic energy scales are set by the charging energy $E_C = \frac{e^2}{2(C_J + C_g)}$ and the Josephson energy E_J. In the transmon limit ($E_J \gg E_C$), we have the usual transmon qubit, while in the charge limit ($E_J \sim E_C$), we have the well-known charge

qubit, or Cooper-pair box (CPB). Here, the capacitance C_g couples an offset voltage V_g to the circuit, leading to the offset charge $N_g = \frac{C_g V_g}{2e}$, with e the elementary electron charge. The sensitivity of the system to this offset charge is an identifying feature of these two limits, with the CPB notoriously susceptible to offset charge noise.

Notably, this system is 2π-periodic in phase, demanding an integer quantization of charge number. This limits the application of the DVRs we discuss to those which are 2π-periodic in phase with a grid size of $\Delta N = 1$. Therefore, in this example, we can consider only two DVRs: the traditional charge number DVR with $\Delta N = 1$ and $\theta \in [-\pi, \pi]$ and the truncated phase DVR with $\Delta N = 1$ and $\Delta\theta = 2\pi/(2M+1)$, with $2M + 1$ corresponding to the size of the state space. As we discuss in Section 2.2.1, the former of these two choices is the usual 'charge basis.' However, the latter offers an alternative numerical description in terms of a discretized phase (which depends on the chosen matrix size), allowing for an investigation and comparison of such an approach to the typical method. Here, we examine the level convergence properties and basis state contributions of these two approaches in both energy regimes of the circuit.

2.3.3.1 Level Convergence

While the Hamiltonian in Eq. (2.30) is exactly solvable in the continuous phase basis in terms of Mathieu functions and their characteristic values [192, 347], these are highly non-trivial functions to work with. As a consequence, standard numeri-

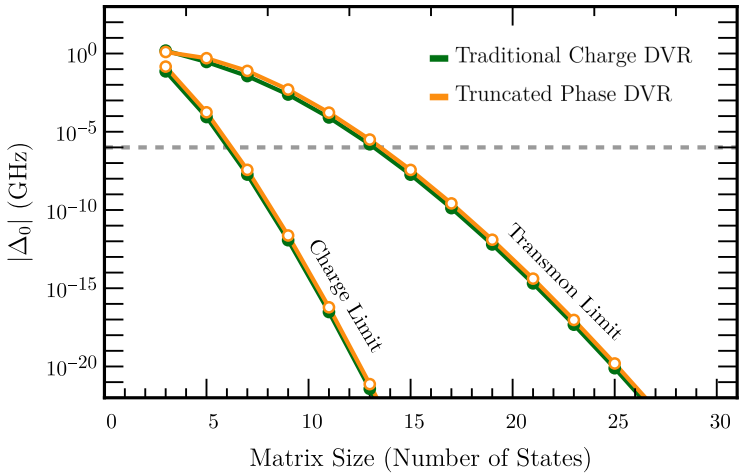


Figure 2.9: The absolute value of the energy difference $|\Delta_0|$ as function of matrix size in the ground state of the transmon in both the transmon limit and the charge limit. Dark green points correspond to the traditional charge DVR with $\Delta N = 1$, a.k.a. the charge basis. Orange points correspond to the truncated phase DVR with $\Delta N = 1$ and $\Delta\theta$ a function of the matrix size $2M + 1$ according to $\Delta\theta = 2\pi/(2M + 1)$. Decoherence accuracy is indicated with a horizontal gray dashed line. Open data points indicate where $\Delta_0 < 0$, in order to note and highlight the non-variational nature of DVRs. Parameters for these plots are $E_C/h = 0.2$ GHz, $E_J/h = 10$ GHz, and $N_g = 1/2$ for the transmon limit and $E_C/h = 5$ GHz, $E_J/h = 5$ GHz, and $N_g = 1/2$ for the charge limit.

cal tools [229] typically employ the charge basis with some associated truncation to represent this system. For our analysis, we take E_n^{ref} to be the exact energies [192, 347] in order to assess the performance of both the charge basis and the truncated phase DVR. This is shown in Fig. 2.9, where we opt instead to show the explicit level convergence of these two DVRs by examining $|\Delta_0|$ as a function of matrix size for each DVR, as we are limited to only two DVRs with one grid size fixed.

Examining the level convergence of both limits of the transmon in Fig. 2.9, we immediately observe that the truncated phase DVR, while converging below the true energy, behaves analogously to the charge basis (the traditional charge DVR, $\Delta N = 1$). Additionally, while the truncated phase DVR yields a marginally worse accuracy

than the charge basis at each matrix size, this is not large enough to significantly affect performance, as evidenced by their identical decoherence-accurate matrix sizes of 7 states in the charge limit and 15 states in the transmon limit. This highlights the more rapid convergence both exhibit when compared to either of the prior examples considered. Interestingly, despite the fact that the truncated phase DVR yields a full Hamiltonian matrix and the charge basis results in a sparse, tri-diagonal Hamiltonian matrix (see Section 2.2.3), the truncated phase DVR still performs on par with the charge basis.

2.3.3.2 Basis State Contributions

We also examine the energy eigenstate decompositions of each approach in either the charge or transmon limit, again evaluating the magnitude of the overlap of the i^{th} energy eigenstate of the transmon $|\Psi_i\rangle$ and the α-indexed state of a particular basis $|\psi_\alpha\rangle$, i.e., $|\langle\Psi_i|\psi_\alpha\rangle|^2$. In particular, we consider a state space of 23 basis states, where both DVRs have converged below decoherence accuracy, shown in Fig. 2.10 and Fig. 2.11 for the transmon limit and charge limit, respectively.

From Figs. 2.10a and 2.11a, it is immediately evident that the charge basis is a far more compact description in either limit. In the charge limit, the charge basis states are very good approximations to the eigenstates of the system, essentially amounting to a superposition of only two charge number states. As E_J grows, moving into the transmon limit, more charge basis states are required to represent an eigenstate.

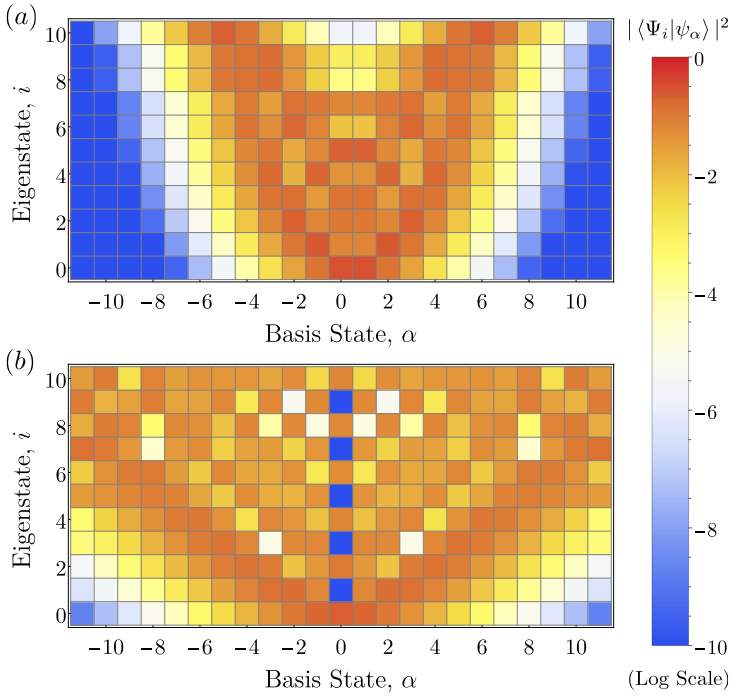


Figure 2.10: Eigenstate decompositions showing $|\langle\Psi_i|\psi_\alpha\rangle|^2$ for the first eleven energy eigenstates of the transmon in the transmon limit across a state space of 23 basis states in (a) the traditional charge DVR ($\Delta N = 1$) and (b) the truncated phase DVR ($\Delta N = 1$, $\Delta\theta = 2\pi/23$). Values are shown on a log scale, colored according to their power, as indicated by the legend. We enforce a cutoff at 10^{-10}, hence grid spaces with values smaller than this cutoff are automatically colored blue. Parameters for these plots are $E_C/h = 0.2$ GHz, $E_J/h = 10$ GHz, and $N_g = 1/2$.

This is a direct reflection of the matrix representation of the Hamiltonian in this basis, where the off-diagonal elements of this tri-diagonal matrix grow in magnitude relative to the diagonal contributions when moving from the charge limit to the transmon limit. On the other hand, using the truncated phase DVR to represent the system requires nearly all of the basis states in a given state space, as shown in Figs. 2.10b and 2.11b. While in the transmon limit the truncated phase DVR is somewhat localized, in the charge limit this description is not at all compact. As before, this can be understood as a reflection of the Hamiltonian matrix in each

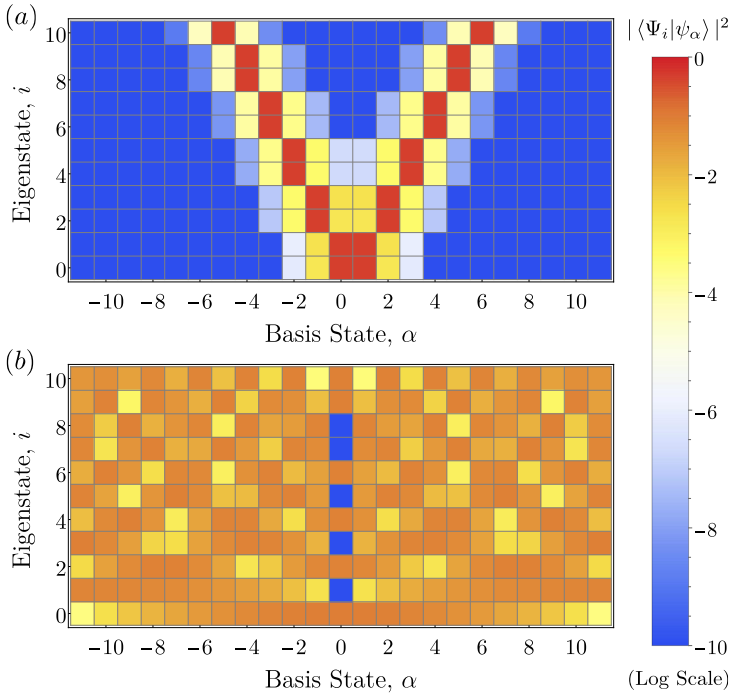


Figure 2.11: Eigenstate decompositions showing $|\langle\Psi_i|\psi_\alpha\rangle|^2$ for the first eleven energy eigenstates of the transmon in the charge limit across a state space of 23 basis states in (a) the traditional charge DVR ($\Delta N = 1$) and (b) the truncated phase DVR ($\Delta N = 1$, $\Delta\theta = 2\pi/23$). Values are shown on a log scale, colored according to their power, as indicated by the legend. We enforce a cutoff at 10^{-10}, hence grid spaces with values smaller than this cutoff are automatically colored blue. Parameters for these plots are $E_C/h = 5$ GHz, $E_J/h = 5$ GHz, and $N_g = 1/2$.

limit. The charging contribution to the Hamiltonian is a full matrix in the phase DVR, which grows in relative magnitude upon moving from the transmon limit to the charge limit, overpowering the diagonal contribution from the tunneling term.

2.4 Outlook

In this work, we have demonstrated the effectiveness of using sinc DVRs to numerically model superconducting circuits. By considering extensions and generalizations of the usual charge basis, we introduce a broad class of both discrete charge number

and discrete phase bases, which can be readily employed in numerous systems that incorporate any combination of capacitors, Josephson junctions, and inductors. Despite their non-variational behavior and lack of sparsity, we find that these DVRs can match, and in many cases outperform, the standard numerical approaches currently used in many software tools today.

We find that these DVRs vastly outperform a typical sparse, tri-diagonal method, the FD method. Further, in the fluxonium, both phase and charge number DVRs of various grid sizes achieve more accurate and efficient level convergence than the harmonic oscillator basis. In the more restrictive case of the transmon, where periodicity limits the usage of DVRs to the charge basis and an analogous discrete phase basis, we still find that the phase DVR can match the performance of this typical representation. We additionally show that both the infinite (the traditional sinc DVR) and finite (the truncated sinc DVR) descriptions perform similarly, a promising feature that may prove valuable in the context of time evolution via trotterization, where the conjugate variables of the truncated sinc DVR are related by a discrete Fourier transform.

While our work offers a potentially more efficient and accurate numerical representation of superconducting circuits, important questions remain regarding the applicability of these representations (and others) to larger-scale systems. Sparsity is likely an important feature for multi-qubit simulations, where smaller and/or truncated state spaces are invaluable for handling numerous degrees of freedom. Other sparse

approaches, such as wavelets or higher-order FD methods, may be able to leverage their sparsity to represent these larger-scale systems while still reaching decoherence accuracy. Moving forward, further investigation into approaches that could combine the level of accuracy provided by DVRs with the sparsity of alternative methods may offer promising solutions for efficiently modeling larger-scale quantum systems and expanding the ever-growing capabilities of software tools for superconducting circuits.

Appendix 2.A Discrete Variable Representations

In this appendix, we provide an introduction to discrete variable representations (DVRs), including derivations of their required properties and clarifications on their limitations in numerical analysis. We outline the construction and show the associated basis states of a classic DVR, the orthogonal polynomial DVR, as well as present the relevant details for building the sinc DVRs utilized in the main text.

A DVR [327–329] is an orthonormal and complete basis set that is generated by taking a discrete set of points from a system's degrees of freedom and projecting them onto another orthonormal and complete basis set. This yields a basis in which individual basis functions are localized around their associated grid points. Different DVRs are constructed by considering different orthonormal and complete function sets to project onto. Explicitly, we construct a DVR by combining a projector $\hat{P}$ and a set of grid points $\{x_\alpha\}$ such that the resulting states,

$$|\psi_{\alpha,x}\rangle = \frac{1}{\sqrt{c_\alpha}} \hat{P} \, |x_\alpha\rangle \quad , \tag{2.A1}$$

are orthonormal and complete. That is to say,

$$\begin{aligned} &\langle \psi_{\alpha,x} | \psi_{\beta,x} \rangle = \delta_{\alpha\beta} \\ &\sum_\alpha |\psi_{\alpha,x}\rangle \, \langle \psi_{\alpha,x}| = \hat{P} \quad . \end{aligned} \tag{2.A2}$$

Here, c_α is a normalization constant while the indices α and x serve to label each DVR state with its grid point α and the discretized variable x. We note that within the subspace defined by $\hat{P}$, the completeness relation in Eq. (2.A2) is the identity, as expected.

The projector $\hat{P}$ is assembled from some orthonormal and complete function set $\{f_k(x)\}$, where k may index each function either discretely or continuously. For a function set with discretely-indexed basis functions and orthonormality and completeness relations

$$\begin{aligned} \int_a^b dx\ f_k^*(x) f_j(x) &= \delta_{kj} \\ \sum_k f_k^*(x) f_k(x') &= \delta(x - x') \ , \end{aligned} \tag{2.A3}$$

the projector takes the form

$$\hat{P} = \sum_{k=1}^{M} |f_k\rangle \langle f_k| \ , \tag{2.A4}$$

where N indicates the subspace defined by the projector and as usual, $f_k(x) = \langle x|f_k\rangle$. If instead the function set is continuously indexed [i.e., $\delta_{kj} \to \delta(k-j)$ and $\sum_k \to \int dk$ in Eq. (2.A3)], the projection operator takes the form

$$\hat{P} = \int_{-k_{\max}}^{k_{\max}} dk\, |f_k\rangle \langle f_k| \ , \tag{2.A5}$$

where now, the subspace of the continuous index k is defined by the boundary values $\pm k_{\max}$.

In both instances, this formulation of a DVR and the conditions in Eq. (2.A2) highlight important features and requirements of this representation. We identify an essential aspect of a DVR's basis functions by re-expressing the orthonormality condition in Eq. (2.A2),

$$\begin{aligned}\langle\psi_{\alpha,x}|\psi_{\beta,x}\rangle &= \frac{1}{\sqrt{c_\alpha^* c_\beta}} \langle x_\alpha| \hat{P}^\dagger \hat{P} |x_\beta\rangle \\ &= \frac{1}{\sqrt{c_\alpha^* c_\beta}} \langle x_\alpha| \hat{P} |x_\beta\rangle \\ &= \frac{1}{\sqrt{c_\alpha^*}} \psi_{\beta,x}(x_\alpha) = \delta_{\alpha\beta} \ ,\end{aligned} \tag{2.A6}$$

where we exploit the projection operator property $\hat{P} = \hat{P}^\dagger = \hat{P}^2$ and define $\langle x_\alpha|\psi_{\beta,x}\rangle = \psi_{\beta,x}(x_\alpha)$. Namely, each basis function, by definition, must vanish at every grid point other than its own. Further, by combining Eq. (2.A1) and either Eq. (2.A4) or (2.A5) with the conditions in Eq. (2.A2), we see that the functions $\{f_k(x)\}$ used to construct $\hat{P}$ must satisfy both an exact quadrature rule that discretizes their orthonormality,

$$\sum_\alpha \frac{1}{|c_\alpha|} f_k^*(x_\alpha) f_{k'}(x_\alpha) = \begin{cases} \delta_{kk'} \\ \\ \delta(k-k') \end{cases} \ , \tag{2.A7}$$

where we can identify the constant $|c_\alpha|$ with the weights of our desired quadrature rule, as well as a discretized completeness relation within the projector's subspace at

the grid points $\{x_\alpha\}$:

$$\sqrt{c_\alpha^* c_\beta}\delta_{\alpha\beta} = \begin{cases} \sum_{k=1}^{N} f_k(x_\alpha) f_k^*(x_\beta) \\ \\ \int_{-k_{\max}}^{k_{\max}} dk f_k(x_\alpha) f_k^*(x_\beta) \end{cases} . \tag{2.A8}$$

Thus in practice, constructing a DVR consists of choosing a function set $\{f_k(x)\}$, projector $\hat{P}$, constant c_α, and grid $\{x_\alpha\}$ such that Eqs. (2.A7) and (2.A8) are satisfied.

The final crucial (and most practical) characteristic of a DVR is the diagonal approximation, where we assume the matrix form of operators that are a function of the discretized variable are diagonal in the DVR's basis, evaluated at each point on the grid:

$$\langle \psi_{\alpha,x} | \, V(\hat{x}) \, | \psi_{\beta,x} \rangle \approx V(x_\alpha)\delta_{\alpha\beta} \ . \tag{2.A9}$$

This property hinges on the quadrature rule in Eq. (2.A7). One can readily confirm that Eq. (2.A9) only holds if we approximate the integral,

$$\begin{aligned} \langle f_k | \, V(\hat{x}) \, | f_{k'} \rangle &= \int_a^b dx \ f_k^*(x) V(x) f_{k'}(x) \\ &\approx \sum_\alpha \frac{1}{|c_\alpha|} f_k^*(x_\alpha) V(x_\alpha) f_{k'}(x_\alpha) \end{aligned} , \tag{2.A10}$$

using a quadrature rule based on Eq. (2.A7). This approximation introduces a potential quadrature error that we interpret to be a consequence of the fact that $V(\hat{x}) \, |\psi_{\beta,x}\rangle$ may not necessarily lie inside the subspace defined by $\hat{P}$. Importantly, these errors

are not guaranteed to be positive. Thus, when DVRs are used to model Hamiltonians, this source of error may not necessarily increase the energy eigenvalues. Since the estimated eigenvalues may be below their actual values, DVRs are non-variational basis representations.

We now consider the details for the construction of three different DVRs. For illustrative purposes, we first discuss a classic DVR based on real orthogonal polynomials. Then, we present the derivation and details of the two DVRs utilized in the main text. These are constructed using variations of the Fourier basis, with the traditional 'sinc DVR' using the continuous Fourier basis and the truncated sinc DVR using the partially discrete Fourier basis.

2.A.1 Orthogonal Polynomial DVRs

Real orthogonal polynomials [348] are characterized by their orthogonality relation,

$$\int_a^b dx\ w(x)p_m(x)p_n(x) = \tilde{c}_n\delta_{mn}\ \ , \tag{2.A11}$$

where $p_m(x)$ is the m^{th}-degree polynomial on the interval $[a, b]$ with coefficient $\tilde{c}_n$ and weight function $w(x)$. Distinct families of orthogonal polynomials (e.g., Hermite polynomials, Legendre polynomials, etc.) are characterized by their different intervals, coefficients, and weight functions. Importantly, via Gaussian quadrature [349, 350],

this orthogonality relation can be rewritten using an exact quadrature rule,

$$\int_a^b dx\ w(x)p_m(x)p_n(x) = \sum_{i=1}^{M} \tilde{w}_i p_m(x_i)p_n(x_i)\ , \tag{2.A12}$$

where $\{x_i\}$ are the zeros of $p_M(x)$ and $\tilde{w}_i$ are the weights,

$$\tilde{w}_i = \int_a^b dx\ L_i(x)w(x)\ , \tag{2.A13}$$

with

$$L_i(x) = \prod_{\substack{j=1 \\ j\neq i}}^{M} \frac{x - x_j}{x_i - x_j}\ . \tag{2.A14}$$

This quadrature rule is exact for polynomial functions with a degree less than or equal to $2M-1$, i.e., the degree of the function $p_m(x)p_n(x)$ such that $m+n \leq 2M-1$.

This quadrature rule yields a straightforward path to creating a DVR based on orthogonal polynomials. With a projector assembled from the functions

$$f_k(x) = \sqrt{\frac{w(x)}{\tilde{c}_k}} p_k(x)\ , \tag{2.A15}$$

we project onto a subspace of up to $M-1$ polynomials, thus ensuring the exact quadrature rule is satisfied. Then, with a grid of points corresponding to the zeros $p_M(x)$ and the coefficients

$$c_\alpha = \frac{w(x_\alpha)}{\tilde{w}_\alpha}\ , \tag{2.A16}$$

the conditions outlined in Eqs. (2.A2), (2.A7), and (2.A8) are satisfied and we find the DVR's basis states to be

$$|\psi_{\alpha,x}\rangle = \sum_{k=1}^{M-1} \sqrt{\frac{\tilde{w}_\alpha}{\tilde{c}_k}} p_k(x_\alpha) \, |f_k\rangle \quad . \tag{2.A17}$$

We see that a set of orthogonal polynomials may always be used to create a DVR, since they are orthonormal and complete on points that correspond to the zeros of the first polynomial excluded from the subspace.

2.A.2 The Traditional Sinc DVR

The usual sinc DVR [327, 330–332] is formed by using the continuous Fourier basis to project onto a discrete set of points, exploiting the orthonormality and completeness of both the continuous Fourier basis as well as its partially discrete representation. The continuous Fourier basis [351],

$$f(x,p) = \frac{e^{ipx/\hbar}}{\sqrt{2\pi\hbar}} \ , \tag{2.A18}$$

is used in the Fourier transform to continuously project a function in real space onto its conjugate space or vice versa, which provides the continuous orthonormality and

completeness relations,

$$\begin{aligned} \delta(p-p') &= \frac{1}{2\pi\hbar}\int_{-\infty}^{\infty} dx\ e^{-i(p-p')x/\hbar} \\ \delta(x-x') &= \frac{1}{2\pi\hbar}\int_{-\infty}^{\infty} dp\ e^{ip(x-x')/\hbar}\ , \end{aligned} \tag{2.A19}$$

where both the real-space variable x and the conjugate variable p are continuous with infinite extent.

We can leverage the continuous Fourier basis to construct a DVR by noting the orthonormality and completeness of the partially discrete Fourier basis, as utilized in the complex Fourier series expansion of a function in real space or conjugate space. A Fourier series expansion uses this partially discrete representation to project a continuous function onto an infinite number of discrete points, representing this function discretely in one space and continuously, but on a finite interval, in the other. The Fourier series expansion of a real-space function provides the orthonormality and completeness of the partially discrete Fourier basis in conjugate space,

$$\begin{aligned} \delta(p-p') &= \frac{1}{2p_{\max}}\sum_{n=-\infty}^{\infty} e^{-i2\pi n(p-p')/2p_{\max}} \\ \delta_{mn} &= \frac{1}{2p_{\max}}\int_{-p_{\max}}^{p_{\max}} dp\ e^{-i2\pi(m-n)p/2p_{\max}}\ , \end{aligned} \tag{2.A20}$$

which we identify as the exact quadrature and completeness relations [Eq. (2.A7) and Eq. (2.A8)] needed to construct a DVR. Similarly, the Fourier series expansion of a conjugate-space function provides the orthonormality and completeness of the

partially discrete Fourier basis in real space,

$$\begin{aligned} \delta(x - x') &= \frac{1}{2x_{\max}} \sum_{n=-\infty}^{\infty} e^{i2\pi n(x-x')/2x_{\max}} \\ \delta_{mn} &= \frac{1}{2x_{\max}} \int_{-x_{\max}}^{x_{\max}} dx \; e^{i2\pi(m-n)x/2x_{\max}} \quad . \end{aligned} \tag{2.A21}$$

Thus, a projector assembled from the continuous Fourier basis [Eq. (2.A18)] can be used in two ways to create a DVR, either discretizing the real-space variable x with the conjugate variable p continuous and bounded or discretizing p with x continuous and bounded.

For a DVR that discretizes x, we use a projector assembled from the real-space functions $\langle x|f_p\rangle = f(x,p)$, which project onto a continuous-p subspace bounded by $\pm p_{\max}$ [as in Eq. (2.A5)]. Examining Eqs. (2.A19) and (2.A20), we see that this projector can be used to build a DVR when combined with an infinite, uniform grid of points $x_\alpha = \alpha\Delta x$, spaced according to $\Delta x = \pi\hbar/p_{\max}$, and a coefficient $c_\alpha = 1/\Delta x = p_{\max}/\pi\hbar$. The resulting DVR states take a form analogous to Eq. (2.1) in the main text, which instead considers phase θ and charge number N as the two (dimensionless) conjugate degrees of freedom.

Analogously, for a DVR that discretizes p, we instead use a projector assembled from the conjugate-space functions $\langle p|f_x\rangle = f(x,p)^*$, which project onto a continuous-x subspace bounded by $\pm x_{\max}$. We note that the sign change in the projector's functions serves to maintain the usual relationship between the conjugate spaces. Examining Eqs. (2.A19) and (2.A21), we see that we can once again construct a DVR,

now with the infinite, uniform grid $p_\alpha = \alpha\Delta p$, spaced according to $\Delta p = \pi\hbar/x_{\max}$, and a coefficient $c_\alpha = 1/\Delta p = x_{\max}/\pi\hbar$. The resulting DVR in this case is given in Eq. (2.3) in the main text, again considering phase θ and charge number N as the two conjugate degrees of freedom.

We note that due to the required infinite number of basis states (and infinite extent of the discretized variable), in practice, these DVRs are subject to a truncation error associated with the number of DVR states included in the state space. Typically, we proceed with the infinite state space description of the states and operators, recognizing that this error is minimized with a sufficiently large state space.

2.A.3 The Truncated Sinc DVR

The notion of truncating the infinite traditional sinc DVR naturally leads to the introduction of the second DVR one can construct using the Fourier basis. In this case, the DVR's basis is instead finite-sized by definition, requiring no additional truncation for numerical implementation. As previously indicated by Eqs. (2.A20) and (2.A21), the partially discrete representation utilized in the Fourier series is also orthonormal and complete, but on a finite interval. Written explicitly, the partially discrete real-space functions

$$f_n(x) = \frac{e^{ip_n x/\hbar}}{\sqrt{2x_{\max}}} \ , \tag{2.A22}$$

are orthonormal and complete on the interval $x \in [-x_{\max}, x_{\max}]$, with $p_n = n\Delta p$, $x_{\max} = \pi\hbar/\Delta p$, and n integer-valued on the range $[-\infty, \infty]$. Analogously, the par-

tially discrete conjugate-space functions

$$g_n(p) = \frac{e^{-ipx_n/\hbar}}{\sqrt{2p_{\max}}} \ , \tag{2.A23}$$

are orthonormal and complete on the interval $p \in [-p_{\max}, p_{\max}]$, with $x_n = n\Delta x$, $p_{\max} = \pi\hbar/\Delta x$, and n integer-valued on the range $[-\infty, \infty]$. We now consider the use of these functions for the projection operator $\hat{P}$ in order to construct a DVR.

The exact quadrature and discrete completeness relations required to build a DVR in this case are enabled by the discrete Fourier transform [351], which defines the orthonormality and completeness of the fully discrete representation of the Fourier basis, given by

$$\delta_{jk} = \frac{1}{2M+1} \sum_{n=-M}^{M} e^{i2\pi n(j-k)/2M+1} \ , \tag{2.A24}$$

where $|j-k| < 2M+1$. In this instance, the creation of the DVR amounts to discretizing the remaining continuous and bounded variable in Eqs. (2.A22) or (2.A23), yielding a basis set which is finite-sized and discrete in both the real-space and conjugate-space variables. As we show in the main text, while these two DVRs are similar in this manner, the resulting basis states are distinct, specifically with regard to periodicity.

Using a projection operator assembled from the functions in Eq. (2.A22), we proceed with a discretization of the real-space variable x by comparing Eqs. (2.A21) and (2.A24). Upon examination, we can construct a DVR provided we project into a finite subspace of $2M+1$ states [as in Eq. (2.A4)], where $n \in [-M, M]$, using the

constant $c_\alpha = 2M + 1/2x_{\max}$ and a grid of points $x_\alpha = \alpha\Delta x$, which is finite-sized ($\alpha \in [-M, M]$) and spaced according to $\Delta x\Delta p = 2\pi\hbar/2M + 1$. Note that from the original basis functions of the projector, we have that $p_n = n\Delta p$ and $x_{\max} = \pi\hbar/\Delta p$, allowing us to re-express the constant as $c_\alpha = (2M+1)\Delta p/2\pi\hbar = 1/\Delta x$. In the main text, the resulting DVR states are given in terms of θ and N in Eq. (2.8).

This procedure is carried out analogously for a projection operator assembled from the functions in Eq. (2.A23). Here, we discretize the conjugate variable p to construct a DVR, comparing Eqs. (2.A20) and (2.A24). In this case, we must project into a finite subspace of $2M+1$ states, where $n \in [-M, M]$, with the constant $c_\alpha = 2M+1/2p_{\max}$ and a grid of points $p_\alpha = \alpha\Delta p$, which is finite-sized ($\alpha \in [-M, M]$) and spaced according to $\Delta x\Delta p = 2\pi\hbar/2M + 1$. Note again that from the original basis functions of the projector, we have that $x_n = n\Delta x$ and $p_{\max} = \pi\hbar/\Delta x$, allowing us to re-express the constant as $c_\alpha = (2M + 1)\Delta x/2\pi\hbar = 1/\Delta p$. In this case, we find DVR states with a form equivalent to that given in Eq. (2.10).

Appendix 2.B Details for the LC Oscillator Example

In this appendix, we provide additional details for the analysis performed for the LC oscillator presented in Section 2.3.1. To generate the results in Fig. 2.4, a numerical analysis for each of the four DVRs is carried out for a collection of grid sizes and matrix sizes, generating the energy eigenvalues associated with each pairing. For the traditional and truncated charge number DVRs, this includes nineteen grid sizes between $\Delta N = 1/20$ and $\Delta N = 2$, the majority of which are visible in Fig. 2.4. Similarly, for the traditional and truncated phase DVRs, this includes eighteen grid sizes between $\Delta\theta = \pi/64$ and $\Delta\theta = 3\pi$. With the differing scale of these ranges, which we attribute to the physical nature of each variable, not all points are visible in Fig. 2.4. In all cases, up to 150 digits of precision are maintained, far beyond any precision of interest, so as to not affect visible results. We set $E_L/h = E_C/h = 1$ GHz for simplicity, however, it is ultimately scaled away by considering $|\Delta_0|/\sqrt{8E_C E_L}$. Additionally, matrix sizes out to 301 basis states are considered to capture the surpassing of decoherence accuracy and saturation behavior. In Fig. 2.12, we include a sampling of these grid sizes in all four DVRs, restricting the range of accuracy and matrix sizes to those most relevant.

Comparing the traditional and truncated DVRs (Fig. 2.12a and Fig. 2.12c or Fig. 2.12b and Fig. 2.12d), we note the improved accuracy of the truncated DVRs at very small matrix sizes. As expected from the theory, this regime is where the

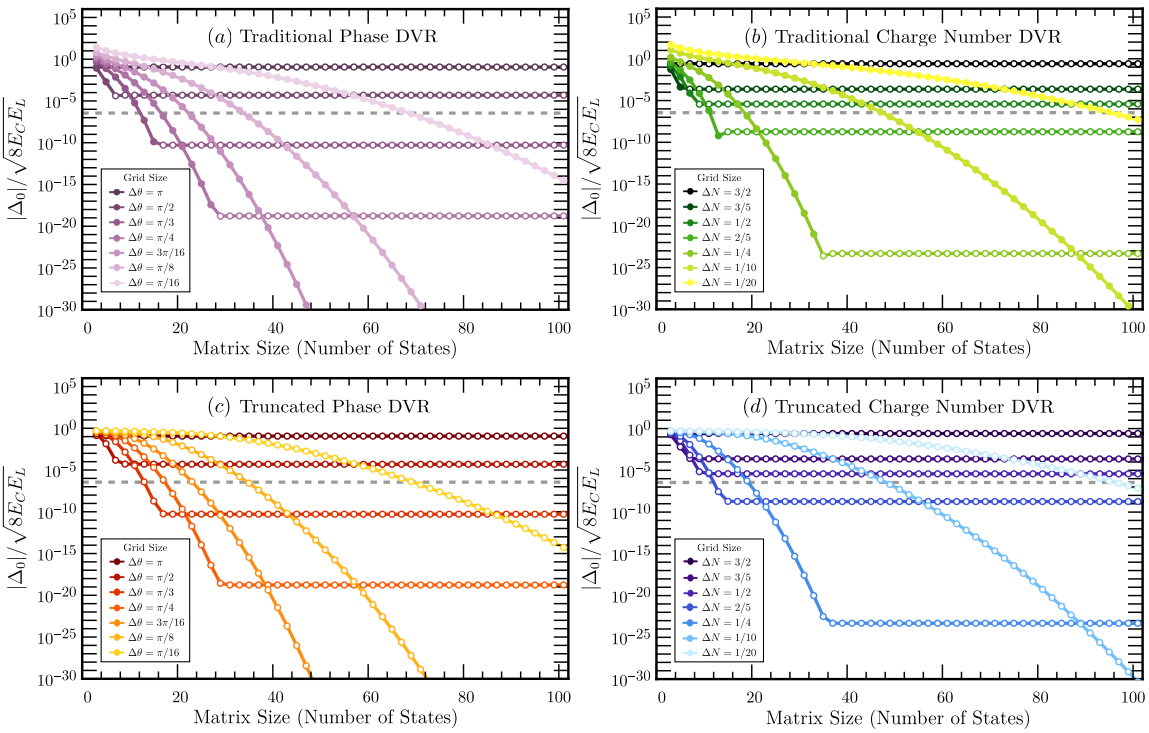


Figure 2.12: The absolute value of the energy difference $|\Delta_0|$ as function of matrix size in the ground state of the LC oscillator, in all four DVRs presented in Section 2.2: (a) the traditional phase DVR, (b) the traditional charge number DVR, (c) the truncated phase DVR, and (d) the truncated charge number DVR. All are scaled according to the LC frequency. Decoherence accuracy (also scaled according to the LC frequency) is indicated with a horizontal gray dashed line. Open data points indicate where $\Delta_0 < 0$, in order to note and highlight the non-variational nature of DVRs.

required numerical truncation of the traditional DVR is most impactful, as we are approximating matrix elements using infinite basis-based expressions in very small matrices. This discrepancy, while dependent on grid size, becomes negligible upon reaching matrix sizes corresponding to saturation precision. We also note the non-variational behavior evident in all four DVRs shown in Fig. 2.12, as evidenced by the regions where $\Delta_0 < 0$. While we can confirm that the energies themselves (E_0^{DVR}) monotonically decrease with increasing matrix size, as anticipated, their difference

from the true energy, Δ_0, is not exclusively positive. In the traditional DVRs, we find that while the DVRs' energies do approach from above the true energy, they ultimately converge below it. Upon passing below the true energy, it occasionally leads to a sharp feature, like that in Fig. 2.12b for $\Delta N = 2/5$, where the saturation precision below the true energy is actually larger than that given by the final matrix size for which $\Delta_0 > 0$. In contrast, in the truncated case, the energies exclusively converge to the true energy from below.

Appendix 2.C Details for the Fluxonium Example

In this appendix, we provide additional details for the analysis performed for the fluxonium presented in Section 2.3.2. To generate the results in Fig. 2.5, a numerical analysis for each of the four DVRs is carried out for a collection of grid sizes and matrix sizes, generating the energy eigenvalues associated with each pairing. For the traditional and truncated charge number DVRs, we consider the subset of grid sizes where $1/\Delta N$ is an integer, in order to consider a simplified matrix form for the cosine operator, as we discuss in Section 2.2.3. Thus, we use the grid sizes $\Delta N = 1/n$ with $n = 1, ..., 15$, generating fifteen grid sizes, the majority of which are visible in Fig. 2.5. Identical to the LC oscillator, for the traditional and truncated phase DVRs, we consider eighteen grid sizes between $\Delta\theta = \pi/64$ and $\Delta\theta = 3\pi$. With the differing scale of these ranges, which we attribute to the physical nature of each variable, not all points are visible in Fig. 2.5. In all cases, up to 150 digits of precision are maintained, far beyond any precision of interest, so as to not affect visible results. We set the energy scales and flux penetration of the circuit to reasonable values [193, 321, 322, 345] for the fluxonium — $E_C/h = 2.5$ GHz, $E_L/h = 0.5$ GHz, $E_J/h = 10$ GHz, and $\mathcal{A} = 1/2$. Additionally, matrix sizes out to 301 basis states are considered to capture the surpassing of decoherence accuracy and saturation behavior. In Fig. 2.13, we include a sampling of these grid sizes in all four DVRs, restricting the range of accuracy and matrix sizes to those most relevant.

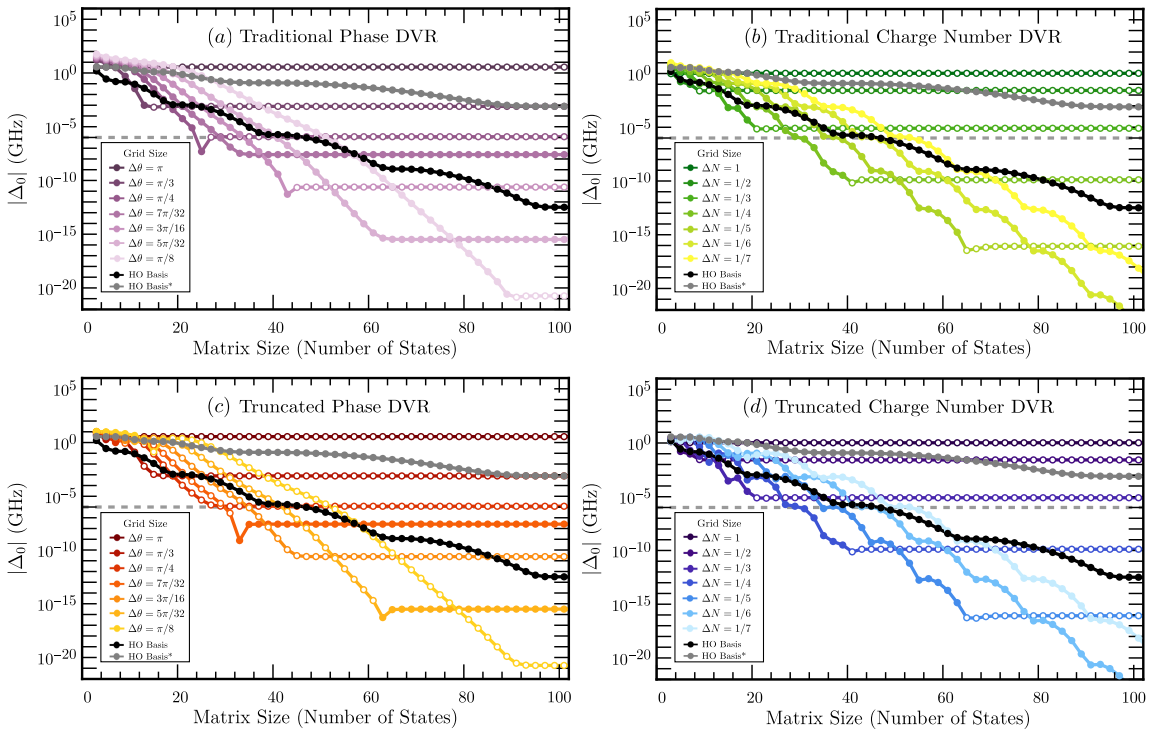


Figure 2.13: The absolute value of the energy difference $|\Delta_0|$ as function of matrix size in the ground state of the fluxonium, in all four DVRs presented in Section 2.2: (a) the traditional phase DVR, (b) the traditional charge number DVR, (c) the truncated phase DVR, and (d) the truncated charge number DVR. Decoherence accuracy is indicated with a horizontal gray dashed line. Open data points indicate where $\Delta_0 < 0$, in order to note and highlight the non-variational nature of DVRs. Included in each subplot are two curves indicating the performance of the harmonic oscillator basis using two different length scales. The black curve represents the standard approach using a length scale corresponding to the LC frequency $\omega_{\mathrm{LC}} = \sqrt{8E_C E_L}/h$. The gray curve modifies the length scale to instead use the plasma frequency $\omega_{\mathrm{PL}} = \sqrt{8E_C E_J}/h$. Parameters for this plot are $E_C/h = 2.5$ GHz, $E_L/h = 0.5$ GHz, $E_J/h = 10$ GHz, and $\mathcal{A} = 1/2$.

Included in Fig. 2.13 are two curves indicating the performance of the harmonic oscillator basis using two different length scales. We define the harmonic oscillator basis in terms of the raising and lowering operators $\hat{a}^\dagger$ and $\hat{a}$ as well as an associated length scale θ_0, where

$$\hat{\theta} = \frac{\theta_0}{\sqrt{2}}(\hat{a}^\dagger + \hat{a}) \tag{2.C1}$$

and

$$\hat{N} = \frac{i}{\sqrt{2}\theta_0}(\hat{a}^\dagger - \hat{a}) \ . \tag{2.C2}$$

Using dimensional analysis in the LC oscillator's Hamiltonian [Eq. (2.20)], this length scale is expressed generally as $\theta_0 = (\hbar\omega/E_L)^{1/2}$, with ω the frequency associated with the desired length scale. In the standard harmonic oscillator basis, ω is taken to be the LC frequency $\omega_{\mathrm{LC}} = \sqrt{8E_C E_L}/h$, yielding the usual length scale $\theta_0 = (8E_C/E_L)^{1/4}$. This approach considers a length scale appropriate for the first two terms of the fluxonium Hamiltonian [Eq. (2.22)], diagonalizing these terms, but still requiring a matrix exponential to be evaluated in the final third term. Alternatively, one can consider using the other relevant frequency scale in the fluxonium, the plasma frequency $\omega_{\mathrm{PL}} = \sqrt{8E_C E_J}/h$, which is appropriate for the first and last terms of the fluxonium Hamiltonian [Eq. (2.22)]. This results in the length scale $\theta_0 = (\sqrt{8E_C E_J}/E_L)^{1/2}$. In both cases, due to the required numerical evaluation of a matrix exponential, each matrix size considered in Fig. 2.13 is a sub-matrix of an original matrix consisting of 1001 basis states.

Upon comparison, we find that the standard harmonic oscillator basis greatly outperforms that with a modified length scale, as indicated by its more rapid descent to decoherence accuracy. The standard harmonic oscillator basis surpasses decoherence accuracy at 47 basis states, as shown in Fig. 2.5a, while the harmonic oscillator basis with a length scale modified according to ω_{PL} requires 209 basis states, outside the visible range in both Fig. 2.5 and Fig. 2.13. However, more promising is the perfor-

mance of all four DVRs in comparison with the standard harmonic oscillator basis. There are various grid sizes for which level convergence is achieved at higher accuracy and smaller matrix sizes when compared to the standard method. While Fig. 2.5 specifically highlights decoherence accuracy and saturation precision, including the improvements in reaching decoherence accuracy that all four DVRs provide, Fig. 2.13 displays a complete picture of performance, specifically with regard to matrix size and its associated precision. Namely, that the DVRs outlined here, for small enough grid sizes, appear capable of outperforming the standard numerical approach with regard to accuracy and matrix size, even beyond the decoherence-accurate level.

Comparison between the traditional and truncated DVRs (Figs. 2.13a and 2.13c or Figs. 2.13b and 2.13d) yields a similar conclusion as in the LC oscillator. We find an improvement in the accuracy of the truncated DVRs over the traditional DVRs at small matrix sizes, which diminishes as the matrix size increases, and becomes negligible as the matrix sizes corresponding to saturation precision are reached. The non-variational behavior of each DVR is similarly on display in this example, albeit with more variety. For the charge number DVRs, we generally observe similar behavior as in the LC oscillator, with energies that converge from above to a value below the reference energy. However, for the phase DVRs, we find grid sizes that converge to values above or below the reference energy, and not exclusively from above. As in the LC oscillator, this transitional behavior from $\Delta_0 > 0$ to $\Delta_0 < 0$ or vice versa is occasionally marked by sharp features in the plots in Fig. 2.13.

Appendix 2.D The Finite Difference Method

In this appendix, we outline and derive one of the most well-known discretization methods, the finite difference (FD) method [352–355], which we use for comparison with DVRs in the main text.

2.D.1 Lowest Order FD Method

In a continuous position basis, the Schrödinger equation takes the usual form

$$-\frac{\hbar^2}{2m}\frac{\partial^2\psi_n(x)}{\partial x^2} + V(x)\psi_n(x) = E_n\psi_n(x) \ . \tag{2.D1}$$

By discretizing this system over a uniform grid of points x_i separated by Δx, such that $x_i = i\Delta x$ for some total number of points $i \in [-N, N]$, we can evaluate and solve Eq. (2.D1) at each point. This requires we consider the second derivative evaluated at each grid point, $\frac{\partial^2\psi_n(x_i)}{\partial x^2}$, which we can approximate using a centered FD approximation,

$$\frac{\partial^2\psi_n(x_i)}{\partial x^2} \approx \frac{\psi_n(x_{i-1}) - 2\psi_n(x_i) + \psi_n(x_{i+1})}{\Delta x^2} \ . \tag{2.D2}$$

The discretized Schrodinger equation then takes the form

$$-\frac{\hbar^2}{2m}\frac{\psi_n(x_{i-1}) - 2\psi_n(x_i) + \psi_n(x_{i+1})}{\Delta x^2} + V(x_i)\psi_n(x_i) = E_n\psi_n(x_i) \ . \tag{2.D3}$$

This equation represents a system of equations for the $2N+1$ points in the grid, which we can write in matrix form as

$$\frac{-\hbar^2}{2m}\frac{1}{\Delta x^2}\begin{bmatrix} \text{-2} & 1 & & & & & \\ 1 & \text{-2} & 1 & & & & \\ & 1 & \text{-2} & & & & \\ & & & \ddots & & & \\ & & & & \text{-2} & 1 & \\ & & & & 1 & \text{-2} & 1 \\ & & & & & 1 & \text{-2} \end{bmatrix} \begin{bmatrix} \psi_n(x_{\text{-}N}) \\ \vdots \\ \psi_n(x_0) \\ \vdots \\ \psi_n(x_N) \end{bmatrix} + \frac{-\hbar^2}{2m}\frac{1}{\Delta x^2} \begin{bmatrix} \psi_n(x_{\text{-}N\text{-}1}) \\ 0 \\ \vdots \\ 0 \\ \psi_n(x_{N+1}) \end{bmatrix} \tag{2.D4}$$

$$+ \begin{bmatrix} V(x_{\text{-}N}) & & & & & \\ & \ddots & & & & \\ & & V(x_0) & & & \\ & & & \ddots & & \\ & & & & V(x_N) \end{bmatrix} \begin{bmatrix} \psi_n(x_{\text{-}N}) \\ \vdots \\ \psi_n(x_0) \\ \vdots \\ \psi_n(x_N) \end{bmatrix} = E_n \begin{bmatrix} \psi_n(x_{\text{-}N}) \\ \vdots \\ \psi_n(x_0) \\ \vdots \\ \psi_n(x_N) \end{bmatrix} .$$

The second term in Eq. (2.D4) is understood as the boundary condition term, as it references points outside of the pre-defined grid. By explicitly including this term, we can consider the cases of either a bounded or periodic potential $V(x)$, as in the examples in Section 2.3.

If the potential $V(x)$ is bounded such that $\psi_n(x) \to 0$ as $x \to \pm\infty$, we take the boundary terms corresponding to $\psi_n(x_{-N-1})$ and $\psi_n(x_{N+1})$ to be zero. This corresponds to letting $V(x) \to \infty$ at the edges of our pre-defined grid, which should be a reasonable approximation so long as $N\Delta x$ is large enough to fully capture an

eigenstate of interest. This leaves a straightforward eigenvalue problem to solve,

$$\left(\frac{-\hbar^2}{2m}\frac{1}{\Delta x^2} \begin{bmatrix} \text{-2} & 1 & & & & & \\ 1 & \text{-2} & 1 & & & & \\ & 1 & \text{-2} & & & & \\ & & & \ddots & & & \\ & & & & \text{-2} & 1 & \\ & & & & 1 & \text{-2} & 1 \\ & & & & & 1 & \text{-2} \end{bmatrix} + \begin{bmatrix} V(x_{\text{-}N}) & & & & \\ & \ddots & & & \\ & & V(x_0) & & \\ & & & \ddots & \\ & & & & V(x_N) \end{bmatrix} \right) \begin{bmatrix} \psi_n(x_{\text{-}N}) \\ \vdots \\ \psi_n(x_0) \\ \vdots \\ \psi_n(x_N) \end{bmatrix} = E_n \begin{bmatrix} \psi_n(x_{\text{-}N}) \\ \vdots \\ \psi_n(x_0) \\ \vdots \\ \psi_n(x_N) \end{bmatrix} , \tag{2.D5}$$

which takes the standard tri-diagonal form upon combining the diagonal potential term and the three-point FD approximation.

If the potential is 2π-periodic, such that the wavefunction must obey the boundary condition $\psi_n(x) = \psi_n(x \pm 2\pi)$, we discretize this boundary condition to find:

$$\begin{aligned} \psi_n(x_i) &= \psi_n(x_i \pm 2\pi) \\ &= \psi_n(\Delta x \left[i \pm 2\pi/\Delta x \right]) \ , \end{aligned} \tag{2.D6}$$

where the final line indicates that $2\pi/\Delta x$ must correspond to an integer in order to have a periodic boundary condition that connects two points in our pre-defined grid. Letting $\Delta x = 2\pi/(2N+1)$, we find that the terms corresponding to $\psi_n(x_{-N-1})$ and $\psi_n(x_{N+1})$ are mapped back inside the grid, i.e.,

$$\psi_n(x_N) = \psi_n(x_N - 2\pi) = \psi_n(\Delta x \left[N - 2N - 1 \right]) = \psi_n(x_{\text{-}N\text{-}1}) \tag{2.D7}$$

and

$$\psi_n(x_{\text{-}N}) = \psi_n(x_{\text{-}N} + 2\pi) = \psi_n(\Delta x\,[-N + 2N + 1]) = \psi_n(x_{N+1}) \ . \tag{2.D8}$$

This allows us to re-write the boundary term in Eq. (2.D4) as

$$\tfrac{-\hbar^2}{2m}\tfrac{1}{\Delta x^2}\begin{bmatrix}\psi_n(x_{\text{-}N\text{-}1})\\0\\\vdots\\0\\\psi_n(x_{N+1})\end{bmatrix} = \tfrac{-\hbar^2}{2m}\tfrac{1}{\Delta x^2}\begin{bmatrix}\psi_n(x_N)\\0\\\vdots\\0\\\psi_n(x_{\text{-}N})\end{bmatrix} = \tfrac{-\hbar^2}{2m}\tfrac{1}{\Delta x^2}\begin{bmatrix}&&&&0&1\\&&&\iddots&&\\&&&&&\\&0&&&&\\1&&&&&\end{bmatrix}\begin{bmatrix}\psi_n(x_{\text{-}N})\\\vdots\\\psi_n(x_0)\\\vdots\\\psi_n(x_N)\end{bmatrix} \ , \tag{2.D9}$$

and find a slightly modified eigenvalue equation to solve,

$$\left(\tfrac{-\hbar^2}{2m}\tfrac{1}{\Delta x^2}\begin{bmatrix}\text{-}2&1&&&&&1\\1&\text{-}2&1&&&&\\&1&\text{-}2&&&&\\&&&\ddots&&&\\&&&&\text{-}2&1&\\&&&&1&\text{-}2&1\\1&&&&&1&\text{-}2\end{bmatrix} + \begin{bmatrix}V(x_{\text{-}N})&&&&\\&\ddots&&&\\&&V(x_0)&&\\&&&\ddots&\\&&&&V(x_N)\end{bmatrix}\right)\begin{bmatrix}\psi_n(x_{\text{-}N})\\\vdots\\\psi_n(x_0)\\\vdots\\\psi_n(x_N)\end{bmatrix} = E_n\begin{bmatrix}\psi_n(x_{\text{-}N})\\\vdots\\\psi_n(x_0)\\\vdots\\\psi_n(x_N)\end{bmatrix} \ , \tag{2.D10}$$

which is not strictly tri-diagonal, but still sparse.

We highlight the implementation of the FD method in the LC oscillator, which has a bounded potential, by considering the continuous phase representation of the LC oscillator's Hamiltonian in Eq. (2.20). We then solve an eigenvalue equation analogous to Eq. (2.D5) for a chosen grid size and matrix size, corresponding to the total number of points considered in the discretization. This enables the creation of Fig. 2.14a, where we plot the absolute value of the energy difference $|\Delta_0|$ as a

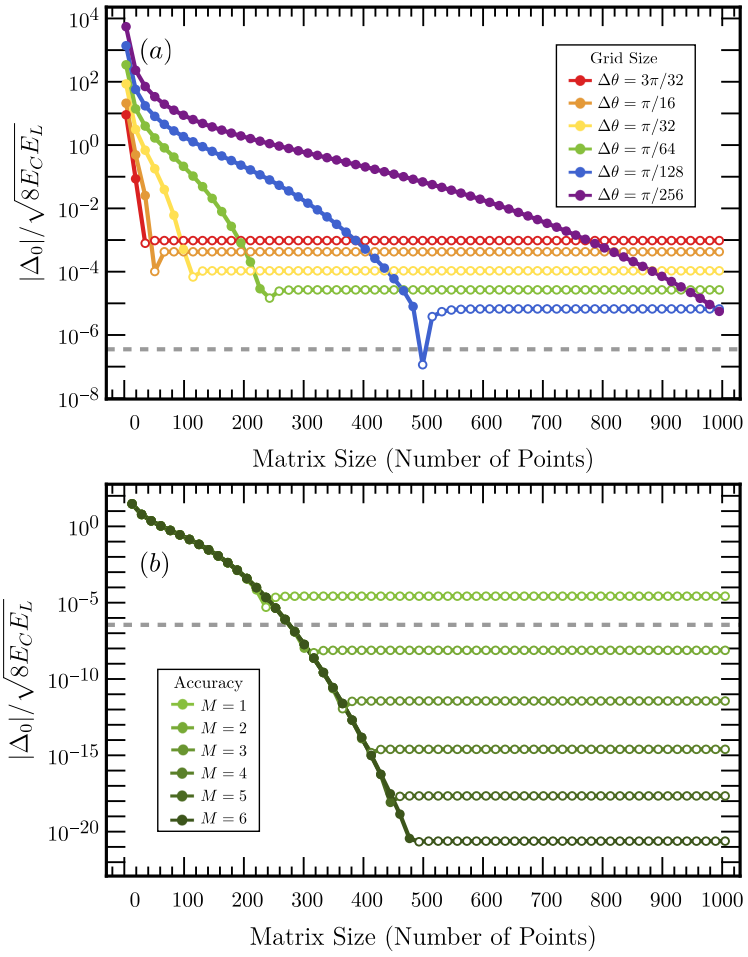


Figure 2.14: The absolute value of the energy difference $|\Delta_0|$ as function of matrix size in the ground state of the LC oscillator. In (a), we utilize the typical, lowest-order FD method to compare various grid sizes $\Delta\theta$, as indicated in the included legend. In (b), we compare higher-order FD approximations in the FD method for a given grid size ($\Delta\theta = \pi/64$), indicated by the accuracy associated with the included number of points M. Both sets of curves are scaled according to the LC frequency. Decoherence accuracy (also scaled according to the LC frequency) is indicated with a horizontal gray dashed line. Open data points indicate where $\Delta_0 < 0$, in order to note and highlight the non-variational nature of the FD approximation and method.

function of matrix size in the ground state of the LC oscillator. Fig. 2.14a includes the curves for six grid sizes $\Delta\theta$ out of a total of seventeen that we consider, ranging from $\Delta\theta = \pi/512$ to $\Delta\theta = 3\pi/4$, which we use to generate the curve present in Fig. 2.4b of the main text. As for each of the numerical analyses we have discussed

so far, up to 150 digits of precision are maintained. Fig. 2.14a demonstrates the overall ineffectiveness of the FD method in approximating the eigenfunctions of the LC oscillator. Decoherence accuracy is only surpassed for a single point, requiring a 499×499 matrix. Despite the increasingly smaller grid sizes, in each case, saturation is above decoherence accuracy and requires matrix sizes that are an order of magnitude larger than those needed by the DVRs we focus on in the main text.

2.D.2 General Derivation of the FD Approximation

We establish the discrete approximation for $\frac{\partial^2\psi_n(x_i)}{\partial x^2}$ (and other derivatives) by using a series expansion of $\psi_n(x)$ about the grid point x_i, which increases in accuracy as we incorporate more of the points surrounding x_i into the approximation.

Consider first the evaluation of $\psi_n(x)$ at $2M$ grid points surrounding x_i, such that we can define the vector $\underline{\psi_n} = \{\psi_n(x_{i-M}), ..., \psi_n(x_i), ..., \psi_n(x_{i+M})\}$. Each of these elements can be expressed using a Taylor series expansion of $\psi_n(x)$ about the grid point x_i,

$$\psi_n(x) = \sum_{m=0}^{\infty} \frac{(x-x_i)^m}{m!} \frac{\partial^m \psi_n(x_i)}{\partial x^m} \quad , \tag{2.D11}$$

evaluated at the element's grid point. By truncating this series at order $2M$, we find a $(2M+1)\times(2M+1)$ matrix equation,

$$\underline{\psi_n} \approx \underline{\underline{F}}\, \underline{\partial\psi_n(x_i)} \quad , \tag{2.D12}$$

where we define the vector $\underline{\partial\psi_n(x_i)} = \{\frac{\partial^0\psi_n(x_i)}{\partial x^0}, \frac{\partial^1\psi_n(x_i)}{\partial x^1}, ..., \frac{\partial^{2M}\psi_n(x_i)}{\partial x^{2M}}\}$ and the matrix $\underline{\underline{F}}$ as that corresponding to the terms of each Taylor series expansion. This matrix has elements $F_{jk} = \frac{[\Delta x(j-M-1)]^{(k-1)}}{(k-1)!}$, explicitly written as

$$\underline{\underline{F}} = \begin{bmatrix} 1 & -M\Delta x & \dots & \dots & \frac{(-M)^{2M}}{2M!}\Delta x^{2M} \\ \vdots & \vdots & \vdots & \vdots & \vdots \\ 1 & 0 & \dots & \dots & 0 \\ \vdots & \vdots & \vdots & \vdots & \vdots \\ 1 & M\Delta x & \dots & \dots & \frac{(M)^{2M}}{2M!}\Delta x^{2M} \end{bmatrix} . \tag{2.D13}$$

Inverting the matrix $\underline{\underline{F}}$ then yields $(2M+1)$-point approximations for the derivatives in $\underline{\partial\psi_n(x_i)}$ in terms of $\psi_n(x)$ evaluated at x_i and the $2M$ surrounding grid points.

For example, taking $M = 1$ leads to the usual centered, three-point FD approximation for the first and second derivatives, incorporating only the point of interest and its nearest neighbors in the grid:

$$\frac{\partial\psi_n(x_i)}{\partial x} \approx \frac{\psi_n(x_{i+1}) - \psi_n(x_{i-1})}{2\Delta x} , \tag{2.D14}$$

$$\frac{\partial^2\psi_n(x_i)}{\partial x^2} \approx \frac{\psi_n(x_{i-1}) - 2\psi_n(x_i) + \psi_n(x_{i+1})}{\Delta x^2} . \tag{2.D15}$$

This is the approximation we utilize in the LC oscillator and in the overview of the FD method in the previous subsection.

Instead of this lowest-order approximation, we could instead incorporate any of the higher-order FD derivative approximations into the FD method in the previous subsection. In that case, we must be mindful of the additional points that appear

in the boundary term, either sending them to zero in the bounded case or mapping them back onto the grid in the periodic case. In the LC oscillator, its bounded potential enables a straightforward investigation of the impact of considering such higher-order approximations. In Fig. 2.14b, we show the absolute value of the energy difference $|\Delta_0|$ as function of matrix size in the ground state of the LC oscillator, for increasingly larger accuracy M, all for the grid size $\Delta\theta = \pi/64$. We do find large improvements in performance upon utilizing these higher-order approximations, however, large matrices are still required. Given the interest in using this approach to provide a straightforward, well-known, and sparse point of comparison for our DVR analysis, higher-order approximations become less desirable. As the accuracy of the FD method increases, sparseness rapidly decreases, while still requiring large matrix sizes for accurate level convergence.

Of note, this symmetric, centered FD approximation has an accuracy of order $2M$, the highest derivative incorporated into each Taylor series expansion. Due to this truncation, the approximations for the derivatives and the FD method outlined in the previous subsection are non-variational, as these truncated terms can add or subtract from the exact solution, depending on the function $\psi_n(x)$. Thus, like each of the DVRs in the main text, using the FD method to model Hamiltonians and evaluate energy eigenvalues does not guarantee energies that are larger than their true value. We see evidence of this feature in Fig. 2.14, as evidenced by the open data points and similarly sharp features in some curves.

Chapter 3: Backaction-Evading Receivers with Magnetomechanical and Electromechanical Sensors[1]

3.1 Introduction

The ability of state-of-the-art quantum sensors to monitor the position of objects with high precision [357, 358] has driven tremendous advances in fundamental physics, particularly in the first detection of gravitational waves [359]. Recently there has been renewed interest in the use of momentum measurement [360, 361] for ultrasensitive force detection, specifically for the purposes of dark matter detection [362]. Approaches for monitoring or measuring particulate dark matter by observing changes in the momentum of test particles, such as those being considered by the Windchime collaboration [363, 364], represent a key motivation to explore and develop impulse metrology for broadband force sensing.

The measurement of weak forces generally requires the transduction of the induced motion of a system into an electrical or optical signal. Thus, estimating such forces is limited by both technical issues, such as thermal noise and instrumental noise, but

[1]This chapter is a reproduction of Ref. [356], published in Phys. Rev. Research.

also by the noise limits arising from the act of measurement itself [357]. This is usually characterized by the standard quantum limit SQL, which places a lower bound on how precisely the conjugate variables of a system can be measured. Recently, efforts to get beyond the SQL with mechanical sensors have yielded substantial successes, in part by reducing or removing the effects of measurement backaction [358, 360, 365–369]. For practical or fundamental applications, including gravitational wave detection [357, 360, 369, 370] and, more recently, the detection of potential dark matter candidates [362, 363, 371], the ability to measure beyond the SQL may also be paired with the need to do so over a wide range of signal frequencies, as in the case of broadband signals from a black hole in-spiral or the case of signals from rapidly moving particulate dark matter.

With these interests in mind, a particular opportunity emerges for going beyond the SQL: quantum non-demolition QND measurement. The simplest example occurs when measuring a free particle, or a harmonic oscillator well above its resonance frequency: measurements of momentum at different times commute, even when accounting for the evolution of the system, and thus backaction can be pushed into the position variable without it disturbing subsequent measurements, thereby circumventing the SQL [357, 372]. In practice, the canonical momentum of a *combined* probe and mechanical system is not a QND variable [361]. Nevertheless, measurement of the mechanical sub-system's momentum, rather than its position, can provide a significant reduction of the measurement backaction.

In this work, we explore options to transduce a force signal to an electrical signal, enabling measurement using a parametric cavity in the microwave or optical regime (Fig. 3.1), a typical paradigm from the optomechanics and electromechanics community [245, 247, 248, 373–375]. In contrast to most work in the field, here we are focused on broadband frequency signals (impulses delivered over very short times), typically well above the mechanical resonance (as indicated in Fig. 3.1e), and thus seek to exploit the QND opportunities such measurements enable. Our detailed examination reveals that the mechanical variable (position or momentum) accessed is dependent on the chosen measurement readout of the electrical system: via charge or flux. This indicates two different approaches for broadband backaction-evading measurement transduced to the microwave domain. Of specific interest in our case is leveraging the intuition of Faraday's law — that velocity creates a voltage — to find a magnetomechanical scheme that utilizes a traditional voice coil, which is used in dynamic microphones and loudspeakers [376, 377]. We find QND measurement of velocity occurs when this coil's voltage is measured rapidly. Surprisingly, we also find that for an electromechanical detector, such as a variable-position capacitor used in a condenser microphone [376–379], we also can get backaction evasion by rapid measurement of the current from the microphone.

We remark that there are other electrical measurement approaches, such as DC current or voltage measurement, that can in principle allow direct velocity measurements to be naturally implemented without the use of a parametric cavity. However,

there are a variety of technical challenges in achieving the SQL with DC current or voltage measurement. We also note that compared to the optical domain, electrical systems overall offer a more energy efficient readout by operating in the microwave regime. As a consequence, far less power is required to interrogate a system's sensors and achieve a SQL-level resolution [380–383].

This chapter is organized as follows. In Section 3.2, we introduce and explore two detector configurations that utilize different electrical transducers: a magnetomechanical detector scheme and an electromechanical detector scheme. The general readout of a transduced electrical signal is considered in Section 3.3, by using a parametric cavity for either electric field or magnetic field sensing. This creates an optomechanical analog that enables the use of standard techniques from optomechanics. In Section 3.4, we assess measurement-added noise and consider an example signal, comparing the four cases given by the combination of the two detector schemes presented in Section 3.2 and the two readout options discussed in Section 3.3. We conclude and discuss the implications of our results in Section 3.5. Additional details of our analysis and background material are included in the appendices that follow.

3.2 Transducers

3.2.1 Magnetomechanical Detector Scheme

We begin by examining the magnetomechanical transducer and detector scheme shown in Figs. 3.1a and 3.1b, respectively, which operate as a consequence of Fara-

day's law [384, 385]. This fundamental principle of electromagnetism describes the voltage generated when a time-varying magnetic flux threads a conducting loop. This allows us to first consider the magnetomechanics of the transducer and establish the transducer constant before deriving the Hamiltonian describing the total detector scheme. A review of Faraday's law and its application in the example we consider can be found in Appendix 3.A.

The magnetomechanical transducer we consider, shown in Fig. 3.1a, consists of two main elements: a magnetic test mass and a pick-up coil. We take the pick-up coil to be superconducting so as to neglect any internal dissipation. The mass is attached to a spring with spring constant k. The test mass is a cylindrical magnetic structure of mass m that contains an annular air gap at a radius R through the length of the cylinder, as shown in the cross-section in Fig. 3.1a. This magnetic mass is arranged such that within the air gap a uniform radial magnetic field $\mathbf{B} = B_r\hat{\mathbf{r}}$ is maintained. Embedded within the air gap is a pick-up coil of radius R and turn number N. This is known as the voice-coil configuration, common to dynamic microphones and loudspeakers [376, 377]. This transducer allows for a simple closed-form expression for the induced voltage, which due to the uniform field, is purely velocity-dependent, as we now show.

We consider an impulse which causes the magnetic mass to move with a velocity $\mathbf{v} = -v\hat{\mathbf{z}}$. For velocities much less than the speed of light, it is both equivalent and convenient to compute the voltage in the rest frame of the magnet, rather than

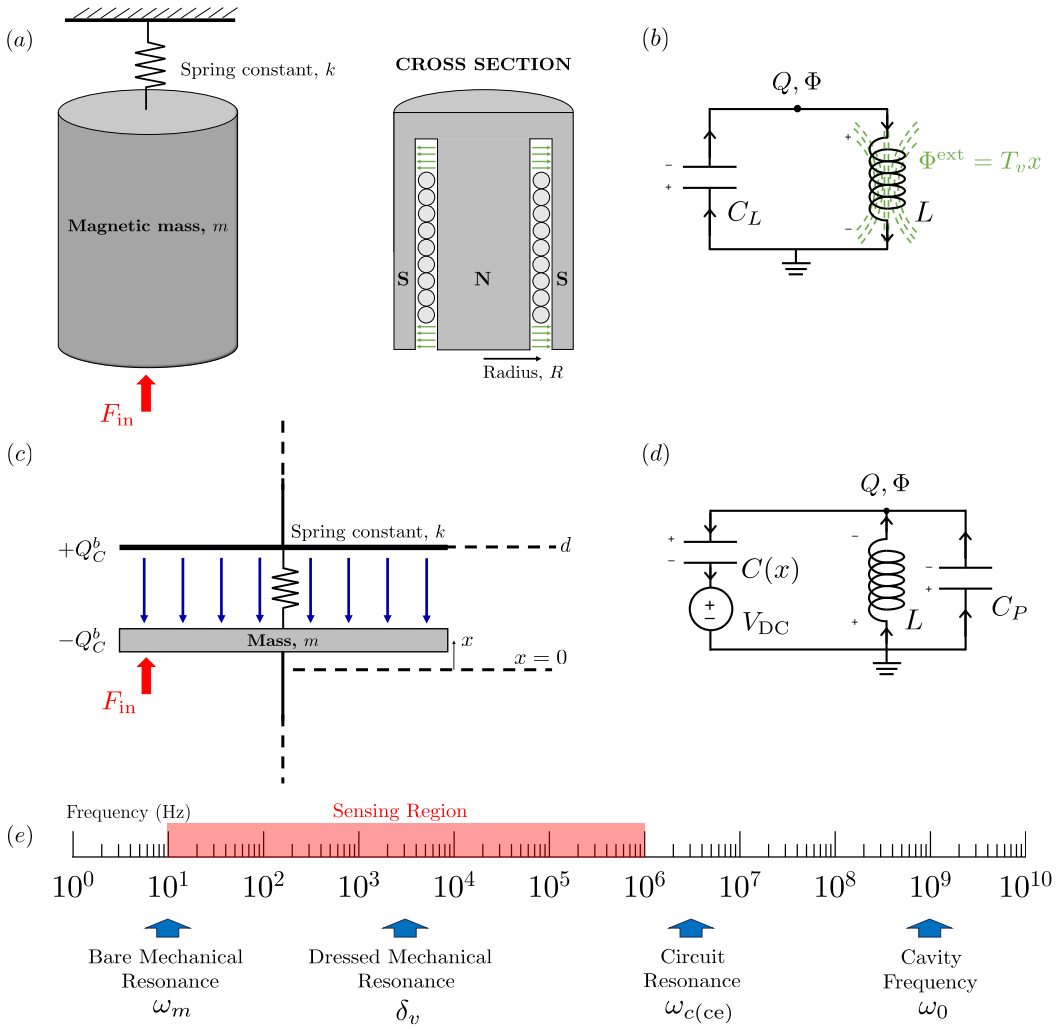


Figure 3.1: (a) Schematic representation of the magnetomechanical transducer, consisting of a structured magnetic mass m suspended by a spring with spring constant k. In the cross section, the radial magnetic field in the air gap experienced by the coil is indicated in green. The lumped-element detector circuit for the magnetomechanical case is shown in (b), where the magnetomechanical element of (a) is modeled as an inductor L threaded by an external flux $\Phi^{\text{ext}} = T_v x$ (shown in green) dependent on the position of the magnetic mass. Sign conventions for analysis are indicated as well as the reference ground node and node variables Q, Φ. (c) Schematic representation of the electromechanical transducer, including the electric field (dark blue) between the charged plates of the mechanical capacitor consisting of a movable plate of mass m and charge $-Q_C^b$ connected to a fixed plate of charge $+Q_C^b$ by a spring with spring constant k. Equilibrium distances are indicated for reference. In (d), the electromechanical element of (c) is depicted in a lumped-element detector circuit via the capacitance $C(x)$. Sign conventions for analysis are indicated as well as the reference ground node and node variables Q, Φ. In (e), we indicate the relative scale of frequencies in the system for our chosen parameters, including that of the to-be-incorporated parametric cavities (see Fig. 3.2). The input force on the test masses is indicated in red, resulting in the broad sensing region indicated by the red shaded region.

the rest frame of the voice coil (as in our detection scheme). In the rest frame of the magnet, the voice coil moves with velocity $\mathbf{v} = v\hat{\mathbf{z}}$, experiencing the magnet's uniform magnetic field $\mathbf{B} = B_r\hat{\mathbf{r}}$ and no electric field ($\mathbf{E} = 0$). We then use Faraday's law to calculate the induced voltage across the voice coil to be

$$\varepsilon = 2\pi NRB_r v = T_v v \ . \tag{3.1}$$

We note that this induced voltage is proportional to velocity via the transducer constant $T_v = 2\pi NRB_r$, which is simply the product of the length of wire used in the voice coil and the magnetic field. Through this constant, the mechanical motion of the magnetic test mass is transduced to a voltage, which may be read out electrically.

The magnetomechanical detector scheme, shown in Fig. 3.1b, is a parallel LC-circuit that models the transducer as an inductor with inductance L threaded by an external flux Φ^{ext}, due to the interaction between the voice coil and magnetic test mass of the transducer, with the capacitance C_L in parallel. We then employ the usual techniques for circuit quantization [325] to come to a Hamiltonian description of the magnetomechanical detector scheme that includes the mechanical motion. This derivation and its associated details can be found in Appendix 3.B. The coupling between the mechanics and the circuit occurs via the presence of the position-dependent external flux $\Phi^{\text{ext}} = T_v x$, where we identify $\dot{\Phi}^{\text{ext}}$ with the induced voltage ε in Eq. (3.1) and x with the position of the test mass.

We first consider a simplified case, treating Φ^{ext} as only a time-dependent external

flux. This leads to two distinct gauge descriptions of the circuit that differ in how they couple to the external flux: one to its time-derivative (a voltage) via a term $Q\dot{\Phi}^{\text{ext}}$ and the other to the external flux via a term $\Phi\Phi^{\text{ext}}/L$, where Q and Φ correspond to the circuit's degrees of freedom. Upon promoting the degrees of freedom to quantum operators $\hat{Q}$ and $\hat{\Phi}$, which satisfy the commutation relation $[\hat{Q}, \hat{\Phi}] = -i\hbar$, we see that these two equivalent descriptions are related by a time-dependent gauge transformation given by the unitary:

$$\hat{U} = e^{-i\hat{Q}\Phi^{\text{ext}}/\hbar} \ . \tag{3.2}$$

We note that recent work [386–389] has focused on the term $Q\dot{\Phi}^{\text{ext}}$ of the first gauge, exploring other equivalent descriptions that eliminate its necessity. In contrast, we focus on both of these gauge choices to highlight and compare how the two gauges couple the circuit to the mechanical degrees of freedom.

Incorporating the mechanical degrees of freedom introduces the canonical momentum p into the Hamiltonian. Importantly, p is not necessarily the mechanical momentum $m\dot{x}$; the gauge choice determines whether or not this is the case. In particular, in the first gauge, $p = m\dot{x} + C_L T_v(\dot{\Phi} + T_v\dot{x})$. In the second gauge, $p = m\dot{x}$. As before, upon promoting the degrees of freedom to operators where $[\hat{Q}, \hat{\Phi}] = -i\hbar$ and $[\hat{p}, \hat{x}] = -i\hbar$, we find these two equivalent descriptions are now related via a more

general unitary (gauge) transformation

$$\hat{U} = e^{-iT_v\hat{Q}\hat{x}/\hbar} \ . \tag{3.3}$$

Altogether, we find the Hamiltonians

$$\hat{H}_1^{(E,v)} = \frac{\hat{p}^2}{2m} + \frac{1}{2}k\hat{x}^2 - \frac{T_v}{m}\hat{Q}\hat{p} + \frac{\hat{Q}^2}{2}\left(\frac{1}{C_L} + \frac{T_v^2}{m}\right) + \frac{\hat{\Phi}^2}{2L} \tag{3.4}$$

and

$$\hat{H}_2^{(E,v)} = \frac{\hat{p}^2}{2m} + \frac{1}{2}k\hat{x}^2 + \frac{\hat{Q}^2}{2C_L} + \frac{(\hat{\Phi} - T_v\hat{x})^2}{2L} \ , \tag{3.5}$$

where $\hat{Q}$ and $\hat{p}$ are the canonical node charge and momentum conjugate to the node flux $\hat{\Phi}$ and position $\hat{x}$, respectively. With only the capacitance C_L connected to the node, $\hat{Q}$ directly corresponds to the charge on this capacitor's plates. The subscripts in Eqs. (3.4) and (3.5) enumerate the two gauge choices in this detector scheme, while the superscripts indicate the readout scheme (explored in Section 3.3) and detector configuration.

Examination of Eqs. (3.4) and (3.5) reveals an interesting feature of this detector configuration: equivalent descriptions contain different couplings to the mechanical degrees of freedom. In the first gauge, the voice coil and its mechanics are coupled through momentum and charge, while in the second gauge, position and flux are coupled. We account for both of these gauge descriptions in the magnetomechanical case as we consider the different readout schemes in Section 3.3. However, these different

gauges are equivalent descriptions and do not yield any differences in performance, as discussed in Section 3.4.

3.2.2 Electromechanical Detector Scheme

In contrast to the magnetomechanical configuration, an electromechanical detection scheme is governed by electrostatic principles. In this case, we begin with the Hamiltonian description and leverage this understanding to establish how mechanical motion translates to an electrical signal. We consider the electromechanical transducer and detector scheme shown in Figs. 3.1c and 3.1d, respectively. The electromechanical transducer consists of two oppositely charged plates with charge $\pm Q_C^b$ connected by a spring with spring constant k. This forms a capacitor with one fixed plate and one movable plate of mass m whose capacitance is a function of the position of the movable plate, namely, $C(x) = \frac{\epsilon_0 A}{d_0 - x}$. We take the area of the plates A to be much larger than their uncharged equilibrium separation d_0. As the massive plate moves due to an impulse, the capacitance changes, thereby altering the charge on the plates and the voltage across them. In the language of fields, as the plate moves, the uniform electric field between the plates changes strength. These are the working principles behind condenser microphones [376–379].

We consider such a mechanically-varying capacitor in the detector circuit shown in Fig. 3.1d. In addition to the capacitance $C(x)$, this circuit consists of a voltage source V_{DC} in series to charge the capacitor, in parallel with a large inductor L and

its parasitic capacitance C_P. We then employ the usual techniques for circuit quantization [325] to come to a Hamiltonian description of the detector circuit. Due to the inverse dependence on position in the capacitance $C(x)$, the coupling between the circuit and mechanical degrees of freedom is nontrivial in form. However, we can linearize the coupling by considering impulses that amount to only small displacements from equilibrium. Details of this derivation can be found in Appendix 3.B.

In total, we come to a linearized Hamiltonian of the form

$$\begin{aligned}\hat{H}^{(E,x)} = \frac{\hat{p}^2}{2m} + \frac{1}{2}k_{\text{eff}}(\hat{x} - x_0)^2 - \frac{T_x}{C_P}(\hat{Q} - Q_0)(\hat{x} - x_0) \\ + \frac{(\hat{Q} - Q_0)^2}{2C_{\text{eff}}} + \frac{\hat{\Phi}^2}{2L} + V(Q_0, x_0) \ ,\end{aligned} \tag{3.6}$$

where $\hat{Q}$ and $\hat{p}$ are the canonical node charge and canonical momentum, which are conjugate to the node flux $\hat{\Phi}$ and position $\hat{x}$, respectively. In this case, $\hat{Q}$ corresponds to the sum of the charge on the plates of the two capacitors connected to the node, while $\hat{p}$ is the mechanical momentum of the movable plate. We define the effective capacitance as $C_{\text{eff}} = C(x_0) + C_P$ and the effective spring constant to be $k_{\text{eff}} = k - \frac{C_{\text{eff}} T_x^2}{C(x_0) C_P}$. The point $\{Q_0, x_0\}$ corresponds to the equilibrium node charge and position when the plates are charged. While the distance d_0 corresponds to the separation of the plates when uncharged, as the plates charge, the plate separation decreases as electrostatic attraction shifts the position of the movable plate closer to its counterpart. This equilibrium point corresponds to the position where the force of electrostatic attraction and the restorative force of the spring exactly balance, and is

a function of the spring constant k, the voltage bias V_{DC}, and the geometry of $C(x)$, namely, the area A and plate separation d_0. We define the energy associated with this equilibrium charge and position configuration as $V(Q_0, x_0)$, whose functional form is given in Appendix 3.B.

Importantly, this linearization procedure enables us to define the transducer constant T_x in this system:

$$T_x = C_P \frac{(Q_0 - C_P V_{\mathrm{DC}})}{\epsilon_0 A} \left(\frac{C(x_0)}{C_{\mathrm{eff}}} \right)^2 \quad , \tag{3.7}$$

which characterizes how changes in the position x of the movable plate result in changes of the charge on the mechanically-varying capacitor's plates $\pm Q_C^b$, i.e.,

$$Q_C^b \approx \frac{C(x_0)}{C_{\mathrm{eff}}} (Q - C_P V_{\mathrm{DC}}) + T_x (x - x_0) \ . \tag{3.8}$$

With this description, it is clear that the charge on the plates of the capacitor is sensitive to the position of the movable plate while the current through the mechanically-varying capacitor is sensitive to the velocity:

$$i_C^b = \dot{Q}_C^b \approx \frac{C(x_0)}{C_{\mathrm{eff}}} \dot{Q} + T_x \dot{x} \ . \tag{3.9}$$

From Eqs. (3.8) and (3.9), we see how the position of the movable plate affects the charge (and by extension, the voltage) on the mechanically-varying capacitor and how

the motion of the plate results in a current. Together with Eq. (3.6), these equations characterize the behavior and response of the electromechanical transducer shown in Fig. 3.1c.

Up until this point, we have focused on the detector configurations and the corresponding electrical signals produced as a result of the motion of a test mass. In the following section, we shift our attention to the measurement of this signal by considering various readout schemes.

3.3 Idealized Receivers

Our interest lies in the measurement-added noise associated with each detector scheme, in which a mechanical signal of interest is transduced to an electrical one. In this section, we consider readout schemes to access the mechanical degrees of freedom via the detector circuits' degrees of freedom. Because measurement-added noise in optomechanical systems is well understood, we imagine reading out the degrees of freedom of the detector circuits using a parametric cavity whose frequency depends on the electric or magnetic fields generated in each detector circuit, as shown in Fig. 3.2. This parametric cavity approach is exemplified by the RF-SET (radio-frequency single-election transistor) [234, 235], a CPB connected to a resonant circuit where variations in the local electric field change the circuit properties and can be detected in reflectometry. Thus, our approach amounts to a measurement of the mechanically generated electrical signal as a voltage via the electric field of a capacitor

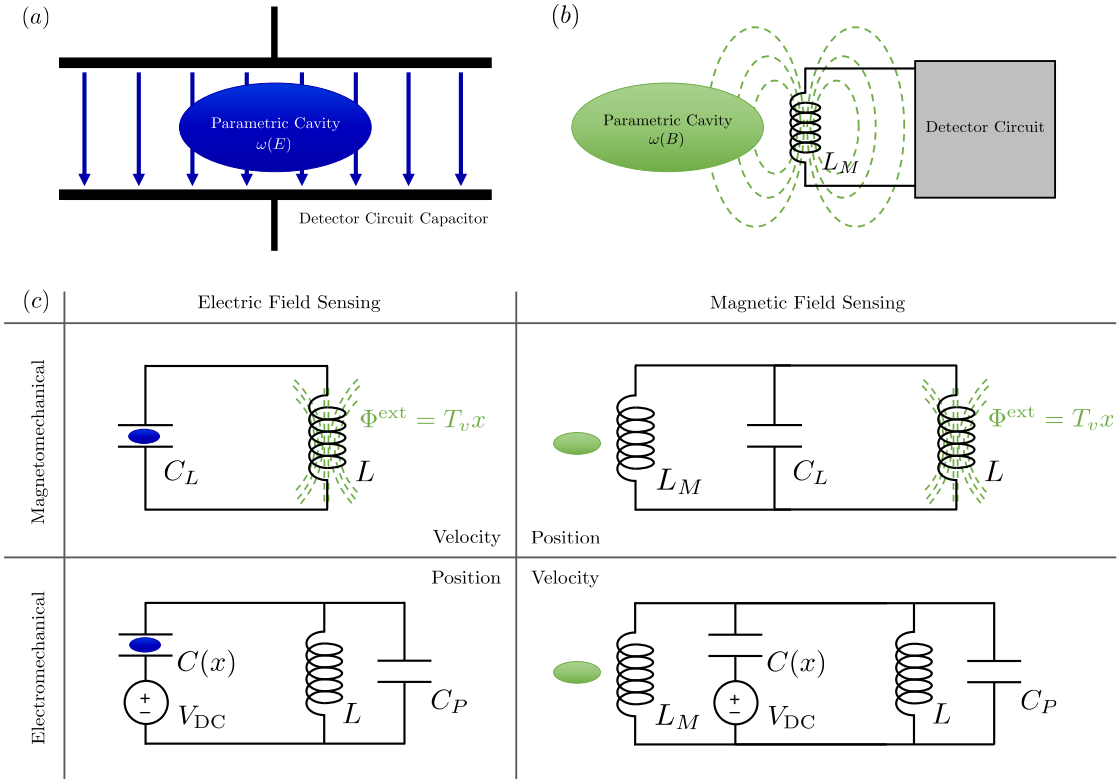


Figure 3.2: (a) Schematic representation of the configuration for voltage measurement via electric field sensing using a parametric cavity (such as a RF-SET) with a resonance frequency that depends on the electric field E (indicated in dark blue) inside a capacitor of each detector circuit. (b) Schematic representation of the configuration for current measurement via magnetic field sensing using a parametric cavity (such as a resonator terminated with a DC SQUID) with a resonance frequency that depends on the magnetic field B (indicated in green) generated by an inductor L_M connected to each detector circuit. We show here that the parametric cavity readout depends on the electric field or the magnetic field and is naturally gauge invariant. In (c), we provide a visual table showing the different combinations of measurement schemes and detector configurations considered in the main text, including small blue and green ovals representing the cavities to indicate which circuit elements interact with the parametric cavities in each case as well as a labeling of which schemes access the mechanical position or velocity.

or a current via the magnetic field of an inductor. As such, we consider voltage and current readout schemes for both the magnetomechanical and electromechanical detection schemes of Section 3.2, including the two gauge descriptions outlined in Section 3.2.1.

We note again that in practice, there are methods for reading out the degrees of freedom of an electrical circuit which may be more direct, such as using a CPB or a Superconducting Quantum Interference Device (SQUID) [240, 249–251, 390–396]. However, this Gedankenexperiment serves as a useful scaffolding for us to develop our understanding of measurement-added noise in electrical systems.

3.3.1 Electric Field Sensing

To access a detector circuit's voltage, we consider measuring the electric field across a capacitor using a parametric cavity sensitive to electric fields, as indicated in Fig. 3.2a and the left column of Fig. 3.2c, and exemplified in a RF-SET [234, 235] or similar device from circuit quantum electrodynamics (circuit QED) [240, 390–393] in the microwave domain. We then imagine the parametric cavity to have a resonance frequency that depends on the electric field of a capacitor coupled to the cavity. For a parallel plate capacitor, we express the electric field in terms of the charge on the plates Q^b and their area A, or in terms of the voltage across the plates v^b and their separation d': $E = \frac{Q^b}{\epsilon_0 A} = \frac{v^b}{d'}$. Here, Q^b and v^b refer to the branch charge and branch voltage of the capacitor, which are unique to each detector configuration. We use the superscript b to denote branch variables throughout the text; this is to distinguish from other variables, such as velocity v, present in our analysis. Branch variables and their role in circuit analysis are discussed in Appendix 3.B.

In the magnetomechanical detector configuration, we take the parallel capacitance

C_L as the capacitor coupled to the parametric cavity. As described in Section 3.2.1, the charge on this capacitor's plates corresponds to the node charge Q. One can also confirm, using Appendix 3.B, that the voltage across the capacitor, $v^b_{C_L} = \dot{\Phi}^b_{C_L} = -Q/C_L$, is gauge-independent.

Therefore, in both gauges we express the electric field in terms of the degrees of freedom of the circuit as

$$E^v = -\frac{Q}{\epsilon_0 A} = -\frac{Q}{C_L d_L} \ , \tag{3.10}$$

where we have taken $C_L = \frac{\epsilon_0 A}{d_L}$ with d_L the separation of the plates.

In the electromechanical case, we take the mechanically varying capacitor $C(x)$ to be the capacitor coupled to the parametric cavity. To express the electric field in this capacitor in terms of the degrees of freedom of the circuit, we use the linearized expression for the charge on the plates of the capacitor $C(x)$, given by Eq. (3.8). This yields an approximate expression for the electric field of the form

$$E^x \approx \frac{C(x_0)}{C_{\text{eff}}} \frac{(Q - C_P V_{\text{DC}})}{\epsilon_0 A} + \frac{T_x}{\epsilon_0 A}(x - x_0) \ , \tag{3.11}$$

and ensures a linear coupling of position to the cavity for small displacements.

We then incorporate the parametric cavity into the Hamiltonian description from Section 3.2, given by Eqs. (3.4), (3.5), and (3.6). The cavity Hamiltonian takes the usual form,

$$\hat{H}^E_{\text{cav}} = \hbar\omega(E)\hat{a}^\dagger\hat{a} \ , \tag{3.12}$$

where $\hat{a}^\dagger, \hat{a}$ are the creation and annihilation operators of the cavity mode that satisfy the commutation relation $[\hat{a}, \hat{a}^\dagger] = 1$ and $\omega(E)$ is the resonance frequency of the cavity that depends on the electric field E. To generate the usual optomechanical coupling, we expand $\omega(E)$ about some equilibrium field value E_0:

$$\omega(E) = \omega(E_0) + \eta_E(E - E_0) + ... \ , \tag{3.13}$$

where we define the cavity's sensitivity to electric fields $\eta_E = \frac{d\omega(E)}{dE}|_{E=E_0}$. We then make the substitutions for E^v and E^x from Eqs. (3.10) and (3.11) and truncate at linear order to define the cavity frequencies

$$\omega(E^v) = \omega_0^{(E,v)} - g_Q^{(E,v)}\hat{Q} \tag{3.14}$$

and

$$\omega(E^x) = \omega_0^{(E,x)} + g_Q^{(E,x)}\hat{Q} + g_x\hat{x} \ , \tag{3.15}$$

where we define the coupling constants $g_Q^{(E,v)} = \frac{\eta_E}{C_L d_L}$, $g_Q^{(E,x)} = \frac{\eta_E C(x_0)}{C_{\text{eff}}\epsilon_0 A}$, and $g_x = \frac{\eta_E T_x}{\epsilon_0 A}$. We have also defined the rescaled cavity frequencies $\omega_0^{(E,v)} = \omega(E_0^v) - \eta_E E_0^v$ and $\omega_0^{(E,x)} = \omega(E_0^x) - \eta_E E_0^x - g_Q^{(E,x)} C_P V_{\text{DC}} - g_x x_0$.

Altogether, we write the cavity Hamiltonian in Eq. (3.12) for the magnetomechanical and electromechanical detector configurations as

$$\hat{H}_{\text{cav}}^{(E,v)} = \hbar\omega_0^{(E,v)}\hat{a}^\dagger\hat{a} - \hbar g_Q^{(E,v)}\hat{Q}\hat{a}^\dagger\hat{a} \tag{3.16}$$

and

$$\hat{H}_{\text{cav}}^{(E,x)} = \hbar\omega_0^{(E,x)}\hat{a}^\dagger\hat{a} + \hbar\left(g_Q^{(E,x)}\hat{Q} + g_x\hat{x}\right)\hat{a}^\dagger\hat{a} \ , \tag{3.17}$$

respectively, where in both cases, we have generated the coupling between the cavity and the circuit, akin to the optomechanical treatment.

3.3.2 Magnetic Field Sensing

For current measurement via magnetic field sensing, we exploit the magnetic fields generated by the current flowing through an inductor and read out the magnetic field using a magnetic-field sensitive parametric cavity, as shown in Fig. 3.2b, and exemplified by a microwave transmission line resonator terminated with a DC SQUID [249–251, 394–396]. In this case, we take the parametric cavity to be characterized by a resonance frequency dependent on the magnetic field of a coupled inductor, adding a parallel inductance L_M to the circuits considered thus far, as shown in the right column of Fig. 3.2c. We choose this inductance such that $L_M < L$ in order for this additional inductor to act as a relatively low-impedance element for current to flow through.

Noting that the motion of the test masses will alter the current through the inductor L_M, thereby changing the magnetic field it generates, we consider the expression of this magnetic field in terms of circuit quantities. For a long solenoid,

$$B = \mu n i_{L_M}^b = \frac{\mu n \Phi_{L_M}^b}{L_M} \ , \tag{3.18}$$

where μ is the magnetic permeability of the material making up the core of the inductor and n is its turn density. The current flowing through the inductor $i^b_{L_M}$ is expressed in terms of its branch flux $\Phi^b_{L_M}$ in the usual way. We note that expressing the branch flux in terms of circuit degrees of freedom is dependent on the detector configuration, and in the magnetomechanical case, also dependent on the gauge choice. This necessitates some care in expressing $\Phi^b_{L_M}$ in terms of the circuit degrees of freedom.

One can perform an analogous treatment of the current measurement circuits in Fig. 3.2c, following the procedures in Appendix 3.B, and confirm that in the magnetomechanical case, the first gauge yields $\Phi^b_{L_M} = -(\Phi + T_v x)$ and the second gauge yields $\Phi^b_{L_M} = -\Phi$, while in the electromechanical case $\Phi^b_{L_M} = \Phi$. The associated Hamiltonians are equivalent to their voltage counterparts except for the addition of an inductive term, $(\Phi^b_{L_M})^2/2L_M$. For the magnetomechanical detector scheme, the Hamiltonians for each gauge are

$$H_1^{(B,v)} = H_1^{(E,v)} + \frac{(\Phi + T_v x)^2}{2L_M} \tag{3.19}$$

and

$$H_2^{(B,v)} = H_2^{(E,v)} + \frac{\Phi^2}{2L_M} \ . \tag{3.20}$$

In the electromechanical case,

$$H^{(B,x)} = H^{(E,x)} + \frac{\Phi^2}{2L_M} \ . \tag{3.21}$$

To include the parametric cavity, we proceed analogously to the voltage measurement case, exchanging $\omega(E)$ for $\omega(B)$ and remaining mindful of the various expressions of the magnetic field appropriate for different detector configurations and gauges. We then find the cavity Hamiltonians appropriate for each gauge in the magnetomechanical detection scheme to be

$$\hat{H}^{(B,v)}_{\text{cav},1} = \hbar\omega_0^B \hat{a}^\dagger \hat{a} - \hbar g^B (\hat{\Phi} + T_v \hat{x}) \hat{a}^\dagger \hat{a} \tag{3.22}$$

and

$$\hat{H}^{(B,v)}_{\text{cav},2} = \hbar\omega_0^B \hat{a}^\dagger \hat{a} - \hbar g^B \hat{\Phi} \hat{a}^\dagger \hat{a} \ , \tag{3.23}$$

where we have defined the coupling constant $g^B = \frac{\eta_B \mu n}{L_M}$, the rescaled resonance frequency $\omega_0^B = \omega(B_0) - \eta_B B_0$, and the cavity's sensitivity to magnetic fields $\eta_B = \frac{d\omega(B)}{dB}|_{B=B_0}$. Similarly, we find the cavity Hamiltonian

$$\hat{H}^{(B,x)}_{\text{cav}} = \hbar\omega_0^B \hat{a}^\dagger \hat{a} + \hbar g^B \hat{\Phi} \hat{a}^\dagger \hat{a} \tag{3.24}$$

for the electromechanical case.

3.3.3 Exploiting the Optomechanics Analogy

To consider the measurement-added noise in these toy models, we incorporate a drive to probe the parametric cavities. We follow the usual formulation for optomechanical systems [397–399] to include the drive and model the noise associated with quantum fluctuations of the vacuum. Details of this analysis can be found in Appendix 3.C. Altogether, we arrive at the Hamiltonians for voltage and current measurement in both the magnetomechanical and electromechanical detection schemes, accounting for the two gauges in the magnetomechanical case.

For voltage measurement in the magnetomechanical case, we obtain the Hamiltonian

$$\hat{H'}_i^{(E,v)} = -\hbar\Delta\hat{a}^\dagger\hat{a} - \hbar G_Q^{(E,v)}\hat{Q}\hat{X} + \hat{H}_i^{(E,v)} + \hat{H}_B + \hat{H}_{\text{int}} \ , \tag{3.25}$$

where $i = 1, 2$ for the two gauge choices. We have defined the detuning $\Delta = \omega_L - \omega_0^{(E,v)}$ with ω_L the drive frequency, while the Hamiltonians $\hat{H}_B$ and $\hat{H}_{\text{int}}$ describe those of the bath and the bath-cavity coupling, respectively, as defined in Appendix 3.C. Relevant constants have been collected to define $G_Q^{(E,v)} = \sqrt{2}\alpha g_Q^{(E,v)}$, with α corresponding to the drive strength. Similarly, in the electromechanical case the Hamiltonian is

$$\hat{H'}^{(E,x)} = -\hbar\Delta\hat{a}^\dagger\hat{a} + \hbar\left(G_Q^{(E,x)}\hat{Q} + G_x\hat{x}\right)\hat{X} + \hat{H}^{(E,x)} + \hat{H}_B + \hat{H}_{\text{int}} \ , \tag{3.26}$$

where $G_Q^{(E,x)} = \sqrt{2}\alpha g_Q^{(E,x)}$ and $G_x = \sqrt{2}\alpha g_x$. In both detector schemes, we take the drive strength α to be real, enabling the cavity-circuit coupling to be written in

terms of the amplitude quadrature of the cavity, $\hat{X} = (\hat{a} + \hat{a}^\dagger)/\sqrt{2}$. We note there is no loss of generality with this choice of α; taking α to be purely imaginary yields a circuit-cavity coupling that goes instead as the phase quadrature of the cavity, $\hat{Y} = \frac{-i}{\sqrt{2}}(\hat{a} - \hat{a}^\dagger)$.

For current measurement in each of the detector configurations and gauges, we find the Hamiltonians

$$\hat{H'}_1^{(B,v)} = -\hbar\Delta\hat{a}^\dagger\hat{a} - \hbar G^B(\hat{\Phi} + T_v\hat{x})\hat{X} + \hat{H}_1^{(B,v)} + \hat{H}_B + \hat{H}_{\text{int}} \ , \tag{3.27}$$

$$\hat{H'}_2^{(B,v)} = -\hbar\Delta\hat{a}^\dagger\hat{a} - \hbar G^B\hat{\Phi}\hat{X} + \hat{H}_2^{(B,v)} + \hat{H}_B + \hat{H}_{\text{int}} \ , \tag{3.28}$$

and

$$\hat{H'}^{(B,x)} = -\hbar\Delta\hat{a}^\dagger\hat{a} + \hbar G^B\hat{\Phi}\hat{X} + \hat{H}^{(B,x)} + \hat{H}_B + \hat{H}_{\text{int}} \ , \tag{3.29}$$

where here we have defined the coupling constant $G^B = \sqrt{2}\alpha g^B$.

In what follows, we use the Hamiltonians in Eqs. (3.25)–(3.29) to find and solve the Heisenberg-Langevin equations, enabling the assessment of noise sensitivities.

3.4 Combinations of Transducers and Receivers

We now turn our attention to measurement and the consequences of different transducer and receiver combinations, given by the Hamiltonians in Eqs. (3.25)–(3.29). For each of these combinations, we solve the Heisenberg equations of motion to find the force noise power spectral density (PSD). We then use the force noise PSD

to compare the sensitivities of the different configurations at different frequencies.

3.4.1 The Equations of Motion

We begin with the usual methods from input-output theory [400], writing down and solving the Heisenberg equation of motion for the bath modes $\hat{b}(\omega)$. This enables the equations of motion for the cavity operators $\hat{a}, \hat{a}^\dagger$ to be expressed in terms of the input modes $\hat{b}_{\rm in}$ and output modes $\hat{b}_{\rm out}$. The details of this procedure can be found in Appendix 3.D.

At this stage, it is preferable to recast the equations of motion for the cavity operators in terms of quantities accessible to measurement, namely, the amplitude and phase quadratures of the cavity, $\hat{X}$ and $\hat{Y}$, respectively, where $[\hat{X}, \hat{Y}] = i$. We also define the quadratures of the input and output bath modes as $\hat{X}_{\rm in} = (\hat{b}_{\rm in}+\hat{b}_{\rm in}^\dagger)/\sqrt{2}$, $\hat{Y}_{\rm in} = -i(\hat{b}_{\rm in} - \hat{b}_{\rm in}^\dagger)/\sqrt{2}$, $\hat{X}_{\rm out} = (\hat{b}_{\rm out} + \hat{b}_{\rm out}^\dagger)/\sqrt{2}$, and $\hat{Y}_{\rm out} = -i(\hat{b}_{\rm out} - \hat{b}_{\rm out}^\dagger)/\sqrt{2}$. Using these definitions and the input-output relation given by Eq. (3.D7) in Appendix 3.D, it can be verified that each of the input and output quadratures satisfy their own input-output relations of the form

$$\hat{X}_{\rm out} = \hat{X}_{\rm in} + \sqrt{\kappa}\hat{X} \tag{3.30}$$

and

$$\hat{Y}_{\rm out} = \hat{Y}_{\rm in} + \sqrt{\kappa}\hat{Y} \ , \tag{3.31}$$

where κ corresponds to the cavity decay rate.

By combining the equations of motion for $\hat{a}$ and $\hat{a}^\dagger$ we find the equations of motion for each cavity quadrature. These equations, in combination with the Heisenberg equations of motion for the remaining system operators ($\hat{x}$, $\hat{p}$, $\hat{\Phi}$, and $\hat{Q}$), specify the complete system of equations describing each case. Below, we explicitly show the equations of motion for each detector configuration, measurement scheme, and gauge. We also include an input force $\hat{F}_{\text{in}}$ in the equation for the canonical momentum to account for the impulse we wish to detect. We note that while the impulse acts upon the mechanical subsystem, its appearance in the equation for the canonical momentum is appropriate, as in each instance we consider, the canonical momentum is either strictly the mechanical momentum or a linear combination that includes the mechanical momentum.

We first consider the equations of motion for voltage measurement via electric field sensing. In the magnetomechanical case, the first gauge yields the equations

$$\begin{aligned}
\frac{d\hat{x}}{dt} &= \frac{\hat{p}}{m} - \frac{T_v}{m}\hat{Q} \ , \\
\frac{d\hat{p}}{dt} &= -k\hat{x} + \hat{F}_{\text{in}} \ , \\
\frac{d\hat{\Phi}}{dt} &= -\hbar G_Q^{(E,v)}\hat{X} - \frac{T_v}{m}\hat{p} + \left(\frac{1}{C_L} + \frac{T_v^2}{m}\right)\hat{Q} \ , \\
\frac{d\hat{Q}}{dt} &= -\frac{\hat{\Phi}}{L} \ , \\
\frac{d\hat{X}}{dt} &= -\Delta\hat{Y} - \frac{\kappa}{2}\hat{X} - \sqrt{\kappa}\hat{X}_{\text{in}} \ , \\
\frac{d\hat{Y}}{dt} &= \Delta\hat{X} + G_Q^{(E,v)}\hat{Q} - \frac{\kappa}{2}\hat{Y} - \sqrt{\kappa}\hat{Y}_{\text{in}} \ .
\end{aligned} \tag{3.32}$$

It is convenient to rewrite these equations in a more compact form. Defining the matrix

$$\underline{\underline{M_1}}^{(E,v)} = \begin{bmatrix} 0 & \frac{1}{m} & 0 & -\frac{T_v}{m} & 0 & 0 \\ -k & 0 & 0 & 0 & 0 & 0 \\ 0 & -\frac{T_v}{m} & 0 & \frac{1}{C'_L} & -\hbar G_Q^{(E,v)} & 0 \\ 0 & 0 & -\frac{1}{L} & 0 & 0 & 0 \\ 0 & 0 & 0 & 0 & -\frac{\kappa}{2} & -\Delta \\ 0 & 0 & 0 & G_Q^{(E,v)} & \Delta & -\frac{\kappa}{2} \end{bmatrix} , \tag{3.33}$$

we can rewrite Eq. (3.32) as

$$\frac{d}{dt}\underline{\hat{Z}} = \underline{\underline{M_1}}^{(E,v)}\underline{\hat{Z}} + \underline{\hat{Z}_{\text{in}}} \ , \tag{3.34}$$

where we have defined the vector of operators $\underline{\hat{Z}} = \{\hat{x}, \hat{p}, \hat{\Phi}, \hat{Q}, \hat{X}, \hat{Y}\}$ and the vector of inputs $\underline{\hat{Z}_{\text{in}}} = \{0, \hat{F}_{\text{in}}, 0, 0, -\sqrt{\kappa}\hat{X}_{\text{in}}, -\sqrt{\kappa}\hat{Y}_{\text{in}}\}$. We also define the capacitance C'_L for convenience to be $\frac{1}{C'_L} = \frac{1}{C_L} + \frac{T_v^2}{m}$. The equations of motion for the second gauge can be similarly represented via Eq. (3.34) with the matrix $\underline{\underline{M_2}}^{(E,v)}$, defined as

$$\underline{\underline{M_2}}^{(E,v)} = \begin{bmatrix} 0 & \frac{1}{m} & 0 & 0 & 0 & 0 \\ -k' & 0 & \frac{T_v}{L} & 0 & 0 & 0 \\ 0 & 0 & 0 & \frac{1}{C_L} & -\hbar G_Q^{(E,v)} & 0 \\ \frac{T_v}{L} & 0 & -\frac{1}{L} & 0 & 0 & 0 \\ 0 & 0 & 0 & 0 & -\frac{\kappa}{2} & -\Delta \\ 0 & 0 & 0 & G_Q^{(E,v)} & \Delta & -\frac{\kappa}{2} \end{bmatrix} , \tag{3.35}$$

where we have defined for convenience $k' = k + \frac{T_v^2}{L}$. Likewise, the electromechanical

case is described by the matrix

$$\underline{\underline{M}}^{(E,x)} = \begin{bmatrix} 0 & \frac{1}{m} & 0 & 0 & 0 & 0 \\ -k_{\text{eff}} & 0 & 0 & \frac{T_x}{C_P} & -\hbar G_x & 0 \\ -\frac{T_x}{C_P} & 0 & 0 & \frac{1}{C_{\text{eff}}} & \hbar G_Q^{(E,x)} & 0 \\ 0 & 0 & -\frac{1}{L} & 0 & 0 & 0 \\ 0 & 0 & 0 & 0 & -\frac{\kappa}{2} & -\Delta \\ -G_x & 0 & 0 & -G_Q^{(E,x)} & \Delta & -\frac{\kappa}{2} \end{bmatrix} . \tag{3.36}$$

We can analogously describe the equations of motion for the current measurement scheme. In the magnetomechanical case, we find for the two gauges

$$\underline{\underline{M_1}}^{(B,v)} = \begin{bmatrix} 0 & \frac{1}{m} & 0 & -\frac{T_v}{m} & 0 & 0 \\ -k'_M & 0 & -\frac{T_v}{L_M} & 0 & \hbar G^B T_v & 0 \\ 0 & -\frac{T_v}{m} & 0 & \frac{1}{C'_L} & 0 & 0 \\ -\frac{T_v}{L_M} & 0 & -\frac{1}{L'} & 0 & \hbar G^B & 0 \\ 0 & 0 & 0 & 0 & -\frac{\kappa}{2} & -\Delta \\ G^B T_v & 0 & G^B & 0 & \Delta & -\frac{\kappa}{2} \end{bmatrix} , \tag{3.37}$$

and

$$\underline{\underline{M_2}}^{(B,v)} = \begin{bmatrix} 0 & \frac{1}{m} & 0 & 0 & 0 & 0 \\ -k' & 0 & \frac{T_v}{L} & 0 & 0 & 0 \\ 0 & 0 & 0 & \frac{1}{C_L} & 0 & 0 \\ \frac{T_v}{L} & 0 & -\frac{1}{L'} & 0 & \hbar G^B & 0 \\ 0 & 0 & 0 & 0 & -\frac{\kappa}{2} & -\Delta \\ 0 & 0 & G^B & 0 & \Delta & -\frac{\kappa}{2} \end{bmatrix} , \tag{3.38}$$

where we have defined for convenience the quantities $k'_M = k + \frac{T_v^2}{L_M}$ and $\frac{1}{L'} = \frac{1}{L} + \frac{1}{L_M}$.

For the electromechanical detector configuration, we have

$$\underline{\underline{M}}^{(B,x)} = \begin{bmatrix} 0 & \frac{1}{m} & 0 & 0 & 0 & 0 \\ -k_{\text{eff}} & 0 & 0 & \frac{T_x}{C_P} & 0 & 0 \\ -\frac{T_x}{C_P} & 0 & 0 & \frac{1}{C_{\text{eff}}} & 0 & 0 \\ 0 & 0 & -\frac{1}{L'} & 0 & -\hbar G^B & 0 \\ 0 & 0 & 0 & 0 & -\frac{\kappa}{2} & -\Delta \\ 0 & 0 & -G^B & 0 & \Delta & -\frac{\kappa}{2} \end{bmatrix} . \tag{3.39}$$

3.4.2 Assembling the Noise PSD

These linear equations are straightforward to solve in the frequency domain. Defining the Fourier transform of our relevant operators as follows:

$$\begin{aligned} \hat{f}(\nu) &= \frac{1}{\sqrt{2\pi}} \int_{-\infty}^{\infty} \hat{f}(t) e^{-i\nu t} dt \\ \hat{f}(t) &= \frac{1}{\sqrt{2\pi}} \int_{-\infty}^{\infty} \hat{f}(\nu) e^{i\nu t} d\nu \end{aligned} , \tag{3.40}$$

where the frequency dependence of $\hat{f}(\nu)$ is explicit, the time derivatives in the equation of motion given by Eq. (3.34) for each matrix $\underline{\underline{M}}$ simply transform as $\frac{d\hat{f}(t)}{dt} \rightarrow i\nu\hat{f}(\nu)$.

Solving the systems of equations given by Eq. (3.34) in the frequency domain, for zero detuning ($\Delta = 0$), yields a general solution of the form

$$\underline{\hat{Z}}(\nu) = \left(i\nu \underline{\underline{\mathbb{1}}} - \underline{\underline{M}}\right)^{-1} \underline{\hat{Z}}_{\text{in}}(\nu) \ , \tag{3.41}$$

where we focus on the solutions for the phase quadrature of the cavity $\hat{Y}(\nu)$, given by the final row of Eq. (3.41). The circuit degrees of freedom are coupled to $\hat{X}$, hence, the information about the circuit, the mechanics, and ultimately $\hat{F}_{\rm in}$ are found in the equation of motion and solution of its conjugate, $\hat{Y}$ (as opposed to $\hat{X}$, the other quantity accessible to measurement).

In the magnetomechanical system, the solutions found in each gauge are identical, sans the solutions for $\hat{p}$ and $\hat{\Phi}$. This is unsurprising, since these quantities are those affected by the unitary [Eq. (3.3)] that connects the gauges. This is true in both the voltage and current measurement cases. For both the magnetomechanical and electromechanical detector schemes, the solutions for $\hat{Y}(\nu)$ may then be used in the input-output relation, Eq. (3.31), to find the output quadrature $\hat{Y}_{\rm out}(\nu)$. These solutions are explicitly shown in Appendix 3.E.

We then use the solution for the output quadrature $\hat{Y}_{\rm out}(\nu)$ to assess the noise sensitivity. We define the force estimator as the output phase quadrature in force units (i.e., we divide $\hat{Y}_{\rm out}$ by the coefficient of $\hat{F}_{\rm in}$):

$$\hat{F}_E(\nu) = \hat{F}_{\rm in} + \beta(\nu)\hat{X}_{\rm in} + \gamma(\nu)\hat{Y}_{\rm in} \ , \tag{3.42}$$

where β represents the coefficient for the measurement backaction noise term and γ corresponds to the shot noise term in this measurement, as we are measuring the $\hat{Y}$ quadrature.

The frequency dependence of the noise sensitivity is given by the force noise PSD:

$$S_{\mathrm{FF}}(\nu) = \int_{-\infty}^{\infty} \left\langle \hat{F}_E^\dagger(\nu)\hat{F}_E(\nu') \middle| \hat{F}_E^\dagger(\nu)\hat{F}_E(\nu') \right\rangle d\nu' \ . \tag{3.43}$$

To evaluate the noise PSD in Eq. (3.43), we note the following regarding the resulting noise correlation functions:

$$\begin{aligned} \left\langle \hat{X}_{\mathrm{in}}^\dagger(t)\hat{X}_{\mathrm{in}}(t') \middle| \hat{X}_{\mathrm{in}}^\dagger(t)\hat{X}_{\mathrm{in}}(t') \right\rangle &= \left\langle \hat{Y}_{\mathrm{in}}^\dagger(t)\hat{Y}_{\mathrm{in}}(t') \middle| \hat{Y}_{\mathrm{in}}^\dagger(t)\hat{Y}_{\mathrm{in}}(t') \right\rangle = \frac{1}{2}\delta(t-t') \\ \left\langle \hat{F}_{\mathrm{in}}^\dagger(t)\hat{F}_{\mathrm{in}}(t') \middle| \hat{F}_{\mathrm{in}}^\dagger(t)\hat{F}_{\mathrm{in}}(t') \right\rangle &= N_{\mathrm{BM}}\delta(t-t') \end{aligned} \ , \tag{3.44}$$

where we have taken the vacuum fluctuations of the cavity to be white noise and the input signal noise from the mechanics to be thermal noise. We consider here an Ohmic model for thermal noise corresponding to Brownian motion[2] with noise amplitude N_{BM}. We assume there is no correlation between the signal noise and vacuum fluctuations, and no correlation between the vacuum fluctuations. Taking all of the above into consideration, Eq. (3.43) can be rewritten as

$$S_{\mathrm{FF}}(\nu) = \frac{|\beta(\nu)|^2}{2} + \frac{|\gamma(\nu)|^2}{2} + N_{\mathrm{BM}} \ . \tag{3.45}$$

[2]In this analysis, we are considering only an idealized mass, i.e., one without any damping beyond that provided by the electromagnetic system it is coupled to. If we were to analyze frequencies closer to, or below, the mechanical resonance, mechanical damping would be a key element of the response of the total system. However, it is a straightforward exercise to include mechanical damping in the linear response theory provided in Section 3.4. More important than the mechanical damping per se is the role the bath that leads to the damping plays: we expect, via the fluctuation-dissipation theorem, that this bath will lead to Brownian-motion-like noise on the mechanics, which may overwhelm any impulse signal we look for. Our example in Section 3.4.5 elucidates a specific case where this noise may be the limit, once quantum measurement-added noise is sufficiently reduced.

In what follows, we list the noise PSD expressions for each combination of detector configuration and measurement scheme (recalling that the solutions across gauges are identical) in terms of relevant susceptibilities. In each case, we optimize the coupling strength (and as a result, the drive strength) to balance the backaction and shot noise terms at some fixed frequency, thereby identifying the SQL at this frequency for each case. Then, we compare the performances of different detector and measurement combinations and discuss the features of these noise PSD expressions.

It is convenient to first define the frequencies

$$\begin{gathered}\omega_m^2 = \frac{k}{m},\ \omega_{c(\mathrm{ce})}^2 = \frac{1}{LC_{L(\mathrm{eff})}},\ \omega_{l(\mathrm{le})}^2 = \frac{1}{L_M C_{L(\mathrm{eff})}} \\ \delta_v^2 = \frac{T_v^2}{mL},\ \delta_x^2 = \frac{C_{\mathrm{eff}} T_x^2}{mC_P^2}\ ,\end{gathered} \tag{3.46}$$

as well as the cavity and bare mechanical susceptibilities χ_κ and χ_m, respectively:

$$\chi_\kappa = \frac{-\sqrt{\kappa}}{\frac{\kappa}{2} + i\nu},\ \chi_m = \frac{-1}{\nu^2 - \omega_m^2}\ . \tag{3.47}$$

For the magnetomechanical detector scheme, voltage measurement via electric field sensing yields the noise PSD

$$S_{\mathrm{FF}}^{(E,v)} = \frac{\hbar^2 {G_Q^{(E,v)}}^2 m |\chi_\kappa|^2}{2L\delta_v^2 \chi_m^2 \nu^2} + \frac{mL}{2{G_Q^{(E,v)}}^2 \delta_v^2 |\chi_\kappa|^2 \chi_m^2 {\chi_{\mathrm{lc}}^{(E,v)}}^2 \nu^2} + N_{\mathrm{BM}}\ , \tag{3.48}$$

where we define the circuit susceptibility as

$$\chi_{\rm lc}^{(E,v)} = \frac{-1}{\nu^2 - \omega_c^2 - \delta_v^2(1 - \chi_m \omega_m^2)} \ . \tag{3.49}$$

Upon balancing the backaction and shot noise terms for some fixed frequency, we find the optimized coupling strength

$$G_Q^{(E,v)^2} = \frac{L}{\hbar |\chi_\kappa|^2 |\chi_{\rm lc}^{(E,v)}|} \ . \tag{3.50}$$

For current measurement via magnetic field sensing, we find the noise PSD

$$S_{\rm FF}^{(B,v)} = \frac{\hbar^2 G^{B^2} m L |\chi_\kappa|^2}{2\delta_v^2 {\chi'_m}^2} + \frac{m}{2G^{B^2} L \delta_v^2 |\chi_\kappa|^2 {\chi'_m}^2 {\chi_{\rm lc}^{(B,v)}}^2 \omega_c^4} + N_{\rm BM} \ , \tag{3.51}$$

where we have instead defined the dressed mechanical susceptibility

$$\chi'_m = \frac{-1}{\nu^2 - \omega_m^2 - \delta_v^2} \tag{3.52}$$

as well as the circuit susceptibility in this case as

$$\chi_{\rm lc}^{(B,v)} = \frac{-1}{\nu^2 - \omega_c^2 - \omega_l^2 + \delta_v^2 \omega_c^2 \chi'_m} \ . \tag{3.53}$$

In this instance, we find the optimized coupling strength to be

$$G^{B\,2} = \frac{1}{\hbar|\chi_\kappa|^2|\chi_{\rm lc}^{(B,v)}|L\omega_c^2} \ . \tag{3.54}$$

We note that in the magnetomechanical detector scheme, the various mechanical and circuit susceptibilities are gauge-dependent — just as the canonical momenta are different across the two gauges, so are the associated response functions. The physical meaning of these susceptibilities therefore depends on the gauge choice. We emphasize that the noise PSDs are gauge-independent, however, expressing the noise PSDs in terms of these gauge-dependent functions yields different functional forms of the noise PSDs. We direct the reader to Appendix 3.F for the explicit forms of the noise PSDs written in terms of the relevant frequencies defined in Eq. (3.46).

For the electromechanical detector scheme, voltage measurement via electric field sensing yields the noise PSD

$$S_{\rm FF}^{(E,x)} \approx \frac{\hbar^2 {G_Q^{(E,x)}}^2 m|\chi_\kappa|^2}{2\delta_x^2\chi_m^2 L\omega_{\rm ce}^2} + \frac{mL}{2{G_Q^{(E,x)}}^2\delta_x^2|\chi_\kappa|^2\chi_m^2{\chi_{\rm lc}^{(E,x)}}^2\omega_{\rm ce}^2} + N_{\rm BM} \ , \tag{3.55}$$

where in this case we define the circuit susceptibility

$$\chi_{\rm lc}^{(E,x)} = \frac{-1}{\nu^2 - \omega_{\rm ce}^2 + \delta_x^2\omega_{\rm ce}^2\chi_m} \ . \tag{3.56}$$

In Eq. (3.55), we have taken $G_x \to 0$, as for our chosen parameters, $G_Q^{(E,x)} \gg G_x$. The

exact noise PSD, including the contributions from G_x, can be found in Appendix 3.F. We note that this contribution is included in the numerics we present in Sections 3.4.3 and 3.4.4, which confirms the negligible contribution from G_x. Therefore, we optimize the coupling to balance the backaction and shot noise terms with respect to $G_Q^{(E,x)}$ only, using Eq. (3.55). We find this coupling strength to be

$$G_Q^{(E,x)^2} = \frac{L}{\hbar|\chi_\kappa|^2|\chi_{\rm lc}^{(E,x)}|} \ . \tag{3.57}$$

For current measurement via magnetic field sensing we find the expression

$$S_{\rm FF}^{(B,x)} = \frac{\hbar^2 G^{B^2} m L \omega_{\rm ce}^2 |\chi_\kappa|^2 \left(1-\delta_x^2\chi_m\right)^2}{2\delta_x^2\chi_m^2\nu^2} + \frac{m}{2G^{B^2}L\delta_x^2|\chi_\kappa|^2\chi_m^2\chi_{\rm lc}^{(B,x)^2}\omega_{\rm ce}^2\nu^2} + N_{\rm BM} \ , \tag{3.58}$$

where we define the circuit susceptibility

$$\chi_{\rm lc}^{(B,x)} = \frac{-1}{\nu^2 - \omega_{\rm ce}^2 - \omega_{\rm le}^2 + \delta_x^2(\omega_{\rm ce}^2+\omega_{\rm le}^2)\chi_m} \ . \tag{3.59}$$

To balance backaction noise and shot noise, we find the optimized coupling

$$G^{B^2} = \frac{1}{\hbar|\chi_\kappa|^2|\chi_{\rm lc}^{(B,x)}||1-\delta_x^2\chi_m|L\omega_{\rm ce}^2} \ . \tag{3.60}$$

In what follows, we examine the noise PSDs given by Eqs. (3.48), (3.51), (3.55), and (3.58), comparing their behavior to the standard optomechanical case and exam-

ining their specific functional features.

3.4.3 Comparison to Optomechanical Systems

Our goal is to look for signals which have broad characteristics in frequency space (i.e., an impulse in the time domain), requiring an integration of the noise over a frequency band to be able to predict a signal-to-noise ratio (SNR). Thus, our interest is in the broadband sensitivity of the noise PSDs. Additionally, if we can directly access a QND-like variable, such as the velocity of the mechanical system, we expect the measurement backaction to decrease over a broad frequency spectrum. Therefore, we restrict our discussion to the broadband frequency response of the noise PSDs in an effort to understand the best readout strategies for certain kinds of transducers subject to broadband signals.

In Fig. 3.3, we show the total measurement-added noise for each detector circuit and measurement readout combination, given by Eqs. (3.48), (3.51), (3.55), and (3.58). We note that we have taken the thermal noise N_{BM} affecting the mechanical oscillator to be negligible. In addition, we have fixed the coupling coefficients to their optimized SQL values, given by Eqs. (3.50), (3.54), (3.57), and (3.60), for a target frequency of 1 MHz. Taken together, the total noise and its associated behavior are particularly relevant in the context of the standard optomechanical position-sensing problem as well as previous work on velocity sensing in optomechanical systems [362, 401]. For convenience of comparison, we include Fig. 3.4, which shows the expected

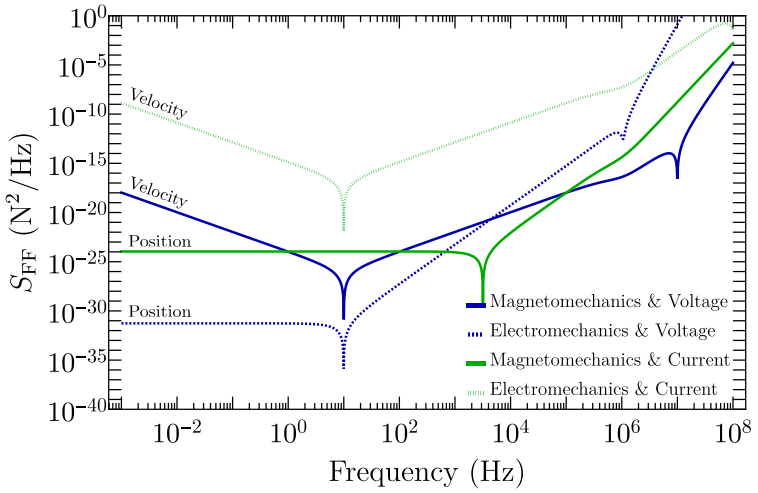


Figure 3.3: Total measurement-added noise for each detector configuration and readout choice. The dark blue curves correspond to voltage readout via electric field sensing for the magnetomechanical and electromechanical configurations. Here, the magnetomechanical system displays a backaction-evading characteristic absent in the electromechanical case. The green curves correspond to current readout via magnetic field sensing for each detector configuration. However, in this case the electromechanical system displays a backaction-evading feature rather than the magnetomechanical case. The parameters used for generating these plots are as follows: detector mass $m = 1$ g, mechanical resonance frequency $\omega_m/2\pi = 10$ Hz, cavity decay rate $\kappa/2\pi = 1$ MHz, inductance $L = 10$ μH, mutual inductance $L_M = 1$ nH, circuit resonance frequencies $\omega_c/2\pi = 10$ MHz and $\omega_{\mathrm{ce}}/2\pi \approx 1$ MHz, capacitance $C_P = 25$ fF, with transducer constants $T_v = 2$ T $\cdot$ m and $T_x = \text{-}10^{-10}$ C/m. The coupling coefficients are fixed to their SQL values for a target frequency of 1 MHz, as given by Eqs. (3.50), (3.54), (3.57), and (3.60), with $G_x \approx T_x G_Q^{(E,x)}$.

noise PSD for both position- and velocity-sensing scenarios in an optomechanical analog, specifically for use with a broadband signal. Details associated with this plot can be found in Appendix 3.G.

Upon comparison, it is immediately clear that current readout of the magnetomechanical detector scheme and voltage readout of the electromechanical detector scheme share similarities with the noise PSD for standard optomechanical position sensing, specifically the "flat at low frequency" feature. Furthermore, voltage readout

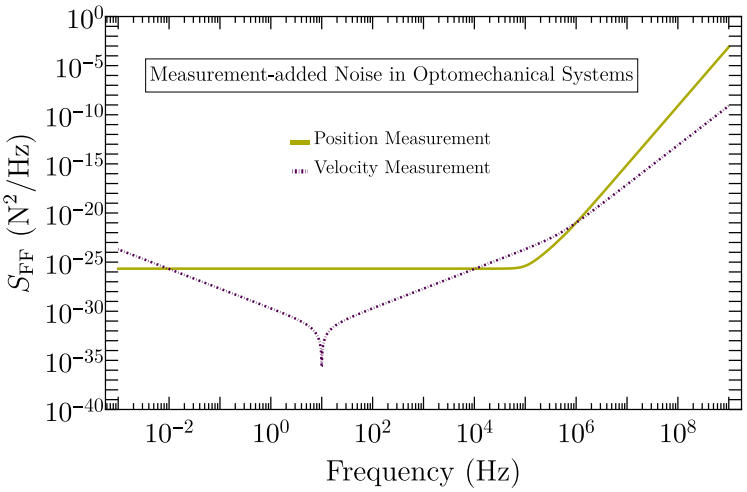


Figure 3.4: The noise PSD representing total measurement-added noise in an optomechanical system is plotted for both position- and velocity-sensing protocols while operating at the optimal power for position sensing with a 0.1 MHz target frequency [using Eq. (3.G6)]. This is derivative of work from Refs. [362, 401]. The noise for velocity sensing is lower than position sensing across a broad frequency range, with the functional dependence ν^{-2} below resonance and ν^2 above. The optomechanical coupling strengths in these techniques are related by the velocity coupling coefficient $G' \to G/(m\kappa)$, with position coupling coefficient $G/2\pi \approx 10^{23}$ Hz/m, mechanical frequency $\omega_m/2\pi = 10$ Hz, cavity decay rate $\kappa/2\pi = 1$ MHz, detector mass $m = 1$ g, and mechanical damping rate $\mu/2\pi = 0.1$ mHz.

of the magnetomechanical detector scheme and current readout of the electromechanical detector scheme bear striking similarity to the noise PSD for velocity sensing. Both show a decrease in total noise near the mechanical resonance, and share the same frequency dependence in this region, namely, going as ν^{-2} below resonance and ν^2 above resonance.

We understand these similarities by using the fundamental relations describing how the mechanics are transduced to an electrical signal in each detector configuration, outlined in Section 3.2. In the magnetomechanical case, the flux (comparable to current) is proportional to the position x of the mechanical oscillator, while in the

electromechanical case, charge (comparable to voltage) is proportional to position. Thus, by coupling the parametric cavity to a specific circuit degree of freedom, both of these readout schemes access the position of the mechanical oscillator. Alternatively, it is voltage in the magnetomechanical case and current in the electromechanical case which are directly proportional to velocity. Therefore, electromechanical current readout and magnetomechanical voltage readout directly access the velocity of the oscillator, providing a way to reduce the measurement-added backaction noise over certain bandwidths of frequencies.

These results indicate that if we want to attain a QND-like measurement using an electrical circuit setup in the microwave domain, we need to combine a magnetomechanical or electromechanical detection scheme with the appropriate measurement readout. Namely, voltage readout for a magnetomechanical detector and current readout for an electromechanical detector may yield a QND-like measurement with reduced backaction over a broad frequency range. We note that upon comparing the relative scale of the noise between these cases, voltage readout of the magnetomechanical detector scheme yields a considerably lower noise floor than current readout of the electromechanical detector scheme. However, the total noise and its associated resonances (discussed in Section 3.4.4) are dependent on the system parameters and relevant frequencies.

3.4.4 Details of the Noise Curves

Upon closer inspection of Eqs. (3.48), (3.51), (3.55), and (3.58), we find that each of the noise PSDs has a term inversely proportional to the coupling coefficient squared, i.e., $G_Q^{(E,x)^2}$ and $G_Q^{(E,v)^2}$ for the voltage measurement scenarios or G^{B^2} for the current measurement scenarios. These terms originate from the $\left\langle \hat{Y}_{\text{in}}^2 \middle| \hat{Y}_{\text{in}}^2 \right\rangle$ contribution to the noise PSD, corresponding to the factor $\frac{|\gamma|^2}{2}$ in Eq. (3.45). As we are interested in monitoring the $\hat{Y}_{\text{out}}$ quadrature, we understand this contribution as shot noise — it constitutes the statistical counting error at the output port. In addition, each noise PSD has another term which is directly proportional to the coupling coefficient squared. These terms arise from the $\left\langle \hat{X}_{\text{in}}^2 \middle| \hat{X}_{\text{in}}^2 \right\rangle$ contribution to the noise PSD, corresponding to the factor $\frac{|\beta|^2}{2}$ in Eq. (3.45). These terms form the basis of backaction noise on the measurement of the output phase quadrature. Fig. 3.5 shows curves representing these shot noise and backaction noise contributions to the total noise PSD, for each of the different detector and readout combinations. Also included in Fig. 3.5 is a comparison of two different coupling strengths for each noise contribution, where we see that the shot noise decreases with an increase in coupling strength (i.e., a stronger drive) while the backaction noise increases.

We also note the presence of various resonances. For voltage readout of the magnetomechanical system, shown in Fig. 3.5a and described by Eq. (3.48), the backaction noise term exhibits a resonance at the mechanical frequency ω_m while the shot noise term has two resonances: one near ω_m and the other near the self-resonance of the

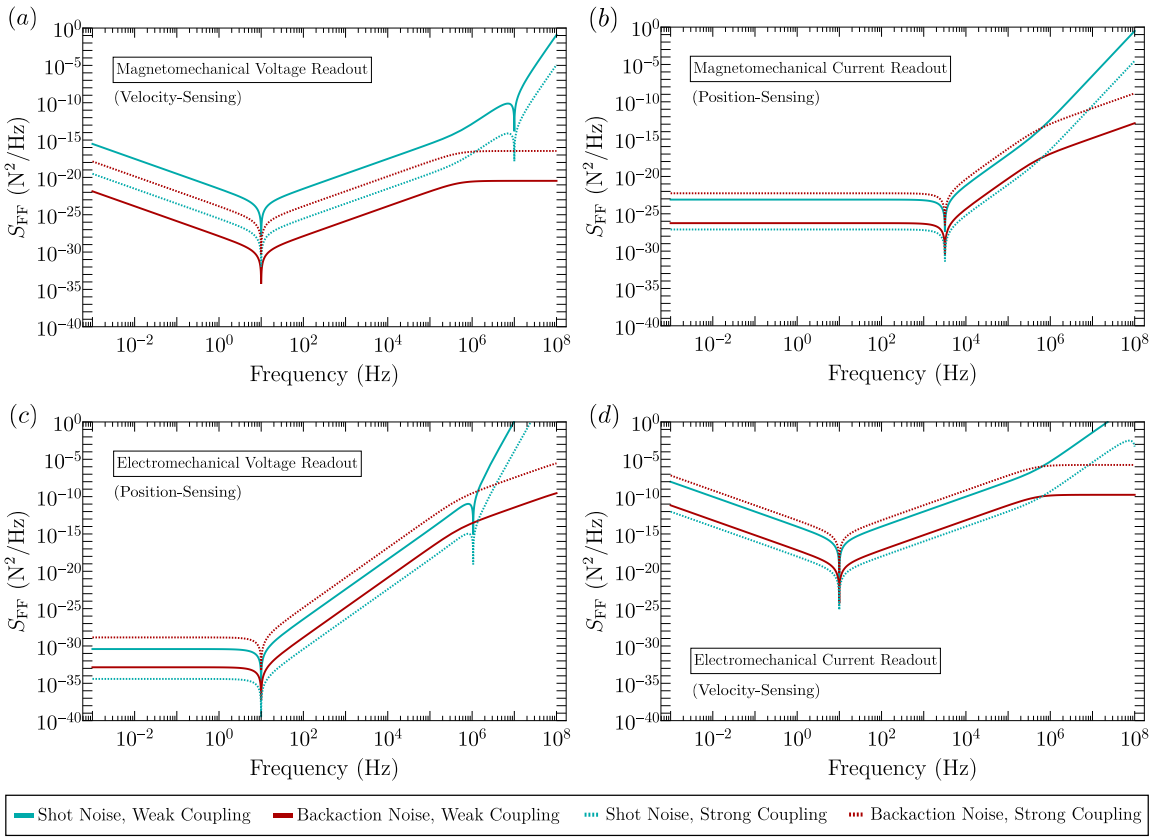


Figure 3.5: Shot noise (light blue) and backaction noise (dark red) curves at different coupling strengths for the magnetomechanical and electromechanical setups. In all instances solid curves correspond to weaker coupling strengths relative to the dashed curves, as indicated in the legend. The weak coupling strengths correspond to the values $G_Q^{(E,v)}/2\pi = G_Q^{(E,x)}/2\pi = 10^{23}$ Hz/C and $G^B/2\pi = 10^{23}$ Hz/Wb, while strong coupling strengths correspond to the values $G_Q^{(E,v)}/2\pi = G_Q^{(E,x)}/2\pi = 10^{25}$ Hz/C and $G^B/2\pi = 10^{25}$ Hz/Wb. Plots in (a) and (b) show the curves for the magnetomechanical detector configuration, where (a) represents the electric field-dependent parametric cavity or voltage readout and (b) represents the magnetic field-dependent parametric cavity or current readout. Plots in (c) and (d) show the curves for the electromechanical detector configuration, where (c) represents the electric field-dependent parametric cavity or voltage readout and (d) represents the magnetic field-dependent parametric cavity or current readout. The parameters used for generating these plots are as follows: detector mass $m = 1$ g, mechanical resonance frequency $\omega_m/2\pi = 10$ Hz, cavity decay rate $\kappa/2\pi = 1$ MHz, inductance $L = 10$ μH, mutual inductance $L_M = 1$ nH, circuit resonance frequencies $\omega_c/2\pi = 10$ MHz and $\omega_{\mathrm{ce}}/2\pi \approx 1$ MHz, capacitance $C_P = 25$ fF, with transducer constants $T_v = 2$ T $\cdot$ m and $T_x =$ -10^{-10} C/m and coupling coefficient $G_x \approx T_x G_Q^{(E,x)}$.

detector circuit ω_c. This is a consequence of our chosen parameters which result in $\omega_l^2 \gg \omega_c^2 \gg \delta_v^2 \gg \omega_m^2$, where the frequency δ_v represents the shift in the mechanical resonance due to the circuit coupling. Similarly, for current readout in the magnetomechanical system, shown in Fig. 3.5b and described by Eq. (3.51), resonances occur near δ_v in both the backaction and shot noise terms. Here the mechanics are dressed by the circuit, yielding an effective mechanical resonance at δ_v with a negligible contribution from ω_m.

For the electromechanical system, described by Eqs. (3.55) and (3.58) and shown in Figs. 3.5c and 3.5d, both voltage and current readout demonstrate resonances near ω_m. In addition, a resonance near the circuit's self-resonance ω_{ce} is visible in the voltage measurement case in Fig. 3.5c. As before, the locations of these resonances are a consequence of our chosen parameters and the coupling between the mechanical system and the circuit, where we note $G_Q^{(E,x)} \gg G_x$ and $\omega_{\mathrm{le}}^2 \gg \omega_{\mathrm{ce}}^2 \gg \omega_m^2 \gg \delta_x^2$. Here again, the mechanics dress the circuit; however, in contrast to the magnetomechanical case, the contribution from δ_x is negligible in comparison to the bare mechanical resonance at ω_m.

While these resonance features might be useful for some applications, our interest is in the broadband sensitivity, rather than the sensitivity to monochromatic signals. With monochromatic signals, noise optimization at a specific frequency, especially efforts to tune a setup around the resonance frequencies, is important. In particular, the resonances present in the backaction noise term correspond to target frequencies

for which backaction noise is completely eliminated. This strict backaction evasion is distinct from a reduction in backaction noise over a broad range of frequencies, characteristic of QND-like measurements, as we now discuss.

Of particular interest is the behavior observed in the region of frequency above the mechanical resonance but below the cavity decay rate κ. This is a consequence of our signal of interest: an impulse delivered over a very short time. Thus, we are interested in making measurements on the timescale associated with this frequency range. We note a sharp contrast in the behavior of the magnetomechanical current readout and electromechanical voltage readout cases (Figs. 3.5b and 3.5c) when compared to that of magnetomechanical voltage readout and electromechanical current readout (Figs. 3.5a and 3.5d) — a consequence of the different mechanical degrees of freedom accessed in each set of cases. In the former, backaction and shot noise are constant in the regions for which $\nu < \omega_m$, δ_v, and in the region ω_m, $\delta_v < \nu < \kappa$, diverge as ν^4. This is consistent with the behavior observed in the position-sensing case shown in Fig. 3.4. In the latter, backaction and shot noise go as ν^{-2} for $\nu < \omega_m$ and ν^2 for $\omega_m < \nu < \kappa$. In other words, the magnetomechanical voltage and electromechanical current schemes exhibit a decrease in backaction noise in the vicinity of the mechanical resonance, analogous to the velocity-sensing case.

At high frequency where $\nu > \kappa$, we see similar behavior in the backaction and shot noise terms across all of the detector and readout combinations. In particular, backaction noise is either constant in this region, as in Figs. 3.5a and 3.5d for mag-

netomechanical voltage readout and electromechanical current readout, respectively, or diverges as ν^2, as in Figs. 3.5b and 3.5c for magnetomechanical current readout and electromechanical voltage readout, respectively. On the other hand, shot noise diverges as either ν^4 for magnetomechanical voltage readout and electromechanical current readout or ν^6 for magnetomechanical current readout and electromechanical voltage readout.

3.4.5 Analysis in the Context of Windchime

Recent advances in sensing technologies suggest that we can search for dark matter (DM) candidates through their gravitational interaction alone by building an array of many mechanical sensors [363]. Based on this proposal, the Windchime collaboration is developing the necessary experimental techniques and devices for the gravitational detection of DM candidates around the Planck mass range ($\sim 21.76\ \mu$g) [364]. In particular, we are considering milligram- to gram-scale sensors with very low natural resonance frequencies (about 1–100 Hz) and with significant environmental isolation using a dilution refrigerator at temperatures of 10 mK, which makes the thermal noise floor extremely low. We are thus mostly limited by measurement-added noise. We wish to compare the performances of voltage and current readout of the magnetomechanical detector scheme to the SQL-level benchmark associated with force measurement, specifically in the context of a signal of interest for the Windchime collaboration.

For an individual sensor of mass m in the array, a DM candidate of mass $m_{\rm dm}$, passing at a distance b and with velocity v, interacts with the sensor through the Newtonian gravitational force. We are interested in the component of the gravitational force which is perpendicular to the DM candidate's trajectory. This is our intended signal [362],

$$F_{\rm sig}(t) = \frac{G_N m m_{\rm dm} b}{(b^2 + v^2 t^2)^{3/2}} \ . \tag{3.61}$$

In the frequency domain, it takes the form

$$F_{\rm sig}(\nu) = \sqrt{\frac{2}{\pi}} \frac{G_N m m_{\rm dm} |\nu|}{v^2} K_1 \left(\frac{b}{v} |\nu| \right) \ , \tag{3.62}$$

where G_N is the gravitational constant and K_1 is a modified Bessel function. We note that this signal is well approximated by

$$F_{\rm sig}^{\rm approx}(\nu) = \sqrt{\frac{2}{\pi}} \frac{G_N m m_{\rm dm}}{bv} e^{-b|\nu|/2v} \ , \tag{3.63}$$

which we use to estimate a SNR.

The signal is delivered over a very short period of time, set by the timescale $\tau \sim b/v$. In the frequency domain, this translates to a constant broadband signal that rapidly diminishes at a frequency set by the timescale τ, thereby determining the signal bandwidth. For example, if we consider a DM candidate with a velocity around 200 km/s [402] passing at a distance $b \sim 1$ mm, the timescale of the signal is approximately $\tau \sim 10^{-8}$ s. In the frequency domain, this signal is constant until very

high frequency, approximately 1 GHz, after which the signal falls off to zero. We wish to identify this signal amidst collected time series data. As explored in Ref. [362], an efficient search strategy for such a broadband signal is to use an optimal filter to scan through the time series data, yielding the SNR

$$\mathrm{SNR}^2_{\mathrm{opt}} = \int_0^\infty \frac{|F_{\mathrm{sig}}(\nu)|^2}{S_{\mathrm{FF}}(\nu)} d\nu \ , \tag{3.64}$$

where the effective bandwidth of integration is set by the signal's timescale.

We estimate the SNR using the approximated signal in Eq. (3.63) and the noise PSDs appropriate for voltage or current readout of the magnetomechanical detector scheme, given by Eqs. (3.48) and (3.51), respectively. In Fig. 3.6, we show the SNRs as a function of the radius R of the cylindrical test mass (i.e., the sensor of mass m). Scaling the radius impacts a variety of parameters and circuit quantities, including the mass of the magnetic sensor, the inductance of the voice coil, and the transducer constant, as increasing the size of the magnetic mass requires the voice coil to scale up as well. Relevant details can be found in the caption of Fig. 3.6. We note that we take the distance b to scale linearly with R, which yields a timescale τ that inherently depends on R. Therefore, in calculating the SNR in Eq. (3.64), the effective bandwidth of integration is implicitly set by the size of the mass.

We compare these SNRs with that of the SQL-level noise floor associated with a force measurement [357], in which we infer the force acting on the sensor by monitoring the position of a free particle over time, where the measurements are separated by

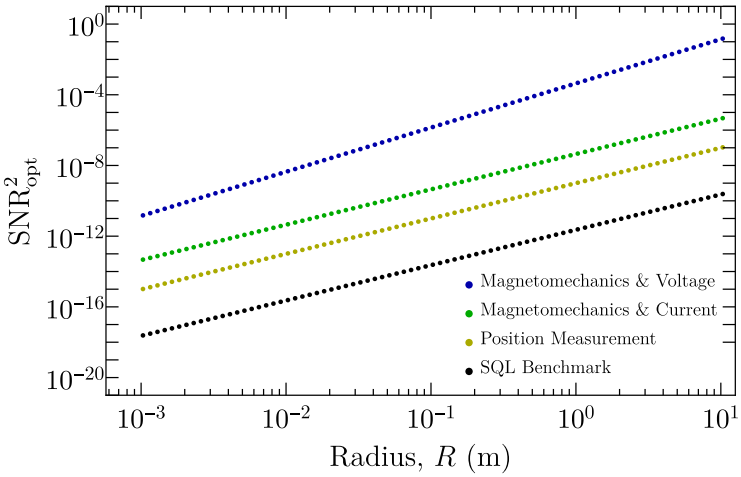


Figure 3.6: The $\mathrm{SNR}^2_{\mathrm{opt}}$ plotted as a function of the radius of the sensor, starting from an original radius of $R \approx 1$ mm and the parameters listed in Figs. 3.3 and 3.5 for the magnetomechanical detector scheme. The mass scales according to $m = \rho\pi R^2 h$, where we fix the mass density to $\rho = 7500$ kg/m^3 and allow the height h to scale linearly with R to maintain a fixed height to radius ratio of approximately 40. The transducer constant T_v and inductance of the voice coil L scale according to Eq. (3.1) and $L = \frac{\mu_0 N^2 \pi R^2}{h}$, respectively, where the total turn number scales according to $N = nh$ and we fix the turn density to $n \approx 7725$ turns/m and the magnetic field to $B = 1$ T. We fix the characteristic impedance of each LC circuit to $Z_0^v = 2\pi \cdot 10^2\ \Omega$ for voltage readout and $Z_0^x \approx 2\pi\ \Omega$ for current readout, maintaining the ratio $L/L_M = 10^4$ and forcing the capacitance C_L to scale with R. As the optimized coupling strengths given by Eqs. (3.50) and (3.54) depend on these scaling parameters, $G_Q^{(E,v)}$ and G^B also scale with R where we opt to scale the target frequency as R^{-1} from the original 1 MHz. The same scaling applies to the $\mathrm{SNR}^2_{\mathrm{opt}}$ for position measurement (yellow), using the noise PSD and initial parameters indicated in Fig. 3.4 where we neglect damping and scale the target frequency down from 0.1 MHz. In all cases, we take the DM mass and velocity to be $m_{\mathrm{dm}} = 21.76\ \mu$g (the Planck mass) and $v = 200$ km/s, with the distance $b \sim R$ such that $\tau \sim R/v$.

time τ. This is given by the relation

$$\Delta F_{\mathrm{SQL}} \sim \sqrt{\frac{\hbar m}{\tau^3}}\ . \tag{3.65}$$

In Fig. 3.6, we plot the ratio $[F_{\mathrm{sig}}(\tau)/\Delta F_{\mathrm{SQL}}]^2$ as a function of R, noting that the timescale τ and test mass m scale with R according to $\tau \sim R/v$ and $m \propto R^3$,

respectively. Relevant details can be found in the caption of Fig. 3.6. For additional comparison, we include the $\mathrm{SNR}^2_{\mathrm{opt}}$ corresponding to the position-sensing noise PSD of an optomechanical system shown in Fig. 3.4 and described in Appendix 3.G.

We find the magnetomechanical detection scheme with either readout option offers an improved sensitivity over both the SQL benchmark and standard optomechanical position sensing. In particular, voltage readout demonstrates orders of magnitude improvement in the SNR. For example, at a radius of approximately 10 cm, we observe about a 39 dB improvement over the SQL benchmark and a 26 dB improvement relative to standard position sensing. In contrast, current readout of the magnetomechanical detector scheme only offers about a 21 dB improvement over the SQL benchmark and a 8 dB improvement over standard position sensing. In addition, we see an overall improved sensitivity as the size of the test mass is scaled up, with the SQL benchmark, position-sensing case, and current readout of the magnetomechanical detector scheme scaling as R^2 and voltage readout of the magnetomechanical detector scheme scaling as $R^{2.5}$. We attribute the difference in scaling between the two readout options to be a consequence of the distinct circuits associated with each scheme, resulting in unique noise PSDs each with a different dependence on R. While these are encouraging results, we caution that these improvements indicate a 10-cm-radius sensor requires a test mass of 10^3 kg (1 metric ton) in order to measure a voltage signal on the order of attovolts. Granted, these estimates may be improved by considering instead the density and magnetic field of a superconducting material,

rather than a strong permanent magnet (neodymium), as we have here.

3.5 Outlook

Here we develop specific approaches for velocity and position sensing using voltage or current measurements of magnetomechanical and electromechanical transducers. We find that our specific electrical circuit-based approach to velocity sensing, namely voltage measurement of a magnetomechanical transducer, allows for a reduction in measurement-added noise while monitoring the mechanical motion in the microwave domain. While it is well known that Faraday's law connects voltage and velocity, this has not been used as a method for velocity measurement to date. Here we have shown that this may be a very fruitful domain for future exploration that is immediately compatible with existing mechanical systems, such as levitated superconducting spheres (e.g., the ones described in Refs. [249–251]), by effectively changing their motional readout from current to voltage.

Applying the approaches we describe here to the challenge of direct dark matter detection showcases how this type of readout enables scaling to very large masses while keeping a very low floor of quantum noise. In this work, using very large objects is advantageous for measuring gravitational signals, as we focus primarily on observing small accelerations. In contrast, the observation of small forces requires a very different operating regime, offering an intriguing prospect for future work: the design of an effective small force sensor.

This type of velocity measurement is a QND-like measurement — a consequence of the QND structure of the velocity variable in the context of a mechanical oscillator well above its resonance frequency, i.e., in the free particle limit. Consequently, we anticipate that this could be a critical choice to make for future systems that incorporate sensors that need to operate in an impulse-sensing domain. Furthermore, our simple implementation of voltage measurement for a magnetomechanical transducer, which is a variation on the well-known RF-SET, can likely be improved with modern circuit QED techniques.

Appendix 3.A Faraday's Law

In the magnetomechanical detection scheme, our interest lies in the voltage generated when the magnetic mass moves through the stationary voice coil as a result of some impulse. This induced voltage ε is given by Faraday's law [384, 385]. Faraday's law relates ε to the time derivative of the magnetic flux $\Phi_B = \int_S \mathbf{B} \cdot \mathbf{dA}$ through an open surface S:

$$\varepsilon = -\frac{d\Phi_B}{dt} = -\frac{d}{dt}\left(\int_S \mathbf{B} \cdot \mathbf{dA}\right) \ . \tag{3.A1}$$

However, in this case it is advantageous to re-express Eq. (3.A1) in terms of two contributions, both integrated around the closed path C that bounds the surface S:

$$\varepsilon = \oint_C \mathbf{E} \cdot \mathbf{d}\ell + \oint_C (\mathbf{v} \times \mathbf{B}) \cdot \mathbf{d}\ell \ . \tag{3.A2}$$

The first term accounts for the electric field $\mathbf{E}$ generated by a time-varying magnetic field, while the second term accounts for time-varying changes in S and C, i.e., motion of the curve with some velocity $\mathbf{v}$. By considering the rest frame of the magnetic mass and taking the coil to be moving with a velocity $\mathbf{v} = v\hat{\mathbf{z}}$, Eq. (3.A2) can be evaluated to yield the induced voltage given by Eq. (3.1) in the main text.

By expressing Faraday's law as in Eq. (3.A2) we more readily understand the equivalence between the rest frames of the magnetic mass and voice coil. In the rest frame of the coil, the velocity is zero, however, a time-varying magnetic field will

be present due to the magnet's motion, yielding a non-zero electric field. We use a transformation between rest frames [384, 385] to express this electric field in terms of the magnetic field in the magnet's rest frame: $\mathbf{E} = \mathbf{v} \times \mathbf{B}$. In this way, we see how the induced voltage in our detection scheme is equivalent to that given by Eq. (3.1).

Appendix 3.B Circuit Analysis of the Detector Schemes

In this appendix, we provide a pedagogical presentation of circuit quantization techniques (specifically the node flux method, following Ref. [325]) as applied to the detector schemes outlined in Section 3.2 of the main text. This connects the circuit degrees of freedom to those of the mechanical systems we consider to arrive at the Hamiltonians in Eqs. (3.4), (3.5), and (3.6).

In an electrical circuit, every circuit element is characterized by a branch voltage and a branch current, whose time integral defines the element's branch flux and branch charge, respectively:

$$\begin{aligned} \Phi^b(t) &= \int_{-\infty}^{t} v^b(t')dt' \ , \\ Q^b(t) &= \int_{-\infty}^{t} i^b(t')dt' \ . \end{aligned} \tag{3.B1}$$

We use the superscript b to denote branch variables throughout the text; this is to distinguish from other variables, such as velocity v, present in our analysis. Circuit elements are characterized by fundamental equations that relate their branch current or charge to their branch voltage or flux. For example, in capacitors, $v^b = \dot{\Phi}^b = Q^b/C$, while for inductors $i^b = \dot{Q}^b = \Phi^b/L$. A nonlinear element such as a Josephson junction is characterized by the relation $i^b = \dot{Q}^b = I_C \sin\big(2\pi\Phi^b/\Phi_0\big) + C_J\ddot{\Phi}^b$, with I_C its critical current, C_J its self-capacitance, and Φ_0 the magnetic flux quantum.

Kirchhoff's laws determine how the branch variables of each element of a circuit

relate. Kirchhoff's current law enforces charge conservation at each node by equating the currents flowing into and out of each node. Kirchhoff's voltage law (an instance of Faraday's law) demands that the voltage around a closed loop must sum to zero. However, the branch variables do not constitute the degrees of freedom of the circuit, as they are not independent variables. In order to appropriately define independent degrees of freedom for a circuit, a so-called 'spanning tree' [325] must be chosen. The spanning tree determines how each of the branch variables may be expressed in terms of the defined independent degrees of freedom.

In the node flux formulation, a spanning tree is constructed as follows. Starting from a designated ground or reference node, a path is chosen along each branch element such that each non-reference node of the circuit is reached by a single path. Each non-reference node is then associated with a node flux, defined as the sum (or difference) of the branch fluxes along the path to each node. The various possible spanning trees for a given circuit amount to different gauge choices and are therefore distinct but equivalent descriptions. Once expressed in terms of node fluxes, the set of equations found from Kirchhoff's current law become the equations of motion for each degree of freedom, which are used to then infer the Lagrangian of the system. With this method, capacitive terms yield time derivatives of the node flux, thereby playing the role of kinetic energy terms. In contrast, inductive terms are written in terms of the node flux, hence acting like potential energy terms. In this way, Kirchhoff's current laws become equations of motion, while the Kirchhoff's voltage

laws determine how the branch fluxes are defined in terms of the node fluxes.

We use this general procedure to find the Lagrangians and derive the Hamiltonians for each of the detector configurations presented in the main text. In the magnetomechanical case (Section 3.2.1), we consider the lumped-element circuit shown in Fig. 3.1b. We highlight two distinct yet equivalent gauge descriptions, which when combined with the mechanics of the system, reveal different couplings between the circuit and mechanical degrees of freedom. In the electromechanical case (Section 3.2.2), we examine the lumped-element circuit shown in Fig. 3.1d, where we find a nonlinear coupling between the circuit and mechanical degrees of freedom. We then perform an expansion about the minimum energy configuration to linearize this coupling.

3.B.1 Magnetomechanical Circuit Analysis

For the magnetomechanical case, we consider the detector circuit shown in Fig. 3.1b of the main text. Upon choosing the bottom node as the ground node, we write the equations found using Kirchhoff's laws as

$$\begin{aligned} C_L \ddot{\Phi}^b_{C_L} &= \frac{\Phi^b_L}{L} \\ \dot{\Phi}^b_L + \dot{\Phi}^{\text{ext}} &= -\dot{\Phi}^b_{C_L} \ , \end{aligned} \tag{3.B2}$$

where we have chosen an orientation of the coil relative to the magnet such that the self-induced voltage and externally generated voltage are additive. Note that the inductor's voltage must reflect both its own contribution (the self-induced voltage) as

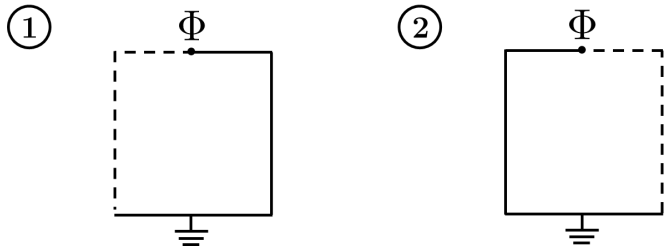


Figure 3.7: Schematic highlighting the two spanning trees associated with each gauge in the magnetomechanical detector configuration.

well as that from the external flux of the magnet, namely, its time derivative, given that Φ^{ext} is generally a time-dependent quantity.

In this case, there is only one non-reference node and only two potential paths to reach it: through the capacitor or through the inductor. For each of these spanning trees, shown in Fig. 3.7, we define an appropriate node flux. The presence of an external flux results in two spanning trees with distinct definitions of each branch flux in term of the node flux. For the first path (through the inductor), we define $\Phi = \Phi_L^b$. Alternatively, for the second path (through the capacitor) we find $\Phi = -\Phi_{C_L}^b$. By implementing these distinct node flux definitions in Eq.(3.B2), we see that the voltage law defines each alternate branch flux in terms of the node flux, and the current law provides the equation of motion governing Φ.

In the first case, where $\Phi = \Phi_L^b$, Eq.(3.B2) implies that $\dot{\Phi}_{C_L}^b = -(\dot{\Phi} + \dot{\Phi}^{\text{ext}})$ and yields the equation of motion

$$C_L(\ddot{\Phi} + \ddot{\Phi}^{\text{ext}}) = -\frac{\Phi}{L} \ . \tag{3.B3}$$

In the second case, where $\Phi = -\Phi^b_{C_L}$, Eq.(3.B2) implies that $\dot{\Phi}^b_L = \dot{\Phi} - \dot{\Phi}^{\text{ext}}$ and yields the equation of motion

$$C_L\ddot{\Phi} = -\frac{(\Phi - \Phi^{\text{ext}})}{L} \ . \tag{3.B4}$$

These equations of motion can be used to obtain the Lagrangians, which for each respective spanning tree are written as

$$\mathcal{L}_1 = \frac{1}{2}C_L(\dot{\Phi} + \dot{\Phi}^{\text{ext}})^2 - \frac{\Phi^2}{2L} \tag{3.B5}$$

and

$$\mathcal{L}_2 = \frac{1}{2}C_L\dot{\Phi}^2 - \frac{(\Phi - \Phi^{\text{ext}})^2}{2L} \ . \tag{3.B6}$$

With the Lagrangians of each spanning tree specified, we use the usual Legendre transformation to obtain the Hamiltonians [403] in each case:

$$H_1 = \frac{Q^2}{2C_L} + \frac{\Phi^2}{2L} - Q\dot{\Phi}^{\text{ext}} \tag{3.B7}$$

and

$$H_2 = \frac{Q^2}{2C_L} + \frac{(\Phi - \Phi^{\text{ext}})^2}{2L} \ , \tag{3.B8}$$

where $Q = \frac{d\mathcal{L}_i}{d\dot{\Phi}}$ represents the canonical charge degree of freedom, conjugate to the node flux Φ. With only the lone capacitance C_L connected to the node, Q represents

the charge on this capacitor's plates. These Hamiltonians are related by the gauge transformation given by Eq. (3.2) in Section 3.2.1 of the main text.

To incorporate the mechanical degrees of freedom due to the magnetic mass's motion, we recall that Φ^{ext} represents the flux penetrating the voice coil due to the presence of the magnetic mass. Therefore, $\dot{\Phi}^{\text{ext}}$ corresponds to the induced voltage ε in Eq. (3.1) of the main text. This enables us to rewrite Eq. (3.1) in terms of Φ^{ext}, the mechanical degrees of freedom, and the transducer constant T_v:

$$\begin{aligned} \dot{\Phi}^{\text{ext}} &= T_v \dot{x} \\ \Phi^{\text{ext}} &= T_v x \ , \end{aligned} \tag{3.B9}$$

where x represents the mass's position and $\dot{x}$ its velocity v. We then incorporate the motion of the mass and its attached spring in the Lagrangians of Eqs. (3.B5) and (3.B6) by making the substitutions indicated in Eq. (3.B9) and including terms that describe the energy associated with the mechanical motion. In full, we come to the Lagrangians

$$\mathcal{L}_1^{(E,v)} = \frac{1}{2}m\dot{x}^2 - \frac{1}{2}kx^2 + \frac{1}{2}C_L(\dot{\Phi} + T_v\dot{x})^2 - \frac{\Phi^2}{2L} \tag{3.B10}$$

and

$$\mathcal{L}_2^{(E,v)} = \frac{1}{2}m\dot{x}^2 - \frac{1}{2}kx^2 + \frac{1}{2}C_L\dot{\Phi}^2 - \frac{(\Phi - T_v x)^2}{2L} \ . \tag{3.B11}$$

Moving to the Hamiltonian description via a Legendre transform yields the Hamiltonians given in Eqs. (3.4) and (3.5).

As an aside, we can confirm the Lagrangians in Eqs. (3.B10) and (3.B11) appropriately characterize the mechanics by considering the forces acting on the magnetic mass. These forces include the restorative force of the spring as well as a magnetic force due to the interaction between the current-carrying voice coil and the magnetic mass. Due to the interaction between the current in the voice coil and the magnetic field in the air gap of the magnetic mass, the voice coil experiences a magnetic force of the form $F = \int i_L^b \mathbf{d}\ell \times \mathbf{B} = -T_v i_L^b$. As a result of Newton's third law, the force felt by the magnetic mass is equal and opposite to the force felt by the voice coil. The equation of motion for the position of the magnetic mass can then be written as

$$m\ddot{x} = -kx + \frac{T_v}{L}\Phi_L^b \ , \tag{3.B12}$$

where we have made the substitution for the branch flux of the inductor via $i_L^b = \Phi_L^b/L$. One can confirm that by making the appropriate substitutions for branch flux in each gauge yields an equation of motion [combined with either Eq. (3.B3) or Eq. (3.B4)] generated by the Lagrangians in either Eq. (3.B10) or Eq. (3.B11).

3.B.2 Electromechanical Circuit Analysis

For the electromechanical configuration, we begin with the lumped-element circuit shown in Fig. 3.1d of the main text and designate the bottom node as the ground or reference node and assemble the appropriate expressions from Kirchhoff's laws. This

yields the equations

$$\begin{aligned} \frac{d}{dt}\left[C(x)\dot{\Phi}^b_C\right] &= \frac{\Phi^b_L}{L} + C_P\ddot{\Phi}^b_{C_P} \ , \\ V_{\mathrm{DC}} + \dot{\Phi}^b_C + \dot{\Phi}^b_L &= 0 \ , \\ \dot{\Phi}^b_L &= \dot{\Phi}^b_{C_P} \ , \end{aligned} \tag{3.B13}$$

where the first equation arises from applying Kirchhoff's current law to the top node and the remaining equations are the result of applying Kirchhoff's voltage law around each of the circuit's two loops. Note that we have written the current through the mechanically varying capacitor generally in terms of the total time derivative of the charge on the capacitor's plates $Q^b_C = C(x)\dot{\Phi}^b_C$. This is due to the fact that the capacitance is a function of the mechanical position.

We next construct a spanning tree to define the node flux Φ. While there are three potential spanning trees in this circuit, without any externally threaded flux all three choices yield identical definitions of the branch fluxes in terms of the node flux. Namely, $\dot{\Phi}^b_C = \dot{\Phi} - V_{DC}$ and $\dot{\Phi}^b_L = \dot{\Phi}^b_{C_P} = -\dot{\Phi}$. Expressing Kirchhoff's current law in Eq. (3.B13) in terms of the node flux, we find the equation of motion

$$\frac{d}{dt}\left[C(x)\left(\dot{\Phi} - V_{\mathrm{DC}}\right)\right] = -\frac{\Phi}{L} - C_P\ddot{\Phi} \ . \tag{3.B14}$$

Working backwards, we infer the Lagrangian that describes the circuit dynamics:

$$\mathcal{L} = \frac{1}{2}C(x)\left(\dot{\Phi} - V_{\mathrm{DC}}\right)^2 + \frac{1}{2}C_P\dot{\Phi}^2 - \frac{\Phi^2}{2L} \ . \tag{3.B15}$$

This Lagrangian does not fully describe the system as it does not completely account for the mechanical motion. However, we need only add the usual mechanical contributions due to the kinetic energy of the plate and the potential energy of the attached spring, yielding the total Lagrangian

$$\mathcal{L}^{(E,x)} = \frac{1}{2}m\dot{x}^2 - \frac{1}{2}kx^2 + \frac{1}{2}C(x)\left(\dot{\Phi} - V_{\mathrm{DC}}\right)^2 + \frac{1}{2}C_P\dot{\Phi}^2 - \frac{\Phi^2}{2L} \ . \tag{3.B16}$$

We can confirm that this Lagrangian appropriately accounts for the mechanical degrees of freedom by considering the forces acting on the movable plate: the restorative force of the attached spring and the electrostatic attraction between the oppositely charged plates of the capacitor. When the plates are uncharged, we take the spring to be in its equilibrium position so that the plate's position is $x = 0$ and the plate separation is d_0. In this coordinate system, we express the mechanically varying capacitance as $C(x) = \frac{\epsilon_0 A}{d_0 - x}$ where A is the area of the two plates and ϵ_0 the permittivity of free space. Assuming that the area of plates is much larger than their original separation such that they may be treated approximately as two infinite sheets with charge $\pm Q_C^b$, the electric field between them is uniform, given by $E = \frac{Q_C^b}{\epsilon_0 A}$, and the force of attraction felt by the movable plate is given by $F = \frac{1}{2}EQ_C^b = \frac{(Q_C^b)^2}{2\epsilon_0 A}$.

Using Newton's second law, the equation of motion for the position of the movable plate is then

$$\begin{aligned} m\ddot{x} &= -kx + \frac{(Q_C^b)^2}{2\epsilon_0 A} \\ &= -kx + \frac{C(x)^2(\dot{\Phi} - V_{\mathrm{DC}})^2}{2\epsilon_0 A} \\ &= -kx + \frac{1}{2}\frac{\partial C(x)}{\partial x}(\dot{\Phi} - V_{\mathrm{DC}})^2 \ , \end{aligned} \tag{3.B17}$$

where in the second line we have made the substitution $Q_C^b = C(x)\dot{\Phi}_C^b = C(x)(\dot{\Phi} - V_{\mathrm{DC}})$ such that the mechanical equation of motion is expressed in terms of the circuit's degree of freedom, the node flux Φ. This is further simplified in the third line by noting $\frac{\partial C(x)}{\partial x} = \frac{\epsilon_0 A}{(d_0 - x)^2} = \frac{C(x)^2}{\epsilon_0 A}$. Working backwards, we can confirm that this equation of motion for x is generated by the Lagrangian in Eq. (3.B16).

We then use this Lagrangian and the usual Legendre transformation [403] to find the Hamiltonian:

$$H^{(E,x)} = \frac{p^2}{2m} + \frac{\Phi^2}{2L} + V(Q, x) \ , \tag{3.B18}$$

where we define the quantity $V(Q, x)$ as

$$V(Q, x) = \frac{1}{2}kx^2 + \frac{Q^2 + 2C(x)V_{\mathrm{DC}}Q - C_P C(x)V_{\mathrm{DC}}^2}{2(C(x) + C_P)} \tag{3.B19}$$

and identify Q and p as the canonical node charge and momenta conjugate to the node flux Φ and position x, respectively. In this case, Q corresponds to the sum of the charge on the plates of the two capacitors connected to the node, while p is

the mechanical momentum of the movable plate. The coupling between the circuit and the mechanical degrees of freedom is contained in $V(Q, x)$ and unsurprisingly, this coupling is nontrivial since the capacitance $C(x)$ is inversely proportional to x. However, by considering small displacements of the movable plate of the capacitor, we can linearize the Hamiltonian by expanding about the equilibrium of the circuit and mechanical systems.

We understand this equilibrium as follows. When the plates are uncharged, the separation between them is given by d_0 and the location of the movable plate is at $x = 0$. Once charged, the electrostatic attraction between the oppositely charged plates brings them closer together, resulting in a new position for the movable plate at $x = x_0$. This position corresponds to the position where the restorative force of the spring and the force of electrostatic attraction are balanced. Examining the Hamiltonian, the contribution $V(Q, x)$ describes a two-dimensional potential energy landscape dependent on charge and position in which this point must be minimum. This equilibrium is where the plate exists upon perturbation due to some detection event. If we assume these perturbations are small, we can approximate this two-dimensional landscape by considering just the region in the vicinity of the equilibrium $\{Q_0, x_0\}$, thereby linearizing the charge-position interaction. Therefore, we seek the solution $\{Q_0, x_0\}$ to the equation $\nabla V(Q, x) = 0$ such that $\{Q_0, x_0\}$ is a minimum.

With this equilibrium point in hand, we expand $V(Q,x)$ about this point to find

$$V(Q,x) = V(Q_0,x_0) + \nabla V(Q_0,x_0)\cdot \underline{Q} + \frac{1}{2}\underline{Q}^T \underline{\underline{D}}\, \underline{Q} + ... \ , \tag{3.B20}$$

where we define the vector $\underline{Q} = \{Q - Q_0, x - x_0\}$ and the matrix $\underline{\underline{D}}$ as the Hessian matrix evaluated at the minimum $\{Q_0, x_0\}$. We express $\underline{\underline{D}}$ in the compact form

$$\underline{\underline{D}} = \begin{bmatrix} \frac{1}{C_{\text{eff}}} & -\frac{T_x}{C_P} \\ -\frac{T_x}{C_P} & k_{\text{eff}} \end{bmatrix} \tag{3.B21}$$

where have defined the effective capacitance $C_{\text{eff}} = C(x_0) + C_P$, the effective spring constant $k_{\text{eff}} = k - \frac{C_{\text{eff}} T_x^2}{C(x_0) C_P}$, and the transducer constant T_x as

$$T_x = C_P \frac{(Q_0 - C_P V_{\text{DC}})}{\epsilon_0 A} \left(\frac{C(x_0)}{C_{\text{eff}}}\right)^2 \ . \tag{3.B22}$$

We understand this transducer constant to be the constant of proportionality that takes changes in the position of the movable plate to changes in the charge on the capacitor's plates. That is, if we examine the expression for the charge on the mechanically varying capacitor's plates and expand about the minimum $\{Q_0, x_0\}$,

$$\begin{aligned} Q_C^b &= \frac{C(x)\,(Q - C_P V_{\text{DC}})}{C(x) + C_P} \\ &\approx \frac{C(x_0)}{C_{\text{eff}}}(Q - C_P V_{\text{DC}}) + T_x(x - x_0) \ + ... \ , \end{aligned} \tag{3.B23}$$

we find the approximately linear relationship between the movable plate's position

and the charge on the mechanically varying capacitor's plates via the transducer constant T_x.

Inserting the expansion of $V(Q, x)$ from Eq. (3.B20) into the Hamiltonian of Eq. (3.B18) (noting that the linear order term is zero at the minimum), the expanded linearized Hamiltonian takes the form given by Eq. (3.6) in the main text.

Appendix 3.C Adding the Drive and Moving to the Linearized Regime

In this appendix, we provide a brief overview of the standard methods employed in optomechanical analyses [397–399] (as applied to our systems of interest) that lead to Eqs. (3.25)-(3.29) in Section 3.3 of the main text. We begin by coupling the schemes for electric and magnetic field sensing to a bath that serves as a source of drive and mode of dissipation. Thus, we include in the Hamiltonians the terms

$$\hat{H}_B = \int_{-\infty}^{\infty} d\omega \hbar\omega \hat{b}^\dagger(\omega)\hat{b}(\omega) \ , \tag{3.C1}$$

and

$$\hat{H}_{\text{int}} = i\hbar\sqrt{\frac{\kappa}{2\pi}}\int_{-\infty}^{\infty} d\omega \left[\hat{b}^\dagger(\omega)\hat{a} - \hat{b}(\omega)\hat{a}^\dagger\right] \ , \tag{3.C2}$$

where $\hat{b}^\dagger(\omega), \hat{b}(\omega)$ are the creation and annihilation operators for the bath modes, which satisfy the commutation relation $[\hat{b}(\omega), \hat{b}^\dagger(\omega')] = \delta(\omega - \omega')$, and κ corresponds to the cavity decay rate. Eq. (3.C1) represents the Hamiltonian of the bath while Eq. (3.C2) is the coupling between the parametric cavity and the bath.

Upon coherently driving the cavity, the cavity modes are displaced from their average value such that $\hat{a} \to (\alpha + \delta\hat{a})e^{i\omega_L t}$, where α represents the drive strength, $\delta\hat{a}$ the operators corresponding to the dynamical quantum fluctuations about the average, and ω_L the frequency of the drive. It is then convenient to move to a frame

rotating with the drive via the unitary transformation

$$\hat{H} \to \hat{H}' = \hat{U}\hat{H}\hat{U}^\dagger + i\hbar\frac{d\hat{U}}{dt}\hat{U}^\dagger \tag{3.C3}$$

with

$$\hat{U} = e^{i\omega_L \hat{a}^\dagger \hat{a} t} \ . \tag{3.C4}$$

This unitary transformation serves to eliminate the time dependence from the Hamiltonian, namely, in the cavity-bath interaction term $\hat{H}_{\text{int}}$, as well as introduce a term $-\hbar\omega_L \hat{a}^\dagger \hat{a}$.

Finally, we move to the linearized regime of optomechanics and assume a strong drive such that we can linearize the interaction between the parametric cavity and the circuits for both voltage and current measurement. For a strong drive, the drive strength α increases in magnitude while also increasing the fluctuations associated with the operators $\delta\hat{a}, \delta\hat{a}^\dagger$. Thus, in the cavity-circuit coupling term (across all detector schemes, readout options, and gauges), we neglect the term going as $\delta\hat{a}^\dagger\delta\hat{a}$ as being a factor smaller in α than the terms $\alpha^*\delta\hat{a} + \alpha\delta\hat{a}^\dagger$. We also neglect contributions which do not dynamically affect the evolution of the system, namely, constant terms and terms linear in system operators.

By choosing the drive strength α to be real, and letting $\delta\hat{a}, \delta\hat{a}^\dagger \to \hat{a}, \hat{a}^\dagger$ (for convenience) we arrive at the Hamiltonians given by Eqs. (3.25)-(3.29) in Section 3.3 of the main text.

Appendix 3.D Defining the Input and Output Bath Modes

Here we provide a review of input-output theory [400] to establish the quantum Langevin equation and define the input and output modes for the system. We begin with the Heisenberg equation of motion for the bath modes $\hat{b}(\omega)$. This equation is identical across all detector schemes, readout options, and gauges,

$$\frac{d\hat{b}(\omega,t)}{dt} = \frac{-i}{\hbar}\left[\hat{b}(\omega), \hat{H}'\right] = -i\omega\hat{b}(\omega) + \sqrt{\frac{\kappa}{2\pi}}\hat{a} \ , \tag{3.D1}$$

and may be solved in reference to either an initial time or final time. This solution is written as

$$\hat{b}(\omega,t) = e^{-i\omega(t-t_0)}\hat{b}(\omega,t_0) + \sqrt{\frac{\kappa}{2\pi}}\int_{t_0}^{t} dt' e^{-i\omega(t-t')}\hat{a}(t') \ , \tag{3.D2}$$

where for times $t > t_0$ the solution references an initial state at time t_0 and for times $t < t_0$ the solution references a final state at time t_0.

We then substitute this solution into the Heisenberg equations of motion for $\hat{a}, \hat{a}^\dagger$ to find the quantum Langevin equation. In doing so, we define the input and output modes as

$$\frac{1}{\sqrt{2\pi}}\int_{-\infty}^{\infty} d\omega \ e^{-i\omega(t-t_0)}\hat{b}(\omega,t_0) = \begin{cases} \hat{b}_{\text{in}}(t) & \text{if } t > t_0 \\ \\ \hat{b}_{\text{out}}(t) & \text{if } t < t_0 \end{cases} \tag{3.D3}$$

and note the identities

$$\int_{-\infty}^{\infty} d\omega e^{\pm i\omega(t-t')} = 2\pi\delta(t-t') \tag{3.D4}$$

and

$$\int_a^b dx f(x)\delta(x-a) = \begin{cases} \frac{f(a)}{2} & \text{if } b > a \\ \\ \frac{-f(a)}{2} & \text{if } b < a \end{cases} . \tag{3.D5}$$

We note that the equations of motion for $\hat{a}, \hat{a}^\dagger$ are unique to each detector scheme, readout option, and gauge. As an example, for electric field sensing in the magnetomechanical detector scheme, the equation takes the gauge-independent form

$$\frac{d\hat{a}}{dt} = i\Delta\hat{a} + iG_Q^{(E,v)}\hat{Q} - \sqrt{\kappa}\hat{b}_{\text{in}} - \frac{\kappa}{2}\hat{a} \ . \tag{3.D6}$$

Taking the difference between the equations which reference an initial time $t > t_0$ (in terms of $\hat{b}_{\text{in}}$) or a final time $t < t_0$ (in terms of $\hat{b}_{\text{out}}$) yields the input-output relation

$$\hat{b}_{\text{out}}(t) = \hat{b}_{\text{in}}(t) + \sqrt{\kappa}\hat{a}(t) \ , \tag{3.D7}$$

which describes how the output bath modes are related to the input bath modes and the cavity operator.

Appendix 3.E Explicit Solutions for the Output Phase Quadratures

Here we list the solutions for the output phase quadratures found from different transducer and receiver combinations, as outlined in Section 3.4 of the main text. For the magnetomechanical detector configuration, voltage measurement via electric field sensing yields the solution

$$\begin{aligned}\hat{Y}_{\mathrm{out}}^{(E,v)}(\nu) = &-\left(\frac{\frac{\kappa}{2}-i\nu}{\frac{\kappa}{2}+i\nu}\right)\hat{Y}_{\mathrm{in}} + \frac{\hbar {G_Q^{(E,v)}}^2 \kappa(\nu^2-\omega_m^2)}{L(\frac{\kappa}{2}+i\nu)^2\left[(\nu^2-\omega_c^2)(\nu^2-\omega_m^2)-\delta_v^2\nu^2\right]}\hat{X}_{\mathrm{in}} \\ &+ \frac{iG_Q^{(E,v)}\sqrt{\kappa}\delta_v\nu}{\sqrt{mL}(\frac{\kappa}{2}+i\nu)\left[(\nu^2-\omega_c^2)(\nu^2-\omega_m^2)-\delta_v^2\nu^2\right]}\hat{F}_{\mathrm{in}}\end{aligned}, \tag{3.E1}$$

while for current measurement via magnetic field sensing we find the expression

$$\begin{aligned}\hat{Y}_{\mathrm{out}}^{(B,v)}(\nu) = &-\left(\frac{\frac{\kappa}{2}-i\nu}{\frac{\kappa}{2}+i\nu}\right)\hat{Y}_{\mathrm{in}} + \frac{\hbar {G^B}^2 \kappa L\omega_c^2\left(\nu^2-\omega_m^2-\delta_v^2\right)}{(\frac{\kappa}{2}+i\nu)^2\left[(\nu^2-\omega_c^2-\omega_l^2)(\nu^2-\omega_m^2)-\delta_v^2(\nu^2-\omega_l^2)\right]}\hat{X}_{\mathrm{in}} \\ &+ \frac{G^B\sqrt{\kappa L}\delta_v\omega_c^2}{\sqrt{m}(\frac{\kappa}{2}+i\nu)\left[(\nu^2-\omega_c^2-\omega_l^2)(\nu^2-\omega_m^2)-\delta_v^2(\nu^2-\omega_l^2)\right]}\hat{F}_{\mathrm{in}}\end{aligned}. \tag{3.E2}$$

For the electromechanical case, voltage measurement via electric field sensing yields

$$\begin{aligned}\hat{Y}_{\mathrm{out}}^{(E,x)}(\nu) = &-\left(\frac{\frac{\kappa}{2}-i\nu}{\frac{\kappa}{2}+i\nu}\right)\hat{Y}_{\mathrm{in}} + \frac{\hbar\kappa\left[{G_Q^{(E,x)}}^2 m(\nu^2-\omega_m^2) - 2G_Q^{(E,x)}G_x\sqrt{mL}\delta_x\omega_{\mathrm{ce}} + G_x^2L(\nu^2-\omega_{\mathrm{ce}}^2)\right]}{mL(\frac{\kappa}{2}+i\nu)^2\left[(\nu^2-\omega_{\mathrm{ce}}^2)(\nu^2-\omega_m^2)-\delta_x^2\omega_{\mathrm{ce}}^2\right]}\hat{X}_{\mathrm{in}} \\ &+ \frac{\kappa\left[G_xL(\nu^2-\omega_{\mathrm{ce}}^2) - G_Q^{(E,x)}\sqrt{mL}\delta_x\omega_{\mathrm{ce}}\right]}{mL(\frac{\kappa}{2}+i\nu)\left[(\nu^2-\omega_{\mathrm{ce}}^2)(\nu^2-\omega_m^2)-\delta_x^2\omega_{\mathrm{ce}}^2\right]}\hat{F}_{\mathrm{in}}\end{aligned}, \tag{3.E3}$$

while for current measurement via magnetic field sensing we find the expression

$$\hat{Y}_{\rm out}^{(B,x)}(\nu) = -\left(\frac{\frac{\kappa}{2}-i\nu}{\frac{\kappa}{2}+i\nu}\right)\hat{Y}_{\rm in} + \frac{\hbar G^{B^2}\kappa L\omega_{\rm ce}^2\left(\nu^2-\omega_m^2+\delta_x^2\right)}{(\frac{\kappa}{2}+i\nu)^2\left[(\nu^2-\omega_{\rm ce}^2-\omega_{\rm le}^2)(\nu^2-\omega_m^2)-\delta_x^2(\omega_{\rm ce}^2+\omega_{\rm le}^2)\right]}\hat{X}_{\rm in} + \frac{iG^B T_x\sqrt{\kappa L}\omega_{\rm ce}\nu}{\sqrt{m}(\frac{\kappa}{2}+i\nu)\left[(\nu^2-\omega_{\rm ce}^2-\omega_{\rm le}^2)(\nu^2-\omega_m^2)-\delta_x^2(\omega_{\rm ce}^2+\omega_{\rm le}^2)\right]}\hat{F}_{\rm in} \quad . \tag{3.E4}$$

In all instances, we have utilized the frequencies defined Eq. (3.46) of the main text.

Appendix 3.F Explicit Noise PSD Solutions

In this appendix, we list the noise PSD expressions for each combination of detector configuration and measurement scheme. In contrast to those shown in the main text, here we write these expressions explicitly in terms of their frequency dependence and the relevant frequencies given in Eq. (3.46). We also include the coupling G_x present in the electromechanical scheme, which we neglect due to its small size in the expressions in the main text. For the magnetomechanical detector configuration, voltage measurement via electric field sensing yields the noise PSD

$$S_{\mathrm{FF}}^{(E,v)} = \frac{\hbar^2 {G_Q^{(E,v)}}^2 \kappa m(\nu^2-\omega_m^2)^2}{2L\delta_v^2\nu^2\left(\frac{\kappa^2}{4}+\nu^2\right)} + \frac{mL\left(\frac{\kappa^2}{4}+\nu^2\right)\left[(\nu^2-\omega_m^2)(\nu^2-\omega_c^2)-\delta_v^2\nu^2\right]^2}{2{G_Q^{(E,v)}}^2\kappa\delta_v^2\nu^2} + N_{\mathrm{BM}} \ , \tag{3.F1}$$

while for current measurement via magnetic field sensing we find the expression

$$S_{\mathrm{FF}}^{(B,v)} = \frac{\hbar^2 {G^B}^2 \kappa mL\left(\nu^2-\omega_m^2-\delta_v^2\right)^2}{2\delta_v^2\left(\frac{\kappa^2}{4}+\nu^2\right)} + \frac{m\left(\frac{\kappa^2}{4}+\nu^2\right)\left[(\nu^2-\omega_m^2)(\nu^2-\omega_c^2-\omega_l^2)-\delta_v^2(\nu^2-\omega_l^2)\right]^2}{2{G^B}^2\kappa L\delta_v^2\omega_c^4} + N_{\mathrm{BM}} \ . \tag{3.F2}$$

In the electromechanical case, voltage measurement via electric field sensing yields the noise PSD

$$\begin{aligned} S_{\mathrm{FF}}^{(E,x)} =& \frac{\hbar^2\kappa\left[{G_Q^{(E,x)}}^2 m(\nu^2-\omega_m^2) - 2G_Q^{(E,x)}G_x\sqrt{mL}\delta_x\omega_{\mathrm{ce}} + G_x^2L(\nu^2-\omega_{\mathrm{ce}}^2)\right]^2}{2\left(\frac{\kappa^2}{4}+\nu^2\right)\left[G_Q^{(E,x)}\sqrt{mL}\delta_x\omega_{\mathrm{ce}} - G_xL(\nu^2-\omega_{\mathrm{ce}}^2)\right]^2} \\ &+ \frac{m^2L^2\left(\frac{\kappa^2}{4}+\nu^2\right)\left[(\nu^2-\omega_m^2)(\nu^2-\omega_{\mathrm{ce}}^2)-\delta_x^2\omega_{\mathrm{ce}}^2\right]^2}{2\kappa\left[G_Q^{(E,x)}\sqrt{mL}\delta_x\omega_{\mathrm{ce}} - G_xL(\nu^2-\omega_{\mathrm{ce}}^2)\right]^2} + N_{\mathrm{BM}} \ , \end{aligned} \tag{3.F3}$$

while for current measurement via magnetic field sensing we find the expression

$$S_{\rm FF}^{(B,x)} = \frac{\hbar^2 G^{B\,2}\kappa m L\omega_{\rm ce}^2\left(\nu^2-\omega_m^2+\delta_x^2\right)^2}{2\delta_x^2\nu^2\left(\frac{\kappa^2}{4}+\nu^2\right)} + \frac{m\left(\frac{\kappa^2}{4}+\nu^2\right)\left[(\nu^2-\omega_m^2)(\nu^2-\omega_{\rm ce}^2-\omega_{\rm le}^2)-\delta_x^2(\omega_{\rm ce}^2+\omega_{\rm le}^2)\right]^2}{2G^{B\,2}\kappa L\delta_x^2\omega_{\rm ce}^2\nu^2} + N_{\rm BM}\ . \tag{3.F4}$$

Appendix 3.G Analysis of Optomechanical Systems for Comparison

Here we consider the continuous measurement of an optomechanical system subject to either direct position or direct momentum coupling. In the case where the probing optical amplitude quadrature $\hat{X}$ directly interacts with the position $\hat{x}$ of the mechanical system, the interaction Hamiltonian takes the form

$$\hat{H}_{\rm int} = \hbar G \hat{x} \hat{X} \ . \tag{3.G1}$$

This is the basis of the standard optomechanical position-sensing problem. If instead the optical quadrature directly interacts with the velocity, i.e., the mechanical momentum of the system, which can be practically implemented by specific designs of the system as in Refs. [362, 401], the interaction Hamiltonian becomes

$$\hat{H}_{\rm int} = \hbar G' \hat{p} \hat{X} \ . \tag{3.G2}$$

Following the standard procedures in Appendix 3.D and Section 3.4, we write down the full Hamiltonian and derive the equations of motion for these systems. Here we additionally consider a mechanical damping with damping rate μ. Then, we solve for the output phase quadrature of light $\hat{Y}_{\rm out}$ using the input-output relations.

These yield the estimated force expressions [401]

$$\hat{F}_{E_x} = -G\hbar\chi_c\hat{X}_{\text{in}} + \frac{e^{i\phi_c}\hat{Y}_{\text{in}}}{G\chi_c\chi_m} + \hat{F}_{\text{in}} \ , \tag{3.G3}$$

and

$$\hat{F}_{E_v} = -iG'\hbar\chi_c m\frac{\omega_m^2}{\nu}\hat{X}_{\text{in}} + \frac{ie^{i\phi_c}}{G'm\nu\chi_c\chi_m}\hat{Y}_{\text{in}} + \hat{F}_{\text{in}} \ . \tag{3.G4}$$

Here we define the cavity response function χ_c, the mechanical response function χ_m, and the cavity phase shift $e^{i\phi_c}$ as

$$\begin{aligned} \chi_c &= \frac{\sqrt{\kappa}}{-i\nu + \kappa/2} \ , \\ \chi_m &= \frac{-1}{m(\nu^2 - \omega_m^2 + i\mu\nu)} \ , \\ e^{i\phi_c} &= \frac{-i\nu - \kappa/2}{-i\nu + \kappa/2} \ . \end{aligned} \tag{3.G5}$$

For position sensing, this helps us establish the target frequency-dependent optimization of the coupling strength G:

$$G(\nu) \to \frac{1}{\sqrt{\hbar}|\chi_m(\nu)|^{1/2}|\chi_c(\nu)|} \ . \tag{3.G6}$$

Using these estimated force expressions, we derive the noise PSD solutions analogously to those derived in the main text and use them to generate the broadband noise PSD plot shown Fig. 3.4 for comparison with that of our electrical readout schemes.

Chapter 4: Circulation by Microwave-Induced Vortex Transport for Signal Isolation[1]

4.1 Introduction

In order to scale up quantum computing devices, the supporting hardware for qubits must appropriately scale down. Essential components include elements for signal routing and isolation, such as circulators, as well as low-noise amplifiers, filters, and cooling systems. While development in improving miniaturization and effectiveness of these components progresses apace [257, 274, 275, 278, 280, 281, 286–288], traditional circulators remain bulky and require high magnetic fields for operation.

Creating a circulator requires nonreciprocal behavior induced by implicit or explicit breaking of time-reversal symmetry. This is then combined with microwave engineering to enable unidirectional transmission with little to no loss in a clockwise (CW) or counterclockwise (CCW) fashion over a large operating bandwidth. The nonreciprocal behavior observed in commercial ferrite junction circulators, which are commonly utilized in smaller systems, is a result of the Faraday effect. The interaction

[1]This chapter is largely a reproduction of Ref. [404], published in PRX Quantum, with the inclusion of additional details in the appendices.

between a magnetic field (e.g., from a permanent magnet) and the central ferrite disks of the device creates circulation via wave interference and magnetically induced gyration [405]. As a result, commercial ferrite junction circulators are fundamentally limited in size by the signal wavelength. However, their passive operation necessarily eliminates any additional control hardware. Nonetheless, with their large size and reliance on strong fields, the prospect of employing ferrite circulators in large quantum computing schemes is a challenge for the field, although some progress in wavelength-size devices [406] has been made. This requires finding small-volume, on-chip solutions that operate at low magnetic field and enable the isolation of quantum devices and corresponding precise qubit control and measurement.

One partial solution to this problem is generating nonreciprocity via the quantum Hall effect, where large magnetic fields break time-reversal symmetry and quantum Hall edge modes are utilized in passive devices to observe circulation [407–409]. Other proposed solutions are actively controlled and take a nonmagnetic or small-field approach, using frequency conversion in driven systems and irreversible dynamics (loss) or synthetic gauge fields in a Floquet basis to generate nonreciprocity [279–283, 285, 410]. However, due to their active nature, they necessarily require additional control hardware that is undesirable in larger-scale systems. To date, the only passive, low-field, subwavelength approach uses particle tunneling in small Josephson junction arrays (JJAs) or quantum phase slip (QPS) junctions, utilizing their behavior in magnetic fields—the Peierls phase in tunneling—to break time-reversal symmetry [276,

284]. Both of these proposed devices suffer from challenges in implementation due to susceptibility to charge noise, difficulties in implementing robust QPS devices, and poor performance in operational bandwidth.

Here we address these challenges by moving from a Cooper pair tunneling device to a persistent-current (vortex) tunneling device via insertion of additional Josephson junctions. Our approach, shown schematically in Figs. 4.1a and 4.1b, builds upon the three-island Josephson junction loop proposed by Koch *et al.* [276] and further explored by Müller *et al.* [284]. In contrast to those works, we suggest operating in a non-charge-conserved, intermediate regime of Josephson energy and charging energy being similar. By keeping the Josephson energy similar to the charging energy, we can maintain quantum-coherent vortex dynamics rather than having the microwave response behavior be dominated by spin waves, as occurs at large Josephson energy. We show a reduction in sensitivity to charge noise, while enabling large-bandwidth operation.

To understand this performance, we draw an analogy to bulk superconductors, where the Meissner effect leads to persistent currents around holes in a superconductor. In the limit of large tunneling rates, these currents are fixed to each hole. This is related to the dual picture of a lattice of vortices with large effective mass trapped around each hole. However, as the kinetic term increases by decreasing capacitance, and phase slips are made available by the introduction of tunnel junctions (Josephson junctions), the vortices are able to move. Some devices, such as the flux

qubit [186, 187], have demonstrated the ability to prepare a superposition of different vortex states for a small circuit [188, 189]. We suggest that the successful operation of our proposed device arises by exploiting the behavior of such coherent vortices in a magnetic field, analogous to the behavior of the ferrite system where the XY model of the junctions acts as an effective ferromagnet. Here we propose circulation is achieved via the rotation of these persistent-current vortices: the voltage induced by an incoming signal generates a vortex in the circuit, and this vortex then rotates about the circuit, leading to re-radiation into each port.

This chapter is organized as follows. Section 4.2 introduces the central circuit model to be explored, and explains the motivation for this choice by presenting an investigation of vortices in the model and their potential role in device functionality. Section 4.3 couples the central circuit to external circuits to investigate transmission properties of the system. A theoretical analysis in the single excitation limit is presented, resulting in the single-photon scattering matrix (S-matrix), followed by conditions for ideal circulation. Numerical results related to bandwidth, circulation, and noise performance are given in Section 4.4, and we conclude and provide an overview of results in Section 4.5. In the appendices that follow, we explore an alternative circuit model to the one presented in Section 4.2, followed by a semi-classical analysis of the model to identify relevant vortex configurations and spin-wave frequencies. We also consider a numerical examination of two flux points in addition to the one investigated in Section 4.4 and derive the full system Hamiltonian. This is followed by

additional details of the S-matrix analysis as well as a generalized approach to finding ideal parametrizations. We then discuss various parameter effects and provide additional details to supplement the noise analysis presented in Section 4.4.

4.2 Vortex-Based Nonreciprocity

4.2.1 Model Circuit

Here we investigate a minimal model of a circuit for our proposed system, which consists of three superconducting islands connected to each other and a central grounded island via Josephson junctions, as shown in Fig. 4.1b, all threaded by an external flux Φ. We note that the central ground can, in principle, be replaced by a capacitive island with $C_0 \gg C_\mathrm{J}$, the nominal capacitance of each island. This alternative circuit is shown in Fig. 4.1c and is explored in detail in Appendix 4.A. For the circuit in Fig. 4.1b, the overall Hamiltonian is:

$$H_\mathrm{CC} = 4E_\Sigma \, (\underline{\hat{N}} - \underline{N}_\mathrm{g})^T \underline{\underline{K}}^{-1} (\underline{\hat{N}} - \underline{N}_\mathrm{g}) + E_\mathrm{J} \, V(\underline{\hat{\varphi}}, \Phi) \ . \tag{4.1}$$

The operators $\underline{\hat{N}}$ and $\underline{\hat{\varphi}}$ are the vectors of number and phase operators for each island of the circuit, with individual elements satisfying the commutation relation $[\hat{\varphi}_j, \hat{N}_k] = i\delta_{jk}$. E_J is the Josephson energy of each junction and E_Σ is the circuit's charging energy, defined as $E_\Sigma = \frac{e^2}{2C_\mathrm{M}}$ where C_M is the largest eigenvalue of the circuit's capacitance matrix $\underline{\underline{C}}$, defined in Eq. (4.2). $\underline{\underline{K}}^{-1}$ is the dimensionless inverse

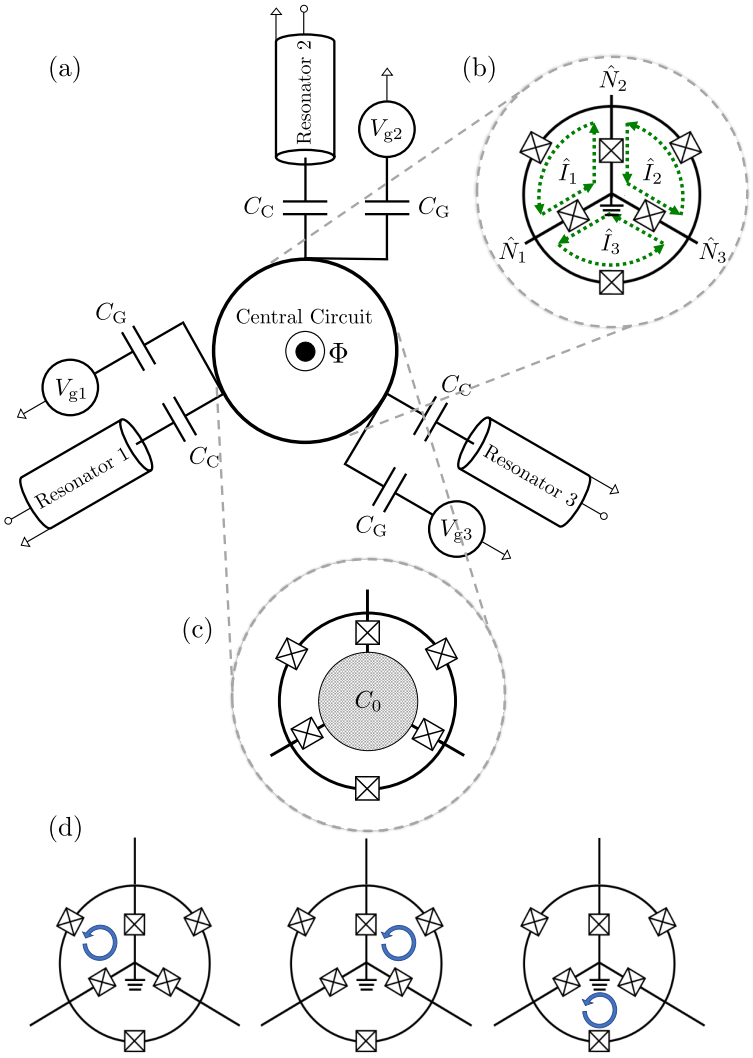


Figure 4.1: (a) A schematic representation of the model with a generic central circuit threaded by external flux Φ via an external magnetic field applied perpendicular to the plane. Each resonator (enumerated above) and voltage source V_{gi} is coupled to an island of the central circuit via capacitors C_C and C_G, respectively. (b) The central circuit model, with identical Josephson junctions $\boxtimes$ having Josephson energy E_J and capacitance C_J, with labeled loop currents through each third of the model: $\hat{I}_1$, $\hat{I}_2$, and $\hat{I}_3$. (c) An alternative circuit design (explored in Appendix 4.A) that replaces the central ground with a large central island with self-capacitance C_0. (d) A visual of the persistent-current vortices that may exist in each third of the circuit.

capacitance matrix appropriate for the circuit, which is found by factoring C_M from $\underline{\underline{C}}^{-1}$. As written, H_{CC} stipulates the central circuit be a superconducting, three-island

system containing identical Josephson junctions. By specifying the elements of $\underline{\underline{K}}^{-1}$ and the tunneling potential $V(\underline{\hat{\varphi}}, \Phi)$, we establish the particular central circuit for the system explored in this work. This allows us to compare to prior work without substantial computational difficulty.

We define $\underline{\underline{K}}^{-1}$ by inverting the capacitance matrix $\underline{\underline{C}}$,

$$\underline{\underline{C}} = \begin{bmatrix} C_{\mathrm{S}} & -C_{\mathrm{J}} & -C_{\mathrm{J}} \\ -C_{\mathrm{J}} & C_{\mathrm{S}} & -C_{\mathrm{J}} \\ -C_{\mathrm{J}} & -C_{\mathrm{J}} & C_{\mathrm{S}} \end{bmatrix} \ , \tag{4.2}$$

where $C_{\mathrm{S}} = C_{\mathrm{C}} + C_{\mathrm{G}} + 3C_{\mathrm{J}}$, with C_{J} the capacitance of each Josephson junction, C_{C} the coupling capacitance, and C_{G} the residual capacitance to ground. For this matrix, $C_{\mathrm{M}} = C_{\mathrm{C}} + C_{\mathrm{G}} + 4C_{\mathrm{J}}$ is the largest eigenvalue. Factoring C_{M} from $\underline{\underline{C}}^{-1}$, we can then find

$$\underline{\underline{K}}^{-1} = \begin{bmatrix} 1+\delta & \delta & \delta \\ \delta & 1+\delta & \delta \\ \delta & \delta & 1+\delta \end{bmatrix} \ , \tag{4.3}$$

where $\delta = \frac{C_{\mathrm{J}}}{C_{\mathrm{C}}+C_{\mathrm{G}}+C_{\mathrm{J}}}$.

The inductive terms, corresponding to tunneling through the Josephson junctions, are described by

$$V(\underline{\hat{\varphi}}, \Phi) \ = \ -\sum_{i=1}^{3} [\cos(\hat{\varphi}_{i+1} - \hat{\varphi}_i - 2\pi A) + \cos(\hat{\varphi}_i)] \ , \tag{4.4}$$

where we take $i+1 = 4$ and $i = 1$ to be the same. This potential is equivalent to the XY model where the phase φ represents the angle of the $U(1)$ degrees of freedom.

The acquired Peierls phase factor, $2\pi A$, is equal to the line integral of the vector potential in a counterclockwise fashion around each third of the device:

$$2\pi A = \frac{2\pi}{\Phi_0} \oint \mathbf{A} \cdot d\mathbf{l} = \frac{2\pi\Phi}{3\Phi_0} \ . \tag{4.5}$$

This A corresponds to the frustration of the circuit, i.e., the flux penetration per loop of the device in terms of the magnetic flux quantum.

In what follows, we denote the eigenstates of H_{CC} as $|\varepsilon_m\rangle$ with eigenenergy ε_m, and label the ground state as $|G\rangle$. These are parametric functions of A, and are periodic in A.

4.2.2 Entering the Vortex Regime

The behavior and properties of the central circuit, shown in Fig. 4.1b, depend on the relative size of the two characteristic energy scales in the system: the energy associated with Cooper pair tunneling between islands, E_{J}, and the energy associated with putting a single electron on an island, $E_{\mathrm{C}} \sim E_{\Sigma}$. In the two extreme energy limits, $E_{\mathrm{J}} \ll E_{\mathrm{C}}$ or $E_{\mathrm{J}} \gg E_{\mathrm{C}}$, the relevant excitations are charges or vortices, respectively [346, 411, 412]. Charges have the same properties in the charged-dominated regime that vortices have in the tunneling-dominated regime [411, 413]. In the charge-dominated regime, where $E_{\mathrm{J}} \ll E_{\mathrm{C}}$, charges are well-defined, massive particles that feel a Lorentz force in the presence of an electromagnetic field and acquire an Aharanov-Bohm phase (represented in the charge basis as a Peierls phase)

when moving around an area containing a magnetic field [414, 415]. However, in this regime, external voltages and other sources of charge disorder, such as offset charge, have a dramatic effect on circuit behavior due to the very small capacitances necessary to achieve large E_{C}.

In the classical tunneling limit, where $E_{\mathrm{J}} \gg E_{\mathrm{C}}$, vortices are the topological excitations of the XY model that behave as massive (and essentially classical) particles. They respond to the presence of external current by experiencing a force perpendicular to the current flow (a Lorentz force), and the presence of external charge on the islands affects a moving vortex the same way a magnetic field affects a moving charge (an Aharanov-Casher effect for vortices) [16, 411–413]. In this way, charges and vortices are dual to each other, with these mirrored properties being manifestations of the charge-vortex duality that exists in JJAs. However, the vortex domain has two characteristic excitations: topological excitations, as just described, and plasma oscillations (spin waves in the XY model language) that correspond to the response of a classical circuit of inductors and capacitors with values set by the expectation value of the Josephson inductance for the nominal ground state (see, e.g., Ref. [312]). The plasma oscillations do not break time-reversal symmetry; in essence, the Meissner effect traps flux in the vortices, and thus, all time-reversal symmetry-breaking terms arise only from vortex motion. When $E_{\mathrm{J}} \gg E_{\mathrm{C}}$, this motion becomes exponentially slow due to the challenge of tunneling between allowed current configurations, and thus, one cannot make a circulator in this regime.

We wish to identify an energy regime using this duality, where time-reversal symmetry is broken in the microwave regime and charge noise is not relevant. We thus focus on $E_\mathrm{J} \sim E_\mathrm{C}$ as a regime where vortices can move and charge noise may be reduced, enabling the potential for noise-resistant nonreciprocity in the form of unidirectional signal transmission that is robust in the presence of random variation in offset charge. In this way, the model may act as an ideal circulator.

This intermediate regime has been partially explored by Koch *et al.* [276] and Müller *et al.* [284]. However, in those works, the system was defined with a charge-conserving three-island Josephson junction loop, and the total charge on the small-capacitance region was fixed. In what follows, we leverage the connection of each island to ground via an additional Josephson junction to enable large charge number fluctuations and suppress charge noise. This leads to circulator performance driven by vortex behavior rather than Cooper pair behavior.

4.2.3 Quantum Behavior of Vortices in the Intermediate Tunneling Regime

To explore the vortex picture, we set $E_\mathrm{J} = 4E_\mathrm{C}$ to ensure that there are sufficient phase fluctuations to warrant a quantum treatment of the vortex dynamics, and numerically diagonalize H_CC [given by Eq. (4.1)] for a range of A from 0 to 0.5, as the eigenvalues are symmetric in $A \to -A$ and periodic (same for $A + 1$ as for A). We denote the corresponding energy eigenstates $|\varepsilon_n\rangle$ and eigenvalues ε_n, with implicit

dependence on A understood. For our chosen parameters ($E_{\mathrm{J}} = 4E_{\mathrm{C}} \approx 45$ GHz) and eventual optimum operating point (near $A = 0.2478$), the lowest-energy spin-wave excitation occurs at 20 GHz, far higher than the low-energy excitations (in the few GHz regime) we consider here. As a result, we expect the predominant dynamics to be that of vortices not spin waves. In Appendix 4.B, we consider a semi-classical analysis of the central circuit that identifies relevant vortex configurations and examines the spin-wave excitations.

We approximate the full Hilbert space using a charge basis $|n_1, n_2, n_3\rangle$ for Cooper pairs on each island, with $|n_i| \leq 4$. We check truncation and find no difference in increasing the maximum allowed charge by one. This creates a Hilbert space dimension of 9^3, for which the circuit Hamiltonian's eigensystem is straightforward to solve with a personal computer. The energy eigenvalues of the circuit as a function of A are shown in Fig. 4.2a. We note the presence of level crossings at $A \approx 0.2$ and $A \approx 0.26$ within the first four energy levels due to the high symmetry of the system.

We now consider the low-energy space of this system, and examine the presence and behavior of localized vortices. For low-frequency excitations (in the few GHz regime), and starting from the circuit ground state, we can expect to explore superpositions of only the first few eigenstates. To see the vortices, we identify the operators associated with the persistent currents around each of the small loops in

our central circuit, shown in Fig. 4.1b:

$$\hat{I}_i = \sin(\hat{\varphi}_{i+1} - \hat{\varphi}_i - 2\pi A) + \sin(\hat{\varphi}_i) - \sin(\hat{\varphi}_{i+1}) \ , \tag{4.6}$$

where we take $i + 1 = 4$ and $i = 1$ to be the same. To find the true current in the system, one multiplies Eq. (4.6) by I_{C}, the single-junction critical current. Figure 4.1d shows a schematic representation of each of these loop currents for our model of interest.

A local vortex is identified by a nonzero loop current in one or two of the three loops. If all three loop currents are equal, there is a persistent current circulating only about the exterior. For the energy eigenstates, Fig. 4.2b shows that the expectation values of each of the three loop currents are the same, and thus the eigenstates do not correspond to localized vortex states, although each eigenstate has a distinct persistent current around the exterior of the circuit. We also see that the level crossings manifest themselves in the subsequent persistent-current analysis, proving them to be regions of flux that create dramatic changes in behavior due to changes in the nature of the ground state, as seen in Figs. 4.2b, 4.2c, 4.3d, and 4.3e. Our chosen operating point for circulation, shown with a vertical grey line, is away from these crossings.

While there are no localized vortices for energy eigenstates, an incoming microwave photon can lead to the excitation of superpositions of circuit states. To examine this, we consider the matrix elements of the three loop currents over the first three eigenstates $\{|\varepsilon_0\rangle\,(=|G\rangle), |\varepsilon_1\rangle\,, |\varepsilon_2\rangle\}$, denoted $I_i^{kl} = \langle\varepsilon_k|\,\hat{I}_i\,|\varepsilon_l\rangle$, whose magnitudes are shown

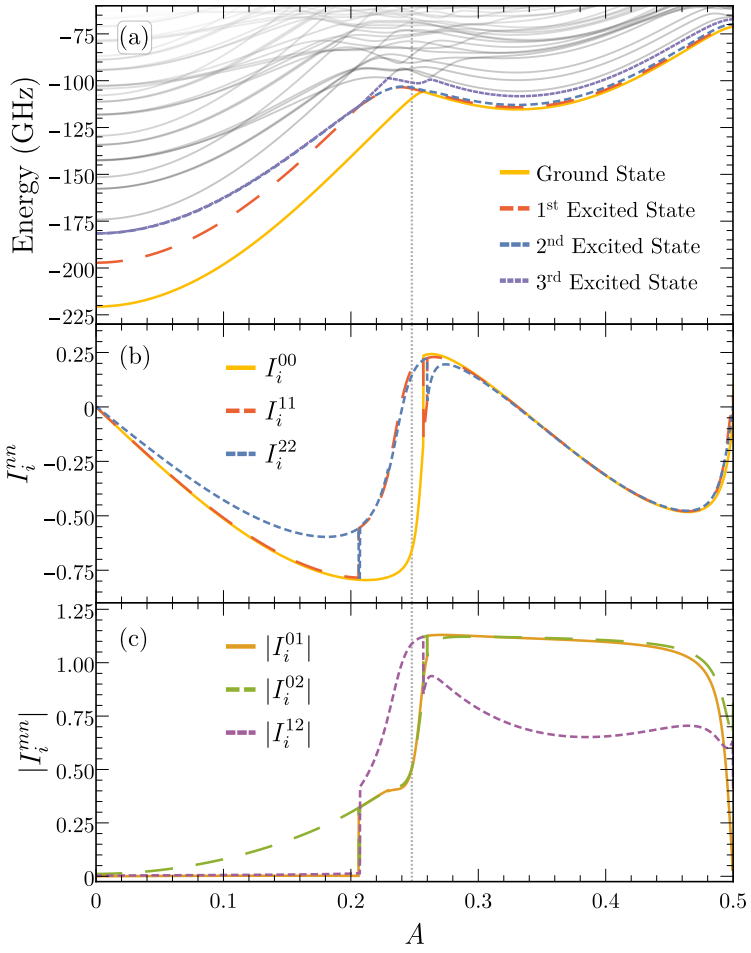


Figure 4.2: (a) The first fifty energy eigenvalues as a function of A, the flux penetration per loop. The relevant levels for this analysis are indicated in the legend; higher levels are grayed out. (b) Expectation values of the persistent currents in the ground state, first excited state, and second excited state for each loop ($i = 1, 2, 3$) of the circuit shown in Fig. 4.1b as a function of A. (c) Magnitudes of three of the off-diagonal elements of the loop-current operators in the eigenbasis for each loop ($i = 1, 2, 3$) as a function of A. Note that the true currents require re-scaling by I_C (here taken to be one). The circuit is periodic on $A \in \{0, 1\}$ and anti-symmetric about $A = 0.5$, hence only $0 \leq A \leq 0.5$ is shown here. Parameters chosen for these plots are $E_J/h = 4E_C/h \approx 45$ GHz, where $E_C = \frac{e^2}{2C_J}$, $E_J/E_\Sigma \approx 40$, $C_C = 6C_J$ and $C_G = 0.02C_J$. Offset charge is tuned such that the total Cooper pair number in the ground state is ≈ 1.2, with $N_{g1} = N_{g2} = N_{g3} \approx 0.4$.

in Figs. 4.2b and 4.2c. The symmetry of the circuit requires that the absolute value of each of the loop-current operator matrix elements be independent of i (i.e., the loop to which they correspond). However, as we now show, superpositions of eigenstates

exhibit localized vortices due to nontrivial phases of the off-diagonal matrix elements I_i^{kl} for $k \neq l$.

We write the argument of the I_i^{mn} matrix elements as ϕ_i^{mn}. The differences $\phi_i^{mn} - \phi_{i+1}^{mn}$ take only the values $\{0, \pm 2\pi/3\}$, as expected by the three-fold symmetry of the system. We now consider their role in circulation. Examining a superposition $c_m |\varepsilon_m\rangle + c_n |\varepsilon_n\rangle$, with $m > n$, we see that the i^{th} loop-current operator has an expectation value at time t of

$$\langle \hat{I}_i(t) \rangle \;=\; |c_m|^2 I_i^{mm} \;+\; |c_n|^2 I_i^{nn} + \; 2|c_m||c_n||I_i^{mn}| \cos\left(\omega_{mn} t - \theta_{mn} + \phi_i^{mn}\right) \quad , \qquad (4.7)$$

where ϕ_i^{mn} is the argument of the off-diagonal matrix element I_i^{mn}, θ_{mn} is the argument of $c_m^* c_n$, and $\omega_{mn} = \frac{(E_m - E_n)}{\hbar}$. Thus, we find a superposition of two states has, in general, a local vortex, and that these local vortices circulate (countercirculate) about the system when $\phi_i^{mn} - \phi_{i+1}^{mn} = \pm 2\pi/3$ at a frequency ω_{mn}. This is shown schematically in Fig. 4.3a.

Accordingly, we define the directional function for the difference in ϕ_i^{mn} variables modulo 2π as

$$\Theta^{mn} = \begin{cases} +1 \\ \;\;0 \\ -1 \end{cases} \quad \text{if } \phi_i^{mn} - \phi_{i+1}^{mn} = \begin{cases} +2\pi/3 \\ 0 \\ -2\pi/3 \end{cases} \quad , \qquad (4.8)$$

to allow us to plot the behavior of potential local vortices for different values of

m, n, and A, including the existence or absence of vortex circulation and in what direction. Θ^{mn} takes the value +1 for CW circulation, -1 for CCW circulation, and 0 for no circulation (absence of a local vortex). The directionality of vortex circulation associated with the two-state superpositions $0-1$ and $0-2$ as a function of A is shown in Figs. 4.3d and 4.3e, respectively.

4.2.4 Connecting Vortex Behavior with the Microwave Response

We now consider what happens if an oscillating voltage is applied to the j^{th} island of the central circuit via a coupling capacitor. We denote the coupling as $\hbar\Omega_j(t)\hat{B}_j$, with $\underline{\hat{B}} = \underline{\underline{K}}^{-1}\underline{\hat{N}}$ the vector of dimensionless voltages on each island. Using linear response theory [416–418], we can evaluate the expected loop currents at a later time for a perturbation $\Omega_j(t) \propto \delta(t)$ as

$$P_{ij}(t) = -i\left\langle [\hat{I}_i(t), \hat{B}_j(0)] \right\rangle \quad , \tag{4.9}$$

where we use P as in a dimensional setting this quantity has the unit of power, scaling as $\frac{2eI_{\text{C}}}{C_{\text{M}}}$, and can be interpreted as the power in the circuit induced by the drive. Using the Green's function relations, we then also expect that a monochromatic excitation at frequency ω gives the Fourier transform of this value for the expected long-time response of the different loop-current operators. We also examine, for the microwave

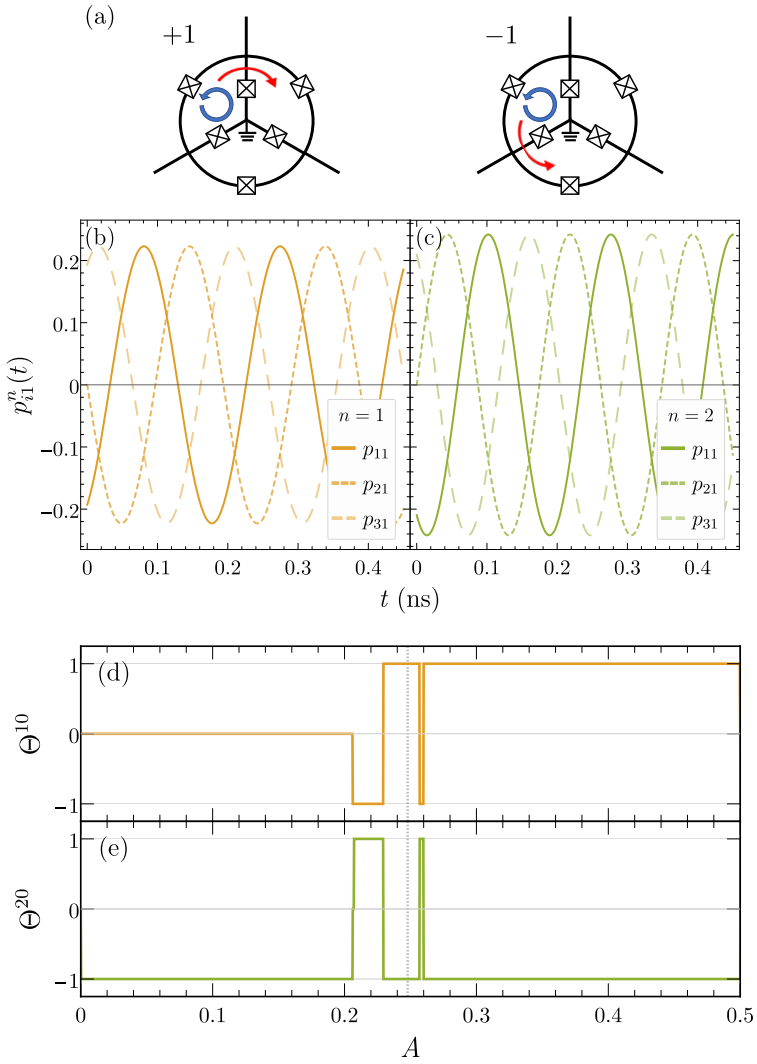


Figure 4.3: In (a), a schematic of the CW or CCW vortex tunneling shown in (b)-(e). The linear response of the loop currents in the central circuit due to the presence of a voltage on the first island is shown in (b)-(c). The contributions from the (b) first excited state and (c) second excited state are shown, demonstrating the creation and motion of vortices as a result of an incoming signal at our chosen operating point $A \approx 0.2478$. Vortex tunneling is shown in the two-state superpositions of (d) the ground state and first excited state and (e) the ground state and second excited state as a function of A, the flux penetration per loop. As in Fig. 4.2, the circuit is periodic on $A \in \{0, 1\}$ and anti-symmetric about $A = 0.5$, hence only $0 \leq A \leq 0.5$ is shown here. +1.0 indicates CW vortex tunneling, -1.0 indicates CCW vortex tunneling, and 0 indicates the absence of a vortex. Parameters for these plots are the same as Fig. 4.2.

response, the voltage-voltage correlation function,

$$T_{ij}(t) = -i \left\langle [\hat{B}_i(t), \hat{B}_j(0)] \right\rangle \quad , \tag{4.10}$$

whose Fourier transform is identified later as the transmission matrix of the circuit.

Working this out explicitly, we obtain

$$\begin{aligned} P_{ij}(t) &= -i \langle G | \, [e^{iHt} \hat{I}_i e^{-iHt}, \hat{B}_j] \, | G \rangle \\ &= -i \langle G | \, \hat{I}_i \sum_n e^{-i\varepsilon_n t} \, |\varepsilon_n\rangle\langle\varepsilon_n| \, \hat{B}_j \, | G \rangle + \text{h.c.} \ , \end{aligned} \tag{4.11}$$

and

$$\tilde{P}_{ij}(\omega) = -i \langle G | \, \hat{I}_i \sum_n \frac{|\varepsilon_n\rangle\langle\varepsilon_n|}{\omega - \varepsilon_n + i\gamma/2} \hat{B}_j \, | G \rangle \quad , \tag{4.12}$$

where $\gamma \to 0^+$ is taken to ensure causal ordering and $P_{ij}(\omega) = \tilde{P}_{ij}(\omega) + \tilde{P}^*_{ij}(-\omega)$. Note that a narrowband signal will preferentially excite states near the signal frequency, as is apparent in the denominator of Eq. (4.12).

Examining Eq. (4.11), we can interpret the linear response behavior as the evaluation of $\langle \hat{I}_i \rangle$ for a state of the form $|G\rangle - i \sum_n |\varepsilon_n\rangle\langle\varepsilon_n| \, (\sum_j \Omega_j \hat{B}_j) \, |G\rangle$ for $\Omega_j \to 0$. Thus, we can conclude that, insofar as $\hat{B}_j$ produces superpositions of energy eigenstates, we can expect the creation of moving vortices within the array upon an incoming signal. As we expect sinusoidal signals near the $0-1$ and $0-2$ transition frequencies, we plot the terms of $P_{i1}(t)$ corresponding to the first and second excited states in Figs. 4.3b and 4.3c [denoting the n^{th} term of $P_{i1}(t)$ as $p^n_{i1}(t)$] to illustrate the basic expected

dynamics of the system.

Noting that $-P_{1j}(-t)$ corresponds to the expected voltage at island j due to a current at loop 1, we can see the emergence of circulator dynamics: a voltage creates vortices, which rotate and re-radiate into the leads. Crucially, the observed rotation of vortices corresponds to highly nonreciprocal behavior, and thus we can expect generically that this central circuit will provide the opportunity for building a circulator. However, substantial practical details must now be worked out. We do so below, focusing on the linear response (low-power) regime.

4.3 Central Circuit Coupled to External Circuits

4.3.1 The Full Circuit Model

We now consider the central, three-island superconducting circuit capacitively coupled at each island to a resonator and voltage source, as shown in Fig. 4.1a. These resonators are included to enable effective impedance matching between incoming microwave signals and the central circuit, and are tuned in frequency and coupling to enable optimal performance. Each resonator port is opened to an external source of microwaves (i.e., a transmission line), allowing signals to flow into and out of the system. The central circuit, specified in Section 4.2.1, is threaded by an external flux Φ via the application of an external magnetic field.

The Hamiltonian for this model is composed of terms corresponding to the transmission lines, resonators, and central circuit, as well as each circuit-resonator inter-

action and resonator-transmission line interaction. Generally, this may be written as

$$H \;=\; H_{\mathrm{TL}} \;+\; H_{\mathrm{R}} \;+\; H_{\mathrm{CC}} \;+\; H_{\text{CC-R}} \;+\; H_{\text{R-TL}} \;. \tag{4.13}$$

Taking the weak-coupling limit, the rotating-wave approximation, and the Markov approximation, we can express each term of the Hamiltonian in Eq. (4.13) as follows:

$$\begin{aligned}
H_{\mathrm{TL}} &= \sum_{k=1}^{3} \int d\nu \; \hbar\nu \; \hat{b}_k^\dagger(\nu)\hat{b}_k(\nu) \\
H_{\mathrm{R}} &= \sum_{k=1}^{3} \; \hbar\omega_{\mathrm{R}} \; \hat{a}_k^\dagger \hat{a}_k \\
H_{\mathrm{CC}} &= 4E_\Sigma \; (\underline{\hat{N}} - \underline{N}_{\mathrm{g}})^T \underline{\underline{K}}^{-1} (\underline{\hat{N}} - \underline{N}_{\mathrm{g}}) + E_{\mathrm{J}} \; V(\underline{\hat{\varphi}}, \Phi) \;\cdot \\
H_{\text{CC-R}} &= \sum_{k=1}^{3} \; \hbar g \; (\hat{a}_k + \hat{a}_k^\dagger)\hat{B}_k \\
H_{\text{R-TL}} &= \sum_{k=1}^{3} \int d\nu \; i\hbar\sqrt{\frac{\kappa}{2\pi}} \; \left(\hat{b}_k^\dagger(\nu)\hat{a}_k - \hat{a}_k^\dagger \hat{b}_k(\nu)\right)
\end{aligned} \tag{4.14}$$

H_{TL} [400] describes each transmission line as containing an identical continuous spectrum of modes over frequency ν. H_{R} [276] is the contribution from the system's three identical resonators, consisting of a single low-lying mode with a characteristic frequency ω_{R}. The operators $\hat{a}_k^\dagger$ and $\hat{a}_k$ create or destroy a photon in the k^{th} resonator and satisfy the usual commutation relation $[\hat{a}_j, \hat{a}_k^\dagger] = \delta_{jk}$. Similarly, $\hat{b}_k^\dagger(\nu)$ and $\hat{b}_k(\nu)$ create or destroy a photon in the k^{th} transmission line and satisfy the commutation relation $[\hat{b}_j(\nu), \hat{b}_k^\dagger(\nu')] = \delta_{jk}\delta(\nu - \nu')$.

$H_{\text{CC-R}}$ and $H_{\text{R-TL}}$ [276, 400] are the interactions between each circuit island and

resonator and between each resonator and transmission line, respectively. By treating all resonators and all transmission lines as identical, we take the coupling constants, g and κ, to be identical across all three interactions, and later optimize them to ensure the best circulator performance. The operator $\hat{B}_k$, as defined in Section 4.2.4, is a dimensionless operator corresponding to the dimensionless voltage on the k^{th} island, defined as the k^{th} row of $\underline{\hat{B}} \;=\; \underline{\underline{K}}^{-1}\underline{\hat{N}}$.

Lastly, H_{CC} is as defined in Section 4.2.1 and describes the central superconducting circuit. Here we also include applied voltages V_{gk} (shown in Fig. 4.1a), which can lead to charge offset noise N_{gk} on each island. Appendix 4.C provides a term-by-term derivation of this Hamiltonian and the associated details of its coupling constants.

4.3.2 Single-Excitation S-Matrix Analysis

For this analysis, we work in the low-power, single-excitation limit, where we consider only one photon as input to or output from the system and require that the excitation energy in the system exist only in one component of the system at any one time — in one of the resonators, one of the transmission lines, or as an excited state of the central circuit. Upon enforcing this limit, we establish the S-matrix of the system using input-output theory. First, we write a generic state in this single-excitation manifold as:

$$|\Psi_0\rangle \;=\; \sum_{k=1}^{3} d_k \hat{a}_k^\dagger |G\rangle \;+\; \sum_n c_n |\varepsilon_n\rangle + \sum_{k=1}^{3} \int d\nu f_k(\nu)\; \hat{b}_k^\dagger(\nu) |G\rangle \quad , \tag{4.15}$$

where d_k, c_n, and $f_k(\nu)$ are time-dependent complex probability amplitudes for each state, and we abbreviate, with a slight abuse of notation, the system's ground state $|0,0,0,G,0,0,0\rangle$ as $|G\rangle$, and the excited circuit state with no photons in any resonator or transmission line $|0,0,0,\varepsilon_n,0,0,0\rangle$ as $|\varepsilon_n\rangle$. The summation over n is a summation over only the excited states of the circuit— it excludes the ground state as this state is not in the manifold being considered.

By using the Schrödinger equation, we establish equations of motion for the time-varying complex probability amplitudes appearing in Eq. (4.15). Details of this analysis can be found in Appendix 4.D. With these equations of motion, we can utilize input-output theory [400, 419] to develop a relation connecting in-going and out-going mode amplitudes via the S-matrix. Proceeding with this analysis results in the usual input-output relation

$$\underline{f_{\text{out}}}(\omega) = \underline{\underline{S}}(\omega)\ \underline{f_{\text{in}}}(\omega)\ , \tag{4.16}$$

where $f_{\text{in}}(\omega)$ and $f_{\text{out}}(\omega)$ are the in-going and out-going single-photon mode amplitudes in frequency space that reference either the initial or the final time t_{s} defined by

$$\frac{1}{\sqrt{2\pi}}\int d\nu\ e^{-i\nu(t-t_{\text{s}})} f_k(\nu,t_{\text{s}}) = \begin{cases} f_{\text{in},k} & \text{if } t > t_{\text{s}} \\ \\ f_{\text{out},k} & \text{if } t < t_{\text{s}} \end{cases} . \tag{4.17}$$

The single-photon S-matrix is found by solution in the frequency domain for the

coefficients in our ansatz, $|\Psi_0\rangle$. In frequency space we have

$$\underline{\underline{S}}(\omega) = \mathbb{1}_{3\times 3} + \kappa \, \underline{\underline{\chi}}(\omega) \ , \tag{4.18}$$

where the inverse susceptibility of the resonators combined with the central circuit is given by

$$\underline{\underline{\chi}}^{-1}(\omega) = [\, i(\omega - \omega_{\mathrm{R}}) - \frac{\kappa}{2} \,] \, \mathbb{1}_{3\times 3} + g^2 \, \underline{\underline{T}}(\omega) \ . \tag{4.19}$$

The elements of the term $\underline{\underline{T}}(\omega)$ are defined relative to starting in the ground state of the central circuit:

$$T_{jk}(\omega) = \sum_n \frac{1}{i\omega - i\varepsilon_n/\hbar} \langle G| \, \hat{B}_j \, |\varepsilon_n\rangle \, \langle \varepsilon_n| \, \hat{B}_k \, |G\rangle \ \ , \tag{4.20}$$

where we drop the tilde to indicate the complex-valued Fourier transform of the voltage-voltage linear response function given by Eq. (4.10) in Section 4.2.4. Having established the constituent pieces of this single-photon S-matrix, we can now move forward to determine the necessary conditions for the desired ideal circulation.

4.3.3 Conditions for Ideal Circulation

Having established the S-matrix using input-output theory, we wish to determine what conditions exist on parameters of the circuit such that this matrix matches that

of an ideal circulator's S-matrix:

$$\underline{\underline{S_{\text{ccw}}}} = \begin{bmatrix} 0 & 1 & 0 \\ 0 & 0 & 1 \\ 1 & 0 & 0 \end{bmatrix} \qquad \underline{\underline{S_{\text{cw}}}} = \begin{bmatrix} 0 & 0 & 1 \\ 1 & 0 & 0 \\ 0 & 1 & 0 \end{bmatrix} \quad . \tag{4.21}$$

Examination of Eqs. (4.18) and (4.19) indicates that any nonreciprocal behavior must originate from the circuit-specific term in the S-matrix, $\underline{\underline{T}}(\omega)$, as all other components are trivially diagonal. Focusing on this coupling matrix, we now work to find conditions for nonreciprocity. Since the central circuit of our model is symmetric with respect to cyclic permutation, the diagonal elements of $\underline{\underline{T}}(\omega)$ are all equal, as are the off-diagonal elements that are cyclic permutations of each other (i.e., $T_{12} = T_{23} = T_{31}$ and $T_{21} = T_{32} = T_{13}$). With this in mind, we rewrite Eq. (4.20) as

$$\underline{\underline{T}}(\omega) = -i \begin{bmatrix} \beta & \alpha & \alpha^* \\ \alpha^* & \beta & \alpha \\ \alpha & \alpha^* & \beta \end{bmatrix} \quad , \tag{4.22}$$

with $\alpha = iT_{jj+1}$ and $\beta = iT_{jj}$.

We note that this problem can be solved exactly— doing so reveals that optimal performance will occur when frequency shifts of the resonators due to the central circuit are compensated, and when the coupling to the central circuit is matched to the resonator decay. Explicitly, for a signal at target frequency ω_{T}, these conditions are

$$\omega_{\text{R}} = \omega_{\text{T}} - g^2\beta \quad , \tag{4.23}$$

and

$$\kappa = 2|\alpha|g^2 \ . \tag{4.24}$$

Rewriting $\underline{\underline{S}}(\omega_{\mathrm{T}})$ for these optimal values, we have the following matrix equation:

$$\underline{\underline{S}}(\omega_{\mathrm{T}}) = \mathbb{1} - \frac{2}{\mathbb{1} + i \begin{pmatrix} 0 & e^{-i\Delta\theta/6} & e^{i\Delta\theta/6} \\ e^{i\Delta\theta/6} & 0 & e^{-i\Delta\theta/6} \\ e^{-i\Delta\theta/6} & e^{i\Delta\theta/6} & 0 \end{pmatrix}} \ . \tag{4.25}$$

This shows that near resonance ($\omega \approx \omega_{\mathrm{T}}$), the S-matrix will be dominated by the behavior of $\underline{\underline{T}}(\omega)$. The first terms that contribute to nonreciprocal behavior can be understood by expanding $(\mathbb{1} + i\eta\underline{\underline{T}}(\omega))^{-1}$ in $\eta < |T|$. We see terms in the series that correspond to CW or CCW circulation beginning and ending at the same port— namely $T_{21}T_{32}T_{13}$ and $T_{12}T_{23}T_{31}$, respectively. If the central circuit is reciprocal, the quantity $|T_{12}T_{23}T_{31} - T_{21}T_{32}T_{13}|$, which represents the destructive interference between a signal going CW and a signal going CCW around the circuit, should be zero. However, if the system is ideally nonreciprocal, they instead constructively interfere. Writing $\alpha = |\alpha|e^{-i\Delta\theta/6}$, where the phase is written in terms of the difference accumulated between a CW path and a CCW path $\Delta\theta$, we have $|T_{12}T_{23}T_{31} - T_{21}T_{32}T_{13}| = 2|\alpha|^3|\sin(\Delta\theta/2)|$. Thus for optimal behavior,

$$\Delta\theta = \begin{cases} 0, \pm 2\pi ... \ , & \text{Reciprocal} \\ \\ \pm\pi, \pm 3\pi ... \ , & \text{Nonreciprocal} \end{cases} \ . \tag{4.26}$$

We now have three conditions on our system that, when satisfied, yield ideal circulation in either the CW direction or the CCW direction:

$$\begin{aligned} &\text{(a)} \quad \omega_{\mathrm{T}} \text{ s.t. } \Delta\theta = \pm\pi, \pm 3\pi ... \\ &\text{(b)} \quad \kappa = 2|\alpha| g^2 \\ &\text{(c)} \quad \omega_{\mathrm{R}} = \omega_{\mathrm{T}} - g^2 \beta \end{aligned} \quad . \tag{4.27}$$

With these conditions, as long as the central circuit has a target frequency for which the phase difference condition in Eq. (4.27a) holds, we may choose one of the external circuit parameters and let the conditions given in Eqs. (4.27b) and (4.27c) determine the others. Note that these results are consistent with those of previous work (e.g., Ref. [420]). Additionally, these results specify the phase differences corresponding to CW or CCW transmission, yielding

$$\Delta\theta = \begin{cases} -\pi, 3\pi, -5\pi ... \ , & \text{CW Transmission} \\ \\ \pi, -3\pi, 5\pi ... \ , & \text{CCW Transmission} \end{cases} \quad . \tag{4.28}$$

We also note the existence of more general conditions for ideal circulation, without a constraint on the phase difference, which we detail in Appendix 4.E. We now have all we need to explore our system.

4.4 Numerical Results

We proceed now with a numerical analysis, examining the input-output properties of the entire system using the analytical results established in Sections 4.3.2 and 4.3.3. Broadly speaking, we wish to enforce the conditions for ideal circulation given in Eq. (4.27) and then examine the S-matrix given altogether by Eqs. (4.18)-(4.20). As there are a variety of different regimes of the central circuit, we investigated several values of external flux A, described in Appendix 4.F. The best performing region was identified near $A \approx 0.2478$, and we focus on this in what follows.

To evaluate performance, we compute the elements of $\underline{\underline{T}}(\omega)$ [Eq. (4.20)] using the energy eigenstates and eigenvalues established numerically in Section 4.2.3. With the elements of $\underline{\underline{T}}(\omega)$, we find the phase difference $\Delta\theta$ as a function of potential incoming signal frequency ω. Examining the phase difference allows us to identify target frequencies where $\Delta\theta = \pm\pi, \pm 3\pi...$, and use Eqs. (4.27b) and (4.27c) to set external circuit parameters that fix κ, ω_{R}, and g. We then examine relevant S-matrix properties, as well as introduce variation in the offset charge on each island and flux penetration per loop to test the system's susceptibility to charge and flux disorder (i.e., variations of these parameters on timescales well below the circuit's bandwidth).

There are numerous points for which the phase difference condition is satisfied, as indicated in Fig. 4.4c. Of particular interest are instances such as the third and fourth points, found at $\Delta\theta = -\pi$, where $\omega_{\mathrm{T3}} \approx 4$ GHz, and at $\Delta\theta = -\pi$, where

$\omega_{\mathrm{T4}} \approx 5.46$ GHz, respectively. At the third point, the first derivative of the phase difference is zero, indicating much more stability with regard to frequency than at other target frequencies. At other points, the first derivative is much larger, and a small change in frequency results in significantly larger changes to $\Delta\theta$. The fourth point is situated between the first excited energy and the second excited energy of the central circuit. Due to the close proximity of this target frequency to two resonances of the circuit, it may be easier to inject energy into the circuit here than at other nonreciprocal points. In both cases, intuition suggests that these target frequencies, ω_{T3} and ω_{T4}, may allow for increased bandwidth of the system. This possibility is explored upon examination of elements of the S-matrix in Section 4.4.1.

4.4.1 Bandwidth, Nonreciprocity, and Circulation

We now determine performance via the S-matrix property that the normalized output power at the i^{th} port provided input at the j^{th} port is given by $|S_{ij}|^2$. Setting the external circuit parameters g, κ, and ω_{R} for the center frequencies $\omega_{\mathrm{T}i}$, with $i = 1, 2, 3, 4$, the target frequencies identified in Fig. 4.4c, we fix g to a reasonable but large value of $g = 1.6$ GHz and use Eq. (4.27) to determine κ and ω_{R}. Table 4.1 shows the resulting parameters for the first four target frequencies in Fig. 4.4c. For large bandwidth operation, g needs to be large, but making stronger coupling to the resonator has limits in other relevant parameters, as discussed in Appendix 4.G.

For each set of external circuit parameters specified by the target frequencies in

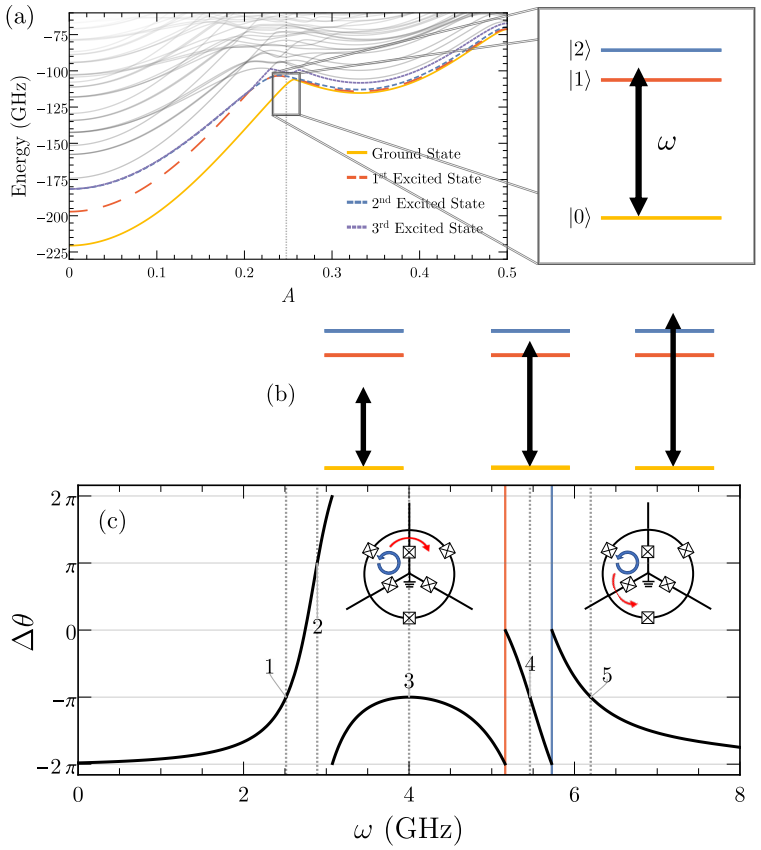


Figure 4.4: In (a) and (b), we highlight the energy level structure at our chosen operating point $A \approx 0.2478$ and the available transitions from the ground state. The phase difference $\Delta\theta$ as a function of driving frequency ω in shown in (c), with insets that indicate the predominant vortex dynamics. Dashed vertical lines indicate the target frequencies at which $\Delta\theta = \pm\pi,\ \pm 3\pi ...$— the values that satisfy the conditions for nonreciprocity. These points are enumerated for future reference. The red and blue vertical lines indicate the first and second excited energies, respectively, for the central circuit. Parameters chosen for this plot are $E_J/h = 4E_C/h \approx 45$ GHz, where $E_C = \frac{e^2}{2C_J}$, $E_J/E_\Sigma \approx 40$, $C_C = 6C_J$, $C_G = 0.02C_J$, and $A \approx 0.2478$. Offset charge is tuned such that the total Cooper pair number in the ground state is ≈ 1.2, with $N_{g1} = N_{g2} = N_{g3} \approx 0.4$.

Table 4.1, we wish to examine the bandwidth of the resulting transmission between two ports. For each case, the direction of maximum transmission is identified by the phase difference in Fig 4.4c, and we plot the normalized output power (in dB), displaced by the target frequency of each nonreciprocal point for comparison. These results are shown in Fig. 4.5a.

Table 4.1: External Circuit Parameters for Nonreciprocal Points

Point	ω_{T} (GHz)	g (GHz)	κ (GHz)	ω_{R} (GHz)
1	2.5137	1.6	0.01321	2.7408
2	2.8904	1.6	0.00995	3.1343
3	4.0005	1.6	0.08998	4.3396
4	5.4618	1.6	1.67917	5.7508

We define the bandwidth as a 3 dB window: the width of the signal in frequency space over which transmission is greater than 50%. Examination of Fig. 4.5a indicates that the parameters for the first and second points result in bandwidths of approximately 23 MHz and 17 MHz, respectively. At the third and fourth points, however, we see much larger bandwidths. At the third point we find a bandwidth of approximately 144 MHz, while the parameter set for the fourth point yields a very large bandwidth of approximately 1.34 GHz. These considerably larger bandwidths appear to confirm the intuition described previously: features in the phase difference such as that at the third point in Fig. 4.4c can lead to increased bandwidth, but even larger bandwidth is achieved when nonreciprocal points are situated near resonances (e.g., the fourth point), providing greater ease in inserting energy into the system (that is, a large $|\alpha|$) and a larger range of frequencies over which it is possible to do so. Since this large bandwidth is desirable in systems such as these, we proceed now using the external circuit parameters for the fourth point (at $\Delta\theta = -\pi$, where $\omega_{\mathrm{T4}} \approx 5.46$ GHz).

Upon fixing external circuit parameters to maximize bandwidth, we examine nonreciprocal behavior and ideal circulation in the system. To do so, we compare trans-

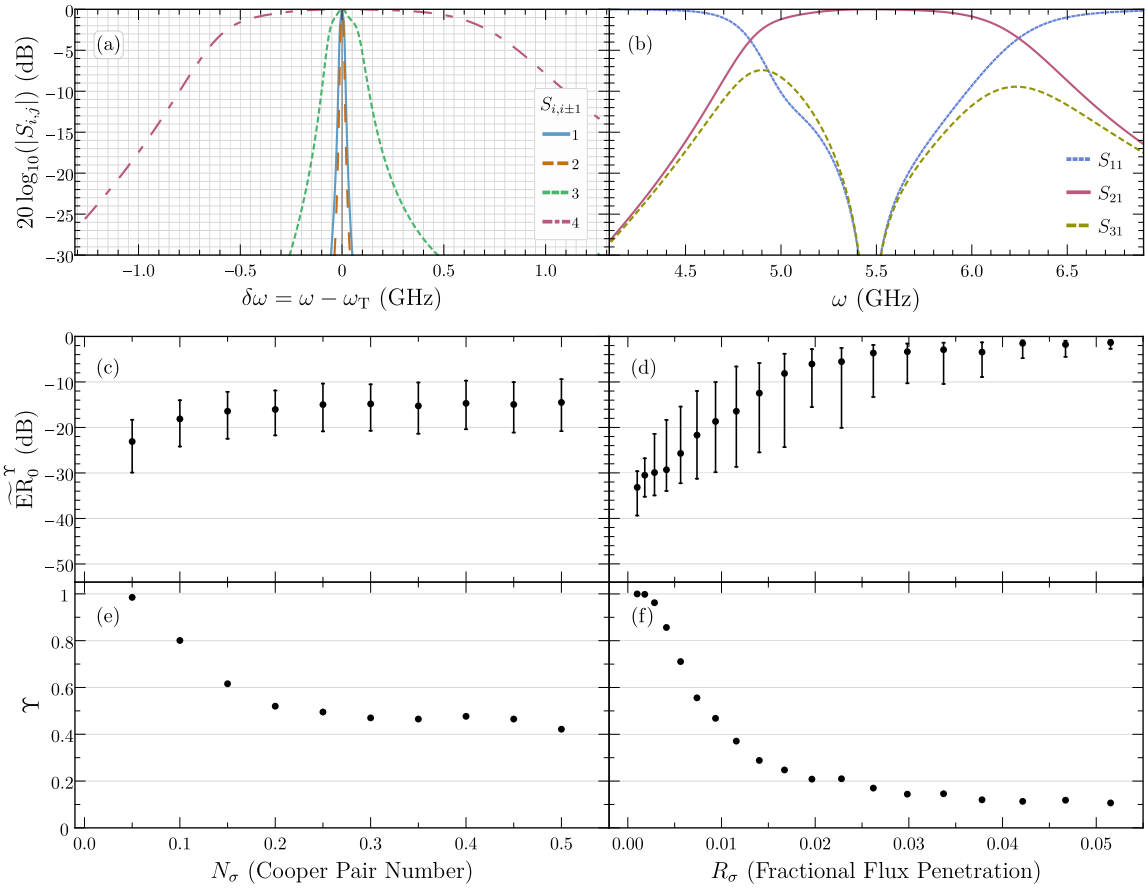


Figure 4.5: (a) A comparison of the normalized output power at the i^{th} port given input at the $i \pm 1^{\text{th}}$ port for each set of external circuit parameters shown in Table 4.1. For the first, second, and fourth points, transmission direction is such that $|S_{i,i-1}|^2$ is plotted. For the second point, $|S_{i,i+1}|^2$ is plotted. (b) A comparison of normalized output powers at each port assuming input at port one. At $\omega \approx 5.46$ GHz we observe full transmission in a CW fashion to the second port with zero transmission in the opposite direction, indicative of circulator behavior. Parameters and offset charge used are the same as in Fig. 4.4. External circuit parameters are set according to the fourth point, shown in Table 4.1. The median of ER_0^{Υ} (defined in Appendix 4.H.1 as the extinction ratio for devices with less than 1 dB of insertion loss), $\widetilde{\mathrm{ER}}_0^{\Upsilon}$, is plotted as a function of the standard deviation of (c) the charge noise distribution N_σ and (d) R_σ, the distribution of fractional flux penetration per loop. Error bars indicate the spread from the first to third quartile of ER_0^{Υ} for each value of N_σ and R_σ. Device yield Υ (defined in Appendix 4.H.1 as the fraction of devices with less than 1 dB of insertion loss) is plotted as a function of (e) N_σ and (f) R_σ. Parameters for ideal tuning in plots (c)-(f) are the same as in (b).

mission from a single port to each of the three outputs, plotting the normalized output powers (in dB) at each port provided input at a single port to observe any circulator

behavior. Figure 4.5b shows the resulting transmission to each port provided input at port one.

We see in Fig. 4.5b that microwave signals propagate in only one direction; there is a clear preferred direction of signal transmission, with full transmission at $\omega \approx 5.46$ GHz in the CW direction. Figure 4.5b demonstrates the system is lossless and nonreciprocal, and at $\omega \approx 5.46$ GHz is matched— all characteristics of an ideal circulator's S-matrix [405]. Note that due to the three-fold rotational symmetry of the system, these results are reproduced under all cyclic permutations.

4.4.2 Resilience to Charge and Flux Noise

Thus far, our analysis has assumed high symmetry: identical, static offset charges N_{gi} on each island due to the presence of applied voltages V_{gi} as well as identical loop areas in the central circuit (ensuring identical flux penetration per loop). In particular, given our expectation that charge offset is not a strong effect, we arbitrarily set $N_{g1} = N_{g2} = N_{g3} \approx 0.4$ Cooper pairs, $A \approx 0.2478$, and subsequently tuned the external circuit parameters for ideal circulation in the prior parts of this section. However, sources of noise that break this high symmetry are inevitable. Each island of the superconducting circuit may be subject to random variation in the offset charge that will necessarily affect performance given the intermediate energy regime in which we have chosen to work. Similarly, static flux variations across the device due to imperfections in manufacture of the central circuit or local impurities, unexpected

magnetic field gradients, and other phenomena will likely degrade the ideal circulation we have observe in Section 4.4.1. Therefore, we wish to address to what degree this is the case by introducing these sources of noise into our analysis. We note that an additional source of disorder is that of the Josephson junctions themselves; we examine this fabrication disorder in Appendix 4.H.2.

To test the system's susceptibility to local charge noise, we begin with the system tuned for ideal circulator behavior with equal, fixed offset charges N_{gi}. We then introduce an additional offset charge Δ_i that is unique for each island and randomly sampled from a normal distribution with a mean of $N_\mu = 0$ and a standard deviation N_σ in units of Cooper pair number. As detailed and defined in Appendix 4.H, we assess performance in the presence of charge noise by examining ER_0^Υ and Υ as a function of N_σ, shown in Figs. 4.5c and 4.5e, respectively. These quantities convey the distribution of the minimum of the extinction ratio for those noise samples resulting in less than 1 dB of insertion loss and the likelihood that this is the case for a sample size of 1200 noise samples.

Upon increasing N_σ, we observe an initial slight decrease in performance indicated by the increase in $\widetilde{\mathrm{ER}}_0^\Upsilon$ (the median of the distribution of ER_0^Υ), as shown in Fig. 4.5c. However, at $N_\sigma \approx 0.25$ Cooper pairs we observe saturation to $\widetilde{\mathrm{ER}}_0^\Upsilon \approx$ -15 dB. This saturation is reasonable given that the behavior of the circuit is unchanged upon rescaling by any integer number of Cooper pairs. Once N_σ exceeds ≈ 0.25, the distribution is wide enough to encompass this rescaling. The device yield Υ displays

similar behavior with increasing N_σ, as shown in Fig. 4.5e, where the likelihood of large transmission also saturates at ≈ 0.25 to about 50%. It is very promising that even in the presence of essentially arbitrary, static charge noise, the system retains its nonreciprocity.

To test the system's susceptibility to flux noise, we begin with the system tuned for ideal circulator behavior where all three loops of the central circuit are equal in area and penetrated by a flux $A \approx 0.2478$. We then introduce variation in the flux penetration of each loop, Δ_i', that is unique for each loop but maintains the total area and flux penetration of the ideal case (i.e., $\Delta_1' + \Delta_2' + \Delta_3' = 0$) to account for tuning the flux optimally for a given device (where the total field can be varied but not, perhaps, the individual loop fields). We take Δ_i' to be a fraction of A, the original flux penetration per loop, randomly sampling from a normal distribution with a mean of $R_\mu = 0$ and a standard deviation R_σ. As detailed and defined in Appendix 4.H, we assess performance in the presence of flux noise by examining ER_0^Υ and Υ as a function of R_σ, shown in Figs. 4.5d and 4.5f, respectively. As stated above, ER_0^Υ and Υ convey the distribution of the minimum of the extinction ratio for those noise samples resulting in less than 1 dB of insertion loss and the likelihood that this is the case for a sample size of 1200 noise samples.

Upon increasing R_σ, we observe a decrease in performance indicated by the increase in $\widetilde{\mathrm{ER}}_0^\Upsilon$ (the median of the distribution of ER_0^Υ), as shown in Fig. 4.5d. This degradation in performance is more substantial than in the charge noise case — de-

creasing more rapidly and saturating at $R_\sigma \approx 0.025$ to $\widetilde{\mathrm{ER}}_0^{\Upsilon} \approx$ -1 dB. Note that this flux noise model encompasses both random variations in loop area (e.g., imperfections in manufacture) as well as static flux variations across the device that may occur. We do not consider variation in total flux penetration, as this quantity can be calibrated experimentally.

4.5 Outlook

In this work, we have presented a theoretical analysis of a compact superconducting circuit operating as a circulator. Our investigation shows that operating in a non-charge-conserved regime with mobile vortices in the XY model, where the charging energy and Josephson energy scales are similar, leads to performance with a reduced dependence on static charge noise. Furthermore, the presence of both clockwise and counterclockwise vortex circulation at nearby energies appears to enable wide bandwidth performance that exceeds one GHz.

However, a variety of open questions remain for further investigation. It is likely possible to generalize the understanding achieved in this three-port model to a circulator with more than three ports (e.g., a double-junction circulator), which could be explored in future work. In addition, in the context of quantum computing and hardware, circulators are typically needed to handle both lower-power signal routing as well as higher-power device isolation. In this work, our single-photon analysis suggests the model is suitable for such low-power signal routing. However, a crucial

operational question is the performance of the system at higher powers, beyond the single-photon limit, thereby expanding the model's potential use cases. We anticipate that further exploration of the vortex-tunneling picture may elucidate regimes of operation where photon-vortex-photon terms enable high-power operation, but may also require more complex circuit designs. Another key question is whether ordered vortex states, such as those arising in larger arrays, can exhibit robust edge modes for vortex circulation that may further reduce the effects of noise and disorder in circulator performance. Additionally, implementation of this type of system in an experimental setting will help improve our understanding of quantum vortex dynamics and may lead to other avenues of exploration (see, e.g., Ref. [306]) for these and other topological excitations.

Appendix 4.A Alternative Circuit — Floating Central Island

The implementation of the grounded node present in the proposed central circuit (as shown in Fig. 4.1b) is a difficult experimental task. A simple modification — floating the central node — provides an alternative circuit that is easier to realize. In this appendix, we explore this alternative circuit (as shown in Fig. 4.1c), highlighting the connection between this model and the original and showing that similar behavior can be achieved without the presence of a central grounded node.

By replacing the central ground with a floating island, we introduce two additional degrees of freedom — the charge number and phase on this new island, $\hat{N}_0$ and $\hat{\varphi}_0$, respectively. To achieve similarity with the original model, the new central island should mimic a ground node, which we can accomplish by increasing the island's capacitance via its physical size. However, in doing so, we can no longer neglect the self-capacitance of the now large central island as well as the associated mutual capacitance it has with the outer three islands.

In all, the modified Hamiltonian is given by

$$\begin{aligned} H =& \frac{(2e)^2}{2} \left(\underline{\hat{N}} - \underline{N}_{\mathrm{g}}\right)^{\mathrm{T}} \underline{\underline{C}}^{-1} \left(\underline{\hat{N}} - \underline{N}_{\mathrm{g}}\right) \\ & - E_{\mathrm{J}} \sum_{i=1}^{3} \left[\cos(\hat{\varphi}_i - \hat{\varphi}_0) + \cos(\hat{\varphi}_{i+1} - \hat{\varphi}_i - 2\pi A)\right] \end{aligned} , \tag{4.A1}$$

where now $\underline{\hat{N}} = \{\hat{N}_1, \hat{N}_2, \hat{N}_3, \hat{N}_0\}$ and $\underline{N}_{\mathrm{g}} = \{N_{\mathrm{g1}}, N_{\mathrm{g2}}, N_{\mathrm{g3}}, 0\}$. The capacitance

matrix $\underline{\underline{C}}$ is now a 4x4 matrix with the form

$$\underline{\underline{C}} = \begin{bmatrix} C'_{\mathrm{S}} & -C_{\mathrm{J}} & -C_{\mathrm{J}} & -C_{\mathrm{F}} \\ -C_{\mathrm{J}} & C'_{\mathrm{S}} & -C_{\mathrm{J}} & -C_{\mathrm{F}} \\ -C_{\mathrm{J}} & -C_{\mathrm{J}} & C'_{\mathrm{S}} & -C_{\mathrm{F}} \\ -C_{\mathrm{F}} & -C_{\mathrm{F}} & -C_{\mathrm{F}} & C_0 + 3C_{\mathrm{F}} \end{bmatrix} , \tag{4.A2}$$

where $C'_{\mathrm{S}} = C_{\mathrm{C}} + C_{\mathrm{G}} + C_\mu + 3C_{\mathrm{J}}$ and $C_{\mathrm{F}} = C_{\mathrm{J}} + C_\mu$, with C_0 the self-capacitance of the central island, C_μ the mutual capacitance between it and the outer islands, and all other capacitances as defined in Section 4.2.1. We express the eigenvalues of the capacitance matrix in Eq.(4.A2) as

$$\begin{aligned} \lambda_1 = \lambda_2 &= C_{\mathrm{C}} + C_{\mathrm{G}} + C_\mu + 4C_{\mathrm{J}} \\ \lambda_3\lambda_4 &= C_0(C_{\mathrm{C}} + C_{\mathrm{G}} + C_\mu + C_{\mathrm{J}}) + 3(C_\mu + C_{\mathrm{J}})(C_{\mathrm{C}} + C_{\mathrm{G}}) \end{aligned} , \tag{4.A3}$$

and we define the quantity $\lambda' = C_0 C_{\mathrm{J}} + (C_{\mathrm{J}} + C_\mu)(4C_{\mathrm{J}} + C_\mu)$ so that we may write the inverse capacitance matrix $\underline{\underline{C}}^{-1}$ in the compact form

$$\underline{\underline{C}}^{-1} = \frac{1}{\lambda_1} \begin{bmatrix} 1+\delta' & \delta' & \delta' & \eta \\ \delta' & 1+\delta' & \delta' & \eta \\ \delta' & \delta' & 1+\delta' & \eta \\ \eta & \eta & \eta & \xi \end{bmatrix} , \tag{4.A4}$$

where $\delta' = \frac{\lambda'}{\lambda_3\lambda_4}$, $\eta = \frac{\lambda_1(C_{\mathrm{J}}+C_\mu)}{\lambda_3\lambda_4}$, and $\xi = \frac{\lambda_1(\lambda_1-3C_{\mathrm{J}})}{\lambda_3\lambda_4}$.

Notably, by replacing the central ground with a floating island, this alternative central circuit is now charge-conserving. We therefore define the total charge operator $\hat{N}_{\mathrm{T}} = \hat{N}_0 + \sum_{i=1}^{3} \hat{N}_i$, which commutes with the Hamiltonian $[H, \hat{N}_{\mathrm{T}}] = 0$ and whose expectation value is constant, yielding the total charge in the system $\langle \hat{N}_{\mathrm{T}} \rangle = n$. With

this conserved quantity, we can eliminate a dynamical degree of freedom.

In particular, by considering the unitary transformation

$$\hat{U} = e^{-i\sum_{i=1}^{3}\hat{N}_i\hat{\varphi}_0} \ , \tag{4.A5}$$

we can eliminate the charge number and phase operators of the central island from the Hamiltonian. Under this transformation, the charge number operators of the outer islands are unaffected while the charge number operator of the central island transforms as $\hat{N}_0 \to \hat{N}_0 - \sum_{i=1}^{3}\hat{N}_i$. Similarly, the phase operators of the outer islands transform as $\hat{\varphi}_i \to \hat{\varphi}_i + \hat{\varphi}_0$, while that of the central island is unchanged. Note that the total charge operator transforms as $\hat{N}_{\mathrm{T}} \to \hat{N}_0$, i.e., in this new frame, $\hat{N}_0$ represents the total charge and is the conserved quantity.

Performing the unitary transformation given in Eq. (4.A5) on the Hamiltonian in Eq. (4.A1), we find that the Hamiltonian in this frame takes the form

$$H' = 4E'_{\Sigma}\ (\underline{\hat{N}} - \underline{N}'_{\mathrm{g}})^{\mathrm{T}}\ \underline{\underline{K'}}^{-1}\ (\underline{\hat{N}} - \underline{N}'_{\mathrm{g}}) - E_{\mathrm{J}}\sum_{i=1}^{3}\left[\cos(\hat{\varphi}_i) + \cos(\hat{\varphi}_{i+1} - \hat{\varphi}_i - 2\pi A)\right] \ , \tag{4.A6}$$

where $\underline{\hat{N}} = \{\hat{N}_1, \hat{N}_2, \hat{N}_3\}$ and $\underline{N}'_{\mathrm{g}} = \{N'_{\mathrm{g}1}, N'_{\mathrm{g}2}, N'_{\mathrm{g}3}\}$. The form of the Hamiltonian in this frame is identical to that of our original model [H_{CC} given by Eq.(4.1)], where now the charging energy of the circuit E'_{Σ}, its dimensionless inverse capacitance matrix $\underline{\underline{K'}}^{-1}$, and the offset charges $N'_{\mathrm{g}i}$ all take on slightly modified forms. E'_{Σ} is defined as $E'_{\Sigma} = \frac{e^2}{2\lambda_1}$, where $\lambda_1 = C_{\mathrm{C}} + C_{\mathrm{G}} + C_{\mu} + 4C_{\mathrm{J}}$ plays the role of C_{M} from the main text

but modified by the presence of C_μ. We find that $\underline{\underline{K'}}^{-1}$ takes a familiar form,

$$\underline{\underline{K'}}^{-1} = \begin{bmatrix} 1+\rho & \rho & \rho \\ \rho & 1+\rho & \rho \\ \rho & \rho & 1+\rho \end{bmatrix} \quad , \tag{4.A7}$$

where $\rho = \delta' - 2\eta + \xi$, and we see upon comparison with Eq.(4.3), we just have $\delta \to \rho$. Finally, the new offset charges are uniformly shifted from their original value:

$$N'_{\mathrm{g}i} = N_{\mathrm{g}i} - \frac{\eta - \xi}{1+3\rho}\left(\hat{N}_0 - \sum_{j=1}^{3} N_{\mathrm{g}j}\right) \quad . \tag{4.A8}$$

Note that in the limit where $C_0 \to \infty$ and $C_\mu \to 0$, these modified components revert to the forms specific to H_{CC} (the original model's Hamiltonian). However, provided we have a relatively large C_0 and small C_μ (e.g., $C_0 = 30C_{\mathrm{J}}$ and $C_\mu = 0.25C_{\mathrm{J}}$ suffice), we find similar transmission performance in a zero-noise setting as compared with that of the original circuit with a central ground. Importantly, we see that aside from the more straightforward parameter-related modifications to E'_Σ and $\underline{\underline{K'}}^{-1}$, the presence of this new floating central island is equivalent to our original model with the addition of an offset charge that acts symmetrically on each island.

In Section 4.4.2, we examine the effects of random charge disorder on performance by introducing a shift in offset charge that is randomly sampled and unique to each island. Having uncovered the equivalence between our original model and this alternative circuit, we can examine the effect of replacing the central ground with a floating island by instead looking at uniform charge disorder, i.e., introducing a shift

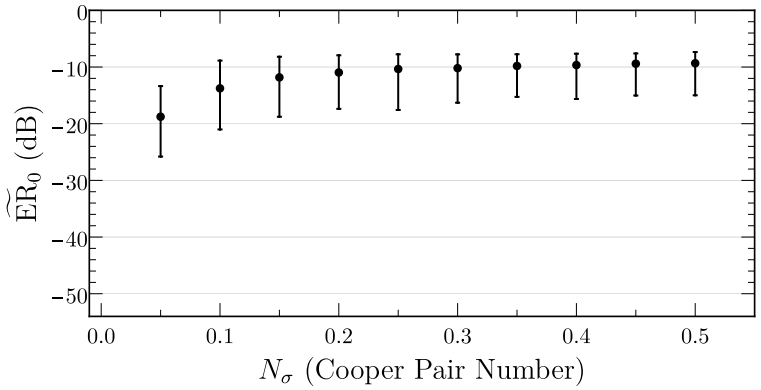


Figure 4.6: Uniform charge disorder in the original model. The median of ER_0, $\widetilde{\mathrm{ER}}_0$, is plotted as a function of the standard deviation of the charge noise distribution N_σ. Error bars indicate the spread from the first to third quartile of ER_0 for each value of N_σ. Parameters for ideal tuning are the same as in Fig. 4.5b.

in offset charge that is randomly sampled but identical for each island, in the original circuit with a central ground. This is shown in Fig. 4.6 without implementing any transmission threshold (as described Appendix 4.H.1).

Regarding performance, we see in Fig. 4.6 a saturation to $\widetilde{\mathrm{ER}}_0 \approx -10$ dB at $N_\sigma \approx 0.25$. We can understand the increase in N_σ shown on the x-axis in Fig. 4.6 as an increase in total charge N_0, since the uniform shift we introduce is linearly dependent on N_0 as shown by Eq.(4.A8). Generally, this total charge can be taken to be a constant scalar quantity, as it is typically fixed to some value in the process of cooling the system in an experimental setting. However, these results suggest continued performance even with the addition of a central island and some variation in N_0. While it may be possible in an experimental setting to compensate for the shift in offset charge due to the additional island, it is promising that without any intervention, we find good performance.

Appendix 4.B Classical and Semi-Classical Analysis of the Central Circuit

4.B.1 Classical Ground State Vortex Configuration

A fully classical analysis of the central circuit neglects the charging contribution to the Hamiltonian of the central circuit in Eq. 4.1, focusing solely on the tunneling potential $V(\underline{\varphi}, \Phi)$ [Eq. (4.4)] to find the phase configuration corresponding to an energy minimum and its associated vortex configuration. To this end, we numerically minimize the tunneling potential $V(\underline{\varphi}, \Phi)$ as a function of A, the flux penetration per loop. This yields a set of phase minima $\{\varphi_i^0\}$ for a given value of A such that $\frac{\partial V(\underline{\varphi},\Phi)}{\partial \varphi_i}|_{\varphi_i=\varphi_i^0} = 0$ for $i = 1,\ 2,\ 3$. We then evaluate the persistent current around the smallest loop of the circuit in Fig. 4.1b as a function of A, given by

$$I_i/I_{\rm C} = \sin\big(\varphi_{i+1}^0 - \varphi_i^0 - 2\pi A\big) + \sin\big(\varphi_i^0\big) - \sin\big(\varphi_{i+1}^0\big)\ , \tag{4.B1}$$

where $I_{\rm C}$ is the single-junction critical current and $i+1 = 4$ and $i = 1$ are equal. This expression is the classical counterpart to the loop current operators in Eq. (4.6). As in that case, a localized vortex is identified by a distinct loop current in one or two of the three loops. In Fig. 4.7, we plot the loop currents in each third of the central circuit as a function of A.

Of note, in the region of flux penetration between $0.25 < A < 0.5$, there is

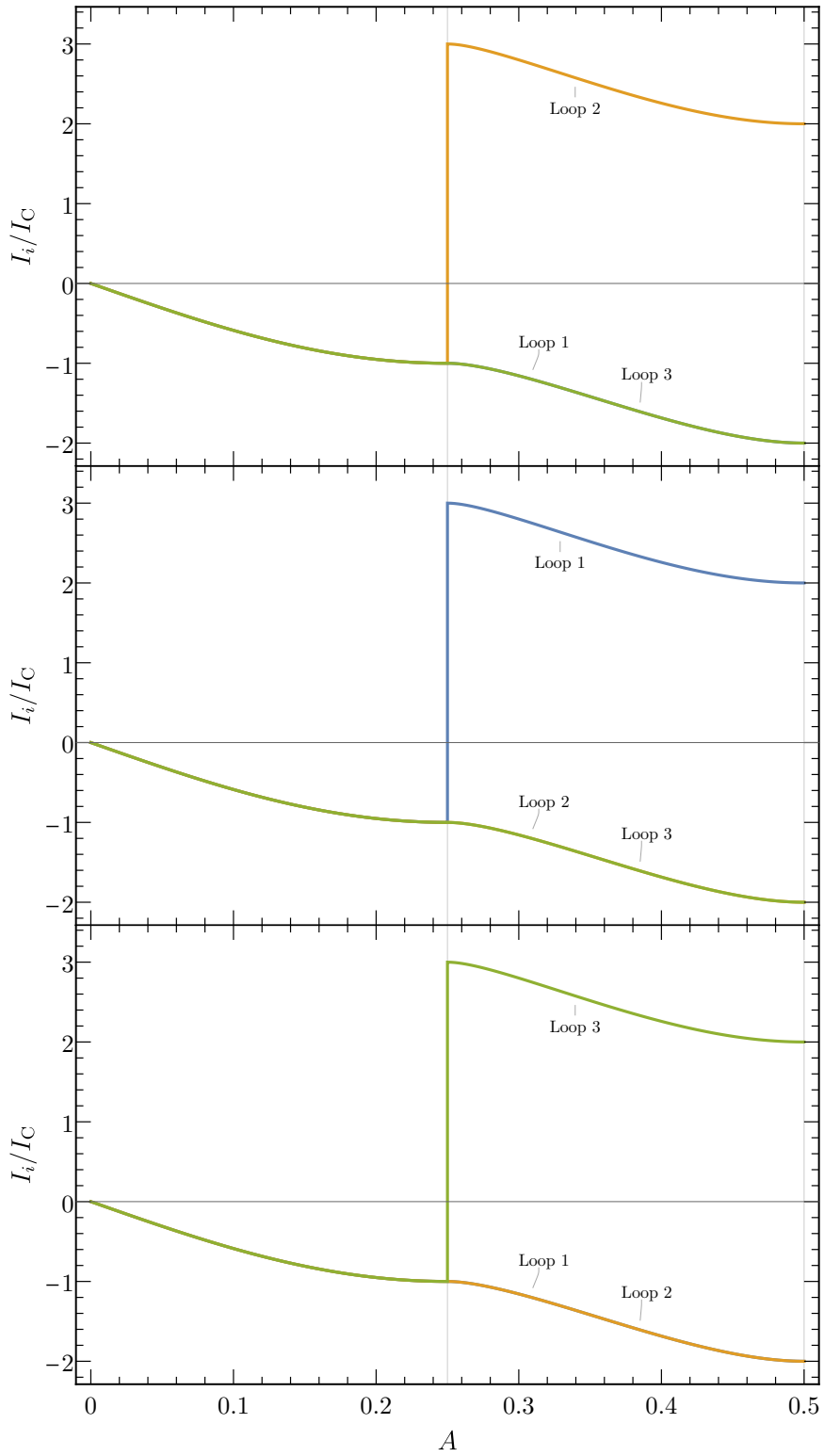


Figure 4.7: Loop currents corresponding to the classical ground state vortex configuration as a function of A. The circuit is periodic on $A \in \{0, 1\}$ and anti-symmetric about $A = 0.5$, hence only $0 \leq A \leq 0.5$ is shown here.

a three-fold degeneracy of phase minima, resulting in the three equivalent vortex configurations shown in Fig. 4.7. In the region of flux from $0 < A < 0.25$, the loop currents are equal, leading to a net zero current through the central junctions and a circulating current about the exterior. Between $0.25 < A < 0.5$, we find distinct current in one of the loops, i.e., a vortex, while the other two loops exhibit equivalent currents that cancel through their shared junction. This behavior is identical across all three degenerate configurations, occurring in cyclic permutation, indicating that it is energetically equivalent to have a vortex in any loop of the model. While the charging contribution to the Hamiltonian ultimately breaks the degeneracy, the presence of this three-fold degeneracy serves as the basis of our understanding for the operation of our circulator model in an intermediate tunneling regime, where the quantum tunneling of vortices between configurations may drive nonreciprocal behavior.

4.B.2 Semi-Classical Analysis of the Central Circuit

In a semi-classical regime, we incorporate the presence of small, perturbative charging effects by including a nonzero charging energy where $E_{\mathrm{J}} \gg E_{\mathrm{C}}$. The charging term then acts like a small kinetic energy for the phases, introducing phase fluctuations where the phases on each island experience small, collective oscillations, i.e., spin waves, about their minimum configuration $\{\varphi_i^0\}$.

To find the spin-wave frequencies, we begin by expanding the tunneling potential

$V(\underline{\varphi}, \Phi)$ about its minimum configuration $\{\varphi_i^0\}$,

$$V(\underline{\varphi}, \Phi) \;=\; V(\underline{\varphi}^0, \Phi) \,+\, \nabla V(\underline{\varphi}^0, \Phi)\cdot(\underline{\varphi}-\underline{\varphi}^0) \,+\, \frac{1}{2}(\underline{\varphi}-\underline{\varphi}^0)^{\mathrm{T}}\, \underline{\underline{D}}\, (\underline{\varphi}-\underline{\varphi}^0) \,+\ldots\;, \quad \text{(4.B2)}$$

where $\underline{\underline{D}}$ represents the Hessian matrix of $V(\underline{\varphi}, \Phi)$ with elements given by $D_{ij} = \frac{\partial^2 V(\underline{\varphi},\Phi)}{\partial_i \partial_j}|_{\underline{\varphi}=\underline{\varphi}^0}$. Scaling away the zeroth-order term and noting that the first-order term is zero by definition yields an approximately harmonic potential, appropriate for small oscillations. The Hamiltonian then takes the approximated form,

$$H_{\mathrm{CC}} \approx 4E_\Sigma\, \underline{\rho}^{\mathrm{T}}\, \underline{\underline{K}}^{-1}\, \underline{\rho} \;+\; \frac{1}{2}E_{\mathrm{J}}\, \underline{\eta}^{\mathrm{T}}\, \underline{\underline{D}}\, \underline{\eta}\;, \quad \text{(4.B3)}$$

where we have defined $\underline{\rho} = \underline{N} - \underline{N}_{\mathrm{g}}$ and $\underline{\eta} = \underline{\varphi} - \underline{\varphi}^0$.

The Hamiltonian in Eq. (4.B3) represents a set of coupled harmonic oscillators governed by the equation of motion

$$\frac{d^2\underline{\eta}}{dt^2} = -8E_\Sigma E_{\mathrm{J}}\, \underline{\underline{K}}^{-1}\underline{\underline{D}}\, \underline{\eta}\;, \quad \text{(4.B4)}$$

where the frequencies of the spin-wave modes are given by the square root of the eigenvalues of the matrix $8E_\Sigma E_{\mathrm{J}}\, \underline{\underline{K}}^{-1}\underline{\underline{D}}$. We plot each of the three spin-wave modes for the central circuit as a function of A in Fig. 4.8, where we observe a discontinuity at $A = 0.25$, analogous to the ground state vortex configuration in Section 4.B.1.

The spin-wave response of the system, analogous to coupled oscillator systems,

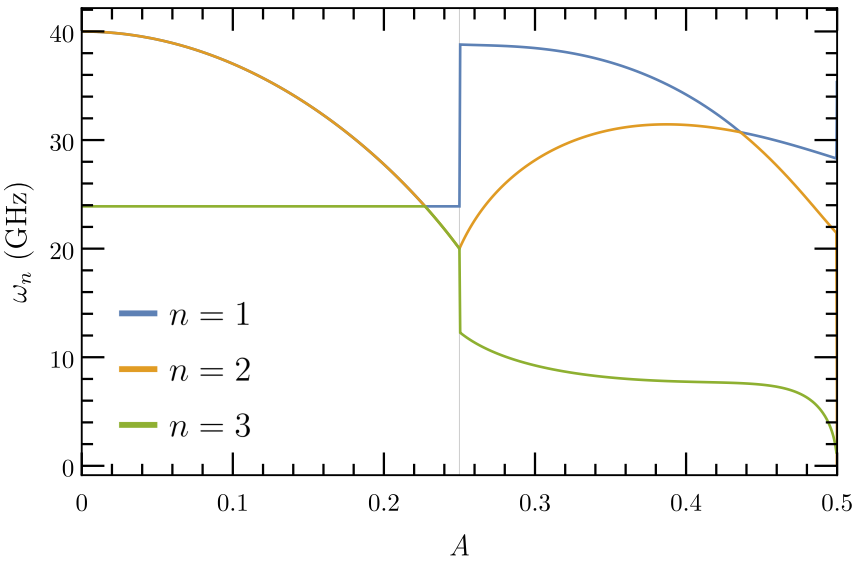


Figure 4.8: The three spin wave frequencies of the central circuit as a function of the flux penetration A. The circuit is periodic on $A \in \{0, 1\}$ and anti-symmetric about $A = 0.5$, hence only $0 \leq A \leq 0.5$ is shown here. Parameters chosen for these plots are $E_\mathrm{J}/h = 4E_\mathrm{C}/h \approx 45$ GHz, where $E_\mathrm{C} = \frac{e^2}{2C_\mathrm{J}}$, $E_\mathrm{J}/E_\Sigma \approx 40$, $C_\mathrm{C} = 6C_\mathrm{J}$ and $C_\mathrm{G} = 0.02C_\mathrm{J}$.

corresponds to combinations of the collective motion characterized by these frequencies and the associated eigenvectors. When treated quantum mechanically, these excitations are quantized, analogous to a system of quantum harmonic oscillators. To do so, we promote the conjugate variables N and φ to operators $\hat{N}$ and $\hat{\varphi}$ that obey the usual canonical commutation relation $[\hat{N}_i, \hat{\varphi}_j] = -i\delta_{ij}$. The Hamiltonian then takes the form

$$\hat{H}_\mathrm{CC} \approx 4E_\Sigma \, \underline{\hat{\rho}}^\mathrm{T} \, \underline{\underline{K}}^{-1} \, \underline{\hat{\rho}} \; + \; \frac{1}{2} E_\mathrm{J} \, \underline{\hat{\eta}}^\mathrm{T} \, \underline{\underline{D}} \, \underline{\hat{\eta}} \;, \tag{4.B5}$$

where $[\hat{\rho}_i, \hat{\eta}_j] = -i\delta_{ij}$. To define the usual creation and annihilation operators and diagonalize this Hamiltonian requires that we identify a transformation to new vari-

ables that simultaneously diagonalizes the matrices in both terms of Eq. (4.B5) while maintaining the canonical commutation relation of the original variables $\underline{\hat{\rho}}$ and $\underline{\hat{\eta}}$.

This diagonalization procedure is well-established (see, e.g., Refs. [403, 421]), as such, we do not include the specific details here. The resulting diagonalized Hamiltonian takes a form corresponding to a set of de-coupled harmonic oscillators,

$$\hat{H}_{\mathrm{CC}} = \frac{1}{2}\sum_i \left(\hat{P}_i^2 + \omega_i^2 \hat{X}_i^2\right) \quad , \tag{4.B6}$$

where normal-mode frequencies are given by ω_i and the new operators resulting from the diagonalization, $\hat{P}_i$ and $\hat{X}_i$, obey the commutation relation $[\hat{P}_i, \hat{X}_j] = -i\delta_{ij}$. Introducing the familiar operator transformation for the harmonic oscillator, we express $\hat{P}_i$ and $\hat{X}_i$ in terms of creation and annihilation operators,

$$\hat{X}_i = \sqrt{\frac{\hbar}{2\omega_i}}\left(\hat{a}_i^\dagger + \hat{a}_i\right) \quad , \qquad \hat{P}_i = i\sqrt{\frac{\hbar\omega_i}{2}}\left(\hat{a}_i^\dagger - \hat{a}_i\right) \quad , \tag{4.B7}$$

and re-express the Hamiltonian in terms of number operators for each mode $\hat{n}_i = \hat{a}_i^\dagger \hat{a}_i$,

$$\hat{H}_{\mathrm{CC}} = \sum_i \hbar\omega_i \left(\hat{n}_i + \frac{1}{2}\right) \quad . \tag{4.B8}$$

The quantized energy levels associated with the spin-wave modes are then specified by three quantum numbers — the occupation numbers associated with each mode. Fig. 4.9 shows the energy of the ground state and first three excited states as a function

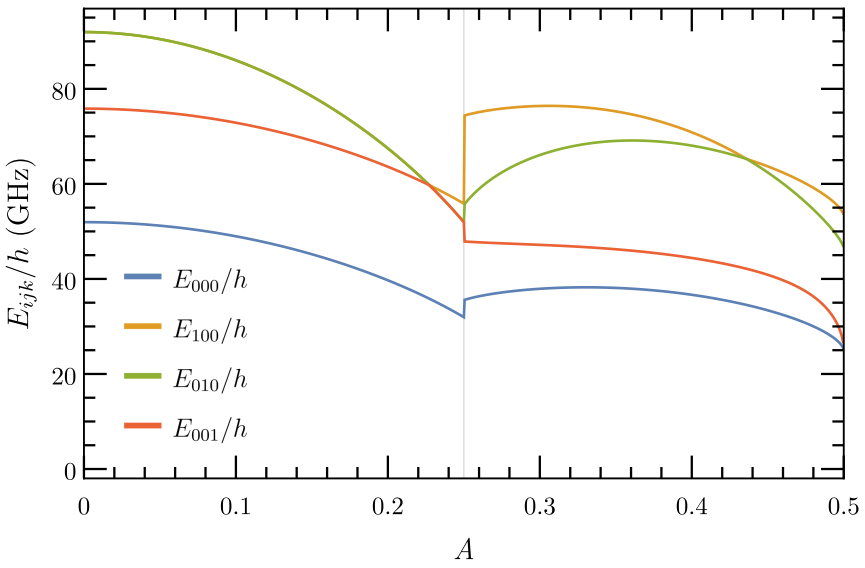


Figure 4.9: The first four energy levels associated with the spin-wave excitations of the central circuit as a function of the flux penetration A. The circuit is periodic on $A \in \{0, 1\}$ and anti-symmetric about $A = 0.5$, hence only $0 \leq A \leq 0.5$ is shown here. Parameters chosen for these plots are $E_\mathrm{J}/h = 4E_\mathrm{C}/h \approx 45$ GHz, where $E_\mathrm{C} = \frac{e^2}{2C_\mathrm{J}}$, $E_\mathrm{J}/E_\Sigma \approx 40$, $C_\mathrm{C} = 6C_\mathrm{J}$ and $C_\mathrm{G} = 0.02C_\mathrm{J}$.

of A. We note the continued presence of a discontinuity at $A = 0.25$, as well as the lowest-energy spin-wave excitation at our eventual operating point ($A = 0.2478$), approximately 20 GHz, corresponding to the transition frequency of $E_{001} - E_{000}$.

Appendix 4.C Derivation of the Full System Hamiltonian

In this appendix, we derive from first principles the Hamiltonian for the full circuit, shown schematically in Fig. 4.1a and given by Eq. (4.13) and Eq. (4.14). To do so, we consider a single 'arm' of the central circuit, which capacitively couples a transmission-line resonator to an island of the central circuit on one side and a semi-infinite transmission line on the other, shown in Fig. 4.10a. We assemble the Hamiltonian of this system by considering the continuum limit of the transmission-line resonator's lumped-element representation, shown in Figs. 4.10b, and extending this treatment to the semi-infinite transmission line, where we ultimately enforce the limit where $L_{\mathrm{TL}} \to \infty$.

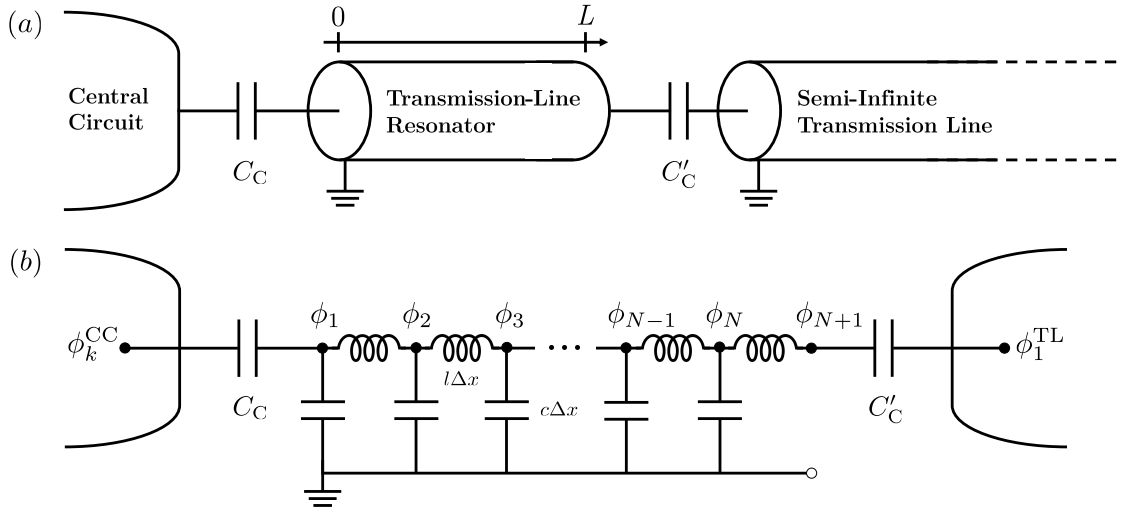


Figure 4.10: (a) Schematic of the k^{th} arm of the model that capacitively couples a transmission-line resonator to the k^{th} island of the central circuit as well as a semi-infinite transmission line. In (b), we depict the lumped-element representation of the transmission-line resonator, including generalized node flux variables ϕ_n and coupling capacitances C_{C} and C'_{C}.

4.C.1 Lagrangian of the Transmission-Line Resonators

We begin by establishing the Lagrangian of the transmission-line resonator, where we take the continuum limit of its lumped-element representation, shown in Fig. 4.10b. For a transmission-line resonator of length L with a capacitance and inductance per unit length of c and l, respectively, we take its lumped-element representation to be a ladder of LC oscillators [398]. This consists of N segments of length Δx such that $L = N\Delta x$, where each segment contains a capacitor with capacitance $c\Delta x$ and an inductor with inductance $l\Delta x$ as shown in Fig. 4.10b. The transmission-line resonator is capacitively coupled via the capacitance C_{C} to the k^{th} island of the central circuit on one side, while on the other, it is capacitively coupled to the semi-infinite transmission line via the capacitance C'_{C}.

We find the equations of motion governing the node fluxes by proceeding with the usual methods of circuit quantization outlined in Appendix 3.B of this dissertation and Ref. [325]. Choosing a ground node as shown in Fig. 4.10 and a spanning tree along the capacitive branches, we find the equation of motion for the node fluxes of the interior ($i \neq 1, N+1$) to be

$$c\Delta x\ddot{\phi}_i = \frac{[(\phi_{i-1} - \phi_i) - (\phi_i - \phi_{i+1})]}{l\Delta x} \ . \tag{4.C1}$$

For $i = 1$ and $i = N + 1$, we have

$$c\Delta x\ddot{\phi}_1 - C_{\rm C}(\ddot{\phi}_k^{\rm CC} - \ddot{\phi}_1) = \frac{-(\phi_1 - \phi_2)}{l\Delta x} \tag{4.C2}$$

and

$$C'_{\rm C}(\ddot{\phi}_{N+1} - \ddot{\phi}_1^{\rm TL}) = \frac{(\phi_N - \phi_{N+1})}{l\Delta x} \ , \tag{4.C3}$$

respectively. These equations of motion imply a Lagrangian of the form,

$$\begin{aligned}\mathcal{L} = \frac{1}{2}C_{\rm C}(\dot{\phi}_1 - \dot{\phi}_k^{\rm CC})^2 + \frac{1}{2}C'_{\rm C}(\dot{\phi}_{N+1} - \dot{\phi}_1^{\rm TL})^2 + \mathcal{L}'_{\rm CC} + \mathcal{L}'_{\rm TL} \\ + \sum_{i=1}^{N}\frac{1}{2}c\Delta x\dot{\phi}_i^2 - \sum_{i=1}^{N}\frac{1}{2l\Delta x}(\phi_i - \phi_{i+1})^2 \ ,\end{aligned} \tag{4.C4}$$

where we have incorporated the degrees of freedom of the central circuit and the semi-infinite transmission line by adding the terms $\mathcal{L}'_{\rm CC}$ and $\mathcal{L}'_{\rm TL}$, which depend only on their respective degrees of freedom.

We then re-express the total Lagrangian compactly in terms of the contributions from all three systems as well as their couplings,

$$\mathcal{L} = \mathcal{L}_{\rm CC} + \mathcal{L}_{\rm TL} + \mathcal{L}_{\rm R} + \mathcal{L}_{\text{CC-R}} + \mathcal{L}_{\text{R-TL}} \ . \tag{4.C5}$$

Here, $\mathcal{L}_{\rm CC}$ and $\mathcal{L}_{\rm TL}$ represent the (for now) general contributions from the central

circuit and semi-infinite transmission line,

$$\begin{aligned} \mathcal{L}_{\mathrm{CC}} &= \mathcal{L}'_{\mathrm{CC}} + \frac{1}{2}\, C_{\mathrm{C}} (\dot{\phi}_k^{\mathrm{CC}})^2 \\ \mathcal{L}_{\mathrm{TL}} &= \mathcal{L}'_{\mathrm{TL}} + \frac{1}{2}\, C'_{\mathrm{C}} (\dot{\phi}_1^{\mathrm{TL}})^2 \end{aligned} \quad , \tag{4.C6}$$

while the coupling between the central circuit and the transmission-line resonator as well as the coupling between the transmission-line resonator and the semi-infinite transmission line are given by

$$\begin{aligned} \mathcal{L}_{\text{CC-R}} &= -C_{\mathrm{C}} \dot{\phi}_k^{\mathrm{CC}} \dot{\phi}_1 \\ \mathcal{L}_{\text{R-TL}} &= -C'_{\mathrm{C}} \dot{\phi}_1^{\mathrm{TL}} \dot{\phi}_{N+1} \end{aligned} \quad . \tag{4.C7}$$

Finally, the Lagrangian for the transmission-line resonator is written as

$$\mathcal{L}_{\mathrm{R}} = \sum_{i=1}^{N} \frac{1}{2} c \Delta x \dot{\phi}_i^2 - \sum_{i=1}^{N} \frac{1}{2l\Delta x} (\phi_i - \phi_{i+1})^2 + \frac{1}{2} C_{\mathrm{C}} \dot{\phi_1}^2 + \frac{1}{2} C'_{\mathrm{C}} \dot{\phi}_{N+1}^2 \ . \tag{4.C8}$$

Focusing on the resonator's contribution to the Lagrangian, whose equations of motion are similarly written to those in Eqs. (4.C1)-(4.C3) (sans contributions from $\dot{\phi}_k^{\mathrm{CC}}$ and $\dot{\phi}_1^{\mathrm{TL}}$), we take the continuum limit, fixing the length of the resonator L and taking $N \to \infty$, forcing $\Delta x \to 0$. In doing so, the discrete node fluxes along the length of the resonator become a continuous function, where the differences between ϕ_i and the associated summations over i that appear in $\mathcal{L}_{\mathrm{R}}$ and its equations of motion become derivatives and integrals in the usual way [422]. Thus, we find the

Lagrangian,

$$\mathcal{L}_{\mathrm{R}} = \int_0^L \left[\frac{c}{2} \left(\frac{\partial \phi(x,t)}{\partial t} \right)^2 - \frac{1}{2l} \left(\frac{\partial \phi(x,t)}{\partial x} \right)^2 \right] dx + \frac{1}{2} C_{\mathrm{C}} \left[\frac{\partial \phi(x,t)}{\partial t} \bigg|_{x=0} \right]^2 + \frac{1}{2} C'_{\mathrm{C}} \left[\frac{\partial \phi(x,t)}{\partial t} \bigg|_{x=L} \right]^2 , \tag{4.C9}$$

as well as the equation of motion and its associated boundary conditions,

$$\frac{\partial^2 \phi(x,t)}{\partial t^2} = \frac{1}{lc} \frac{\partial^2 \phi(x,t)}{\partial x^2} , \tag{4.C10}$$

and

$$\begin{aligned} lC_{\mathrm{C}} \frac{\partial^2 \phi(x,t)}{\partial t^2} \bigg|_{x=0} &= \frac{\partial \phi(x,t)}{\partial x} \bigg|_{x=0} \\ lC'_{\mathrm{C}} \frac{\partial^2 \phi(x,t)}{\partial t^2} \bigg|_{x=L} &= -\frac{\partial \phi(x,t)}{\partial x} \bigg|_{x=L} \end{aligned} . \tag{4.C11}$$

Upon examination of Eq. (4.C10), the equation of motion governing the flux $\phi(x,t)$ inside the resonator is the wave equation, which is solved via a separable trial solution. Decomposing the flux into a time-varying amplitude $\psi(t)$ and a spatially-varying mode $u(x)$, i.e. $\phi(x,t) = \psi(t)u(x)$, and substituting this trial solution into the equation of motion, we find the expected separation of variables with a common constant of separation. Choosing this constant to be $-\omega^2$, we find that each satisfies its own ordinary differential equation, with known oscillatory solutions [422]. These differential

equations and solutions are

$$\frac{d^2\psi(t)}{dt^2} = -\omega^2\psi(t) \;\Rightarrow\; \psi(t) = A\cos(\omega t) + B\sin(\omega t) \tag{4.C12}$$

and

$$\frac{d^2u(x)}{dx^2} = -\omega^2 lc\; u(x) \;\Rightarrow\; u(x) = \alpha\cos\Big(\omega\sqrt{lc}\; x\Big) + \beta\sin\Big(\omega\sqrt{lc}\; x\Big)\;. \tag{4.C13}$$

Using this trial solution, the boundary conditions in Eq. (4.C11) become boundary conditions on only the spatially varying function $u(x)$,

$$\begin{aligned} -\omega^2 l C_{\mathrm{C}} u(0) &= \left.\frac{\partial u(x)}{\partial x}\right|_{x=0} \\ \omega^2 l C'_{\mathrm{C}} u(L) &= \left.\frac{\partial u(x)}{\partial x}\right|_{x=L} \end{aligned}\;. \tag{4.C14}$$

We can then use the solutions in Eq. (4.C13) combined with the boundary conditions above to establish a transcendental equation in ω,

$$\tan\Big(\omega\sqrt{lc}L\Big) = \frac{-\omega\sqrt{lc}L\frac{(C_{\mathrm{C}}+C'_{\mathrm{C}})}{cL}}{1-(\omega\sqrt{lc}L)^2\frac{C_{\mathrm{C}}C'_{\mathrm{C}}}{c^2L^2}}\;, \tag{4.C15}$$

which when solved, results in discrete mode frequencies ω_n for the system.

Provided the discrete, spatially-varying modes given by Eq. (4.C15), we can establish an orthonormalization condition between them using the boundary conditions

in Eq. (4.C11) combined with the expression

$$u_n^*(x)\ \frac{d^2u_m(x)}{dx^2}\ -\ u_m(x)\ \frac{d^2u_n^*(x)}{dx^2}\ . \tag{4.C16}$$

This expression can be equivalently re-written in terms of a single derivative or using the equation of motion [Eq. (4.C10)],

$$\frac{d}{dx}\left(u_n^*(x)\ \frac{du_m(x)}{dx}\ -\ u_m(x)\ \frac{du_n^*(x)}{dx}\right) = lc\ (\omega_n^2-\omega_m^2)u_m(x)u_n^*(x)\ , \tag{4.C17}$$

which can be integrated over the length of the resonator to find

$$\int_0^L \frac{d}{dx}\left(u_n^*(x)\frac{du_m(x)}{dx} - u_m(x)\frac{du_n^*(x)}{dx}\right)dx = lc(\omega_n^2-\omega_m^2)\int_0^L u_m(x)u_n^*(x)dx \tag{4.C18}$$

The above is simplified by using the boundary conditions in Eq. (4.C11) to evaluate the left-hand side, resulting in the orthonormalization condition,

$$c\int_0^L u_m(x)u_n^*(x)dx + C_{\mathrm{C}}'u_m(L)u_n^*(L) + C_{\mathrm{C}}u_m(0)u_n^*(0) = \delta_{mn}\ . \tag{4.C19}$$

We have now fully specified the spatially-varying part of the total solution, which consists of various discrete modes n. To write the most general solution, we assemble

a superposition of all modes,

$$\phi(x,t) = \sum_n \psi_n(t) u_n(x) \tag{4.C20}$$

where we have added a mode index to both $\psi(t)$ and $u(x)$.

We use the established solutions for the resonator's equation of motion to re-express $\mathcal{L}_{\mathrm{R}}$ in terms of these discrete spatial modes, leaving only the time-varying solution. Inserting the general solution into $\mathcal{L}_{\mathrm{R}}$ [Eq. (4.C9)] and recalling the orthonormalization in Eq. (4.C19), we find

$$\mathcal{L}_{\mathrm{R}} = \frac{1}{2} \sum_n \left(\left[\frac{d\psi_n(t)}{dt} \right]^2 - \omega_n^2 \psi_n^2(t) \right) \quad . \tag{4.C21}$$

However, in our particular system, we consider three identical, single-mode resonators in each of the three arms of the full circuit. Thus, we write the Lagrangian for the resonators, along with the associated coupling terms, as

$$\mathcal{L}_{\mathrm{R}} = \frac{1}{2} \sum_{k=1}^{3} \left(\left[\frac{d\psi_k(t)}{dt} \right]^2 - \omega_{\mathrm{R}}^2 \psi_k^2(t) \right) \quad , \tag{4.C22}$$

and

$$\begin{aligned} \mathcal{L}_{\text{CC-R}} &= -C_{\mathrm{C}} \sum_{k=1}^{3} \dot{\phi}_k^{\mathrm{CC}} \frac{d\psi_k(t)}{dt} u_k(0) \\ \mathcal{L}_{\text{R-TL}} &= -C_{\mathrm{C}}' \sum_{k=1}^{3} \dot{\phi}_{1,k}^{\mathrm{TL}} \frac{d\psi_k(t)}{dt} u_k(L) \end{aligned} \quad , \tag{4.C23}$$

where each resonator has a characteristic frequency $\omega_{\mathrm{R}}/2\pi$ and we have replaced the mode index n with an index k corresponding to each arm of the full circuit.

4.C.2 Assembling the Remainder of the Full System Lagrangian

Establishing the Lagrangian for the semi-infinite transmission lines in the full circuit proceeds identically to that of the transmission-line resonators, with one key distinction. Each transmission line acts as an external bath or source of microwave signals, therefore, we retain the sum over all modes in its Lagrangian and associated coupling term. Once we establish the Hamiltonian and quantize the system, the semi-infinite limit $L_{\mathrm{TL}} \to \infty$ is enforced and these discrete mode frequencies become a continuum. We also note that at this stage we take the transmission lines to be of finite length L_{TL}, however, as we ultimately take $L_{\mathrm{TL}} \to \infty$, we neglect any potential contribution to the Lagrangian due to coupling at $x = L_{\mathrm{TL}}$. With these considerations in mind, the Lagrangian for the transmission lines is written as,

$$\mathcal{L}_{\mathrm{TL}} = \frac{1}{2}\sum_{k=1}^{3}\sum_{n}\left(\left[\frac{d\xi_{n,k}(t)}{dt}\right]^2 - \omega_n^2\xi_{n,k}^2(t)\right) \ , \tag{4.C24}$$

while the coupling term between the transmission-line resonators and transmission lines is,

$$\mathcal{L}_{\text{R-TL}} = -C_{\mathrm{C}}'\sum_{k=1}^{3}\left(\sum_{n}\frac{d\xi_{n,k}(t)}{dt}w_{n,k}(0)\right)\frac{d\psi_k(t)}{dt}u_k(L) \ , \tag{4.C25}$$

where we have taken $\phi_k^{\mathrm{TL}}(x,t) = \sum_n \xi_{n,k}(t) w_{n,k}(x)$ to distinguish its solutions from those of the resonators and included the summation over k to account for the three identical arms of the full circuit.

Lastly, we establish the Lagrangian for the central circuit shown in Fig. 4.1b, including the capacitive couplings to the transmission-line resonator and offset voltage V_{g} via the capacitances C_{C} and C_{G}, respectively. Using methods from circuit analysis outlined in Appendix 3.B of this dissertation and Ref. [325], we establish the relevant degrees of freedom and their equations of motion, yielding the Lagrangian,

$$\mathcal{L}_{\mathrm{CC}} = \frac{1}{2}\dot{\underline{\phi}}^T \underline{\underline{C}}\, \dot{\underline{\phi}} \;-\; C_{\mathrm{G}} \underline{V}_{\mathrm{g}}^T \dot{\underline{\phi}} \;-\; E_J\, V(\underline{\phi}, \Phi) \;. \tag{4.C26}$$

Here, we write the Lagrangian in terms of the node fluxes of each island of the central circuit, where $\underline{\underline{C}}$ represents the capacitance matrix of the central circuit, given by Eq. (4.2) and $V(\underline{\phi}, \Phi)$ is its associated tunneling potential, given by Eq. (4.4). We note that the additional terms arising from the coupling to the resonator, which depend on the resonator's degrees of freedom, have already been accounted for in the resonator Lagrangian $\mathcal{L}_{\mathrm{R}}$ and the circuit-resonator coupling $\mathcal{L}_{\text{CC-R}}$. We have also neglected overall constants that do not depend on ϕ or $\dot{\phi}$.

4.C.3 The Weak Coupling Limit

Having specified each term in the total Lagrangian in Eq. (4.C5), we proceed by enforcing the weak coupling limit, where we take the capacitances of the transmission-

line resonators cL and semi-infinite transmission lines $c_{\rm TL}L_{\rm TL}$ to be much larger than the coupling capacitances $C_{\rm C}$ and $C'_{\rm C}$. The effect of this limit is to simplify the form of the resonator's and transmission line's mode frequencies, while directly specifying the general coefficients appearing in the solutions $u_k(x)$ and $w_{n,k}(x)$ as well as the Lagrangian. It also serves to de-couple the conjugate momenta we find from the total Lagrangian, such that the Legendre transform for finding the Hamiltonian is greatly simplified and the interactions take simple forms.

Taking the limit where $C_{\rm C}, C'_{\rm C} \gg cL, c_{\rm TL}L_{\rm TL}$, the transcendental equation in Eq. (4.C15) specifying the mode frequencies ω_n for the resonators and transmission lines simplifies to,

$$\tan\Big(\omega\sqrt{lc}L\Big) \approx 0 \ , \tag{4.C27}$$

which yields solutions $\omega_n = n\pi/\sqrt{lc}L$, where $n = 0, 1, 2....$ For the single-mode transmission-line resonators, we take $n = 1$ to establish $\omega_{\rm R} = \pi/\sqrt{lc}L$. For the transmission lines, we incorporate its specific length $L_{\rm TL}$, capacitance per unit length $c_{\rm TL}$, and inductance per unit length $l_{\rm TL}$, yielding $\omega_n = n\pi/\sqrt{l_{\rm TL}c_{\rm TL}}L_{\rm TL}$. Upon inserting these mode frequencies into the spatial modes $u_k(x)$ and $w_{n,k}(x)$, we substitute these solutions into the boundary conditions and orthonormalization condition for both the resonators and transmission lines. By enforcing the weak coupling limit, we establish relevant coefficients appearing in the Lagrangian's coupling terms, namely,

$$u_k(0) = \sqrt{\frac{2}{cL}}, \quad u_k(L) = -\sqrt{\frac{2}{cL}}, \quad w_{n,k}(0) = \sqrt{\frac{2}{c_{\rm TL}L_{\rm TL}}} \ . \tag{4.C28}$$

We use these coefficients in the coupling terms of the Lagrangian, where they enable a simplified Legendre transform upon enforcing the weak coupling limit. In full, the terms of the Lagrangian now take the form,

$$\begin{aligned}
\mathcal{L}_{\text{TL}} &= \frac{1}{2}\sum_{k=1}^{3}\sum_{n}\left(\dot{\xi}_{n,k}^2 - \omega_n^2\xi_{n,k}\right) \\
\mathcal{L}_{\text{R}} &= \frac{1}{2}\sum_{k=1}^{3}\left(\dot{\psi}_k^2 - \omega_{\text{R}}^2\psi_k^2\right) \\
\mathcal{L}_{\text{CC}} &= \frac{1}{2}\underline{\dot{\phi}}^T\,\underline{\underline{C}}\,\underline{\dot{\phi}} \;-\; C_{\text{G}}\underline{V}_{\text{g}}^T\underline{\dot{\phi}} \;-\; E_J\;V(\underline{\phi},\Phi)\;, \\
\mathcal{L}_{\text{CC-R}} &= -C_{\text{C}}\sqrt{\frac{2}{cL}}\sum_{k=1}^{3}\dot{\phi}_k\dot{\psi}_k \\
\mathcal{L}_{\text{R-TL}} &= C'_{\text{C}}\sqrt{\frac{2}{cL}}\sqrt{\frac{2}{c_{\text{TL}}L_{\text{TL}}}}\sum_{k=1}^{3}\sum_{n}\dot{\xi}_{n,k}\dot{\psi}_k
\end{aligned} \tag{4.C29}$$

where we have suppressed the explicit time-dependence of $\xi_{n,k}$ and ψ_k to compactly express their time derivatives as $\dot{\xi}_{n,k}$ and $\dot{\psi}_k$. With this Lagrangian, we find the conjugate momenta and carry out the Legendre transform to yield the full system's Hamiltonian [403]. In particular,

$$H \;=\; \sum_{i=1}^{3}\left(Q_i\dot{\phi}_i \;+\; P_i\dot{\psi}_i \;+\; \sum_{n}R_{n,i}\dot{\xi}_{n,i}\right) \;-\; \mathcal{L} \tag{4.C30}$$

where we define the conjugate momentum of each coordinate as

$$Q_i \;=\; \frac{\partial\mathcal{L}}{\partial\dot{\phi}_i}, \qquad P_i \;=\; \frac{\partial\mathcal{L}}{\partial\dot{\psi}_i}, \qquad R_{n,i} \;=\; \frac{\partial\mathcal{L}}{\partial\dot{\xi}_{n,i}}\;. \tag{4.C31}$$

Evaluating these derivatives and writing the conjugate momenta explicitly, we have

$$Q_i \;=\; \sum_{j=1}^{3} C_{ij}\dot{\phi}_j \;-\; C_{\rm G}V_{{\rm g}i} \;-\; C_{\rm C}\sqrt{\frac{2}{cL}}\;\dot{\psi}_i \;, \tag{4.C32}$$

$$P_i \;=\; \dot{\psi}_i \;-\; C_{\rm C}\sqrt{\frac{2}{cL}}\;\dot{\phi}_i \;+\; \frac{2C'_{\rm C}}{\sqrt{cLc_{\rm TL}L_{\rm TL}}}\sum_n \dot{\xi}_{n,i} \;, \tag{4.C33}$$

and

$$R_{n,i} \;=\; \dot{\xi}_{n,i} \;+\; \frac{2C'_{\rm C}}{\sqrt{cLc_{\rm TL}L_{\rm TL}}}\;\dot{\psi}_i \;, \tag{4.C34}$$

where by enforcing the weak coupling limit, we can greatly simplify each expression.

In Eq. (4.C32), we re-express the final term as $-C_{\rm C}\sqrt{\frac{2C_{\rm C}}{cL}}\;(\dot{\psi}_i/\sqrt{C_{\rm C}})$ to compare the coefficients of $\dot{\phi}_i$ and $\dot{\psi}_i/\sqrt{C_{\rm C}}$ (now with equivalent dimensions). Assuming that the elements of the capacitance matrix C_{ij} are of the same order as $C_{\rm C}$, we neglect this term in the weak coupling limit due to the presence of the factor $\sqrt{\frac{2C_{\rm C}}{cL}}$. Analogously, the second and third terms of Eq. (4.C33), can be rewritten as $\sqrt{\frac{2C_{\rm C}}{cL}}\;\sqrt{C_{\rm C}}\dot{\phi}_i$ and $\sqrt{\frac{2C'_{\rm C}}{cL}}\sqrt{\frac{2C'_{\rm C}}{c_{\rm TL}L_{\rm TL}}}\sum_n \dot{\xi}_{n,i}$, respectively, where we compare the coefficients of $\dot{\psi}_i$, $\sqrt{C_{\rm C}}\dot{\phi}_i$, and $\dot{\xi}_{n,i}$ to find both terms can be neglected in the weak coupling limit. In Eq. (4.C34), the second term can be similarly neglected by noting it can be written as $\sqrt{\frac{2C'_{\rm C}}{cL}}\sqrt{\frac{2C'_{\rm C}}{c_{\rm TL}L_{\rm TL}}}\;\dot{\psi}_i$. The weak coupling limit effectively decouples the conjugate momenta, leaving the expressions

$$\underline{Q} \;=\underline{\underline{C}}\;\underline{\dot{\phi}} \;-\; \underline{Q}_{\rm g}, \qquad P_i \;=\; \dot{\psi}_i, \qquad R_{n,i} \;=\; \dot{\xi}_{n,i} \;, \tag{4.C35}$$

where we have reverted to a matrix form in the expression for Q_i and defined the offset charge $Q_{\mathrm{g}i} = C_{\mathrm{G}} V_{\mathrm{g}i}$.

4.C.4 Assembling the Total Hamiltonian

With the simplified forms of the conjugate momenta in the weak coupling limit established, it is straightforward to write the total Hamiltonian in this limit, where term-by-term we find

$$\begin{aligned}
H_{\mathrm{TL}} &= \frac{1}{2} \sum_{k=1}^{3} \sum_{n} \left(R_{n,k}^2 + \omega_n^2 \xi_{n,k}^2 \right) \\
H_{\mathrm{R}} &= \frac{1}{2} \sum_{k=1}^{3} \left(P_k^2 + \omega_{\mathrm{R}}^2 \psi_k^2 \right) \\
H_{\mathrm{CC}} &= \frac{1}{2} \, (\underline{Q} + \underline{Q}_{\mathrm{g}})^T \underline{\underline{C}}^{-1} \, (\underline{Q} + \underline{Q}_{\mathrm{g}}) \; + \; E_J V(\underline{\phi}, \Phi) \;\; , \\
H_{\mathrm{CC\text{-}R}} &= C_{\mathrm{C}} \sqrt{\frac{2}{cL}} \, (\underline{Q} + \underline{Q}_{\mathrm{g}})^T \underline{\underline{C}}^{-1} \, \underline{P} \\
H_{\mathrm{R\text{-}TL}} &= -C'_{\mathrm{C}} \sqrt{\frac{2}{cL}} \sqrt{\frac{2}{c_{\mathrm{TL}} L_{\mathrm{TL}}}} \sum_{k=1}^{3} \sum_{n} R_{n,k} \, P_k
\end{aligned} \tag{4.C36}$$

where terms involving the capacitance matrix are written in matrix form. We now proceed with the quantization of the Hamiltonian, after which we enforce the semi-infinite limit, take the rotating wave and Markov approximations, and define relevant coupling constants to find the form of the Hamiltonian given in Eq. (4.14).

The quantization of the Hamiltonian is accomplished in the usual manner, by

elevating all conjugate variables to operators that satisfy the commutation relations,

$$[\hat{Q}_m, \hat{\phi}_n] = -i\hbar\delta_{mn}, \qquad [\hat{P}_m, \hat{\psi}_n] = -i\hbar\delta_{mn}, \qquad [\hat{R}_{m,n}, \hat{\xi}_{m',n'}] = -i\hbar\delta_{mm'}\delta_{nn'} \ . \tag{4.C37}$$

We note that we can diagonalize the resonator and transmission line Hamiltonians by defining their respective operators in terms of creation and annihilation operators. For the resonators, we take

$$\hat{\psi}_m = \sqrt{\frac{\hbar}{2\omega_{\mathrm{R}}}}(\hat{a}_m^\dagger + \hat{a}_m), \qquad \hat{P}_m = i\sqrt{\frac{\hbar\omega_{\mathrm{R}}}{2}}(\hat{a}_m^\dagger - \hat{a}_m) \ , \tag{4.C38}$$

where $[\hat{a}_m, \hat{a}_n^\dagger] = \delta_{mn}$. For the transmission lines,

$$\hat{\xi}_{m,n} = \sqrt{\frac{\hbar}{2\omega_m}}(\hat{b}_{m,n}^\dagger + \hat{b}_{m,n}), \qquad \hat{R}_{m,n} = i\sqrt{\frac{\hbar\omega_m}{2}}(\hat{b}_{m,n}^\dagger - \hat{b}_{m,n}) \ , \tag{4.C39}$$

where $[\hat{b}_{m,n}, \hat{b}_{m',n'}^\dagger] = \delta_{mm'}\delta_{nn'}$. Making these substitutions in the Hamiltonian then

yields the terms

$$\begin{aligned}
H_{\mathrm{TL}} &= \sum_{k=1}^{3} \sum_{n} \hbar\omega_n \ \hat{b}_{n,k}^{\dagger} \hat{b}_{n,k} \\
H_{\mathrm{R}} &= \sum_{k=1}^{3} \hbar\omega_{\mathrm{R}} \ \hat{a}_k^{\dagger} \hat{a}_k \\
H_{\mathrm{CC}} &= \frac{1}{2} \ (\underline{\hat{Q}} + \underline{Q}_{\mathrm{g}})^T \underline{\underline{C}}^{-1} \ (\underline{\hat{Q}} + \underline{Q}_{\mathrm{g}}) \ + \ E_J V(\underline{\hat{\phi}}, \Phi) \\
H_{\text{CC-R}} &= i C_{\mathrm{C}} \sqrt{\frac{\hbar\omega_{\mathrm{R}}}{cL}} \ (\underline{\hat{Q}} + \underline{Q}_{\mathrm{g}})^T \underline{\underline{C}}^{-1} \ (\underline{\hat{a}}^{\dagger} - \underline{\hat{a}}) \\
H_{\text{R-TL}} &= \sum_{k=1}^{3} \sum_{n} \hbar C'_{\mathrm{C}} \sqrt{\frac{\omega_{\mathrm{R}}\omega_n}{cLc_{\mathrm{TL}}L_{\mathrm{TL}}}} \ (\hat{b}_{n,k}^{\dagger} - \hat{b}_{n,k})(\hat{a}_k^{\dagger} - \hat{a}_k)
\end{aligned} \quad , \tag{4.C40}$$

where we have scaled away overall constants.

We now enforce the semi-infinite limit in the transmission lines and let $L_{\mathrm{TL}} \to \infty$. Note that as $L_{\mathrm{TL}} \to \infty$, the discrete mode frequencies $\omega_n = n\pi/\sqrt{l_{\mathrm{TL}}c_{\mathrm{TL}}}L_{\mathrm{TL}}$, separated by $\Delta\omega = \pi/\sqrt{l_{\mathrm{TL}}c_{\mathrm{TL}}}L_{\mathrm{TL}}$, become a continuum with $\Delta\omega \to 0$. In the usual way [423, 424], as $\Delta\omega \to 0$ the summations over the transmission line modes in the Hamiltonian become integrals over frequency, and discrete mode operators become continuous, with $\hat{b}_{n,k}/\sqrt{\Delta\omega} \to \hat{b}_k(\omega)$ where $[\hat{b}_m(\omega), \hat{b}_{m'}^{\dagger}(\omega')] = \delta_{mm'}\delta(\omega - \omega')$. This modifies the Hamiltonian for the semi-infinite transmission lines as well as the coupling term between the resonators and transmission lines, yielding

$$\begin{aligned}
H_{\mathrm{TL}} &= \sum_{k=1}^{3} \int d\omega \ \hbar\omega \ \hat{b}_k^{\dagger}(\omega) \hat{b}_k(\omega) \\
H_{\text{R-TL}} &= \sum_{k=1}^{3} \int d\omega \ \frac{\hbar C'_{\mathrm{C}}}{cL} \sqrt{\frac{\omega Z_{\mathrm{TL}}}{Z_{\mathrm{R}}}} \ \left[\hat{b}_k^{\dagger}(\omega) - \hat{b}_k(\omega)\right] (\hat{a}_k^{\dagger} - \hat{a}_k)
\end{aligned} \quad , \tag{4.C41}$$

where we express the coupling term in terms of the impedances of the semi-infinite transmission line $Z_{\mathrm{TL}} = \sqrt{\frac{l_{\mathrm{TL}}}{c_{\mathrm{TL}}}}$ and the transmission-line resonator $Z_{\mathrm{R}} = \sqrt{\frac{l}{c}}$. At this stage, we make the rotating wave approximation [425, 426], neglecting the terms in $H_{\text{R-TL}}$ that oscillate in the interaction picture at the sum frequency $\omega_{\mathrm{R}} + \omega$, namely, $\hat{b}_k^\dagger(\omega)\hat{a}_k^\dagger$ and $\hat{b}_k(\omega)\hat{a}_k$. These terms do not conserve energy and on any relevant timescale, these rapid oscillations average to zero, making it reasonable to neglect them, particularly near resonance when $\omega_{\mathrm{R}} \approx \omega$ and $|\omega_{\mathrm{R}} - \omega| << \omega_{\mathrm{R}} + \omega$. This is in contrast with the terms that oscillate on resonance at the difference frequency, $\hat{b}_k^\dagger(\omega)\hat{a}_k$ and $\hat{b}_k(\omega)\hat{a}_k^\dagger$. Thus, the transmission line–resonator coupling takes the form,

$$H_{\text{R-TL}} = -\sum_{k=1}^{3} \int d\omega \; \frac{\hbar C'_{\mathrm{C}}}{cL} \sqrt{\frac{\omega Z_{\mathrm{TL}}}{Z_{\mathrm{R}}}} \left[\hat{b}_k^\dagger(\omega)\hat{a}_k + \hat{b}_k(\omega)\hat{a}_k^\dagger\right] \quad . \tag{4.C42}$$

Finally, we implement a phase transformation on the creation and annihilation operators of the resonators such that $\hat{a}, \hat{a}^\dagger \rightarrow -i\hat{a}, i\hat{a}^\dagger$ and $(\hat{a}^\dagger - \hat{a}) \rightarrow i(\hat{a}^\dagger + \hat{a})$, while also expressing contributions from the central circuit in terms of dimensionless variables $\hat{N}_k = \hat{Q}_k/(-2e)$, $\hat{\varphi}_k = 2e\hat{\phi}_k/\hbar$, and $\underline{\underline{K}}^{-1} = \frac{1}{C_{\mathrm{M}}}\underline{\underline{C}}^{-1}$, with C_{M} the largest

eigenvalue of $\underline{\underline{C}}$. Altogether, the terms of the full system's Hamiltonian become

$$\begin{aligned}
H_{\mathrm{TL}} &= \sum_{k=1}^{3} \int d\omega \ \hbar\omega \ \hat{b}_k^\dagger(\omega)\hat{b}_k(\omega) \\
H_{\mathrm{R}} &= \sum_{k=1}^{3} \hbar\omega_{\mathrm{R}} \ \hat{a}_k^\dagger \hat{a}_k \\
H_{\mathrm{CC}} &= 4E_\Sigma \ (\underline{\hat{N}} - \underline{N}_{\mathrm{g}})^T \underline{\underline{K}}^{-1} \ (\underline{\hat{N}} - \underline{N}_{\mathrm{g}}) \ + \ E_{\mathrm{J}} V(\underline{\hat{\varphi}}, \Phi) \ , \\
H_{\text{CC-R}} &= \hbar g \underline{\hat{B}}^T (\underline{\hat{a}}^\dagger + \underline{\hat{a}}) \\
H_{\text{R-TL}} &= \sum_{k=1}^{3} \int d\omega \ i\hbar \sqrt{\frac{\kappa}{2\pi}} \ \left[\hat{b}_k^\dagger(\omega)\hat{a}_k - \hat{b}_k(\omega)\hat{a}_k^\dagger \right]
\end{aligned} \tag{4.C43}$$

where we define $N_{\mathrm{g}i} = Q_{\mathrm{g}i}/2e$ and $E_\Sigma = e^2/2C_{\mathrm{M}}$. We also identify the operators corresponding to dimensionless voltage on each island of the central circuit,

$$\underline{\hat{B}} = \underline{\underline{K}}^{-1}(\underline{\hat{N}} - \underline{\hat{N}}_{\mathrm{g}}) \ , \tag{4.C44}$$

the coupling constants associated with the interaction between the central circuit and transmission-line resonators,

$$\hbar g = \frac{2eC_{\mathrm{C}}}{C_{\mathrm{M}}} \sqrt{\frac{\hbar\omega_{\mathrm{R}}}{cL}} \ , \tag{4.C45}$$

and the coupling constants associated with the interaction between the transmission-

line resonators and the semi-infinite transmission lines,

$$\sqrt{\frac{\kappa}{2\pi}} = \frac{C'_{\mathrm{C}}}{cL}\sqrt{\frac{\omega_{\mathrm{T}} Z_{\mathrm{TL}}}{Z_{\mathrm{R}}}} \ , \tag{4.C46}$$

where in defining $\sqrt{\kappa/2\pi}$, we have taken the Markov approximation [400] by assuming that this coupling is constant for a range of frequencies relevant to the resonators, specifically evaluating it at the probe/target frequency ω_{T}. This final form is consistent with the Hamiltonian terms given in Eq. (4.14) of the main text.

Appendix 4.D Input-Output Theory in the Single Excitation Manifold

Input-output theory [400] typically utilizes a system's operators and the Heisenberg equations of motion to define and relate input and output mode operators. Here, the non-linearity of the Josephson junctions in the central circuit makes this process nontrivial. In this appendix, we outline a modified approach to input-output theory that leverages the single excitation manifold, enabling an analysis in terms of the probability amplitudes of a generic manifold state.

The time evolution of the complex probability amplitudes d_k, c_n, and $f_k(\nu)$ in Eq. (4.15) (a generic state in the single excitation manifold) is governed by the Schrödinger equation. However, the total Hamiltonian [Eqs. (4.13) and (4.14)] contains terms, namely, the coupling terms $H_{\text{CC-R}}$ and $H_{\text{R-TL}}$, which take this generic state out of the single excitation manifold. Therefore, to ensure the time evolution of the probability amplitudes results in a state within the manifold, we consider the Schrödinger equation projected into the single excitation manifold,

$$i\hbar\frac{\partial}{\partial t}\left|\Psi_0\right\rangle = \left[H_{\text{TL}} + H_{\text{R}} + H_{\text{CC}} + \mathbb{1}_{\text{SEM}}\left(H_{\text{CC-R}} + H_{\text{R-TL}}\right)\right]\left|\Psi_0\right\rangle \quad , \tag{4.D1}$$

where we define the projection operator,

$$\mathbb{1}_{\text{SEM}} = \sum_{k=1}^{3}\hat{a}_k^\dagger\left|G\right\rangle\left\langle G\right|\hat{a}_k + \sum_n \left|\varepsilon_n\right\rangle\left\langle\varepsilon_n\right| + \sum_{k=1}^{3}\int d\nu\ \hat{b}_k^\dagger(\nu)\left|G\right\rangle\left\langle G\right|\hat{b}_k(\nu) \quad . \tag{4.D2}$$

This operator acts as an identity operator on states within the single excitation manifold, but projects those outside the manifold back onto it. We note that the projector is assembled from eigenstates of the uncoupled Hamiltonians, H_{TL}, H_{R}, and H_{CC}, therefore, their action on $|\Psi_0\rangle$ will always return a manifold state.

We use Eq. (4.D1) to find the equations of motion for the amplitudes associated with a state in the single excitation manifold, taking the ground state energy of the central circuit to be scaled such that $H_{\mathrm{CC}}\,|G(=\varepsilon_0)\rangle = 0$ and expressed in its diagonal form $H_{\mathrm{CC}} = \sum_{n=0}\varepsilon_n\,|\varepsilon_n\rangle\,\langle\varepsilon_n|$ [rather than that shown in Eq. (4.14)]. Evaluating and expanding the terms in Eq. (4.D1) by substituting in Eqs. (4.14), (4.15), and (4.D2), we find that numerous terms evaluate to zero, enabling the identification of the equations of motion for d_k, c_n, and $f_k(\nu)$,

$$\frac{\partial d_k}{\partial t} = -i\omega_{\mathrm{R}}d_k - \sqrt{\frac{\kappa}{2\pi}}\int d\nu\, f_k(\nu) - ig\sum_n c_n\,\langle G|\,\hat{B}_k\,|\varepsilon_n\rangle \quad , \tag{4.D3}$$

$$\frac{\partial c_n}{\partial t} = -i\frac{\varepsilon_n}{\hbar}c_n - ig\sum_{q=1}^{3} d_q\,\langle\varepsilon_n|\,\hat{B}_q\,|G\rangle \quad , \tag{4.D4}$$

$$\frac{\partial f_k(\nu)}{\partial t} = -i\nu f_k(\nu) + \sqrt{\frac{\kappa}{2\pi}}d_k \quad . \tag{4.D5}$$

Aside from the contributions from the central circuit, the forms of these equations of motion are analogous to the Heisenberg equations of motion of a cavity interacting with a bath, the typical paradigm for utilizing input-output theory. Since the contributions from the central circuit are linear, we can proceed with input-output theory

as usual, outlined in Appendix 3.D of Chapter 3, to relate in-going and out-going modes of the transmission line in the single photon limit, yielding the results shown in Section 4.3.2.

Appendix 4.E General Conditions for Ideal Circulation

Here we consider a generalized approach to establishing conditions for ideal circulation in the central circuit model that places no restrictions on operating frequencies or phase differences, offering a broader parameter space and providing a framework for the consideration of systems with different port numbers.

Beginning with the same intuitive argument outlined in Section 4.3.3 that yields Eq. (4.22), we re-express the circuit-specific coupling matrix $\underline{\underline{T}}(\omega)$ in terms of the CW and CCW permutation matrices equivalent to the ideal circulator matrices given in Eq. (4.21), yielding the form,

$$\underline{\underline{T}}(\omega) = -i\ \beta\ \mathbb{1}_{3\times3} - i\ |\alpha|\ \left(e^{i\theta}\underline{\underline{S_{\text{ccw}}}} + e^{-i\theta}\underline{\underline{S_{\text{cw}}}}\right)\ , \tag{4.E1}$$

where we have explicitly written α in terms of its phase and magnitude, $\alpha = |\alpha|e^{i\theta}$. Inserting Eq. (4.E1) into the expression for the S-matrix [Eqs. (4.19) and (4.18)], we find

$$\underline{\underline{S}}(\omega) = \mathbb{1}_{3\times3} - i\ 2\Upsilon\left[(\Lambda + i\Upsilon)\,\mathbb{1}_{3\times3}\ -\ \left(e^{i\theta}\underline{\underline{S_{\text{ccw}}}} + e^{-i\theta}\underline{\underline{S_{\text{cw}}}}\right)\right]^{-1}\ , \tag{4.E2}$$

where we have defined the quantities

$$\Lambda = \frac{\omega - \omega_{\text{R}} - g^2\beta}{g^2|\alpha|} \qquad \Upsilon = \frac{\kappa}{2g^2|\alpha|}\ . \tag{4.E3}$$

This formulation of the S-matrix in terms of $\underline{\underline{S_{\mathrm{ccw}}}}$, $\underline{\underline{S_{\mathrm{cw}}}}$, and $\mathbb{1}_{3\times3}$ provides a straightforward means of establishing general conditions for ideal circulation, where we find the solutions

$$\Lambda = \frac{\omega_{\mathrm{T}} - \omega_{\mathrm{R}} - g^2\beta}{g^2|\alpha|} = -\cos(3\theta) \qquad \Upsilon = \frac{\kappa}{2g^2|\alpha|} = \pm\sin(3\theta) \ , \tag{4.E4}$$

where the upper or lower signs correspond to resulting circulation in a CW or CCW fashion, respectively. We note that upon taking the coupling constants κ and g to be real and positive, we require $\Upsilon = \pm\sin(3\theta) > 0$. As a result, for CW circulation, $0 < 3\theta < \pi$, and for CCW circulation, $-\pi < 3\theta < 0$. The conditions presented in the main text are a specific instance of these more general conditions, whereby enforcing an additional condition on the phase θ, namely, $\Delta\theta = -6\theta = \pm\pi, \pm3\pi...$ (or alternatively $3\theta = -\Delta\theta/2 = \mp\pi/2, \mp3\pi/2...$), we recover the conditions shown in Eq. (4.27). Given that this phase condition yields $\Upsilon = 1$, these more specific conditions can be interpreted as an attempt to maximize the ratio of coupling strengths κ/g^2 at a given frequency, enabling larger bandwidth performance.

Of note, this general framework for the analysis of the S-matrix, hinging on symmetries of the central circuit as well as a formulation in terms of relevant permutation matrices, enables a straightforward extension to models of varying port number. Preliminary analysis of two-and four-port models, analogous to the three-port model of focus here, indicates a wealth of interesting phenomena may be possible. Mathematically, the four-port S-matrix supports a variety of behavior, with numerous matching

conditions that capture nonreciprocal transmission to one or two ports away from the input port, as well as operating modes that act to divide an incoming signal between two ports (i.e., a beamsplitter) or between three ports. While the two-port model is generally simpler and can only provide matched, reciprocal transmission, more interesting is the possibility of creating a gyrator by introducing asymmetry in this system. Preliminary work suggests this is possible via asymmetries that result in the creation of distinct persistent currents in each loop. While work on these models remains in its early stages, it offers a look into the potential future extensions of our circulator model and the highly nonreciprocal role vortices play in their operation.

Appendix 4.F Investigation of Additional External Flux Regions

Upon examination of the energy levels of the central circuit as a function of A, shown in Fig. 4.2a, we identify three qualitative regions of behavior occurring in the regions $0 \leq A \lesssim 0.2$ (region 1), $0.2 \lesssim A \lesssim 0.26$ (region 2), and $0.26 \lesssim A \leq 0.5$ (region 3). In the main text, we present the results of an analysis from region 2, where $A \approx 0.2478$. Here we investigate two additional flux values, $A \approx 0.17$ and $A \approx 0.36$, in the first and third regions, respectively (highlighted in Figs. 4.11a and 4.12a). In contrast to the large-bandwidth circulator performance found at $A \approx 0.2478$, we find that the chosen points in the first and third regions do not exhibit similar qualities. We understand this behavior as follows.

In region 1, we note that the second and third excited states are nearly degenerate, while the first excited state maintains a nearly constant separation from the ground state, mirroring the ground state, as evidenced in Figs. 4.2a and 4.2b. Furthermore, in this region there are no circulating vortices between the ground state and the first excited state, in contrast to that with the second excited state, shown in Figs. 4.3d and 4.3e. Since the expected mode of circulator operation is via the tunneling of persistent-current vortices, points for ideal transmission should not occur around the first excited state. This is confirmed by examining the phase difference at $A \approx 0.17$, shown in Figs. 4.11b and 4.11c, where ideal nonreciprocal points do not appear until

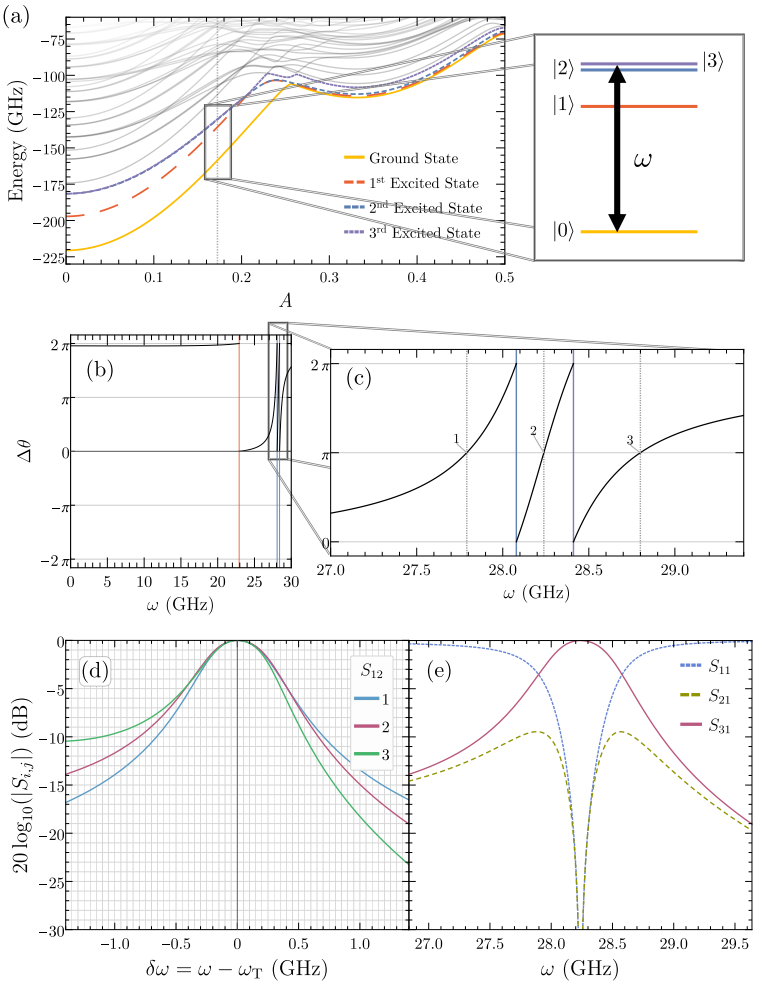


Figure 4.11: In (a), we highlight the energy level structure at $A = 0.1725$ in region 1 and the relevant transition from the ground state. The phase difference $\Delta\theta$ as a function of driving frequency ω is shown below in (b) and (c), where dashed vertical lines indicate the nonreciprocal target frequencies, enumerated for future reference. The red, blue, and purple vertical lines indicate the first, second, and third excited energies, respectively, for the central circuit. Parameters for these plots are as in Fig. 4.4 of the main text, except with $A = 0.1725$. For the enumerated nonreciprocal points in (c), we show (d) transmission bandwidth and (e) signal circulation. Parameters are as in (b) and (c), where the procedure for determining g, κ, and ω_R is identical to that described Section 4.4.1 in the main text.

the second and third excited states. This is understood by noting that between the ground state and both the second excited state and the third excited state there exist circulating and counter-circulating vortices, analogous to the vortex dynamics of the

first and second excited states in region 2. We also note that at $A \approx 0.17$, the energy-level structure of the first, second, and third excited states (highlighted in Fig. 4.11a) is similar to that of the ground, first excited, and second excited states at $A \approx 0.2478$ in region 2 (as investigated in the main text). However, the separation of the second and third excited states at $A \approx 0.17$ is about half the size of the separation of the first and second excited states at $A \approx 0.2478$. Examining performance at $A \approx 0.17$, we find transmission is relatively large around the second and third excited states, shown in Figs. 4.11d and 4.11e, as compared with transmission at higher-energy nonreciprocal points (not shown here). However, due to the closer proximity of the second and third excited states (as compared with the first and second excited states at $A \approx 0.2478$), we find a bandwidth smaller than that found at $A \approx 0.2478$.

In region 3, the energy-level structure is markedly different from that in either of the other two regions. As shown in Fig. 4.12a, the level separations between the ground state, the first excited state, and the second excited state are roughly equivalent, and higher-energy states are overall more accessible. Vortices are present between the ground state and both the first excited state and the second excited state (as well as other excited states). In fact, the first and second excited states exhibit circulating and counter-circulating vortices that are qualitatively similar to those of the second region. For this reason, numerous points for ideal circulation around these resonances should occur, which is confirmed by the phase difference found at $A \approx 0.36$, shown in Fig. 4.12b. However, despite the abundance of vortex

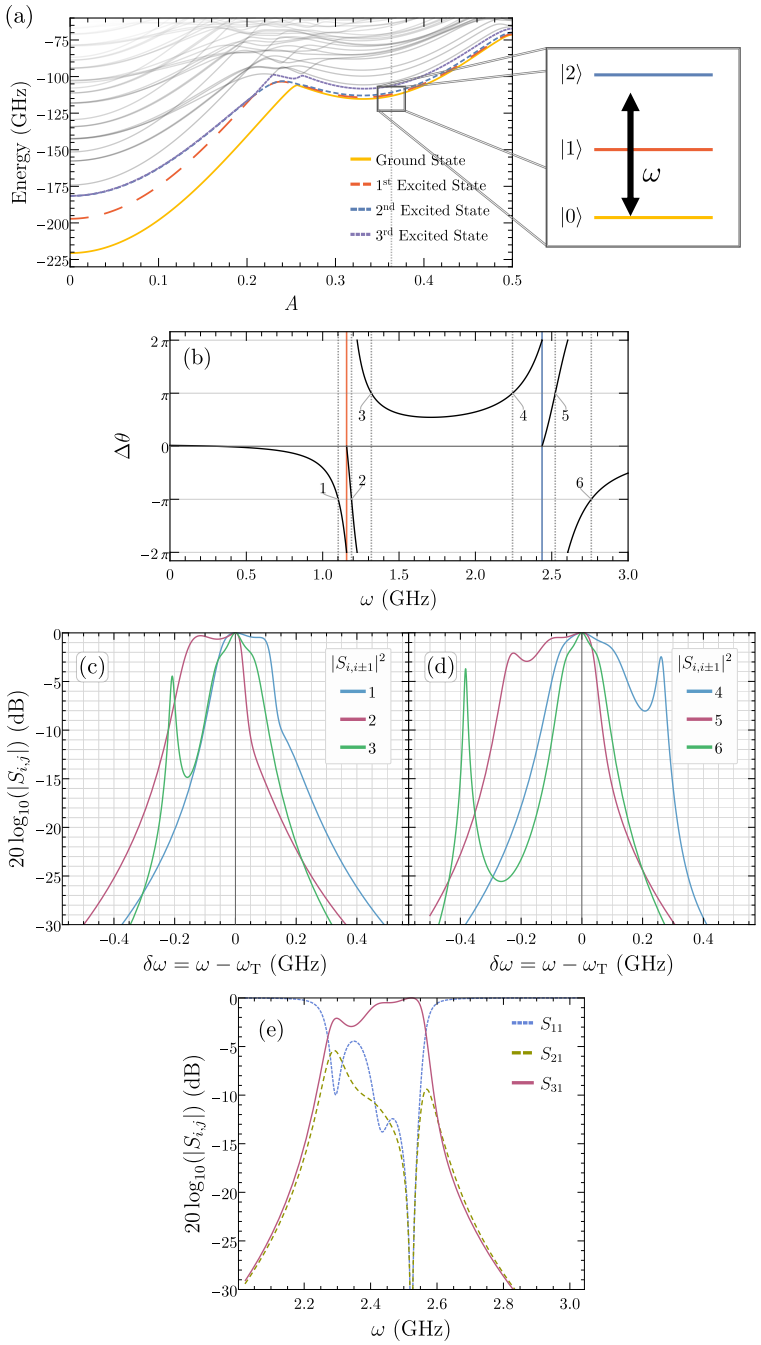


Figure 4.12: In (a), we highlight the energy level structure at $A \approx 0.36$ in region 3. The phase difference $\Delta\theta$ as a function of driving frequency ω is shown below in (b), where dashed vertical lines indicate the nonreciprocal target frequencies, enumerated for future reference. The red and blue vertical lines indicate the first and second excited energies, respectively, for the central circuit. Parameters for these plots are as in Fig. 4.4 of the main text, except with $A \approx 0.36$. For the enumerated nonreciprocal points in (b), we show transmission bandwidth in (c) and (d). For point 5, we show signal circulation in (e). Parameters are as in (b), where the procedure for determining g, κ, and ω_R is identical to that described Section 4.4.1 in the main text.

dynamics and overall lower energy as compared with either the first or second regions, the resulting performance—shown in Figs. 4.12c-4.12e—is not as good as that found in region 2. This is perhaps due to the larger separation of energy levels, in particular between the first excited state and the second excited state, in contrast to the first and second excited states in region 2.

Appendix 4.G Parameter Considerations

In the model we consider, shown in Figs. 4.1a and 4.1b, there are a variety of central circuit and external circuit parameters that can affect system behavior. Unfortunately, not all of these parameters have clear analytic expressions that characterize their influence on device performance. When considering performance metrics such as transmission bandwidth and noise sensitivity, we must strike a balance between these parameters to find the optimum performance. In this appendix, we discuss some of these parameters and our understanding of their effect on the system's performance.

Regarding the central superconducting circuit, of tremendous influence is the ratio of Josephson energy E_{J} to the charging energies E_{C} and E_{Σ}. As touched on in Section 4.2.2, the relative size of these energies impacts the relevant excitations and their quantum behavior; however, it also impacts the circuit's noise sensitivity. As E_{J} increases with fixed plasma frequency (E_{C} and E_{Σ} decreasing together), the circuit becomes more robust with regard to charge noise, but more susceptible to flux noise. The opposite is true as E_{J} decreases. Additionally, our investigation suggests that this ratio impacts the role of fabrication disorder, as discussed in Appendix 4.H.2, whereby increasing E_{J} leads to more susceptibility to noise in E_{J} and less susceptibility to noise in various capacitances. Another important feature is the effect E_{J} has on the separation of adjacent energy levels of the central circuit. As indicated by our investigations in Appendix 4.F, we believe that the proximity of relevant energy levels

impacts the bandwidth achieved in each region of flux. As E_{J} increases with fixed plasma frequency, the separation of the circuit's energy levels decreases, limiting bandwidth performance. Considering all of these effects together, our goal with the results presented in the main text, where $E_{\mathrm{J}}/E_{\mathrm{C}} = 4$ and $E_{\mathrm{J}}/E_{\Sigma} \approx 40$, is to balance the benefits of increased bandwidth with the detriment of decreased resistance to charge noise, all while remaining in a regime where the quantum behavior of vortices may be exploited.

In addition to central circuit parameters, the parameters that characterize the connected external circuits (g, κ, ω_{R}) are also quite important, influencing bandwidth performance as well as placing physical constraints on the elements of the system. Generally speaking, increasing the size of either of the coupling strengths g or κ will provide some increase in bandwidth. However, doing so affects physically relevant quantities such as the capacitance and characteristic impedance of the resonators (C_{R},Z_{R}) and transmission lines (C_{TL},Z_{TL}). A microscopic derivation utilizing the weak coupling limit ($C_{\mathrm{C}} \ll C_{\mathrm{R}}, C_{\mathrm{TL}}$), as done in Appendix 4.C of this dissertation and Refs.[213, 276], yields expressions for both g and κ, the coupling strength between the circuit and the resonators and the coupling strength between the resonators and the transmission lines, respectively. For g we find

$$g = \omega_{\mathrm{R}} \frac{C_{\mathrm{C}}}{C_{\mathrm{M}}} \sqrt{\frac{8Z_{\mathrm{R}}}{R_{\mathrm{K}}}} \ , \tag{4.G1}$$

which corresponds to Eq. (4.G1) in Appendix 4.C where we have expressed g in terms

of the characteristic impedance of the resonators Z_{R} and the von Klitzing constant $R_{\mathrm{K}} = h/e^2$, with the resonator frequency ω_{R}. The capacitances C_{C} and C_{M} are as defined in Section 4.2.1. Increasing g (and necessarily ω_{R}) increases Z_{R} while decreasing the ratio $C_{\mathrm{R}}/C_{\mathrm{C}}$, impacting the validity of the weak coupling limit. When combined with the conditions for ideal circulation given by Eq. (4.27) and the resulting parameter specifications given in Table 4.1, Eq. (4.G1) determines the characteristic impedance of the resonators required to achieve ideal circulation for each operating point. In the results discussed in Section 4.4.1 and shown in Fig. 4.5, the coupling strength is chosen to be $g = 1.6$ GHz for all operating points. For the fourth operating point, which has a particularly large bandwidth, this value of g along with the other parameters given in the main text can be used in Eq. (4.G1) to give $Z_{\mathrm{R}} \approx 700\ \Omega$ — larger than that of a typical coplanar waveguide, but not unreasonable [427–429].

In addition, we find for κ the expression

$$\kappa = 2\pi\omega_{\mathrm{T}} \left(\frac{C_{\mathrm{C}}}{C_{\mathrm{R}}}\right)^2 \frac{Z_{\mathrm{TL}}}{Z_{\mathrm{R}}} \ , \tag{4.G2}$$

which corresponds to Eq. (4.G2) in Appendix 4.C, where ω_{T} is the target frequency, Z_{TL} the characteristic impedance of the transmission lines, and $C_{\mathrm{R}}(= cL)$ the capacitance of the resonators. Increasing κ, given the required conditions for ideal circulation as provided in Eq. (4.27) of the main text, necessarily increases g, resulting in the same impact on Z_{R} and $C_{\mathrm{R}}/C_{\mathrm{C}}$ as described above. Therefore, while gains in bandwidth may be possible by increasing g or κ, this must be weighed against the

resulting increases in these physically constraining parameters.

We can also use Eq. (4.G2) and the parameter values shown in Table 4.1 to obtain the required transmission line impedance for an increased value of g. Unsurprisingly, given the size of κ needed for a larger value of g, we also need the line impedance tuned to enable this strong coupling, resulting in $Z_{\mathrm{TL}} \approx 5$ kΩ. While this is very large, this is a microwave engineering challenge that may have various solutions, such as inductively coupling, rather than capacitively coupling, the transmission lines to the resonators. Despite this, given the numerous parameters (and the necessarily vast parameter space), there may exist as-yet-undiscovered operating points that maintain or improve upon our reported bandwidth and noise performance but decrease these large impedance requirements. Our investigation indicates that the presence of nonreciprocal behavior relies on the tuning of parameters relevant to the central superconducting circuit. While the external circuit parameters place physical constraints on the system, we still find that nonreciprocity can be achieved with any reasonable set of g, κ, and ω_{R}. We note that while in this work we opted to first fix g and then examine the requirements of the resonators, one could alternatively first choose the properties of the resonators and then examine the resulting implications on g and other system parameters.

Appendix 4.H Details of the Noise Investigations

We begin by defining an extinction ratio ER that compares the transmission in each direction between two ports of the circuit:

$$\mathrm{ER} = \begin{cases} 20\ \log_{10}\left(|\frac{S_{ij}}{S_{ji}}|\right) & \text{if } |S_{ij}| < |S_{ji}| \\ \\ 20\ \log_{10}\left(|\frac{S_{ji}}{S_{ij}}|\right) & \text{if } |S_{ij}| > |S_{ji}| \end{cases}. \tag{4.H1}$$

This metric provides a comparison between the desired direction of transmission and the undesired, reverse direction of transmission. For an ideal circulator, $\mathrm{ER} \to -\infty$, and thus in practice, the more negative this quantity, the more nonreciprocal the device. The minimum of the extinction ratio ER_0 (as a function of frequency) is what we use to assess the system's response to noise.

Similarly, we define the insertion loss IL between two ports of the circuit as

$$\mathrm{IL} = \begin{cases} 20\ \log_{10}\left(|S_{ij}|\right) & \text{if } |S_{ij}| > |S_{ji}| \\ \\ 20\ \log_{10}\left(|S_{ji}|\right) & \text{if } |S_{ij}| < |S_{ji}| \end{cases}. \tag{4.H2}$$

The insertion loss quantifies the amount of transmission lost between two ports of the circuit. For zero transmission, $\mathrm{IL} \to -\infty$. However, in an ideal circulator, there is full transmission between two ports of the system, resulting in $\mathrm{IL} = 0$. To help characterize the system's response to noise, we examine the maximum of the insertion

loss IL_0, where the closer this value is to zero, the better the performance.

The introduction of deviations from ideal parameters (noise) will necessarily lead to variations in device performance. These deviations parameterize a multidimensional landscape of device performance, whose dimension is characterized by the degrees of freedom associated with each type of disorder. For example, variations of the static gate voltages on each of the three islands (here translated to effective Cooper pair number) define a three-dimensional landscape characterizing performance for variations from the ideal offset charge. To showcase this landscape, we consider a two-dimensional slice that examines the variations in two of the three charge noise parameters, shown in Fig. 4.13. A landscape of this type exists for flux noise (where it is a three-dimensional space) as well as for fabrication disorder (where it is a six-dimensional space).

In what follows, rather than attempting to tune a given device to a perfect operating point, we instead consider a statistical analysis that samples from all dimensions of each landscape to find the fraction of devices with low insertion loss, and of those devices, the distribution of their minimum extinction ratios, specifically highlighting a median device outcome. In the case of static disorder, this corresponds to finding high-performing devices and provides a yield of viable devices given a performance metric.

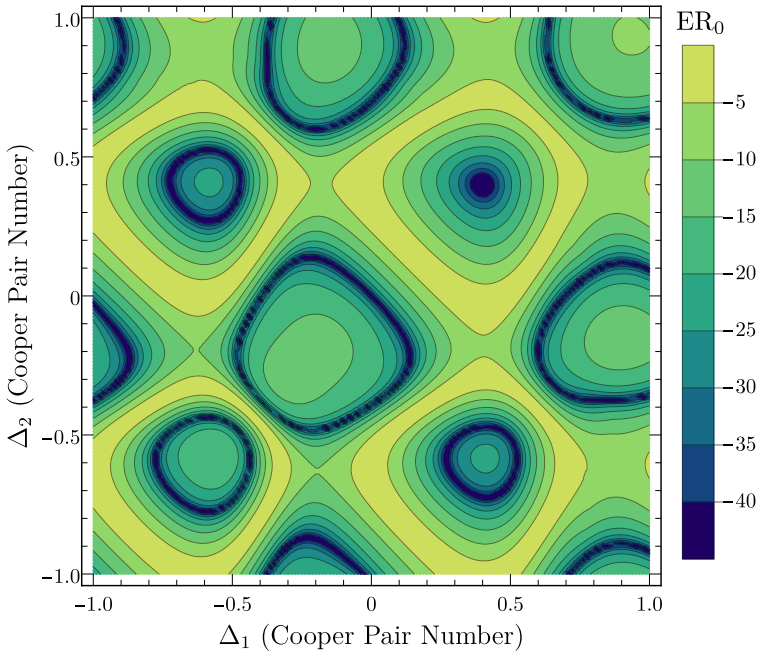


Figure 4.13: The effect of offset charge number variations from the ideal on the minimum of the extinction ratio ER_0 (in dB) between ports one and two. Shown is the two-dimensional slice for $\Delta_3 = 0$, that is, an unchanged N_{g3}, while introducing variations Δ_1 and Δ_2 from -1 to $+1$ in N_{g1} and N_{g2}, respectively. Parameters and offset charge for ideal tuning are the same as in Fig. 4.4.

4.H.1 Statistical Analysis

Upon introducing either charge noise or flux noise (as described in the main text), sampled from a normal distribution with standard deviation N_σ or R_σ, respectively, we examine both ER_0 and IL_0 for a total of 1200 noise samples. As an example, Fig. 4.14a shows the pairwise plot of ER_0 and IL_0 for 1200 charge noise samples for which $N_\sigma = 0.25$. Similarly, Fig. 4.14b shows the same pairwise plot but for 1200 flux noise samples for which $R_\sigma \approx 0.012$.

We then impose a performance threshold, examining only those noise samples for which there is less than 1 dB of insertion loss ($\mathrm{IL} \geq -1$), shown visually by the

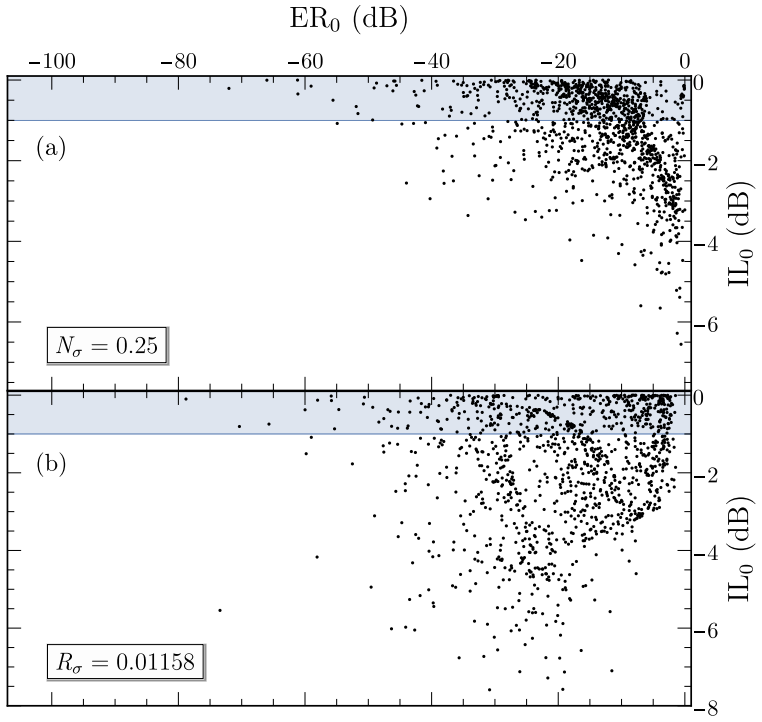


Figure 4.14: A pairwise plot of the minimum of the extinction ratio ER_0 and the maximum of the insertion loss IL_0 in the presence of (a) charge noise for 1200 samples from a noise distribution with a mean of $N_\mu = 0$ and a standard deviation $N_\sigma = 0.25$ and (b) flux noise for 1200 samples from a noise distribution with a mean of $R_\mu = 0$ and a standard deviation $R_\sigma = 0.01158$. Shading indicates the device yield Υ — the fraction of points that constitute ER_0^Υ. Parameters and offset charge for ideal tuning are the same as in Fig. 4.4. Results shown are specifically for transmission between ports one and two, but are representative of the circuit overall due to circuit symmetry and the sampling from identical noise distributions at each island.

points within the shaded regions in Fig. 4.14. We define this subset of points as ER_0^Υ, characterizing this distribution by calculating its quartiles for increasing N_σ or R_σ. Figures 4.5c and 4.5d display the median of this distribution $\widetilde{\mathrm{ER}}_0^\Upsilon$ with error bars from the first to third quartiles as a function of N_σ and R_σ, respectively.

We also define the device yield Υ as the probability for transmission to exceed the

imposed threshold (IL ≥ -1). This is approximated by

$$\Upsilon = \frac{\text{\# of Samples with IL} \geq -1}{\text{Total \# of Samples}} \ . \tag{4.H3}$$

Figures 4.5e and 4.5f display this probability for increasing N_σ and R_σ, respectively. Note that this procedure is also utilized for the fabrication disorder introduced and described in Appendix 4.H.2.

4.H.2 Fabrication Disorder

In addition to considering charge and flux disorder, we also examine the effects of fabrication disorder in the individual Josephson junctions of the model, shown in Fig. 4.1b. The high symmetry present in our analysis also extends to the junctions — we assume identical Josephson energies E_J and junction capacitances C_J (yielding identical charging energies $E_\text{C} = \frac{e^2}{2C_\text{J}}$) for all six junctions. By separately introducing disorder in these quantities, we can then assess the model's subsequent performance when subject to variations in junction parameters.

To test the system's fabrication tolerances, we begin with the system tuned for ideal circulator behavior with all six Josephson junctions having identical E_J and C_J. Analogously to the charge and flux noise cases, we then introduce a variation Δ'' in either E_J or C_J that is unique for each junction. In both the E_J noise case and the C_J noise case, we take Δ'' to be a fraction of the original value, randomly sampling from a normal distribution with a mean of $D_\mu = 0$ and a standard deviation D_σ. As detailed

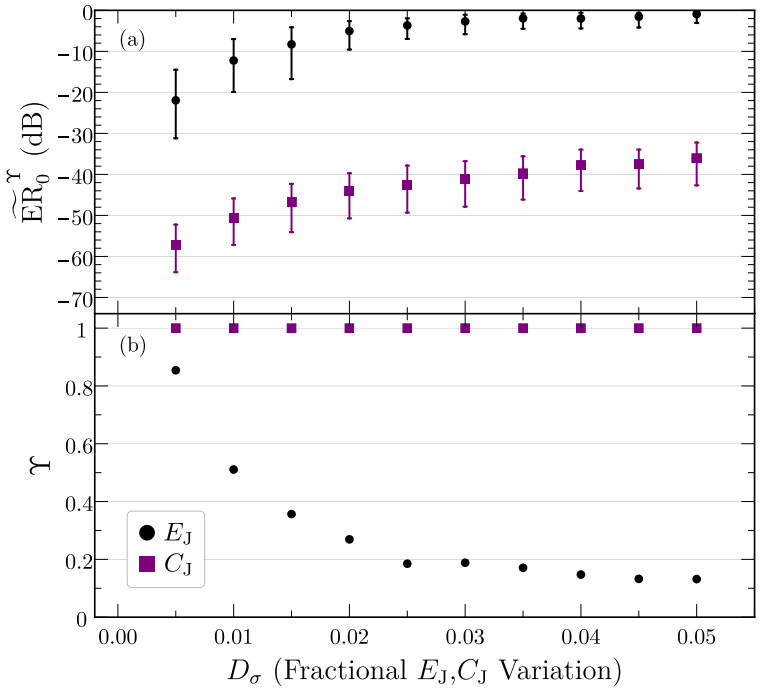


Figure 4.15: (a) The median of ER_0^{Υ} (defined in Appendix 4.H.1 as the extinction ratio for devices with less than 1 dB of insertion loss), $\widetilde{\mathrm{ER}}_0^{\Upsilon}$, is plotted as a function of the standard deviation of the E_J or C_J noise distribution D_σ as indicated by the legend. Error bars indicate the spread from the first to third quartile of ER_0^{Υ} for each value of D_σ. (b) Device yield Υ (defined in Appendix 4.H.1 as the fraction of devices with less than 1 dB of insertion loss) is plotted as a function of D_σ. Parameters for ideal tuning are the same as in Fig. 4.5b.

and defined in Appendix 4.H.1, we assess performance in the presence of either E_J or C_J noise by examining ER_0^{Υ} and Υ as a function of D_σ, shown together in Figs. 4.15a and 4.15b, respectively. As stated above, ER_0^{Υ} and Υ convey the distribution of the minimum of the extinction ratio for those noise samples resulting in less than 1 dB of insertion loss and the likelihood that this is the case for a sample size of 1200 noise samples.

Upon increasing D_σ, we observe markedly different performance between the introduction of noise in E_J and the introduction of noise in C_J, as shown in Fig. 4.15.

In particular, we see that while the introduction of noise in the Josephson energies of the junctions degrades performance, varying the junction capacitances does not. This is best understood by considering that the original ideal parameters are such that $E_{\mathrm{J}} = 4E_{\mathrm{C}} \approx 40E_{\Sigma}$, thereby necessitating that any variations introduced in E_{J} are bound to have a larger effect than those in C_{J} (and subsequently E_{C} and E_{Σ}). Nonetheless, Fig. 4.15 indicates that variations of approximately 1.5% in E_{J} may be tolerated. Beyond 2%, nonreciprocity is extinguished, where we see that $\widetilde{\mathrm{ER}}_0^{\Upsilon} \approx 0$ and $\Upsilon \lesssim 20\%$. In contrast, Fig. 4.15 shows that variations of up to 5% (and likely higher) in C_{J} can be tolerated — for all distribution sizes $\widetilde{\mathrm{ER}}_0^{\Upsilon} < -30$ and $\Upsilon = 100\%$.

Chapter 5: Conclusions

In this dissertation, we explored novel approaches for modeling superconducting circuits and developed applications for quantum computing and quantum sensing, specifically focusing on nonreciprocal devices and impulse metrology. Given their potential to impact both fundamental physics and practical technological applications, these topics have garnered considerable recent attention from the broader scientific community. This dissertation offers insights into improving simulation accuracy, accomplishing velocity-sensing protocols in superconducting circuits, and utilizing vortices to generate nonreciprocal behavior, all of which could have significant applications in quantum technologies.

Chapter 2 presented the general framework for modeling superconducting circuits, including the mathematical construction of DVRs. We focused on infinite- and finite-sized sinc DVRs, and showed that these representations can be applied to superconducting circuits to yield not only the usual charge basis, but also a broad range of both discrete charge number and discrete phase bases. These DVRs can be readily employed in systems that incorporate any combination of capacitors, Josephson junctions, and inductors, which we demonstrated by utilizing them in three prototypical

systems: the LC oscillator, the fluxonium, and the transmon. We have shown the effectiveness of using sinc DVRs to numerically represent superconducting circuits, and that despite their non-variational behavior and lack of sparsity, found that these DVRs can match, and in many cases outperform, the standard numerical approaches currently used in many software tools.

In Chapter 3, we designed circuits for transducing a mechanical signal to an electrical signal via magnetomechanical and electromechanical processes, highlighting the details and features of their respective Hamiltonians. We then leveraged principles from optomechanics to develop specific approaches for velocity and position sensing using voltage or current measurements of these transducers. By creating this optomechanical analog, we were able to apply standard methods for noise analysis to our systems of interest. We found that our specific electrical circuit-based approach to velocity sensing, namely voltage measurement of a magnetomechanical transducer, allows for a reduction in measurement-added noise while monitoring the mechanical motion in the microwave domain.

Finally, Chapter 4 presented the theoretical analysis of a compact superconducting microwave circulator. By modifying the three-junction loop considered by Refs. [276, 284] with the addition of three central Josephson junctions, we created loops within the circuit that supported persistent-current vortices. We investigated the conditions under which these vortices were generated and how their circulation was brought about, namely, that a voltage at an island created a localized vortex, which ro-

tated and reradiated into the leads. We also performed numerous auxiliary analyses to better understand the model, including examinations of additional flux penetrations, a generalization of the conditions for nonreciprocity, and an approach that eliminated the central ground. Our investigation showed that operating in a non-charge-conserved regime with mobile vortices in the XY model, where the charging energy and Josephson energy scales were similar, led to performance with a reduced dependence on static charge noise. Furthermore, the presence of both clockwise and counterclockwise vortex circulation at nearby energies enabled wide bandwidth performance that exceeded one GHz.

The work presented in this dissertation not only offers improvements in existing technologies, but also lays the groundwork for future exploration, with the potential to address key challenges in quantum computing, sensing, and circuit design. It remains to be seen if the efficient representations accessible to sinc DVRs in small-scale systems extend to larger circuits with more degrees of freedom. Moving forward, further investigation into approaches that could combine the level of accuracy provided by DVRs with the sparsity of alternative methods, such as a wavelet basis or higher-order finite difference methods, may offer promising solutions for efficiently modeling larger-scale quantum systems and expanding the capabilities of software tools for superconducting circuits.

Potential investigations into the reduction of measurement-added noise in superconducting circuits via velocity sensing are very accessible near-term, as our work is

immediately compatible with existing mechanical systems, such as levitated superconducting spheres (e.g., the ones described in Refs. [249–251]), enabling a change from position to velocity detection by effectively changing their readout from current to voltage. Finally, there are several avenues for further work related to the circulator model we present, namely, generalizing the understanding of the three-port model to circulators with more than three ports, addressing the operational question of system performance at higher powers, and further exploring the vortex-tunneling picture to enhance its functionality. As the field continues to evolve, the ideas and methodologies introduced in this dissertation will contribute to the development of future superconducting devices and systems, advancing both theoretical and applied physics.

Bibliography

[1] H. Kamerlingh Onnes, "Further experiments with liquid helium. C. On the change of electric resistance of pure metals at very low temperatures, etc. IV. The resistance of pure mercury at helium temperatures", Communications from the Physical Laboratory at the University of Leiden **120b** (1911).

[2] H. Kamerlingh Onnes, "Further experiments with liquid helium. D. On the change of electric resistance of pure metals at very low temperatures, etc. V. The disappearance of the resistance of mercury", Communications from the Physical Laboratory at the University of Leiden **122b** (1911).

[3] H. Kamerlingh Onnes, "Further experiments with liquid helium. G. On the electrical resistance of pure metals, etc. VI. On the sudden change in the rate at which the resistance of mercury disappears", Communications from the Physical Laboratory at the University of Leiden **124c** (1911).

[4] W. Meissner and R. Ochsenfeld, "Ein neuer Effekt bei Eintritt der Supraleitfähigkeit", Naturwissenschaften **21**, 787–788 (1933).

[5] F. London, H. London, and F. A. Lindemann, "The electromagnetic equations of the supraconductor", Proceedings of the Royal Society of London. Series A - Mathematical and Physical Sciences **149**, 71–88 (1935).

[6] C. A. Reynolds, B. Serin, W. H. Wright, and L. B. Nesbitt, "Superconductivity of Isotopes of Mercury", Phys. Rev. **78**, 487–487 (1950).

[7] E. Maxwell, "Isotope Effect in the Superconductivity of Mercury", Phys. Rev. **78**, 477–477 (1950).

[8] W. S. Corak, B. B. Goodman, C. B. Satterthwaite, and A. Wexler, "Exponential Temperature Dependence of the Electronic Specific Heat of Superconducting Vanadium", Phys. Rev. **96**, 1442–1444 (1954).

[9] A. Brown, M. W. Zemansky, and H. A. Boorse, "The Superconducting and Normal Heat Capacities of Niobium", Phys. Rev. **92**, 52–58 (1953).

[10] L. N. Cooper, "Bound Electron Pairs in a Degenerate Fermi Gas", Phys. Rev. **104**, 1189–1190 (1956).

[11] J. Bardeen, L. N. Cooper, and J. R. Schrieffer, "Theory of Superconductivity", Phys. Rev. **108**, 1175–1204 (1957).

[12] L. P. Gor'kov, "Microscopic derivation of the Ginzburg–Landau equations in the theory of superconductivity", Soviet Physics JETP **9**, 1364–1367 (1959).

[13] V. L. Ginzburg and L. D. Landau, "On the Theory of superconductivity", Zh. Eksp. Teor. Fiz. **20**, edited by D. ter Haar, 1064–1082 (1950).

[14] B. D. Josephson, "Possible new effects in superconductive tunnelling", Physics Letters **1**, 251–253 (1962).

[15] M. Tinkham, *Introduction to Superconductivity*, 2nd ed (Dover Publications, Mineola, N.Y., 1996).

[16] R. Newrock, C. Lobb, U. Geigenmüller, and M. Octavio, "The Two-Dimensional Physics of Josephson Junction Arrays", in *Solid State Physics*, Vol. 54, edited by H. Ehrenreich and F. Spaepen (Academic Press, 2000), pp. 263–512.

[17] P. W. Anderson and J. M. Rowell, "Probable Observation of the Josephson Superconducting Tunneling Effect", Phys. Rev. Lett. **10**, 230–232 (1963).

[18] J. M. Rowell, "Magnetic Field Dependence of the Josephson Tunnel Current", Phys. Rev. Lett. **11**, 200–202 (1963).

[19] S. Shapiro, "Josephson Currents in Superconducting Tunneling: The Effect of Microwaves and Other Observations", Phys. Rev. Lett. **11**, 80–82 (1963).

[20] R. C. Jaklevic, J. Lambe, A. H. Silver, and J. E. Mercereau, "Quantum Interference Effects in Josephson Tunneling", Phys. Rev. Lett. **12**, 159–160 (1964).

[21] S. T. Ruggiero and D. A. Rudman, *Superconducting Devices* (San Diego, CA (USA); Academic Press Inc., Jan. 1990).

[22] J. Clarke and A. I. Braginski, eds., *The SQUID Handbook: Fundamentals and Technology of SQUIDs and SQUID Systems Vol. 1*, en, The SQUID Handbook (Wiley-VCH Verlag, Weinheim, Germany, June 2004).

[23] A. H. Silver and J. E. Zimmerman, "Quantum States and Transitions in Weakly Connected Superconducting Rings", Phys. Rev. **157**, 317–341 (1967).

[24] J. Clarke and A. I. Braginski, eds., *The SQUID Handbook: Applications of SQUIDs and SQUID Systems Vol. 2*, en, The SQUID Handbook (Wiley-VCH Verlag, Weinheim, Germany, Aug. 2006).

[25] J. E. Zimmerman, P. Thiene, and J. T. Harding, "Design and Operation of Stable rf-Biased Superconducting Point-Contact Quantum Devices, and a Note on the Properties of Perfectly Clean Metal Contacts", Journal of Applied Physics **41**, 1572–1580 (1970).

[26] D. Cohen, E. A. Edelsack, and J. E. Zimmerman, "MAGNETOCARDIOGRAMS TAKEN INSIDE A SHIELDED ROOM WITH A SUPERCONDUCTING POINT-CONTACT MAGNETOMETER", Applied Physics Letters **16**, 278–280 (1970).

[27] M. Nisenoff, "Superconducting magnetometers with sensitivities approaching 10 -10 gauss", Rev. Phys. Appl. (Paris) **5**, 21–24 (1970).

[28] J. Mercereau, "Superconducting magnetometers", Revue de Physique Appliquée **5**, 13–20 (1970).

[29] D. Cohen, "Magnetoencephalography: Detection of the Brain's Electrical Activity with a Superconducting Magnetometer", Science **175**, 664–666 (1972).

[30] W. S. Goree and M. Fuller, "Magnetometers using RF-driven squids and their applications in rock magnetism and paleomagnetism", Reviews of Geophysics **14**, 591–608 (1976).

[31] B. Cabrera, "First Results from a Superconductive Detector for Moving Magnetic Monopoles", Phys. Rev. Lett. **48**, 1378–1381 (1982).

[32] F. Wellstood, C. Heiden, and J. Clarke, "Integrated dc SQUID magnetometer with a high slew rate", Review of Scientific Instruments **55**, 952–957 (1984).

[33] J. Knuutila, M. Kajola, H. Seppä, R. Mutikainen, and J. Salmi, "Design, optimization, and construction of a dc SQUID with complete flux transformer circuits", Journal of Low Temperature Physics **71**, 369–392 (1988).

[34] J. E. Zimmerman and N. V. Frederick, "Miniature Ultrasensitive Superconducting Magnetic Gradiometer and Its Use in Cardiography and Other Applications", Applied Physics Letters **19**, 16–19 (1971).

[35] J. Opfer, Y. Yeo, J. Pierce, and L. Rorden, "A superconducting second-derivative gradiometer", IEEE Transactions on Magnetics **10**, 536–539 (1974).

[36] M. B. Ketchen, W. M. Goubau, J. Clarke, and G. B. Donaldson, "Superconducting thin-film gradiometer", Journal of Applied Physics **49**, 4111–4116 (1978).

[37] H. J. Paik, E. R. Mapoles, and K. Y. Wang, "Superconducting gravity gradiometers", AIP Conference Proceedings **44**, 166–170 (1978).

[38] W. C. Overton Jr, "Detection of a thin sheet magnetic anomaly by squid-gradiometer systems: possibility of hydrofracture azimuth determination", in (Los Alamos Scientific Lab., NM (USA), Dec. 1978).

[39] W. Podney and R. Sager, "Measurement of Fluctuating Magnetic Gradients Originating from Oceanic Internal Waves", Science **205**, 1381–1382 (1979).

[40] H. J. Paik, "Superconducting Tensor Gravity Gradiometer with SQUID Readout", in *SQUID Applications to Geophysics* (Society of Exploration Geophysicists, Jan. 1981).

[41] E. Mapoles, "A Superconducting Gravity Gradiometer", in *SQUID Applications to Geophysics* (Society of Exploration Geophysicists, Jan. 1981).

[42] V. J. de Waal and T. M. Klapwijk, "Compact integrated dc SQUID gradiometer", Applied Physics Letters **41**, 669–671 (1982).

[43] G. L. Romani, S. J. Williamson, and L. Kaufman, "Tonotopic Organization of the Human Auditory Cortex", Science **216**, 1339–1340 (1982).

[44] G. J. van Nieuwenhuyzen and V. J. de Waal, "Second order gradiometer and dc SQUID integrated on a planar substrate", Applied Physics Letters **46**, 439–441 (1985).

[45] M. Koyanagi, N. Kasai, K. Chinone, M. Nakanishi, S. Kosaka, M. Higuchi, and H. Kado, "An integrated DC SQUID gradiometer for biomagnetic application", IEEE Transactions on Magnetics **25**, 1166–1169 (1989).

[46] J. Clarke, "A superconducting galvanometer employing Josephson tunnelling", The Philosophical Magazine: A Journal of Theoretical Experimental and Applied Physics **13**, 115–127 (1966).

[47] J. M. Martinis and J. Clarke, "Signal and noise theory for a dc SQUID amplifier", Journal of Low Temperature Physics **61**, 227–236 (1985).

[48] C. Hilbert and J. Clarke, "DC SQUIDs as radiofrequency amplifiers", Journal of Low Temperature Physics **61**, 263–280 (1985).

[49] M. B. Ketchen, T. Kopley, and H. Ling, "Miniature SQUID susceptometer", Applied Physics Letters **44**, 1008–1010 (1984).

[50] D. Awschalom and J. Warnock, "Picosecond magnetic spectroscopy with integrated DC SQUIDs", IEEE Transactions on Magnetics **25**, 1186–1192 (1989).

[51] M. Ketchen, D. Awschalom, W. Gallagher, A. Kleinsasser, R. Sandstrom, J. Rozen, and B. Bumble, "Design, fabrication, and performance of integrated miniature SQUID susceptometers", IEEE Transactions on Magnetics **25**, 1212–1215 (1989).

[52] D. N. Langenberg, W. H. Parker, and B. N. Taylor, "Experimental Test of the Josephson Frequency-Voltage Relation", Phys. Rev. **150**, 186–188 (1966).

[53] B. N. Taylor, W. H. Parker, D. N. Langenberg, and A. Denenstein, "On the Use of the AC Josephson Effect to Maintain Standards of Electromotive Force", Metrologia **3**, 89 (1967).

[54] W. H. Parker, B. N. Taylor, and D. N. Langenberg, "Measurement of $\frac{2e}{h}$ Using the ac Josephson Effect and its Implications for Quantum Electrodynamics", Phys. Rev. Lett. **18**, 287–291 (1967).

[55] J. Clarke, "Experimental Comparison of the Josephson Voltage-Frequency Relation in Different Superconductors", Phys. Rev. Lett. **21**, 1566–1569 (1968).

[56] W. H. Parker, D. N. Langenberg, A. Denenstein, and B. N. Taylor, "Determination of $\frac{e}{h}$, Using Macroscopic Quantum Phase Coherence in Superconductors. I. Experiment", Phys. Rev. **177**, 639–664 (1969).

[57] T. F. Finnegan, A. Denenstein, and D. N. Langenberg, "ac-Josephson-Effect Determination of $\frac{e}{h}$: A Standard of Electrochemical Potential Based on Macroscopic Quantum Phase Coherence in Superconductors", Phys. Rev. B **4**, 1487–1522 (1971).

[58] B. F. Field, T. F. Finnegan, and J. Toots, "Volt Maintenance at NBS via 2e/h: A New Definition of the NBS Volt", Metrologia **9**, 155 (1973).

[59] D. W. Palmer and J. E. Mercereau, "Coherent effects in large arrays of superconducting bridges", Applied Physics Letters **25**, 467–469 (1974).

[60] D. Palmer and J. Mercereau, "Coherent effects in series arrays of proximity effect superconducting bridges", IEEE Transactions on Magnetics **11**, 667–670 (1975).

[61] M. T. Levinsen, R. Y. Chiao, M. J. Feldman, and B. A. Tucker, "An inverse ac Josephson effect voltage standard", Applied Physics Letters **31**, 776–778 (1977).

[62] M. Koyanagi, T. Endo, and A. Nakamura, "Higher standard voltage generated by multiple Josephson junctions", AIP Conference Proceedings **44**, 187–191 (1978).

[63] R. L. Kautz, "On a proposed Josephson-effect voltage standard at zero current bias", Applied Physics Letters **36**, 386–388 (1980).

[64] R. L. Kautz, "The ac Josephson effect in hysteretic junctions: Range and stability of phase lock", Journal of Applied Physics **52**, 3528–3541 (1981).

[65] R. Kautz and G. Costabile, "A Josephson voltage standard using a series array of 100 junctions", IEEE Transactions on Magnetics **17**, 780–783 (1981).

[66] T. Endo, M. Koyanagi, and A. Nakamura, "High-Accuracy Josephson Potentiometer", IEEE Transactions on Instrumentation and Measurement **32**, 267–271 (1983).

[67] J. Niemeyer, J. H. Hinken, and R. L. Kautz, "Microwave-induced constant-voltage steps at one volt from a series array of Josephson junctions", Applied Physics Letters **45**, 478–480 (1984).

[68] C. Hamilton, R. Kautz, R. Steiner, and F. Lloyd, "A practical Josephson voltage standard at 1 V", IEEE Electron Device Letters **6**, 623–625 (1985).

[69] J. Niemeyer, L. Grimm, W. Meier, J. H. Hinken, and E. Vollmer, "Stable Josephson reference voltages between 0.1 and 1.3 V for high-precision voltage standards", Applied Physics Letters **47**, 1222–1223 (1985).

[70] F. Lloyd, C. Hamilton, J. Beall, D. Go, R. Ono, and R. Harris, "A Josephson array voltage standard at 10 V", IEEE Electron Device Letters **8**, 449–450 (1987).

[71] C. Hamilton, F. Lloyd, K. Chieh, and W. Goeke, "A 10-V Josephson voltage standard", IEEE Transactions on Instrumentation and Measurement **38**, 314–316 (1989).

[72] S. P. Benz, "Superconductor-normal-superconductor junctions for programmable voltage standards", Applied Physics Letters **67**, 2714–2716 (1995).

[73] S. P. Benz and C. A. Hamilton, "A pulse-driven programmable Josephson voltage standard", Applied Physics Letters **68**, 3171–3173 (1996).

[74] S. P. Benz, C. A. Hamilton, C. J. Burroughs, T. E. Harvey, and L. A. Christian, "Stable 1 volt programmable voltage standard", Applied Physics Letters **71**, 1866–1868 (1997).

[75] C. Burroughs, S. Benz, P. Dresselhaus, and Y. Chong, "Precision measurements of AC Josephson voltage standard operating margins", IEEE Transactions on Instrumentation and Measurement **54**, 624–627 (2005).

[76] Y. Chong, C. Burroughs, P. Dresselhaus, N. Hadacek, H. Yamamori, and S. Benz, "2.6-V high-resolution programmable Josephson voltage standard circuits using double-stacked MoSi/sub 2/-barrier junctions", IEEE Transactions on Instrumentation and Measurement **54**, 616–619 (2005).

[77] S. P. Benz, C. J. Burroughs, P. D. Dresselhaus, N. F. Bergren, T. E. Lipe, J. R. Kinard, and Y.-h. Tang, "An AC Josephson Voltage Standard for AC–DC Transfer-Standard Measurements", IEEE Transactions on Instrumentation and Measurement **56**, 239–243 (2007).

[78] S. P. Benz, P. D. Dresselhaus, A. Rufenacht, N. F. Bergren, J. R. Kinard, and R. P. Landim, "Progress Toward a 1 V Pulse-Driven AC Josephson Voltage Standard", IEEE Transactions on Instrumentation and Measurement **58**, 838–843 (2009).

[79] P. D. Dresselhaus, M. M. Elsbury, D. Olaya, C. J. Burroughs, and S. P. Benz, "10 Volt Programmable Josephson Voltage Standard Circuits Using NbSi-Barrier Junctions", IEEE Transactions on Applied Superconductivity **21**, 693–696 (2011).

[80] J. M. Kosterlitz and D. J. Thouless, "Long range order and metastability in two dimensional solids and superfluids. (Application of dislocation theory)", Journal of Physics C: Solid State Physics **5**, L124 (1972).

[81] J. M. Kosterlitz and D. J. Thouless, "Ordering, metastability and phase transitions in two-dimensional systems", Journal of Physics C: Solid State Physics **6**, 1181 (1973).

[82] J. M. Kosterlitz, "The critical properties of the two-dimensional xy model", Journal of Physics C: Solid State Physics **7**, 1046 (1974).

[83] V. L. Berezinsky, "Destruction of Long-range Order in One-dimensional and Two-dimensional Systems Possessing a Continuous Symmetry Group. I. Classical Systems", Sov. Phys. JETP **32**, 493–500 (1971).

[84] V. L. Berezinsky, "Destruction of Long-range Order in One-dimensional and Two-dimensional Systems Possessing a Continuous Symmetry Group. II. Quantum Systems.", Sov. Phys. JETP **34**, 610 (1972).

[85] A. Altland and B. D. Simons, *Condensed matter field theory*, 2nd Edition (Cambridge University Press, Cambridge, United Kingdom, 2010).

[86] P. M. Chaikin and T. C. Lubensky, *Principles of Condensed Matter Physics* (Cambridge University Press, Cambridge, United Kingdom, 1995).

[87] C. J. Lobb, "Josephson junction arrays and superconducting wire networks", Helvetica Physica Acta **65**, 219 (1992).

[88] M. R. Beasley, J. E. Mooij, and T. P. Orlando, "Possibility of Vortex-Antivortex Pair Dissociation in Two-Dimensional Superconductors", Phys. Rev. Lett. **42**, 1165–1168 (1979).

[89] S. Doniach and B. A. Huberman, "Topological Excitations in Two-Dimensional Superconductors", Phys. Rev. Lett. **42**, 1169–1172 (1979).

[90] B. I. Halperin and D. R. Nelson, "Resistive transition in superconducting films", Journal of Low Temperature Physics **36**, 599–616 (1979).

[91] J. Berchier and D. Sanchez, "Finite size arrays of proximity effect bridges", Rev. Phys. Appl. (Paris) **14**, 757–761 (1979).

[92] D. H. Sanchez and J.-L. Berchier, "Properties of n × n square arrays of proximity effect bridges", Journal of Low Temperature Physics **43**, 65–89 (1981).

[93] D. J. Resnick, J. C. Garland, J. T. Boyd, S. Shoemaker, and R. S. Newrock, "Kosterlitz-Thouless Transition in Proximity-Coupled Superconducting Arrays", Phys. Rev. Lett. **47**, 1542–1545 (1981).

[94] D. W. Abraham, C. J. Lobb, M. Tinkham, and T. M. Klapwijk, "Resistive transition in two-dimensional arrays of superconducting weak links", Phys. Rev. B **26**, 5268–5271 (1982).

[95] C. J. Lobb, D. W. Abraham, and M. Tinkham, "Theoretical interpretation of resistive transition data from arrays of superconducting weak links", Phys. Rev. B **27**, 150–157 (1983).

[96] R. F. Voss and R. A. Webb, "Phase coherence in a weakly coupled array of 20 000 Nb Josephson junctions", Phys. Rev. B **25**, 3446–3449 (1982).

[97] R. A. Webb, R. F. Voss, G. Grinstein, and P. M. Horn, "Magnetic Field Behavior of a Josephson-Junction Array: Two-Dimensional Flux Transport on a Periodic Substrate", Phys. Rev. Lett. **51**, 690–693 (1983).

[98] M. Tinkham, D. W. Abraham, and C. J. Lobb, "Periodic flux dependence of the resistive transition in two-dimensional superconducting arrays", Phys. Rev. B **28**, 6578–6581 (1983).

[99] D. Kimhi, F. Leyvraz, and D. Ariosa, "Resistive transition in two-dimensional arrays of proximity Josephson junctions: Magnetic field dependence", Phys. Rev. B **29**, 1487–1489 (1984).

[100] C. Leemann, P. Lerch, G. .-. Racine, and P. Martinoli, "Vortex Dynamics and Phase Transitions in a Two-Dimensional Array of Josephson Junctions", Phys. Rev. Lett. **56**, 1291–1294 (1986).

[101] R. K. Brown and J. C. Garland, "Effect of magnetic-field-induced frustration on the superconducting transition of proximity-coupled arrays", Phys. Rev. B **33**, 7827–7829 (1986).

[102] B. J. van Wees, H. S. J. van der Zant, and J. E. Mooij, "Phase transitions of Josephson-tunnel-junction arrays at zero and full frustration", Phys. Rev. B **35**, 7291–7294 (1987).

[103] C. Giovannella and M. Tinkham, *Macroscopic Quantum Phenomena and Coherence in Superconducting Networks* (WORLD SCIENTIFIC, 1996).

[104] A. M. Goldman and S. A. Wolf, eds., *Percolation, Localization, and Superconductivity* (Springer, New York, New York, 1984).

[105] H. Cerdeira and S. Shenoy (editors), "Proceedings of the ICTP Workshop on Josephson Junction Arrays", Physica B **222**, 253–406 (1996).

[106] J. Mooji and G. Schön (editors), "Coherence in Superconducting Networks", Physica B **152**, 1–302 (1988).

[107] J. Matisoo, "SUBNANOSECOND PAIR-TUNNELING TO SINGLE-PARTICLE TUNNELING TRANSITIONS IN JOSEPHSON JUNCTIONS", Applied Physics Letters **9**, 167–168 (1966).

[108] J. Matisoo, "The tunneling cryotron—A superconductive logic element based on electron tunneling", Proceedings of the IEEE **55**, 172–180 (1967).

[109] J. Matisoo, "Measurement of current transfer time in a tunneling cryotron flip-flop", Proceedings of the IEEE **55**, 2052–2053 (1967).

[110] W. Anacker, "Potential of superconductive josephson tunneling technology for ultrahigh performance memories and processors", IEEE Transactions on Magnetics **5**, 968–975 (1969).

[111] H. H. Zappe and K. R. Grebe, "Ultra-high-speed Operation of Josephson Tunneling Devices", IBM Journal of Research and Development **15**, 405–407 (1971).

[112] W. Jutzi, T. Mohr, M. Gasser, and H. Gschwind, "Josephson junctions with 1 μm dimensions and with picosecond switching times", Electronics Letters **8**, 589–591 (1972).

[113] R. Broom, P. Gueret, W. Kotyczka, T. Mohr, A. Moser, A. Oosenbrug, and P. Wolf, "Model for a 15ns 16K RAM with Josephson junctions", in 1978 IEEE International Solid-State Circuits Conference. Digest of Technical Papers, Vol. XXI (1978), pp. 60–61.

[114] M. Klein, D. Herrell, and A. Davidson, "Sub-100ps experimental Josephson interferometer logic", in 1978 IEEE International Solid-State Circuits Conference. Digest of Technical Papers, Vol. XXI (1978), pp. 62–63.

[115] W. Anacker, "Computers: Computing at 4 degrees Kelvin: Superconducting technology and unconventional packaging herald an era of ultrafast, ultrareliable computers", IEEE Spectrum **16**, 26–37 (1979).

[116] S. M. Faris, W. H. Henkels, E. A. Valsamakis, and H. H. Zappe, "Basic Design of a Josephson Technology Cache Memory", IBM Journal of Research and Development **24**, 143–154 (1980).

[117] T. R. Gheewala, "Design of 2.5-Micrometer Josephson Current Injection Logic (CIL)", IBM Journal of Research and Development **24**, 130–142 (1980).

[118] W. Anacker, "Josephson Computer Technology: An IBM Research Project", IBM Journal of Research and Development **24**, 107–112 (1980).

[119] W. J. Gallagher, E. P. Harris, and M. B. Ketchen, "Superconductivity at IBM - a Centennial Review: Part I - Superconducting Computer and Device Applications", in IEEE/CSC & ESAS EUROPEAN SUPERCONDUCTIVITY NEWS FORUM, Vol. 6 (2012).

[120] K. Likharev, O. Mukhanov, and V. Semenov, "RESISTIVE SINGLE FLUX QUANTUM LOGIC FOR THE JOSEPHSON-JUNCTION DIGITAL TECHNOLOGY", in *Proceedings of the Third International Conference on Superconducting Quantum Devices, Berlin (West), June 25-28, 1985*, edited by H.-D. Hahlbohm and H. Lübbig (De Gruyter, Berlin, Boston, 1986), pp. 1103–1108.

[121] K. Likharev and V. Semenov, "RSFQ logic/memory family: a new Josephson-junction technology for sub-terahertz-clock-frequency digital systems", IEEE Transactions on Applied Superconductivity **1**, 3–28 (1991).

[122] K. K. Likharev, "Rapid Single-Flux-Quantum Logic", in *The New Superconducting Electronics*, edited by H. Weinstock and R. W. Ralston (Springer Netherlands, Dordrecht, 1993), pp. 423–452.

[123] V. Koshelets, K. Likharev, V. Migulin, O. Mukhanov, G. Ovsyannikov, V. Semenov, I. Serpuchenko, and A. Vystavkin, "Experimental realization of a resistive single flux quantum logic circuit", IEEE Transactions on Magnetics **23**, 755–758 (1987).

[124] O. Mukhanov, V. Semenov, and K. Likharev, "Ultimate performance of the RSFQ logic circuits", IEEE Transactions on Magnetics **23**, 759–762 (1987).

[125] O. Mukhanov, S. Polonsky, and V. Semenov, "New elements of the RSFQ logic family", IEEE Transactions on Magnetics **27**, 2435–2438 (1991).

[126] S. Polonsky, V. Semenov, P. Bunyk, A. Kirichenko, A. Kidiyarov-Shevchenko, O. Mukhanov, P. Shevchenko, D. Schneider, D. Zinoviev, and K. Likharev, "New RSFQ circuits (Josephson junction digital devices)", IEEE Transactions on Applied Superconductivity **3**, 2566–2577 (1993).

[127] O. Mukhanov, "Rapid single flux quantum (RSFQ) shift register family", IEEE Transactions on Applied Superconductivity **3**, 2578–2581 (1993).

[128] O. Mukhanov, "RSFQ 1024-bit shift register for acquisition memory", IEEE Transactions on Applied Superconductivity **3**, 3102–3113 (1993).

[129] P. I. Bunyk, A. Oliva, V. K. Semenov, M. Bhushan, K. K. Likharev, J. E. Lukens, M. B. Ketchen, and W. H. Mallison, "High-speed single-flux-quantum circuit using planarized niobium-trilayer Josephson junction technology", Applied Physics Letters **66**, 646–648 (1995).

[130] J. Lin, V. Semenov, and K. Likharev, "Design of SFQ-counting analog-to-digital converter", IEEE Transactions on Applied Superconductivity **5**, 2252–2259 (1995).

[131] O. Mukhanov and A. Kirichenko, "Implementation of a FFT radix 2 butterfly using serial RSFQ multiplier-adders", IEEE Transactions on Applied Superconductivity **5**, 2461–2464 (1995).

[132] K. Gaj, E. Friedman, M. Feldman, and A. Krasniewski, "A clock distribution scheme for large RSFQ circuits", IEEE Transactions on Applied Superconductivity **5**, 3320–3324 (1995).

[133] Q. P. Herr and M. J. Feldman, "Error rate of a superconducting circuit", Applied Physics Letters **69**, 694–695 (1996).

[134] Q. Herr, N. Vukovic, C. Mancini, K. Gaj, Q. Ke, V. Adler, E. Friedman, A. Krasniewski, M. Bocko, and M. Feldman, "Design and low speed testing of a four-bit RSFQ multiplier-accumulator", IEEE Transactions on Applied Superconductivity **7**, 3168–3171 (1997).

[135] Q. Herr, K. Gaj, A. Herr, N. Vukovic, C. Mancini, M. Bocko, and M. Feldman, "High speed testing of a four-bit RSFQ decimation digital filter", IEEE Transactions on Applied Superconductivity **7**, 2975–2978 (1997).

[136] O. Mukhanov and S. Rylov, "Time-to-digital converters based on RSFQ digital counters", IEEE Transactions on Applied Superconductivity **7**, 2669–2672 (1997).

[137] A. Kirichenko, O. Mukhanov, and A. Ryzhikh, "Advanced on-chip test technology for RSFQ circuits", IEEE Transactions on Applied Superconductivity **7**, 3438–3441 (1997).

[138] A. Hodge Worsham, A. Miklich, D. Miller, J. Kang, and J. Przybysz, "Single flux quantum circuits for 2.5 Gbps data switching", IEEE Transactions on Applied Superconductivity **7**, 2476–2479 (1997).

[139] S. Rylov, L. Bunz, D. Gaidarenko, M. Fisher, R. Robertazzi, and O. Mukhanov, "High resolution ADC system", IEEE Transactions on Applied Superconductivity **7**, 2649–2652 (1997).

[140] N. Dubash, P.-F. Yuh, V. Borzenets, T. van Duzer, and S. Whiteley, "SFQ data communication switch", IEEE Transactions on Applied Superconductivity **7**, 2681–2684 (1997).

[141] Z. Deng, N. Yoshikawa, S. Whiteley, and T. Van Duzer, "Data-driven self-timed RSFQ digital integrated circuit and system", IEEE Transactions on Applied Superconductivity **7**, 3634–3637 (1997).

[142] W. Chen, A. V. Rylyakov, V. Patel, J. E. Lukens, and K. K. Likharev, "Superconductor digital frequency divider operating up to 750 GHz", Applied Physics Letters **73**, 2817–2819 (1998).

[143] W. Chen, A. Rylyakov, V. Patel, J. Lukens, and K. Likharev, "Rapid single flux quantum T-flip flop operating up to 770 GHz", IEEE Transactions on Applied Superconductivity **9**, 3212–3215 (1999).

[144] O. Mukhanov, D. Gupta, A. Kadin, and V. Semenov, "Superconductor analog-to-digital converters", Proceedings of the IEEE **92**, 1564–1584 (2004).

[145] N. Yoshikawa and Y. Kato, "Reduction of power consumption of RSFQ circuits by inductance-load biasing", Superconductor Science and Technology **12**, 918 (1999).

[146] Y. Yamanashi, T. Nishigai, and N. Yoshikawa, "Study of LR-Loading Technique for Low-Power Single Flux Quantum Circuits", IEEE Transactions on Applied Superconductivity **17**, 150–153 (2007).

[147] T. Ortlepp, O. Wetzstein, S. Engert, J. Kunert, and H. Toepfer, "Reduced Power Consumption in Superconducting Electronics", IEEE Transactions on Applied Superconductivity **21**, 770–775 (2011).

[148] D. E. Kirichenko, S. Sarwana, and A. F. Kirichenko, "Zero Static Power Dissipation Biasing of RSFQ Circuits", IEEE Transactions on Applied Superconductivity **21**, 776–779 (2011).

[149] O. T. Oberg, Q. P. Herr, A. G. Ioannidis, and A. Y. Herr, "Integrated Power Divider for Superconducting Digital Circuits", IEEE Transactions on Applied Superconductivity **21**, 571–574 (2011).

[150] Q. P. Herr, A. Y. Herr, O. T. Oberg, and A. G. Ioannidis, "Ultra-low-power superconductor logic", Journal of Applied Physics **109**, 103903 (2011).

[151] M. Tanaka, M. Ito, A. Kitayama, T. Kouketsu, and A. Fujimaki, "18-GHz, 4.0-aJ/bit Operation of Ultra-Low-Energy Rapid Single-Flux-Quantum Shift Registers", Japanese Journal of Applied Physics **51**, 053102 (2012).

[152] A. Y. Herr, Q. P. Herr, O. T. Oberg, O. Naaman, J. X. Przybysz, P. Borodulin, and S. B. Shauck, "An 8-bit carry look-ahead adder with 150 ps latency and sub-microwatt power dissipation at 10 GHz", Journal of Applied Physics **113**, 033911 (2013).

[153] M. H. Volkmann, A. Sahu, C. J. Fourie, and O. A. Mukhanov, "Implementation of energy efficient single flux quantum digital circuits with sub-aJ/bit operation", Superconductor Science and Technology **26**, 015002 (2012).

[154] M. Tanaka, A. Kitayama, T. Koketsu, M. Ito, and A. Fujimaki, "Low-Energy Consumption RSFQ Circuits Driven by Low Voltages", IEEE Transactions on Applied Superconductivity **23**, 1701104–1701104 (2013).

[155] I. V. Vernik, S. B. Kaplan, M. H. Volkmann, A. V. Dotsenko, C. J. Fourie, and O. A. Mukhanov, "Design and test of asynchronous eSFQ circuits", Superconductor Science and Technology **27**, 044030 (2014).

[156] W. Wustmann and K. D. Osborn, "Reversible fluxon logic: Topological particles allow ballistic gates along one-dimensional paths", Phys. Rev. B **101**, 014516 (2020).

[157] K. D. Osborn and W. Wustmann, "Reversible Fluxon Logic With Optimized CNOT Gate Components", IEEE Transactions on Applied Superconductivity **31**, 1–13 (2021).

[158] K. Osborn and W. Wustmann, "Asynchronous Reversible Computing Unveiled Using Ballistic Shift Registers", Phys. Rev. Appl. **19**, 054034 (2023).

[159] W. Wustmann and K. D. Osborn, *Boosting fluxons for ballistic-logic power using an Aharonov-Casher ring*, (2024) arXiv:2305.05021 [cond-mat.supr-con].

[160] A. J. Leggett, "PROSPECTS IN ULTRALOW TEMPERATURE PHYSICS", J. Phys. Colloques **39**, C6-1264-C6–1269 (1978).

[161] A. J. Leggett, "Macroscopic Quantum Systems and the Quantum Theory of Measurement", Progress of Theoretical Physics Supplement **69**, 80–100 (1980).

[162] A. Widom, "Quantum electrodynamic circuits at ultralow temperature", Journal of Low Temperature Physics **37**, 449–460 (1979).

[163] R. H. Koch, D. J. Van Harlingen, and J. Clarke, "Quantum-Noise Theory for the Resistively Shunted Josephson Junction", Phys. Rev. Lett. **45**, 2132–2135 (1980).

[164] A. Widom, G. Megaloudis, J. E. Sacco, and T. D. Clark, "Theory of quantum-electrodynamic flux tunneling in a superconducting ring with a Josephson weak link", Il Nuovo Cimento B (1971-1996) **61**, 112–122 (1981).

[165] A. O. Caldeira and A. J. Leggett, "Influence of Dissipation on Quantum Tunneling in Macroscopic Systems", Phys. Rev. Lett. **46**, 211–214 (1981).

[166] A. Widom, G. Megaloudis, T. Clark, H. Prance, and R. Prance, "Quantum electrodynamic charge space energy bands in singly connected superconducting weak links", Journal of Physics A: Mathematical and General **15**, 3877 (1982).

[167] A. O. Caldeira and A. J. Leggett, "Quantum tunnelling in a dissipative system", Annals of Physics **149**, 374–456 (1983).

[168] K. K. Likharev, "True quantum-mechanical macroscopic effects in weak superconductivity", Soviet Physics Uspekhi **26**, 87 (1983).

[169] W. den Boer and R. de Bruyn Ouboter, "Flux transition mechanisms in superconducting loops closed with a low capacitance point contact", Physica B+C **98**, 185–190 (1980).

[170] R. J. Prance, A. P. Long, T. D. Clark, A. Widom, J. E. Mutton, J. Sacco, M. W. Potts, G. Megaloudis, and F. Goodall, "Macroscopic quantum electrodynamic effects in a superconducting ring containing a Josephson weak link", Nature **289**, 543–549 (1981).

[171] R. F. Voss and R. A. Webb, "Macroscopic Quantum Tunneling in 1-μm Nb Josephson Junctions", Phys. Rev. Lett. **47**, 265–268 (1981).

[172] L. D. Jackel, J. P. Gordon, E. L. Hu, R. E. Howard, L. A. Fetter, D. M. Tennant, R. W. Epworth, and J. Kurkijärvi, "Decay of the Zero-Voltage State in Small-Area, High-Current-Density Josephson Junctions", Phys. Rev. Lett. **47**, 697–700 (1981).

[173] M. H. Devoret, J. M. Martinis, and J. Clarke, "Measurements of Macroscopic Quantum Tunneling out of the Zero-Voltage State of a Current-Biased Josephson Junction", Phys. Rev. Lett. **55**, 1908–1911 (1985).

[174] J. M. Martinis, M. H. Devoret, and J. Clarke, "Energy-Level Quantization in the Zero-Voltage State of a Current-Biased Josephson Junction", Phys. Rev. Lett. **55**, 1543–1546 (1985).

[175] C. D. Tesche, "Schrödinger's Cat: A Realization in Superconducting Devices", Annals of the New York Academy of Sciences **480**, 36–50 (1986).

[176] K. K. Likharev and A. B. Zorin, "Theory of the Bloch-wave oscillations in small Josephson junctions", Journal of Low Temperature Physics **59**, 347–382 (1985).

[177] D. Averin, A. Zorin, and K. Likharev, "Bloch oscillations in small Josephson junctions", Sov. Phys. - JETP (Engl. Transl.) **61** (1985).

[178] D. Averin and K. Likharev, "Chapter 6 - Single Electronics: A Correlated Transfer of Single Electrons and Cooper Pairs in Systems of Small Tunnel Junctions", in *Mesoscopic Phenomena in Solids*, Vol. 30, edited by B. Alt-

shuler, P. Lee, and R. Webb, Modern Problems in Condensed Matter Sciences (Elsevier, 1991), pp. 173–271.

[179] L. S. Kuzmin and D. B. Haviland, "Observation of the Bloch oscillations in an ultrasmall Josephson junction", Phys. Rev. Lett. **67**, 2890–2893 (1991).

[180] P. Lafarge, P. Joyez, D. Esteve, C. Urbina, and M. H. Devoret, "Two-electron quantization of the charge on a superconductor", Nature **365**, 422–424 (1993).

[181] P. Joyez, P. Lafarge, A. Filipe, D. Esteve, and M. H. Devoret, "Observation of parity-induced suppression of Josephson tunneling in the superconducting single electron transistor", Phys. Rev. Lett. **72**, 2458–2461 (1994).

[182] P. Shor, "Algorithms for quantum computation: discrete logarithms and factoring", in Proceedings 35th Annual Symposium on Foundations of Computer Science (1994), pp. 124–134.

[183] Y. Nakamura, C. D. Chen, and J. S. Tsai, "Spectroscopy of Energy-Level Splitting between Two Macroscopic Quantum States of Charge Coherently Superposed by Josephson Coupling", Phys. Rev. Lett. **79**, 2328–2331 (1997).

[184] V. Bouchiat, D. Vion, P. Joyez, D. Esteve, and M. Devoret, "Quantum coherence with a single Cooper pair", Physica Scripta **1998**, 165 (1998).

[185] Y. Nakamura, Y. A. Pashkin, and J. S. Tsai, "Coherent control of macroscopic quantum states in a single-Cooper-pair box", Nature **398**, 786–788 (1999).

[186] J. E. Mooij, T. P. Orlando, L. Levitov, L. Tian, C. H. van der Wal, and S. Lloyd, "Josephson Persistent-Current Qubit", Science **285**, 1036–1039 (1999).

[187] T. P. Orlando, J. E. Mooij, L. Tian, C. H. van der Wal, L. S. Levitov, S. Lloyd, and J. J. Mazo, "Superconducting persistent-current qubit", Phys. Rev. B **60**, 15398–15413 (1999).

[188] J. R. Friedman, V. Patel, W. Chen, S. K. Tolpygo, and J. E. Lukens, "Quantum superposition of distinct macroscopic states", Nature **406**, 43–46 (2000).

[189] C. H. van der Wal, A. C. J. ter Haar, F. K. Wilhelm, R. N. Schouten, C. J. P. M. Harmans, T. P. Orlando, S. Lloyd, and J. E. Mooij, "Quantum Superposition of Macroscopic Persistent-Current States", Science **290**, 773–777 (2000).

[190] R. C. Ramos, M. A. Gubrud, A. J. Berkley, J. R. Anderson, C. J. Lobb, and F. C. Wellstood, "Design for effective thermalization of junctions for quantum coherence", IEEE Transactions on Applied Superconductivity **11**, 998–1001 (2001).

[191] J. M. Martinis, S. Nam, J. Aumentado, and C. Urbina, "Rabi Oscillations in a Large Josephson-Junction Qubit", Phys. Rev. Lett. **89**, 117901 (2002).

[192] J. Koch, T. M. Yu, J. Gambetta, A. A. Houck, D. I. Schuster, J. Majer, A. Blais, M. H. Devoret, S. M. Girvin, and R. J. Schoelkopf, "Charge-insensitive qubit design derived from the Cooper pair box", Phys. Rev. A **76**, 042319 (2007).

[193] V. E. Manucharyan, J. Koch, L. I. Glazman, and M. H. Devoret, "Fluxonium: Single Cooper-Pair Circuit Free of Charge Offsets", Science **326**, 113–116 (2009).

[194] F. Arute, K. Arya, R. Babbush, D. Bacon, J. C. Bardin, R. Barends, R. Biswas, S. Boixo, F. G. S. L. Brandao, D. A. Buell, et al., "Quantum supremacy using a programmable superconducting processor", Nature **574**, 505–510 (2019).

[195] G. A. Quantum, Collaborators*†, F. Arute, K. Arya, R. Babbush, D. Bacon, J. C. Bardin, R. Barends, S. Boixo, M. Broughton, et al., "Hartree-Fock on a superconducting qubit quantum computer", Science **369**, 1084–1089 (2020).

[196] K. J. Satzinger, Y.-J. Liu, A. Smith, C. Knapp, M. Newman, C. Jones, Z. Chen, C. Quintana, X. Mi, A. Dunsworth, et al., "Realizing topologically ordered states on a quantum processor", Science **374**, 1237–1241 (2021).

[197] Y. Wu, W.-S. Bao, S. Cao, F. Chen, M.-C. Chen, X. Chen, T.-H. Chung, H. Deng, Y. Du, D. Fan, et al., "Strong Quantum Computational Advantage Using a Superconducting Quantum Processor", Phys. Rev. Lett. **127**, 180501 (2021).

[198] A. Morvan, B. Villalonga, X. Mi, S. Mandrà, A. Bengtsson, P. V. Klimov, Z. Chen, S. Hong, C. Erickson, I. K. Drozdov, et al., "Phase transitions in random circuit sampling", Nature **634**, 328–333 (2024).

[199] R. Acharya, D. A. Abanin, L. Aghababaie-Beni, I. Aleiner, T. I. Andersen, M. Ansmann, F. Arute, K. Arya, A. Asfaw, N. Astrakhantsev, et al., "Quantum error correction below the surface code threshold", Nature **638**, 920–926 (2025).

[200] Y. Kim, A. Eddins, S. Anand, K. X. Wei, E. van den Berg, S. Rosenblatt, H. Nayfeh, Y. Wu, M. Zaletel, K. Temme, et al., "Evidence for the utility of quantum computing before fault tolerance", Nature **618**, 500–505 (2023).

[201] H. Yu, Y. Zhao, and T.-C. Wei, "Simulating large-size quantum spin chains on cloud-based superconducting quantum computers", Phys. Rev. Res. **5**, 013183 (2023).

[202] R. S. Gupta, N. Sundaresan, T. Alexander, C. J. Wood, S. T. Merkel, M. B. Healy, M. Hillenbrand, T. Jochym-O'Connor, J. R. Wootton, T. J. Yoder, et al., "Encoding a magic state with beyond break-even fidelity", Nature **625**, 259–263 (2024).

[203] S. Bravyi, A. W. Cross, J. M. Gambetta, D. Maslov, P. Rall, and T. J. Yoder, "High-threshold and low-overhead fault-tolerant quantum memory", Nature **627**, 778–782 (2024).

[204] D. Vion, A. Aassime, A. Cottet, P. Joyez, H. Pothier, C. Urbina, D. Esteve, and M. H. Devoret, "Manipulating the Quantum State of an Electrical Circuit", Science **296**, 886–889 (2002).

[205] M. Steffen, M. Ansmann, R. McDermott, N. Katz, R. C. Bialczak, E. Lucero, M. Neeley, E. M. Weig, A. N. Cleland, and J. M. Martinis, "State Tomography of Capacitively Shunted Phase Qubits with High Fidelity", Phys. Rev. Lett. **97**, 050502 (2006).

[206] J. Q. You, X. Hu, S. Ashhab, and F. Nori, "Low-decoherence flux qubit", Phys. Rev. B **75**, 140515 (2007).

[207] F. G. Paauw, A. Fedorov, C. J. P. M. Harmans, and J. E. Mooij, "Tuning the Gap of a Superconducting Flux Qubit", Phys. Rev. Lett. **102**, 090501 (2009).

[208] R. Barends, J. Kelly, A. Megrant, D. Sank, E. Jeffrey, Y. Chen, Y. Yin, B. Chiaro, J. Mutus, C. Neill, et al., "Coherent Josephson Qubit Suitable for Scalable Quantum Integrated Circuits", Phys. Rev. Lett. **111**, 080502 (2013).

[209] Y. Chen, C. Neill, P. Roushan, N. Leung, M. Fang, R. Barends, J. Kelly, B. Campbell, Z. Chen, B. Chiaro, et al., "Qubit Architecture with High Coherence and Fast Tunable Coupling", Phys. Rev. Lett. **113**, 220502 (2014).

[210] T. W. Larsen, K. D. Petersson, F. Kuemmeth, T. S. Jespersen, P. Krogstrup, J. Nygård, and C. M. Marcus, "Semiconductor-Nanowire-Based Superconducting Qubit", Phys. Rev. Lett. **115**, 127001 (2015).

[211] G. de Lange, B. van Heck, A. Bruno, D. J. van Woerkom, A. Geresdi, S. R. Plissard, E. P. A. M. Bakkers, A. R. Akhmerov, and L. DiCarlo, "Realization of Microwave Quantum Circuits Using Hybrid Superconducting-Semiconducting Nanowire Josephson Elements", Phys. Rev. Lett. **115**, 127002 (2015).

[212] F. Yan, S. Gustavsson, A. Kamal, J. Birenbaum, A. P. Sears, D. Hover, T. J. Gudmundsen, D. Rosenberg, G. Samach, S. Weber, et al., "The flux qubit revisited to enhance coherence and reproducibility", Nature Communications **7**, 12964 (2016).

[213] D. T. Le, A. Grimsmo, C. Müller, and T. M. Stace, "Doubly nonlinear superconducting qubit", Phys. Rev. A **100**, 062321 (2019).

[214] I. V. Pechenezhskiy, R. A. Mencia, L. B. Nguyen, Y.-H. Lin, and V. E. Manucharyan, "The superconducting quasicharge qubit", Nature **585**, 368–371 (2020).

[215] W. C. Smith, A. Kou, X. Xiao, U. Vool, and M. H. Devoret, "Superconducting circuit protected by two-Cooper-pair tunneling", npj Quantum Information **6**, 8 (2020).

[216] M. Peruzzo, F. Hassani, G. Szep, A. Trioni, E. Redchenko, M. Žemli čka, and J. M. Fink, "Geometric Superinductance Qubits: Controlling Phase Delocalization across a Single Josephson Junction", PRX Quantum **2**, 040341 (2021).

[217] C. Schrade, C. M. Marcus, and A. Gyenis, "Protected Hybrid Superconducting Qubit in an Array of Gate-Tunable Josephson Interferometers", PRX Quantum **3**, 030303 (2022).

[218] P. Brookes, T. Chang, M. Szymanska, E. Grosfeld, E. Ginossar, and M. Stern, "Protection of Quantum Information in a Chain of Josephson Junctions", Phys. Rev. Appl. **17**, 024057 (2022).

[219] E. Hyyppä, S. Kundu, C. F. Chan, A. Gunyhó, J. Hotari, D. Janzso, K. Juliusson, O. Kiuru, J. Kotilahti, A. Landra, et al., "Unimon qubit", Nature Communications **13**, 6895 (2022).

[220] A. J. Kerman, *Efficient numerical simulation of complex Josephson quantum circuits*, (2020) arXiv:`2010.14929 [quant-ph]`.

[221] A. Di Paolo, T. E. Baker, A. Foley, D. Sénéchal, and A. Blais, "Efficient modeling of superconducting quantum circuits with tensor networks", npj Quantum Information **7**, 11 (2021).

[222] D. Ding, H.-S. Ku, Y. Shi, and H.-H. Zhao, "Free-mode removal and mode decoupling for simulating general superconducting quantum circuits", Phys. Rev. B **103**, 174501 (2021).

[223] D. K. Weiss, W. DeGottardi, J. Koch, and D. G. Ferguson, "Variational tight-binding method for simulating large superconducting circuits", Phys. Rev. Res. **3**, 033244 (2021).

[224] Z. K. Minev, Z. Leghtas, S. O. Mundhada, L. Christakis, I. M. Pop, and M. H. Devoret, "Energy-participation quantization of Josephson circuits", npj Quantum Information **7**, 131 (2021).

[225] S. P. Chitta, T. Zhao, Z. Huang, I. Mondragon-Shem, and J. Koch, "Computer-aided quantization and numerical analysis of superconducting circuits", New Journal of Physics **24**, 103020 (2022).

[226] A. Miano, V. Joshi, G. Liu, W. Dai, P. Parakh, L. Frunzio, and M. Devoret, "Hamiltonian Extrema of an Arbitrary Flux-Biased Josephson Circuit", PRX Quantum **4**, 030324 (2023).

[227] A. R. Klots and L. B. Ioffe, *SuperQuantPackage*, 2018.

[228] M. F. Gely and G. A. Steele, "QuCAT: quantum circuit analyzer tool in Python", New Journal of Physics **22**, 013025 (2020).

[229] P. Groszkowski and J. Koch, "Scqubits: a Python package for superconducting qubits", Quantum **5**, 583 (2021).

[230] Z. K. Minev, T. G. McConkey, J. Drysdale, P. Shah, D. Wang, M. Facchini, G. Harper, J. Blair, H. Zhang, N. Lanzillo, et al., *Qiskit Metal: An Open-Source Framework for Quantum Device Design & Analysis*, version 0.0.3, Mar. 2021.

[231] J. Heinsoo, S. Inel, D. Janzso, M. Jenei, J. Kotilahti, A. Landra, C. Ockeloen-Korppi, J. Räbinä, and N. Savola, *KQCircuits*, version v3.0.0, June 2021.

[232] P. Aumann, T. Menke, W. D. Oliver, and W. Lechner, "CircuitQ: an open-source toolbox for superconducting circuits", New Journal of Physics **24**, 093012 (2022).

[233] T. Rajabzadeh, Z. Wang, N. Lee, T. Makihara, Y. Guo, and A. H. Safavi-Naeini, "Analysis of arbitrary superconducting quantum circuits accompanied by a Python package: SQcircuit", Quantum **7**, 1118 (2023).

[234] R. J. Schoelkopf, P. Wahlgren, A. A. Kozhevnikov, P. Delsing, and D. E. Prober, "The Radio-Frequency Single-Electron Transistor (RF-SET): A Fast and Ultrasensitive Electrometer", Science **280**, 1238–1242 (1998).

[235] P. Wahlgren, R. J. Schoelkopf, A. A. Kozhevnikov, P. Delsing, D. E. Prober, and T. Claeson, "Radio Frequency-Single Electron Transistor: A Fast and Sensitive Electrometer Analogous to the Radio Frequency-Superconducting Quantum Interference Device", Journal of Superconductivity **12**, 741–746 (1999).

[236] R. G. Knobel and A. N. Cleland, "Nanometre-scale displacement sensing using a single electron transistor", Nature **424**, 291–293 (2003).

[237] M. D. LaHaye, O. Buu, B. Camarota, and K. C. Schwab, "Approaching the Quantum Limit of a Nanomechanical Resonator", Science **304**, 74–77 (2004).

[238] A. Naik, O. Buu, M. D. LaHaye, A. D. Armour, A. A. Clerk, M. P. Blencowe, and K. C. Schwab, "Cooling a nanomechanical resonator with quantum back-action", Nature **443**, 193–196 (2006).

[239] S. Etaki, M. Poot, I. Mahboob, K. Onomitsu, H. Yamaguchi, and H. S. J. van der Zant, "Motion detection of a micromechanical resonator embedded in a d.c. SQUID", Nature Physics **4**, 785–788 (2008).

[240] M. D. LaHaye, J. Suh, P. M. Echternach, K. C. Schwab, and M. L. Roukes, "Nanomechanical measurements of a superconducting qubit", Nature **459**, 960–964 (2009).

[241] J. D. Teufel, T. Donner, M. A. Castellanos-Beltran, J. W. Harlow, and K. W. Lehnert, "Nanomechanical motion measured with an imprecision below that at the standard quantum limit", Nature Nanotechnology **4**, 820–823 (2009).

[242] A. D. O'Connell, M. Hofheinz, M. Ansmann, R. C. Bialczak, M. Lenander, E. Lucero, M. Neeley, D. Sank, H. Wang, M. Weides, et al., "Quantum ground state and single-phonon control of a mechanical resonator", Nature **464**, 697–703 (2010).

[243] J. D. Teufel, T. Donner, D. Li, J. W. Harlow, M. S. Allman, K. Cicak, A. J. Sirois, J. D. Whittaker, K. W. Lehnert, and R. W. Simmonds, "Sideband cooling of micromechanical motion to the quantum ground state", Nature **475**, 359–363 (2011).

[244] T. A. Palomaki, J. D. Teufel, R. W. Simmonds, and K. W. Lehnert, "Entangling Mechanical Motion with Microwave Fields", Science **342**, 710–713 (2013).

[245] G. Via, G. Kirchmair, and O. Romero-Isart, "Strong Single-Photon Coupling in Superconducting Quantum Magnetomechanics", Phys. Rev. Lett. **114**, 143602 (2015).

[246] E. Romero-Sánchez, W. P. Bowen, M. R. Vanner, K. Xia, and J. Twamley, "Quantum magnetomechanics: Towards the ultrastrong coupling regime", Phys. Rev. B **97**, 024109 (2018).

[247] D. Zoepfl, M. L. Juan, C. M. F. Schneider, and G. Kirchmair, "Single-Photon Cooling in Microwave Magnetomechanics", Phys. Rev. Lett. **125**, 023601 (2020).

[248] P. Schmidt, M. T. Amawi, S. Pogorzalek, F. Deppe, A. Marx, R. Gross, and H. Huebl, "Sideband-resolved resonator electromechanics based on a nonlinear Josephson inductance probed on the single-photon level", Communications Physics **3**, 233 (2020).

[249] J. Hofer, R. Gross, G. Higgins, H. Huebl, O. F. Kieler, R. Kleiner, D. Koelle, P. Schmidt, J. A. Slater, M. Trupke, et al., "High-Q Magnetic Levitation and Control of Superconducting Microspheres at Millikelvin Temperatures", Phys. Rev. Lett. **131**, 043603 (2023).

[250] M. Gutierrez Latorre, G. Higgins, A. Paradkar, T. Bauch, and W. Wieczorek, "Superconducting Microsphere Magnetically Levitated in an Anharmonic Potential with Integrated Magnetic Readout", Phys. Rev. Appl. **19**, 054047 (2023).

[251] P. Schmidt, R. Claessen, G. Higgins, J. Hofer, J. J. Hansen, P. Asenbaum, M. Zemlicka, K. Uhl, R. Kleiner, R. Gross, et al., "Remote sensing of a levitated superconductor with a flux-tunable microwave cavity", Phys. Rev. Appl. **22**, 014078 (2024).

[252] N. Bergeal, R. Vijay, V. E. Manucharyan, I. Siddiqi, R. J. Schoelkopf, S. M. Girvin, and M. H. Devoret, "Analog information processing at the quantum limit with a Josephson ring modulator", Nature Physics **6**, 296–302 (2010).

[253] N. Bergeal, F. Schackert, M. Metcalfe, R. Vijay, V. E. Manucharyan, L. Frunzio, D. E. Prober, R. J. Schoelkopf, S. M. Girvin, and M. H. Devoret, "Phase-preserving amplification near the quantum limit with a Josephson ring modulator", Nature **465**, 64–68 (2010).

[254] N. Roch, E. Flurin, F. Nguyen, P. Morfin, P. Campagne-Ibarcq, M. H. Devoret, and B. Huard, "Widely Tunable, Nondegenerate Three-Wave Mixing Microwave Device Operating near the Quantum Limit", Phys. Rev. Lett. **108**, 147701 (2012).

[255] B. Abdo, A. Kamal, and M. Devoret, "Nondegenerate three-wave mixing with the Josephson ring modulator", Phys. Rev. B **87**, 014508 (2013).

[256] B. Abdo, K. Sliwa, F. Schackert, N. Bergeal, M. Hatridge, L. Frunzio, A. D. Stone, and M. Devoret, "Full Coherent Frequency Conversion between Two Propagating Microwave Modes", Phys. Rev. Lett. **110**, 173902 (2013).

[257] C. Macklin, K. O'Brien, D. Hover, M. E. Schwartz, V. Bolkhovsky, X. Zhang, W. D. Oliver, and I. Siddiqi, "A near–quantum-limited Josephson traveling-wave parametric amplifier", Science **350**, 307–310 (2015).

[258] T. C. White, J. Y. Mutus, I.-C. Hoi, R. Barends, B. Campbell, Y. Chen, Z. Chen, B. Chiaro, A. Dunsworth, E. Jeffrey, et al., "Traveling wave parametric amplifier with Josephson junctions using minimal resonator phase matching", Applied Physics Letters **106**, 242601 (2015).

[259] Y. A. Pashkin, T. Yamamoto, O. Astafiev, Y. Nakamura, D. V. Averin, and J. S. Tsai, "Quantum oscillations in two coupled charge qubits", Nature **421**, 823–826 (2003).

[260] D. V. Averin and C. Bruder, "Variable Electrostatic Transformer: Controllable Coupling of Two Charge Qubits", Phys. Rev. Lett. **91**, 057003 (2003).

[261] B. L. T. Plourde, J. Zhang, K. B. Whaley, F. K. Wilhelm, T. L. Robertson, T. Hime, S. Linzen, P. A. Reichardt, C.-E. Wu, and J. Clarke, "Entangling flux qubits with a bipolar dynamic inductance", Phys. Rev. B **70**, 140501 (2004).

[262] A. M. van den Brink, A. J. Berkley, and M. Yalowsky, "Mediated tunable coupling of flux qubits", New Journal of Physics **7**, 230 (2005).

[263] Y.-x. Liu, L. F. Wei, J. S. Tsai, and F. Nori, "Controllable Coupling between Flux Qubits", Phys. Rev. Lett. **96**, 067003 (2006).

[264] P. Bertet, C. J. P. M. Harmans, and J. E. Mooij, "Parametric coupling for superconducting qubits", Phys. Rev. B **73**, 064512 (2006).

[265] A. O. Niskanen, Y. Nakamura, and J.-S. Tsai, "Tunable coupling scheme for flux qubits at the optimal point", Phys. Rev. B **73**, 094506 (2006).

[266] M. Grajcar, Y.-x. Liu, F. Nori, and A. M. Zagoskin, "Switchable resonant coupling of flux qubits", Phys. Rev. B **74**, 172505 (2006).

[267] S. H. W. van der Ploeg, A. Izmalkov, A. M. van den Brink, U. Hübner, M. Grajcar, E. Il'ichev, H.-G. Meyer, and A. M. Zagoskin, "Controllable Coupling of Superconducting Flux Qubits", Phys. Rev. Lett. **98**, 057004 (2007).

[268] M. D. Reed, B. R. Johnson, A. A. Houck, L. DiCarlo, J. M. Chow, D. I. Schuster, L. Frunzio, and R. J. Schoelkopf, "Fast reset and suppressing spontaneous emission of a superconducting qubit", Applied Physics Letters **96**, 203110 (2010).

[269] E. Jeffrey, D. Sank, J. Y. Mutus, T. C. White, J. Kelly, R. Barends, Y. Chen, Z. Chen, B. Chiaro, A. Dunsworth, et al., "Fast Accurate State Measurement with Superconducting Qubits", Phys. Rev. Lett. **112**, 190504 (2014).

[270] N. T. Bronn, E. Magesan, N. A. Masluk, J. M. Chow, J. M. Gambetta, and M. Steffen, "Reducing Spontaneous Emission in Circuit Quantum Electrodynamics by a Combined Readout/Filter Technique", IEEE Transactions on Applied Superconductivity **25**, 1–10 (2015).

[271] N. T. Bronn, Y. Liu, J. B. Hertzberg, A. D. Córcoles, A. A. Houck, J. M. Gambetta, and J. M. Chow, "Broadband filters for abatement of spontaneous

emission in circuit quantum electrodynamics", Applied Physics Letters **107**, 172601 (2015).

[272] E. Flurin, N. Roch, J. D. Pillet, F. Mallet, and B. Huard, "Superconducting Quantum Node for Entanglement and Storage of Microwave Radiation", Phys. Rev. Lett. **114**, 090503 (2015).

[273] O. Naaman, J. A. Strong, D. G. Ferguson, J. Egan, N. Bailey, and R. T. Hinkey, "Josephson junction microwave modulators for qubit control", Journal of Applied Physics **121**, 073904 (2017).

[274] S. Krinner, S. Storz, P. Kurpiers, P. Magnard, J. Heinsoo, R. Keller, J. Lütolf, C. Eichler, and A. Wallraff, "Engineering cryogenic setups for 100-qubit scale superconducting circuit systems", EPJ Quantum Technology **6**, 2 (2019).

[275] B. Patra, J. P. G. van Dijk, S. Subramanian, A. Corna, X. Xue, C. Jeon, F. Sheikh, E. Juarez-Hernandez, B. P. Esparza, H. Rampurawala, et al., "19.1 A Scalable Cryo-CMOS 2-to-20GHz Digitally Intensive Controller for 4x32 Frequency Multiplexed Spin Qubits/Transmons in 22nm FinFET Technology for Quantum Computers", in 2020 IEEE International Solid- State Circuits Conference - (ISSCC) (2020), pp. 304–306.

[276] J. Koch, A. A. Houck, K. L. Hur, and S. M. Girvin, "Time-reversal-symmetry breaking in circuit-QED-based photon lattices", Phys. Rev. A **82**, 043811 (2010).

[277] A. Kamal, J. Clarke, and M. H. Devoret, "Noiseless non-reciprocity in a parametric active device", Nature Physics **7**, 311–315 (2011).

[278] B. Abdo, K. Sliwa, L. Frunzio, and M. Devoret, "Directional Amplification with a Josephson Circuit", Phys. Rev. X **3**, 031001 (2013).

[279] J. Kerckhoff, K. Lalumière, B. J. Chapman, A. Blais, and K. W. Lehnert, "On-Chip Superconducting Microwave Circulator from Synthetic Rotation", Phys. Rev. Applied **4**, 034002 (2015).

[280] K. M. Sliwa, M. Hatridge, A. Narla, S. Shankar, L. Frunzio, R. J. Schoelkopf, and M. H. Devoret, "Reconfigurable Josephson Circulator/Directional Amplifier", Phys. Rev. X **5**, 041020 (2015).

[281] F. Lecocq, L. Ranzani, G. A. Peterson, K. Cicak, R. W. Simmonds, J. D. Teufel, and J. Aumentado, "Nonreciprocal Microwave Signal Processing with a Field-Programmable Josephson Amplifier", Phys. Rev. Applied **7**, 024028 (2017).

[282] B. Abdo, M. Brink, and J. M. Chow, "Gyrator Operation Using Josephson Mixers", Phys. Rev. Applied **8**, 034009 (2017).

[283] B. J. Chapman, E. I. Rosenthal, J. Kerckhoff, B. A. Moores, L. R. Vale, J. A. B. Mates, G. C. Hilton, K. Lalumière, A. Blais, and K. W. Lehnert, "Widely Tunable On-Chip Microwave Circulator for Superconducting Quantum Circuits", Phys. Rev. X **7**, 041043 (2017).

[284] C. Müller, S. Guan, N. Vogt, J. H. Cole, and T. M. Stace, "Passive On-Chip Superconducting Circulator Using a Ring of Tunnel Junctions", Phys. Rev. Lett. **120**, 213602 (2018).

[285] B. J. Chapman, E. I. Rosenthal, and K. W. Lehnert, "Design of an On-Chip Superconducting Microwave Circulator with Octave Bandwidth", Phys. Rev. Applied **11**, 044048 (2019).

[286] B. Abdo, N. T. Bronn, O. Jinka, S. Olivadese, A. D. Córcoles, V. P. Adiga, M. Brink, R. E. Lake, X. Wu, D. P. Pappas, et al., "Active protection of a superconducting qubit with an interferometric Josephson isolator", Nature Communications **10**, 3154 (2019).

[287] B. Abdo, O. Jinka, N. T. Bronn, S. Olivadese, and M. Brink, "High-Fidelity Qubit Readout Using Interferometric Directional Josephson Devices", PRX Quantum **2**, 040360 (2021).

[288] E. I. Rosenthal, C. M. F. Schneider, M. Malnou, Z. Zhao, F. Leditzky, B. J. Chapman, W. Wustmann, X. Ma, D. A. Palken, M. F. Zanner, et al., "Efficient and Low-Backaction Quantum Measurement Using a Chip-Scale Detector", Phys. Rev. Lett. **126**, 090503 (2021).

[289] R. Asensio-Perea, A. Parra-Rodriguez, G. Kirchmair, E. Solano, and E. Rico, "Chiral states and nonreciprocal phases in a Josephson junction ring", Phys. Rev. B **103**, 224525 (2021).

[290] Y.-X. Zhang, C. R. i Carceller, M. Kjaergaard, and A. S. Sørensen, "Charge-Noise Insensitive Chiral Photonic Interface for Waveguide Circuit QED", Phys. Rev. Lett. **127**, 233601 (2021).

[291] E. N. Pozzo, D. Domínguez, and M. J. Sánchez, "Quantum chaos in the mesoscopic device for the Josephson flux qubit", Phys. Rev. B **77**, 024518 (2008).

[292] E. N. Pozzo and D. Domínguez, "Fidelity and Quantum Chaos in the Mesoscopic Device for the Josephson Flux Qubit", Phys. Rev. Lett. **98**, 057006 (2007).

[293] J. Cohen, A. Petrescu, R. Shillito, and A. Blais, "Reminiscence of Classical Chaos in Driven Transmons", PRX Quantum **4**, 020312 (2023).

[294] H. T. Quan, Y. D. Wang, Y.-x. Liu, C. P. Sun, and F. Nori, "Maxwell's Demon Assisted Thermodynamic Cycle in Superconducting Quantum Circuits", Phys. Rev. Lett. **97**, 180402 (2006).

[295] A. Ronzani, B. Karimi, J. Senior, Y.-C. Chang, J. T. Peltonen, C. Chen, and J. P. Pekola, "Tunable photonic heat transport in a quantum heat valve", Nature Physics **14**, 991–995 (2018).

[296] J. Senior, A. Gubaydullin, B. Karimi, J. T. Peltonen, J. Ankerhold, and J. P. Pekola, "Heat rectification via a superconducting artificial atom", Communications Physics **3**, 40 (2020).

[297] A. Guthrie, C. D. Satrya, Y.-C. Chang, P. Menczel, F. Nori, and J. P. Pekola, "Cooper-Pair Box Coupled to Two Resonators: An Architecture for a Quantum Refrigerator", Phys. Rev. Appl. **17**, 064022 (2022).

[298] N. Ofek, A. Petrenko, R. Heeres, P. Reinhold, Z. Leghtas, B. Vlastakis, Y. Liu, L. Frunzio, S. M. Girvin, L. Jiang, et al., "Extending the lifetime of a quantum bit with error correction in superconducting circuits", Nature **536**, 441–445 (2016).

[299] L. Hu, Y. Ma, W. Cai, X. Mu, Y. Xu, W. Wang, Y. Wu, H. Wang, Y. P. Song, C.-L. Zou, et al., "Quantum error correction and universal gate set operation on a binomial bosonic logical qubit", Nature Physics **15**, 503–508 (2019).

[300] M. Rymarz, S. Bosco, A. Ciani, and D. P. DiVincenzo, "Hardware-Encoding Grid States in a Nonreciprocal Superconducting Circuit", Phys. Rev. X **11**, 011032 (2021).

[301] X. C. Kolesnikow, R. W. Bomantara, A. C. Doherty, and A. L. Grimsmo, "Gottesman-Kitaev-Preskill State Preparation Using Periodic Driving", Phys. Rev. Lett. **132**, 130605 (2024).

[302] L.-A. Sellem, A. Sarlette, Z. Leghtas, M. Mirrahimi, P. Rouchon, and P. Campagne-Ibarcq, "Dissipative Protection of a GKP Qubit in a High-Impedance Superconducting Circuit Driven by a Microwave Frequency Comb", Phys. Rev. X **15**, 011011 (2025).

[303] R. Haenel and O. Can, *Superconducting diode from flux biased Josephson junction arrays*, (2022) arXiv:2212.02657 [cond-mat.supr-con].

[304] M. Gupta, G. V. Graziano, M. Pendharkar, J. T. Dong, C. P. Dempsey, C. Palmstrøm, and V. S. Pribiag, "Gate-tunable superconducting diode effect in a three-terminal Josephson device", Nature Communications **14**, 3078 (2023).

[305] L. Banszerus, C. W. Andersson, W. Marshall, T. Lindemann, M. J. Manfra, C. M. Marcus, and S. Vaitiek ėnas, "Hybrid Josephson Rhombus: A Superconducting Element with Tailored Current-Phase Relation", Phys. Rev. X **15**, 011021 (2025).

[306] V. Fatemi, A. R. Akhmerov, and L. Bretheau, "Weyl Josephson circuits", Phys. Rev. Research **3**, 013288 (2021).

[307] J. J. García-Ripoll, E. Solano, and M. A. Martin-Delgado, "Quantum simulation of Anderson and Kondo lattices with superconducting qubits", Phys. Rev. B **77**, 024522 (2008).

[308] J. Q. You, X.-F. Shi, X. Hu, and F. Nori, "Quantum emulation of a spin system with topologically protected ground states using superconducting quantum circuits", Phys. Rev. B **81**, 014505 (2010).

[309] D. I. Tsomokos, S. Ashhab, and F. Nori, "Using superconducting qubit circuits to engineer exotic lattice systems", Phys. Rev. A **82**, 052311 (2010).

[310] U. L. Heras, A. Mezzacapo, L. Lamata, S. Filipp, A. Wallraff, and E. Solano, "Digital Quantum Simulation of Spin Systems in Superconducting Circuits", Phys. Rev. Lett. **112**, 200501 (2014).

[311] K. Cedergren, R. Ackroyd, S. Kafanov, N. Vogt, A. Shnirman, and T. Duty, "Insulating Josephson Junction Chains as Pinned Luttinger Liquids", Phys. Rev. Lett. **119**, 167701 (2017).

[312] R. Cosmic, H. Ikegami, Z. Lin, K. Inomata, J. M. Taylor, and Y. Nakamura, "Circuit-QED-based measurement of vortex lattice order in a Josephson junction array", Phys. Rev. B **98**, 060501(R) (2018).

[313] R. Cosmic, K. Kawabata, Y. Ashida, H. Ikegami, S. Furukawa, P. Patil, J. M. Taylor, and Y. Nakamura, "Probing XY phase transitions in a Josephson junction array with tunable frustration", Phys. Rev. B **102**, 094509 (2020).

[314] A. B. Özgüler, V. E. Manucharyan, and M. G. Vavilov, *Excitation dynamics in inductively coupled fluxonium circuits*, (2021) arXiv:`2104.03300 [quant-ph]`.

[315] J. Braumüller, A. H. Karamlou, Y. Yanay, B. Kannan, D. Kim, M. Kjaergaard, A. Melville, B. M. Niedzielski, Y. Sung, A. Vepsäläinen, et al., "Prob-

ing quantum information propagation with out-of-time-ordered correlators", Nature Physics **18**, 172–178 (2022).

[316] B. Richman, C. J. Lobb, and J. M. Taylor, *Utilizing discrete variable representations for decoherence-accurate numerical simulation of superconducting circuits*, (2025) arXiv:2503.10607 [quant-ph].

[317] J. A. Pople, "Nobel Lecture: Quantum chemical models", Rev. Mod. Phys. **71**, 1267–1274 (1999).

[318] P. A. Bash, L. L. Ho, A. D. MacKerell, D. Levine, and P. Hallstrom, "Progress toward chemical accuracy in the computer simulation of condensed phase reactions", Proc Natl Acad Sci U S A **93**, 3698–3703 (1996).

[319] S. Rasmussen, K. Christensen, S. Pedersen, L. Kristensen, T. Bækkegaard, N. Loft, and N. Zinner, "Superconducting Circuit Companion—an Introduction with Worked Examples", PRX Quantum **2**, 040204 (2021).

[320] P. Krantz, M. Kjaergaard, F. Yan, T. P. Orlando, S. Gustavsson, and W. D. Oliver, "A quantum engineer's guide to superconducting qubits", Applied Physics Reviews **6**, 021318 (2019).

[321] A. Somoroff, Q. Ficheux, R. A. Mencia, H. Xiong, R. Kuzmin, and V. E. Manucharyan, "Millisecond Coherence in a Superconducting Qubit", Phys. Rev. Lett. **130**, 267001 (2023).

[322] L. B. Nguyen, Y.-H. Lin, A. Somoroff, R. Mencia, N. Grabon, and V. E. Manucharyan, "High-Coherence Fluxonium Qubit", Phys. Rev. X **9**, 041041 (2019).

[323] A. P. M. Place, L. V. H. Rodgers, P. Mundada, B. M. Smitham, M. Fitzpatrick, Z. Leng, A. Premkumar, J. Bryon, A. Vrajitoarea, S. Sussman, et al., "New material platform for superconducting transmon qubits with coherence times exceeding 0.3 milliseconds", Nature Communications **12**, 1779 (2021).

[324] C. Rigetti, J. M. Gambetta, S. Poletto, B. L. T. Plourde, J. M. Chow, A. D. Córcoles, J. A. Smolin, S. T. Merkel, J. R. Rozen, G. A. Keefe, et al., "Superconducting qubit in a waveguide cavity with a coherence time approaching 0.1 ms", Phys. Rev. B **86**, 100506 (2012).

[325] M. H. Devoret, "Quantum Fluctuations in Electrical Circuits", in Quantum Fluctuations (Les Houches Session LXIII), edited by S. Reynaud, E. Giacobino, and J. Zinn-Justin (Jan. 1997), pp. 351–386.

[326] M. H. Devoret and J. M. Martinis, "Implementing Qubits with Superconducting Integrated Circuits", Quantum Information Processing **3**, 163–203 (2004).

[327] R. G. Littlejohn, M. Cargo, J. Carrington Tucker, K. A. Mitchell, and B. Poirier, "A general framework for discrete variable representation basis sets", The Journal of Chemical Physics **116**, 8691–8703 (2002).

[328] J. C. Light, I. P. Hamilton, and J. V. Lill, "Generalized discrete variable approximation in quantum mechanics", The Journal of Chemical Physics **82**, 1400–1409 (1985).

[329] J. C. Light and T. Carrington Jr., "Discrete-Variable Representations and their Utilization", in *Advances in Chemical Physics* (John Wiley & Sons, Ltd, 2000), pp. 263–310.

[330] D. T. Colbert and W. H. Miller, "A novel discrete variable representation for quantum mechanical reactive scattering via the S-matrix Kohn method", The Journal of Chemical Physics **96**, 1982–1991 (1992).

[331] G. C. Groenenboom and D. T. Colbert, "Combining the discrete variable representation with the S-matrix Kohn method for quantum reactive scattering", The Journal of Chemical Physics **99**, 9681–9696 (1993).

[332] J. T. Muckerman, "Some useful discrete variable representations for problems in time-dependent and time-independent quantum mechanics", Chemical Physics Letters **173**, 200–205 (1990).

[333] M. Lombardi, P. Barletta, and A. Kievsky, "Variational estimates using a discrete variable representation", Phys. Rev. A **70**, 032503 (2004).

[334] P. Barletta, M. Lombardi, and A. Kievsky, "Variational DVR Calculations", Few-Body Systems **34**, 11–14 (2004).

[335] V. Szalay, "About the Variational Property of Generalized Discrete Variable Representation", The Journal of Physical Chemistry A **117**, 7075–7080 (2013).

[336] H. Wei, "Ghost levels and near-variational forms of the discrete variable representation: Application to H_2O", The Journal of Chemical Physics **106**, 6885–6900 (1997).

[337] D. Manolopoulos and R. Wyatt, "Quantum scattering via the log derivative version of the Kohn variational principle", Chemical Physics Letters **152**, 23–32 (1988).

[338] S. E. Choi and J. C. Light, "Use of the discrete variable representation in the quantum dynamics by a wave packet propagation: Predissociation of NaI($^1\Sigma^+$) $\rightarrow$

NaI(0^+) $\rightarrow$ Na(^{2}S)+I(^{2}P)", The Journal of Chemical Physics **90**, 2593–2604 (1989).

[339] J. R. Jones, F.-H. Rouet, K. V. Lawler, E. Vecharynski, K. Z. Ibrahim, S. Williams, B. Abeln, C. Yang, W. McCurdy, D. J. Haxton, et al., "An efficient basis set representation for calculating electrons in molecules", Molecular Physics **114**, 2014–2028 (2016).

[340] D. A. Mazziotti, "Spectral difference methods for solving the differential equations of chemical physics", The Journal of Chemical Physics **117**, 2455–2468 (2002).

[341] D. K. Jordan and D. A. Mazziotti, "Spectral differences in real-space electronic structure calculations", The Journal of Chemical Physics **120**, 574–578 (2004).

[342] A. Bulgac and M. M. Forbes, "Use of the discrete variable representation basis in nuclear physics", Phys. Rev. C **87**, 051301 (2013).

[343] M. Bermúdez-Montaña, M. Rodríguez-Arcos, R. Lemus, J. M. Arias, J. Gómez-Camacho, and E. Orgaz, "Algebraic DVR Approaches Applied to Describe the Stark Effect", Symmetry **12**, `10.3390/sym12101719` (2020).

[344] V. V. Albert, S. Pascazio, and M. H. Devoret, "General phase spaces: from discrete variables to rotor and continuum limits", Journal of Physics A: Mathematical and Theoretical **50**, 504002 (2017).

[345] G. Zhu, D. G. Ferguson, V. E. Manucharyan, and J. Koch, "Circuit QED with fluxonium qubits: Theory of the dispersive regime", Phys. Rev. B **87**, 024510 (2013).

[346] F. Tafuri, ed., *Fundamentals and Frontiers of the Josephson Effect*, 1st ed., Springer Series in Materials Science (Springer Nature, Cham, Switzerland, Sept. 2019).

[347] A. Cottet, "Implémentation d'un bit quantique dans un circuit supraconducteur / Implementation of a quantum bit in a superconducting circuit", Theses (Université Pierre et Marie Curie - Paris VI, Sept. 2002).

[348] M. Abramowitz and I. A. Stegun, *Handbook of Mathematical Functions with Formulas, Graphs, and Mathematical Tables* (Dover Publications, New York, New York, 1965).

[349] A. Greenbaum and T. P. Chartier, *Numerical Methods: Design, Analysis, and Computer Implementation of Algorithms* (Princeton University Press, Princeton, NJ, Apr. 2012).

[350] D. Kincaid and W. Cheney, *Numerical Analysis: Mathematics of Scientific Computing*, 1st ed. (Brooks/Cole Publishing Company, Pacific Grove, California, Jan. 1991).

[351] G. B. Arfken, H. J. Weber, and F. E. Harris, *Mathematical Methods for Physicists*, 7th ed. (Academic Press, Waltham, MA, 2013).

[352] N. J. Giordano, *Computational Physics* (Pearson, Upper Saddle River, NJ, July 1996).

[353] T. L. Beck, "Real-space mesh techniques in density-functional theory", Rev. Mod. Phys. **72**, 1041–1080 (2000).

[354] B. Fornberg, "Generation of finite difference formulas on arbitrarily spaced grids", Mathematics of Computation **51**, 699–706 (1988).

[355] R. V. Vichnevetsky, *Computer Methods for Partial Differential Equations*, Prentice-Hall Series in Computational Mathematics (Prentice Hall, Old Tappan, NJ, Dec. 1981).

[356] B. Richman, S. Ghosh, D. Carney, G. Higgins, P. Shawhan, C. J. Lobb, and J. M. Taylor, "Backaction-evading receivers with magnetomechanical and electromechanical sensors", Phys. Rev. Res. **6**, 023141 (2024).

[357] C. M. Caves, K. S. Thorne, R. W. P. Drever, V. D. Sandberg, and M. Zimmermann, "On the measurement of a weak classical force coupled to a quantum-mechanical oscillator. I. Issues of principle", Rev. Mod. Phys. **52**, 341–392 (1980).

[358] D. Mason, J. Chen, M. Rossi, Y. Tsaturyan, and A. Schliesser, "Continuous force and displacement measurement below the standard quantum limit", Nature Physics **15**, 745–749 (2019).

[359] B. P. Abbott et al. (LIGO Scientific Collaboration and Virgo Collaboration), "Observation of Gravitational Waves from a Binary Black Hole Merger", Phys. Rev. Lett. **116**, 061102 (2016).

[360] P. Purdue and Y. Chen, "Practical speed meter designs for quantum nondemolition gravitational-wave interferometers", Phys. Rev. D **66**, 122004 (2002).

[361] S. L. Danilishin, F. Y. Khalili, and H. Miao, "Advanced quantum techniques for future gravitational-wave detectors", Living Reviews in Relativity **22**, 2 (2019).

[362] S. Ghosh, D. Carney, P. Shawhan, and J. M. Taylor, "Backaction-evading impulse measurement with mechanical quantum sensors", Phys. Rev. A **102**, 023525 (2020).

[363] D. Carney, S. Ghosh, G. Krnjaic, and J. M. Taylor, "Proposal for gravitational direct detection of dark matter", Phys. Rev. D **102**, 072003 (2020).

[364] A. Attanasio, S. A. Bhave, C. Blanco, D. Carney, M. Demarteau, B. Elshimy, M. Febbraro, M. A. Feldman, S. Ghosh, A. Hickin, et al., *Snowmass 2021 White Paper: The Windchime Project*, (2022) arXiv:2203.07242 [hep-ex].

[365] S. Schreppler, N. Spethmann, N. Brahms, T. Botter, M. Barrios, and D. M. Stamper-Kurn, "Optically measuring force near the standard quantum limit", Science **344**, 1486–1489 (2014).

[366] L. F. Buchmann, S. Schreppler, J. Kohler, N. Spethmann, and D. M. Stamper-Kurn, "Complex Squeezing and Force Measurement Beyond the Standard Quantum Limit", Phys. Rev. Lett. **117**, 030801 (2016).

[367] S. Vyatchanin and E. Zubova, "Quantum variation measurement of a force", Physics Letters A **201**, 269–274 (1995).

[368] X. Xu and J. M. Taylor, "Squeezing in a coupled two-mode optomechanical system for force sensing below the standard quantum limit", Phys. Rev. A **90**, 043848 (2014).

[369] H. J. Kimble, Y. Levin, A. B. Matsko, K. S. Thorne, and S. P. Vyatchanin, "Conversion of conventional gravitational-wave interferometers into quantum nondemolition interferometers by modifying their input and/or output optics", Phys. Rev. D **65**, 022002 (2001).

[370] C. Cinquegrana, E. Majorana, P. Rapagnani, and F. Ricci, "Back-action-evading transducing scheme for cryogenic gravitational wave antennas", Phys. Rev. D **48**, 448–465 (1993).

[371] J. Beckey, D. Carney, and G. Marocco, *Quantum measurements in fundamental physics: a user's manual*, (2023) arXiv:2311.07270 [hep-ph].

[372] K. S. Thorne, R. W. P. Drever, C. M. Caves, M. Zimmermann, and V. D. Sandberg, "Quantum Nondemolition Measurements of Harmonic Oscillators", Phys. Rev. Lett. **40**, 667–671 (1978).

[373] D. Zoepfl, M. L. Juan, N. Diaz-Naufal, C. M. F. Schneider, L. F. Deeg, A. Sharafiev, A. Metelmann, and G. Kirchmair, "Kerr Enhanced Backaction Cooling in Magnetomechanics", Phys. Rev. Lett. **130**, 033601 (2023).

[374] T. Luschmann, P. Schmidt, F. Deppe, A. Marx, A. Sanchez, R. Gross, and H. Huebl, "Mechanical frequency control in inductively coupled electromechanical systems", Scientific Reports **12**, 1608 (2022).

[375] F. Hocke, X. Zhou, A. Schliesser, T. J. Kippenberg, H. Huebl, and R. Gross, "Electromechanically induced absorption in a circuit nano-electromechanical system", New Journal of Physics **14**, 123037 (2012).

[376] S. H. Crandall, *Dynamics of Mechanical and Electromechanical Systems* (R.E. Krieger Pub. Co, Malabar, Fla, 1982).

[377] A. E. Fitzgerald, C. Kingsley, and S. D. Umans, *Electric Machinery*, 6th ed, McGraw-Hill series in electrical engineering (McGraw-Hill, Boston, Mass, 2003).

[378] L. J. Kamm, *Understanding Electro-Mechanical Engineering: An Introduction to Mechatronics*, IEEE Press understanding science & technology series (Institute of Electrical and Electronics Engineers, New York, 1996).

[379] R. H. Bishop, ed., *The Mechatronics Handbook*, The Electrical Engineering Handbook Series (CRC Press, Boca Raton, Fla, 2002).

[380] F. Lecocq, J. B. Clark, R. W. Simmonds, J. Aumentado, and J. D. Teufel, "Mechanically mediated microwave frequency conversion in the quantum regime", Phys. Rev. Lett. **116**, 043601 (2016).

[381] T. Palomaki, J. Harlow, J. Teufel, R. Simmonds, and K. W. Lehnert, "Coherent state transfer between itinerant microwave fields and a mechanical oscillator", Nature **495**, 210–214 (2013).

[382] C. Regal, J. Teufel, and K. Lehnert, "Measuring nanomechanical motion with a microwave cavity interferometer", Nature Physics **4**, 555–560 (2008).

[383] E. Zeuthen, A. Schliesser, J. M. Taylor, and A. S. Sørensen, "Electrooptomechanical equivalent circuits for quantum transduction", Phys. Rev. Appl. **10**, 044036 (2018).

[384] J. D. Jackson, *Classical Electrodynamics*, 3rd ed (Wiley, New York, 1999).

[385] A. Zangwill, *Modern Electrodynamics* (Cambridge University Press, Cambridge, 2013).

[386] X. You, J. A. Sauls, and J. Koch, "Circuit quantization in the presence of time-dependent external flux", Phys. Rev. B **99**, 174512 (2019).

[387] J. Bryon, D. Weiss, X. You, S. Sussman, X. Croot, Z. Huang, J. Koch, and A. A. Houck, "Time-Dependent Magnetic Flux in Devices for Circuit Quantum Electrodynamics", Phys. Rev. Appl. **19**, 034031 (2023).

[388] R. N. Rajmohan, A. Kenawy, and D. DiVincenzo, *Circuit quantization with time-dependent flux:the parallel-plate SQUID*, (2022) arXiv:2201.01945 [quant-ph].

[389] R.-P. Riwar and D. P. DiVincenzo, "Circuit quantization with time-dependent magnetic fields for realistic geometries", npj Quantum Information **8**, 36 (2022).

[390] X. Ma, J. J. Viennot, S. Kotler, J. D. Teufel, and K. W. Lehnert, "Non-classical energy squeezing of a macroscopic mechanical oscillator", Nature Physics **17**, 322–326 (2021).

[391] J. J. Viennot, X. Ma, and K. W. Lehnert, "Phonon-Number-Sensitive Electromechanics", Phys. Rev. Lett. **121**, 183601 (2018).

[392] J.-M. Pirkkalainen, S. U. Cho, J. Li, G. S. Paraoanu, P. J. Hakonen, and M. A. Sillanpää, "Hybrid circuit cavity quantum electrodynamics with a micromechanical resonator", Nature **494**, 211–215 (2013).

[393] L. Tosi, D. Vion, and H. le Sueur, "Design of a Cooper-Pair Box Electrometer for Application to Solid-State and Astroparticle Physics", Phys. Rev. Appl. **11**, 054072 (2019).

[394] S. Bosco, J. Lindkvist, and G. Johansson, "Simulating moving cavities in superconducting circuits", Phys. Rev. A **100**, 023817 (2019).

[395] J. Clarke, "Principles and applications of SQUIDs", Proceedings of the IEEE **77**, 1208–1223 (1989).

[396] T. Schurig, "Making SQUIDs a practical tool for quantum detection and material characterization in the micro- and nanoscale", Journal of Physics: Conference Series **568**, 032015 (2014).

[397] W. P. Bowen and G. J. Milburn, *Quantum Optomechanics* (CRC Press, Taylor & Francis Group, Boca Raton. FL, 2016).

[398] A. A. Clerk, M. H. Devoret, S. M. Girvin, F. Marquardt, and R. J. Schoelkopf, "Introduction to quantum noise, measurement, and amplification", Rev. Mod. Phys. **82**, 1155–1208 (2010).

[399] M. Aspelmeyer, T. J. Kippenberg, and F. Marquardt, "Cavity optomechanics", Rev. Mod. Phys. **86**, 1391–1452 (2014).

[400] C. W. Gardiner and M. J. Collett, "Input and output in damped quantum systems: Quantum stochastic differential equations and the master equation", Phys. Rev. A **31**, 3761–3774 (1985).

[401] S. Ghosh, M. A. Feldman, S. Hong, C. Marvinney, R. Pooser, and J. M. Taylor, *Combining quantum noise reduction resources: a practical approach*, (2022) arXiv:2211.14460 [quant-ph].

[402] M. Kuhlen, N. Weiner, J. Diemand, P. Madau, B. Moore, D. Potter, J. Stadel, and M. Zemp, "Dark matter direct detection with non-Maxwellian velocity structure", Journal of Cosmology and Astroparticle Physics **2010**, 030 (2010).

[403] H. Goldstein, C. Poole, and J. Safko, *Classical Mechanics* (3rd ed. Addison Wesley, San Francisco, CA, 2002).

[404] B. Richman and J. M. Taylor, "Circulation by Microwave-Induced Vortex Transport for Signal Isolation", PRX Quantum **2**, 030309 (2021).

[405] D. Pozar, *Microwave engineering* (Wiley, Hoboken, NJ, 2012).

[406] C. Owens, A. LaChapelle, B. Saxberg, B. M. Anderson, R. Ma, J. Simon, and D. I. Schuster, "Quarter-flux Hofstadter lattice in a qubit-compatible microwave cavity array", Phys. Rev. A **97**, 013818 (2018).

[407] G. Viola and D. P. DiVincenzo, "Hall Effect Gyrators and Circulators", Phys. Rev. X **4**, 021019 (2014).

[408] A. C. Mahoney, J. I. Colless, S. J. Pauka, J. M. Hornibrook, J. D. Watson, G. C. Gardner, M. J. Manfra, A. C. Doherty, and D. J. Reilly, "On-Chip Microwave Quantum Hall Circulator", Phys. Rev. X **7**, 011007 (2017).

[409] A. C. Mahoney, J. I. Colless, L. Peeters, S. J. Pauka, E. J. Fox, X. Kou, L. Pan, K. L. Wang, D. Goldhaber-Gordon, and D. J. Reilly, "Zero-field edge plasmons in a magnetic topological insulator", Nature Communications **8**, 1836 (2017).

[410] S. Barzanjeh, M. Wulf, M. Peruzzo, M. Kalaee, P. B. Dieterle, O. Painter, and J. M. Fink, "Mechanical on-chip microwave circulator", Nature Communications **8**, 953 (2017).

[411] R. Fazio and H. van der Zant, "Quantum phase transitions and vortex dynamics in superconducting networks", Physics Reports **355**, 235–334 (2001).

[412] H. van der Zant, "Quantum, ballistic vortices", Physica B: Condensed Matter **222**, Proceedings of the ICTP Workshop on Josephson Junction Arrays, 344–352 (1996).

[413] R. Fazio, U. Geigenmüller, and G. Schön, "Quantum Vortices in Josephson Junction Arrays", in *Quantum Fluctuations in Mesoscopic and Macroscopic Systems*, edited by H. A. Cerdeira, F. Guinea López, and U. Weiss (World Scientific, 1991), p. 214.

[414] D. J. Griffiths, *Introduction to Electrodynamics*, 4th ed. (Pearson Education Inc., Boston, MA, 2013).

[415] J. J. Sakurai and J. Napolitano, *Modern Quantum Mechanics*, 2nd ed. (Addison-Wesley, Boston, MA, 2011).

[416] E. Fradkin, *Chapter 3- Linear Response Theory*, Last accessed on May 16, 2019.

[417] P. Coleman, *Introduction to Many-Body Physics* (Cambridge University Press, 2015).

[418] A. Zagoskin, *Quantum theory of many-body systems*, 2nd ed., Graduate texts in physics (Springer International Publishing, Cham, Switzerland, June 2014).

[419] D. F. Walls and G. J. Milburn, *Quantum Optics* (2nd ed. Springer, Berlin, 2008).

[420] L. Ranzani and J. Aumentado, "Graph-based analysis of nonreciprocity in coupled-mode systems", New Journal of Physics **17**, 023024 (2015).

[421] P. K. Aravind, "Geometrical interpretation of the simultaneous diagonalization of two quadratic forms", American Journal of Physics **57**, 309–311 (1989).

[422] K. F. Riley, M. P. Hobson, and S. J. Bence, *Mathematical Methods for Physics and Engineering: A Comprehensive Guide*, 3rd ed. (Cambridge University Press, 2006).

[423] R. Loudon, *The Quantum Theory of Light* (Oxford University Press, Sept. 2000).

[424] K. J. Blow, R. Loudon, S. J. D. Phoenix, and T. J. Shepherd, "Continuum fields in quantum optics", Phys. Rev. A **42**, 4102–4114 (1990).

[425] M. O. Scully and M. S. Zubairy, *Quantum Optics* (Cambridge University Press, 1997).

[426] P. Lambropoulos and D. Petrosyan, *Fundamentals of Quantum Optics and Quantum Information*, en, 2007th ed. (Springer, Berlin, Germany, Oct. 2006).

[427] P. Harvey-Collard, G. Zheng, J. Dijkema, N. Samkharadze, A. Sammak, G. Scappucci, and L. M. K. Vandersypen, "On-Chip Microwave Filters for High-Impedance Resonators with Gate-Defined Quantum Dots", Phys. Rev. Applied **14**, 034025 (2020).

[428] N. Samkharadze, A. Bruno, P. Scarlino, G. Zheng, D. P. DiVincenzo, L. DiCarlo, and L. M. K. Vandersypen, "High-Kinetic-Inductance Superconducting Nanowire Resonators for Circuit QED in a Magnetic Field", Phys. Rev. Applied **5**, 044004 (2016).

[429] A. J. Landig, J. V. Koski, P. Scarlino, U. C. Mendes, A. Blais, C. Reichl, W. Wegscheider, A. Wallraff, K. Ensslin, and T. Ihn, "Coherent spin–photon coupling using a resonant exchange qubit", Nature **560**, 179–184 (2018).